

Electronic Thesis and Dissertation Repository

5-17-2019 10:30 AM


Non-Traditional Metallation of Metallothioneins with Xenobiotic Therapeutic Metals

Daisy L. Wong
The University of Western Ontario

Supervisor
Stillman, Martin J.
The University of Western Ontario

Graduate Program in Chemistry
A thesis submitted in partial fulfillment of the requirements for the degree in Doctor of Philosophy
© Daisy L. Wong 2019

Follow this and additional works at: <https://ir.lib.uwo.ca/etd>

 Part of the [Analytical Chemistry Commons](#), [Inorganic Chemistry Commons](#), [Medicinal-Pharmaceutical Chemistry Commons](#), and the [Other Chemistry Commons](#)

Recommended Citation

Wong, Daisy L., "Non-Traditional Metallation of Metallothioneins with Xenobiotic Therapeutic Metals" (2019). *Electronic Thesis and Dissertation Repository*. 6338.
<https://ir.lib.uwo.ca/etd/6338>

This Dissertation/Thesis is brought to you for free and open access by Scholarship@Western. It has been accepted for inclusion in Electronic Thesis and Dissertation Repository by an authorized administrator of Scholarship@Western. For more information, please contact wlsadmin@uwo.ca.

Abstract

The rise of the Anthropocene has seen more global pollution than before in history. With the explosion of consumer electronics in the last half century, the rise of metal pollution from their extraction and disposal results in the unnatural introduction of heavy and rare metals into the ecosystem. Organisms have a metal defense protein, metallothionein, which has multiple roles in essential metal regulation and protection against toxic metal exposure. However, these modern heavy metals prominent in electronics are not found biologically and their interactions in the body are generally unknown. Some of these metals are employed as therapeutic agents in the treatment of cancers, and as such this Thesis describes an investigation of therapeutic agents as models for heavy metal pollution to provide insight into the mechanisms of metal metabolism. Using electrospray ionization mass spectrometry and spectroscopic techniques, the binding of human metallothionein with the exotic metals platinum and rhodium is explored. Platinum and rhodium bind readily to human metallothionein, raising concerns for toxicity.

Keywords

Metallothionein, metal regulation, metalloprotein, metalation, metallochaperone, glutathione, binding constants, kinetic rate constants, pH-dependence, metal-thiolate clusters, cisplatin, metallodrugs, Platinum Group Metals, rhodium, oxidation, drug resistance, heavy metal pollution, environmental toxicity, anthropogenic waste, xenobiotic metals, electronic waste, Molecular Mechanics, Molecular Dynamics, Time-Dependent Density Functional Theory, Molecular Orbital Theory, UV-visible Absorption Spectroscopy, Circular Dichroism Spectroscopy, Native Electrospray Ionization Mass Spectrometry, Denaturant, Non-platinum cancer therapeutics, Non-traditional metalation.

Summary for Lay Audience

Metals are everywhere. Some metals are required by humans and organisms as nutrients, while some can be extremely toxic. These toxic metals can be deadly depending on amount of exposure, often causing heavy damage to cells and tissues. Life has adapted to light levels of toxic metal exposure with proteins that are involved in metal binding - a group of proteins known as Metallothioneins. When exposed to toxic metals, cells will increase the production of this protein, metallothionein, to counteract the increased exposure. These metallothionein proteins capture the toxic metal and isolate it from performing its toxic activity. This response also can occur in some cancer cells, in response to metal-based therapy (cisplatin, a platinum-based drug), where the metal in the drug triggers the cancer cell to have an aggressively defensive response. At the chemical level, metallothionein acts to break apart the drug molecule and isolate the toxic metal for safe excretion from the body. Recent research in constructing robust molecular frameworks for these drugs to improve cancer treatment efficacy may be able to bypass Metallothionein's defensive nature in these aggressive cancers. Using an extremely precise analytical methods known as mass spectrometry that show the changes in the exact mass as the protein breaks down the metal from the drug. While metal-based drugs are a specific type of toxic metal exposure, there is a fear of the increased impact of human activity on ecosystems, climate, and the environment will result in toxic metal exposure to all life in ways that has not been done before. These involve toxic metals that have never had a biological role and are found in major electronics and consumer goods that are now a standard of living. The implications of these cancer drug analyses with metallothioneins are extended to address this issue of toxic metal pollution and its effects.

Co-Authorship Statement

This thesis contains material from previously published manuscripts. Dr. Martin Stillman is a coauthor of all the published papers and supervised Daisy Wong. For all chapters that were published, Ms. Daisy Wong wrote the initial draft of the paper. Dr. Martin Stillman was involved in all levels of publication and had major roles in both editing and revising the published manuscripts.

For all Chapters except Chapter 2 and 6, Ms. Daisy Wong was solely responsible for acquiring all of the data, preparing the figures, and drafting the manuscripts with guidance and assistance from Dr. Martin Stillman.

The conceptual experimental design for the experiments in Chapter 2 were carried out Ms. Natalie Korkola, Ms. Daisy Wong, and Dr. Martin Stillman. Ms. Natalie Korkola carried out the sample preparation, experimental procedures, data collection, and creating the figures with assistance and guidance from Dr. Martin Stillman and Ms. Daisy Wong. Ms. Daisy Wong wrote the paper for publication. Editing of the draft was carried out by Ms. Daisy Wong, Ms. Natalie Korkola, and Dr. Martin Stillman. Ms. Natalie Korkola is a coauthor of the associated manuscript.

The computational calculations reported, and related discussion in Chapter 6 were carried out by Ms. Angel Zhang. Ms. Daisy Wong carried out the sample preparation, experimental procedures, data collection, and creating the figures with assistance and guidance from Dr. Martin Stillman. Ms. Angel Zhang created figures for the calculated results. Ms. Daisy Wong wrote the paper for publication. Mr. Abayomi Faponle and Dr. Sam P. de Visser carried out initial calculations that led to some of the experiments performed in Chapter 6. Editing of the draft was carried out by Ms. Daisy Wong, Ms. Angel Zhang and Dr. Martin Stillman. Ms. Angel Zhang is listed as a coauthor on the associated manuscript. For their contributions, Mr. Abayomi Faponle and Dr. Sam P. de Visser (University of Manchester, UK) are also listed as coauthors on the associated manuscript.

Acknowledgments

First and foremost, I thank my supervisor and friend Professor Martin Stillman, for introducing me to bioinorganic chemistry and providing me the opportunity to pursue my own original research. I am forever grateful for the mentorship and camaraderie he has given over the years, as well as the many amazing opportunities to network and present my research to the international community.

I have been a member of the Stillman Bioinorganic Group for almost a decade and have watched many members in transit. I would like to thank former group members Dr. Tyler Pinter, Dr. Gordon Irvine, Dr. Duncan Sutherland, and Dr. Mike Tiedemann for my initial training.

I am grateful to have worked closely with Ms. Angel Zhang, Ms. Judith Scheller, Ms. Lina Heinlein, and Dr. Dorothee Ott, and will treasure the many wonderful memories we all shared. A special thank you goes to Ms. Angel Zhang for teaching me the wonders of computational chemistry.

I am thankful to have worked with the upcoming members of the group Ms. Natalie Korkola, Ms. Amelia Yuan, Ms. Adyn Melenbacher, and Mr. Riley Hooper, I believe you are all talented individuals and I wish you the best in whichever paths you carve for yourselves.

This Thesis could not have been completed without the support of the staff at the Electronic Shop at UWO, as the miracles they work keep our equipment and computers running smoothly. Special thanks to Mr. Doug Hairsine for the maintenance, training, and advice on the operation of the ESI-MS. Thank you to Dr. Chris Levy (UWO), Matt Werm (The Grad Club, UWO), Andrew Wall (former Electronic Shop), Matthew Pelletier, Alfred Nataprawira, and Andrew Day (and his cats, Hobbes and Caprica) for your encouragement and unwavering support.

And lastly, thank you to my mum and dad, for without them, I would not be here today.

Table of Contents

Abstract	i
Co-Authorship Statement.....	iii
Acknowledgments.....	iv
Table of Contents	v
List of Tables	xi
List of Figures	xii
List of Appendices	xvi
List of Abbreviations	xvii
Chapter 1	1
1 Introduction to Metallothioneins*	1
1.1 Metals are Ubiquitous	1
1.1.1 Zn(II) is Essential, Cd(II) is Toxic.....	3
1.1.1.1 Homeostasis	4
1.2 Metallothioneins are Ubiquitous.....	8
1.2.1 Human Metallothioneins.....	10
1.3 Structural Elements of Metallothioneins	11
1.3.1 Metal-Induced Structure	11
1.3.2 Non-Traditional Metallation of Metallothioneins.....	12
1.4 Techniques Used in this Thesis.....	13
1.4.1 Expression and Purification of Recombinant Human Metallothionein 1a.....	13
1.4.2 Spectroscopic Methods	16
1.4.3 Native Electrospray Ionization Mass Spectrometry (ESI-MS).....	17

1.4.4	Computational Studies of Metallothionein	25
1.5	Scope.....	26
1.6	References	28
Chapter 2	34
2	Understanding Cd ²⁺ Binding Mechanisms and its Relation to the Intrinsically Disordered Structure of Metallothioneins*	34
2.1	The Native Structure of Metallothionein	34
2.2	Experimental Methods	38
2.2.1	Solution Preparation.....	38
2.2.2	Mass Spectral Studies	41
2.2.3	Stopped Flow Studies	41
2.2.4	Fitting of the Kinetic Traces	42
2.2.5	Molecular Modelling	43
2.3	Results.....	43
2.3.1	Denaturation of MT with Guanidinium Hydrochloride.....	43
2.3.2	Relative k _{obs} Decreases with Increasing Denaturant at pH 5 and Fixed Metal Status	48
2.3.3	The Cd(II) Metallation Rate is pH Dependent.....	49
2.3.4	Relative k _{obs} Decreases with Increasing Metallation	54
2.3.5	Metallation is Temperature Dependent.....	56
2.4	Discussion.....	57
2.4.1	Does Native Apo-MT have a Folded Structure?.....	57
2.4.2	Metallation Slows in the Presence of Denaturant	58
2.4.3	pH Changes the Dominant Metal Binding Pathway: Cluster Formation at pH 5 is Slower than Bead Formation at pH 8	59
2.4.4	Why is Terminal Cysteine Coordination Faster than Cluster Formation?	60

2.4.5	Rate as a Function of Metal Loading	60
2.4.6	Temperature Dependence of Metallation.....	61
2.4.7	Metallation of Unfolded Apo-MT is Slower than Native Folded MT	61
2.5	Conclusions.....	62
2.6	References	63
Chapter 3	68
3	Capturing Platinum in Cisplatin: Kinetic Reactions with Recombinant Human apo-Metallothionein 1a*	68
3.1	Introduction.....	68
3.1.1	Cisplatin: A Standard Treatment for Cancer.....	68
3.1.2	Metallothionein and Drug Resistance	70
3.1.3	Biological Significance	71
3.2	Experimental Methods	72
3.3	Results and Discussion	73
3.4	Conclusion	82
3.5	References	83
Chapter 4	89
4	Destructive Interactions of Dirhodium(II) Tetraacetate with β Metallothionein rh1a*.....	89
4.1	Introduction.....	89
4.1.1	Dirhodium(II) Tetraacetate as a Model Chemotherapeutic Complex.....	90
4.1.2	Electrospray Ionization Mass Spectrometry (ESI-MS)	90
4.2	Experimental Methods	91
4.3	Results.....	92
4.4	Conclusion	97
4.5	References	98

Chapter 5.....	101
5 Metallothionein: an Aggressive Scavenger– The Metabolism of Rhodium(II) Tetraacetate (Rh ₂ (Oac) ₄)*	101
5.1 Heavy Metal Pollution from Anthropogenic Sources.....	101
5.2 Exposure to Xenobiotic Metals from Therapeutics	102
5.3 Cytotoxic Dirhodium(II) Tetraacetate as a Model Metal Complex.....	103
5.4 Scope and Application of Results	104
5.5 Experimental Methods	105
5.6 Results.....	107
5.6.1 Metallation Reactions of MT with Rh ₂ (Oac) ₄ : Optical Spectroscopic Properties	107
5.6.2 Initial Deconstruction of Rh ₂ (Oac) ₄ by Apo-MT: Rapid Displacement of the Tetraacetate Ligands.....	109
5.6.3 Accumulation of Rh ₂ : Formation of Rh ₂ MT, Rh ₄ MT, and Rh ₆ MT.....	110
5.6.4 Modeling the Reaction: Determination of Relative Binding Constants (K _f)	112
5.6.5 Accumulation of Rh ₂ (Oac) ₄ in αMT: Evidence for Structure-Dependent Metallation.....	115
5.6.6 3D Models: Cysteine Accessibility throughout Metallation.....	117
5.7 Discussion.....	119
5.7.1 Chronic Presence of Anthropogenic Pt, Pd, Rh (PGM's).....	119
5.7.2 Binding Reactions of MT with Rh ₂ (Oac) ₄ : Explaining the Spectroscopic Results	120
5.7.3 Metallothionein: Non-Traditional Metallation and Metal Complex Deconstruction is Evident from the Mass Spectra	120
5.7.4 Structure-Dependent Metallation of Metallothioneins: Rigid Rh ₂ Binding and Comparison of Binding Constants	123
5.7.5 Solvent-Cysteine Accessibility and Protein Flexibility throughout Metallation	124

5.8	Conclusions.....	127
5.9	References.....	128
Chapter 6.....		138
6	Glutathione Binding to Dirhodium(II) Tetraacetate: a Spectroscopic, Mass Spectral and Computational Study of an Anti-Tumor Compound Bound to a Model Thiol* .	138
6.1	Introduction.....	138
6.2	Experimental Methods	142
6.3	Results and Discussion	143
6.3.1	UV-Visible and Circular Dichroism Spectroscopy Following the Colourful Reaction of Glutathione with Rh ₂ (Oac) ₄	143
6.3.2	Analysis by Electrospray Ionization Mass Spectrometry	146
6.3.3	Competition by Glutathione for the Axially-Coordinated Methionine in Rh ₂ (Oac) ₄ (Met)	149
6.3.4	DFT Calculations Provide Insight into the Stability of the GSH Complexes.....	153
6.3.5	Origins of the Electronic Absorption Spectrum.....	162
6.4	Conclusions.....	164
6.5	References.....	165
Chapter 7.....		171
7	Conclusions: Xenobiotic Metals in Therapeutic Agents as Models for Toxicity*	171
7.1	Exotic Metals as Medicines	172
7.2	MT Metabolism of Metal-based Drugs.....	177
7.3	A New Biological Role for MT	180
7.4	References.....	182
Appendix A: Observed Rate Constants for Experiments Performed in Chapter 2.....		188
Appendix B: Known Kinetic and Equilibrium Binding Constants for MTs		190
Appendix C: Supplementary Structures and Energies for Rh ₂ bound MT		194

Appendix D: Surfaces and Orbital Energies for GSH bound to Rh ₂ (Oac) ₄	210
Appendix E: Copyright Permissions.....	223
Curriculum Vitae	225

List of Tables

Table 3-1 Fitted reaction rate k values from experimental mass spectral data	81
Table 5-1 Relative equilibrium binding constants for the reaction of $\text{Rh}_2(\text{Oac})_4$ with Apo-MT.....	113
Table 6-1 Computational parameters derived from TD-DFT calculations.....	163

List of Figures

Figure 1-1 Dose-Response Curve (Bertrand Diagram).....	2
Figure 1-2 Donation of Zn(II) in Zn-MT to apo carbonic anhydrase	6
Figure 1-3 Mammalian MT isoforms	9
Figure 1-4 Human MT1 and MT2 protein sequence	10
Figure 1-5 LB agar and LB broth preparation	16
Figure 1-6 An ESI-TOF-MS and its ionization mechanism	19
Figure 1-7 Charge state and deconvoluted mass spectra	20
Figure 1-8 Various cysteine alkylating agents.....	22
Figure 1-9 Decreasing rate constants shown in the stepwise metallation of $\beta\alpha$ MT and its individual domains.....	24
Figure 2-1 The many structures of metallothionein.....	36
Figure 2-2 A schematic of the SFM apparatus.	42
Figure 2-3 Native and denatured MT modified by NEM	44
Figure 2-4 Plot of the observed rate constant as a function of GdmCl concentration.	49
Figure 2-5 Relationship between observed rate constant k of the reaction of native apo-MT.....	50
Figure 2-6 ESI mass spectra for the Cd(II) titration of apo-MT at pH 5	51
Figure 2-7 ESI mass spectra for the Cd(II) titration of apo-MT at pH 8	52
Figure 2-8 Kinetic absorption traces of MT metallation.....	53
Figure 2-9 Comparison of rate constants	54

Figure 2-10 Cadmium equivalence vs. observed metallation rate k	55
Figure 2-11 Arrhenius plot for Cd(II) metallation of MT.....	56
Figure 3-1 ESI mass spectra following the reaction of cisplatin with apo-MT1a.	74
Figure 3-2 ESI mass spectra following the reaction of cisplatin with apo-MT1a in bar graph representation.....	75
Figure 3-3 Detailed ESI mass spectral data of CDDP ₁ MT and CDDP ₂ MT	76
Figure 3-4 Experimental speciation abundance over time.....	78
Figure 3-5 Experimental and simulated relative speciation abundance.....	80
Figure 4-1 Deconvoluted time-dependent ESI-mass spectra recorded following the mixing of apo-β-MT with excess Rh ₂ (Oac) ₄ at pH 7.3.....	94
Figure 4-2 Absorption and CD spectra of the reaction of Rh ₂ (Oac) ₄ and β-MT	95
Figure 4-3 Molecular Dynamics structure for Rh ₂ -bound β-MT.....	97
Figure 5-1 Ball-and-stick representation of (Rh ₂ (Oac) ₄).....	103
Figure 5-2 Spectroscopic results of the Rh ₂ (Oac) ₄ into MT titration.....	108
Figure 5-3 Initial deconstruction of Rh ₂ (Oac) ₄ by apo-MT observed with ESI – MS. ...	109
Figure 5-4 ESI mass spectral data recorded during the titration of apo-MT with aliquots 0.0 to 2.0 mol. eq. Rh ₂ (Oac) ₄	111
Figure 5-5 Experimental and simulated speciation abundance.....	112
Figure 5-6 ESI -mass spectral data of modified and unmodified mixed Rh ₂ metallated species	113
Figure 5-7 Mass spectral data of the alkylation of Rh ₂ -bound MT	114

Figure 5-8 ESI mass spectral data of the low pH titration of Rh ₂ (Oac) ₄ into αMT	116
Figure 5-9 Energy minimized molecular dynamics models of apo-MT, Rh ₂ MT, Rh ₄ MT, and Rh ₆ MT.....	118
Figure 6-1 Structures described in Chapter 6.....	139
Figure 6-2 UV-visible absorption spectra of 500 μM Rh ₂ (Oac) ₄ with aliquots of reduced GSH added at pH 3.0 in deionized water.....	144
Figure 6-3 CD spectral results of glutathione reacting with Rh ₂ (Oac) ₄	145
Figure 6-4 Low pH reaction of Rh ₂ (Oac) ₄ with GSH.....	147
Figure 6-5 Reaction of Rh ₂ (Oac) ₄ with GSH at physiological pH	148
Figure 6-6 UV-visible absorption spectral changes following the reaction of an aqueous solution of 500 μM Rh ₂ (Oac) ₄ with 2 mol. eq. of methionine (Met) following 20 minutes of mixing. 2 mol. eq. of glutathione was then added and the spectrum monitored.	151
Figure 6-7 MO energies and isoelectric density surfaces for the Mos that contribute to the visible-near UV absorption spectra for [Rh ₂ (Oac) ₄], from DFT geometry optimization calculations.	154
Figure 6-8 MO energies and isoelectric density surfaces for the Mos that contribute to the visible-near UV absorption spectra for [Rh ₂ (Oac) ₄ (H ₂ O) ₂] from DFT geometry optimization calculations.	156
Figure 6-9 MO energies and isoelectric density surfaces for the Mos that contribute to the visible-near UV absorption spectra for [Rh ₂ (Oac) ₄ (GS)(H ₂ O)] ⁻ from DFT geometry optimization calculations.	158
Figure 6-10 MO energies and isoelectric density surfaces for the Mos that contribute to the visible-near UV absorption spectra for [Rh ₂ (Oac) ₄ (GS) ₂] ²⁻ from DFT geometry optimization calculations.	159

Figure 6-11 Electron density surface representation of the highest occupied and lowest unoccupied orbitals for $[\text{Rh}_2(\text{Oac})_4(\text{GS})(\text{H}_2\text{O})]^-$ and $[\text{Rh}_2(\text{Oac})_4(\text{GS})_2]^{2-}$	160
Figure 6-12 Calculated absorption and orbital contributions to the excited states from TD-DFT calculations for $\text{Rh}_2(\text{Oac})_4$ and the complex coordinated by water and GS^{1-}	161
Figure 7-1 Cisplatin and its subsequently developed analogs.	174
Figure 7-2 Structures of Ru(II) complexes NAMI-A (Left), KP1019 (Right), and RAPTA-C (bottom).	176
Figure 7-3 Graphical abstract for the breakdown of cisplatin by MT using ESI-MS. <i>Reproduced from reference ²² with permission from the Royal Society of Chemistry.....</i>	178
Figure 7-4 Graphical abstract depicting the encapsulation of a Rh-Rh core by the β -MT domain.....	178
Figure 7-5 Graphical abstract emphasizing the harmony of the methods used to explain the strength of the metal-thiolate bond.	179

List of Appendices

Appendix A: Observed Rate Constants for Experiments Performed in Chapter 2.....	188
Appendix B: Known Kinetic and Equilibrium Binding Constants for MTs	190
Appendix C: Supplementary Structures and Energies for Rh ₂ bound MT	194
Appendix D: Surfaces and Orbital Energies for GSH bound to Rh ₂ (Oac) ₄	210
Appendix E: Copyright Permissions.....	223

List of Abbreviations

CA	Carbonic Anhydrase
CD	Circular Dichroism
CDDP	<i>cis</i> -diamminedichloridoplatinum(II)
cDNA	Complementary DNA
DI	Deionized Water
DNA	Deoxyribonucleic Acid
DTNB	5,5'-Disulfanediylbis(2-nitrobenzoic acid)
ESI-MS	Electrospray Ionisation Mass Spectrometry
EXAFS	Extended X-ray Absorption Fine Structure
FRET	Förster Resonance Energy Transfer
GdmCl	Guanidinium Chloride
GSH	Glutathione
hMT	Human Metallothionein
HPLC	High Performance Liquid Chromatography
IAM	Iodoacetamide
IPTG	Isopropyl β -D-1-thiogalactopyranoside
LB	Luria-Bertani
LMCT	Ligand to metal charge transfer
m/z	Mass to charge ratio
MD	Molecular Dynamics
Met	Methionine
MM3	Molecular Mechanics
MO	Molecular Orbital
MRE	Metal Response Element
mRNA	Messenger RNA
MRP1	Metal response protein 1
MRP2	Metal response protein 2
MS	Mass Spectrometry
MT	Metallothionein
MW	Molecular Weight
MWCO	Molecular Weight Cut Off
NMR	Nuclear Magnetic Resonance
PGM	Platinum Group Metals
rhMT	Recombinant human metallothionein
Rh ₂ (Oac) ₄	Dirhodium(II) Tetraacetate
RNA	Ribonucleic acid
SFM	Stropped-Flow Machine
TD-DFT	Time-Dependent Density Functional Theory
TOF	Time-of-Flight

Chapter 1

1 Introduction to Metallothioneins*

1.1 Metals are Ubiquitous

Living organisms are exposed to metals everywhere on Earth: from its crust and from its bodies of water, and through particulates in the air. Essential, non-essential, and toxic metals are consumed from fruits, vegetables and meats, and drinking water. Some of these metals are necessary for life and play a critical role in biological processes, while others can be extremely harmful. Where one resides geographically is a factor in the dietary source of metals. For instance, living near an active volcano may make one more exposed to airborne metals that settle in surrounding lands, which then become incorporated in the surrounding vegetation. This is also the case of those living downwind from coal power electric stations and living adjacent to landfill sites. In contrast, other regions of the earth are so metal deficient in the soil that they cannot sustain agriculture. Heavily urbanized cities with an abundance of vehicular traffic and industries introduce metals through exhaust and waste products. Alarming, for example the effects of this pollution can also be traced in the correlation of heavy metal content in honey in bee farms in close proximity to urban development.¹ Human exposure to heavy metals is also related to the occupational environment, for instance industrial workers involved in raw material processing are more likely to have higher exposure to toxic xenobiotic metals. Metal bound proteins isolated from fish² such as rainbow trout (*Salmo gairdneri*),³ show that polluting aquatic bodies with mineral waste can result in bioaccumulation in the tissue. Yet despite the ubiquity of heavy toxic metals, there is clearly a defense mechanism in play that protects organisms against such constant, chronic exposures.

Even in the environmentally conscious minds of the 21st century, the trash from the past haunts us.⁴ Widespread global metal poisoning events from industrial malpractices still leave scars (for more information, google search terms like “Itai-itai Disease,” or “Ontario Minamata Disease”). While as a whole, the human population is moving towards “green” technology, waste generation from infrastructure materials and consumer goods is still a major issue. In the current technological age, our love for super computers

*A version of this chapter has been submitted for publication:
In *Comprehensive Coordination Chemistry III, Volume 8: Bio-coordination Chemistry*, Elsevier.
Reproduced with permission from: D. L. Wong and M. J. Stillman.

that fit in our hands demands greater quantities of rare metals. The mining, refining, and production of materials containing these metals can be devastating on the environment.⁴⁻⁶ The end of product life cycles also leaves much metal behind in landfill sites. Some of these metals being discarded have never been biologically present or played any role in physiological chemistry yet is now well known that this pollution is being distributed globally. As a result, all life across the globe will eventually be exposed to a host of xenobiotic metals that are unknown to human and organismal physiology. To understand the effects of this non-traditional metal exposure, we first must understand the metal regulation mechanisms that Life has in play.

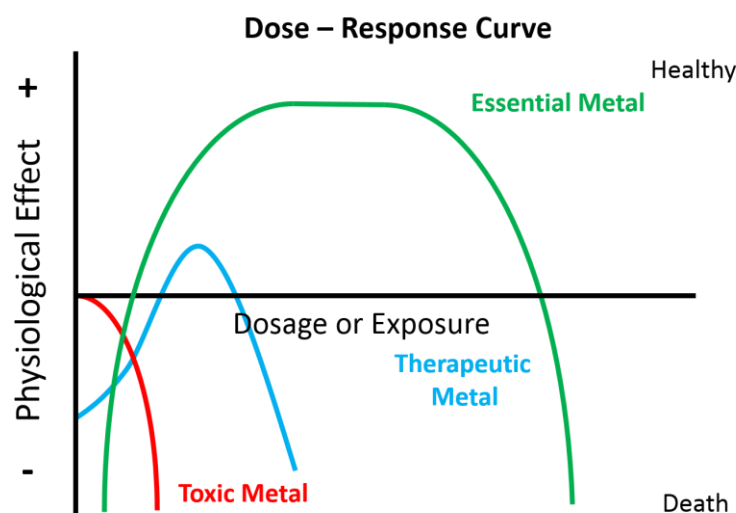


Figure 1-1 Dose-Response Curve (Bertrand Diagram)

Dose-response curve that shows the physiological effect (positive or negative) from exposure to metals under essential, (green line), therapeutic (blue line), and toxic conditions (red line).

Figure 1-1 shows a dose-response curve (more antiquatedly known as a Bertrand Diagram, named by Bert L. Vallee).⁷ Its schematic description illustrates the physiological effects as the exposure to a metal increases from zero. For all organisms, there is a minimum requirement for the intake of essential metals (green line, examples of which include Fe(II), Mg(II), and Zn(II)) that keep the biological machinery functioning optimally. Not achieving that minimum results in a state is described as “Deficient” with negative physiological effects. Like much in Life, moderation is key – saturating a system

with metals will damage the delicate physiological chemistry when there is no mechanism with which it can respond. There are some metals that are always toxic and play no known physiological role, where any amount is detrimental (red line). Small exposures to these metals may be tolerated due to inherent resistance mechanisms, but if the exposure exceeds these levels, death results (for instance, arsenic was used as a classic Shakespearean poison). In rare cases, a metal ion or a metal complex can act therapeutically (blue line) but only in a narrow dosage window can the benefits outweigh the detrimental effects. Often, these metals used for such specific applications will cause negative side effects with long term use. This is the case with cisplatin, a platinum based anti-cancer agent that can cause severe renal damage with long term use.⁸

1.1.1 Zn(II) is Essential, Cd(II) is Toxic

Zn(II) is an abundant d-block metal that is essential in humans in its Zn(II) cationic oxidation state for physiological chemistry. It differs from most d-block metals as it remains in a fixed 2+ oxidation state, but its role is no less exciting. Based on its remarkable Lewis acidity and almost rigid tetrahedral geometry in structural roles, it has been reported that Zn(II) is a required cofactor in thousands of essential metal-dependent enzymes.⁹

Isomorphous to Zn(II) but deadly, Cd(II) is a poisonous metal with toxic effects that result from its similarity to Zn(II) and Ca(II). Cd(II) exists naturally alongside Zn(II) and it is absorbed biotically via the same mechanisms as biological Zn(II). However, any amount of Cd(II) is toxic, with a long biological half-life of several decades in humans.¹⁰ Cd(II) can replace native Zn(II) in enzymes, can cause brittleness in bones, and causes renal damage during excretion.¹¹

Human cellular physiology can tolerate small amounts of Cd(II), which is good considering many plants and the animals that feed on them can draw minute amounts from the soil. This raises the question: how do our cells manage to sort essential metals from those that are toxic?

The focus of this thesis is the metal-binding protein, metallothionein (MT), whose major role has been identified as the metal chaperone for Zn(II) and Cu(I), and a source of

cellular Zn(II) for metal-dependent enzymes. Metallothioneins (MTs) are a large family of small cysteine rich proteins that are found in all Life. It is through the multitude of its cysteine residues (30% of the residue content) that it can sequester metals. MTs have been found to be involved in a large variety of biochemical mechanisms and response pathways. MT has an unusual structure due to its small size and flexibility. With the general mantra that protein structure begets function, this makes MT's function difficult to define. The structural details of holo- and apo-MT are described further below.

What is the role of MTs in Life? Since its discovery in 1957,¹² many original research papers have had trouble strictly defining MT's role in Life; that is, its designed purpose. In the *Proceedings of the second international meeting on metallothionein and other low molecular weight metal-binding proteins*, Vallee, one of the original discoverers of equine MT, describes metallothionein as a "sphinx's riddle".¹³ That enigma is multiplied by the broad genetic diversity of metallothioneins across all of Life, and questions its evolutionary development. The multiple possible roles of MT presented a two-sided coin in terms of how to approach its study. *In vivo* observation of MT activity in wildlife lets us see the native structure in its natural role, and its response to differing environments. *In vitro* observation lets us see what chemistry MT is capable of, depending on the external factor, like metal poisoning or drug resistance.

1.1.1.1 Homeostasis and Regulation of Physiological Zn(II)

MTs are believed to be key players in d-block metal regulation through trafficking and storage, primarily of Zn(II) and Cu(I), and cellular levels are controlled through MT induction.¹⁴⁻¹⁶ However, there is basal level of MT expression, even in Zn(II) deficient situations.¹⁷⁻¹⁹ MT's ability to chelate multiple intermediate and soft metals and to donate these ions individually to enzymes is strong evidence of this role *in vivo*. The stepwise binding coefficient of each preceding metallation event selects the first metal for donation, as the last bound.²⁰ Factors that control stepwise metallation include the solvent accessibility of the bound metal, which MT domain the metal is bound to, and whether the metal ion binding site involves terminal or bridged cysteine coordination.

Udom et al. showed that Zn(II) MT could reconstitute apo-enzymes that had lost their essential metal cofactor and reactivate them to full activity.²¹ Maret and Vallee showed that MT interacts via Zn(II) mediation between itself and the DNA binding domain of the transcription factor Gal4.²² This Zn(II) transfer likely occurs via protein-protein interactions between MT and the receiving peptide, as MT has been shown to transfer metals between other MT molecules in this fashion.^{23, 24} When we consider that Zn(II) makes up cofactors in every chemical class of enzymes, and is essential for gene expression, the regulation of this metal in the cell is vital.²⁵

The concepts of the magnitude of the binding constant strength in relation to the chelate effect theory apply here. Metallothioneins are essentially multiligand chelators that metallate in stepwise fashion. The rate k_n with which the first metal binds is statistically greater than the next k_{n+1} such that the last metal bound (7th for M(II)) is the slowest to bind. When describing this in terms of binding constants, the stepwise reaction with the greatest K_F is most favourable and most stable, from which we can identify the cooperative cluster formation, from its greater K_F . The last metals to bind are, therefore, the weakest bound, and most likely to dissociate first (lowest K_F , highest K_D).²⁰ It is clear that these most labile metals are those that are involved in metal donation to enzymes and biological targets. Corresponding NMR studies show that the most labile metals are bound to the more solvent accessible cysteines, which may explain their lability.²⁶

Figure 1-2 illustrates how the 7 stepwise binding constants for $Zn_{1-7}MT$ overlap the binding constant of apo carbonic anhydrase (CA), with the last two Zn(II) ions bound to MT shared or donated to apo-CA. Competition studies showed that the MT does not donate a Zn(II) ion to the apo-CA until after the fifth metal has bound to the MT. This indicates that the last two metals to bind for fully metallated Zn_7MT are the most labile and available for donation.²⁷

The most effective technique for analyzing the binding constants of the individual metallation steps is by using the resolving power of native electrospray ionisation mass spectrometry (ESI-MS), discussed further in this Chapter.

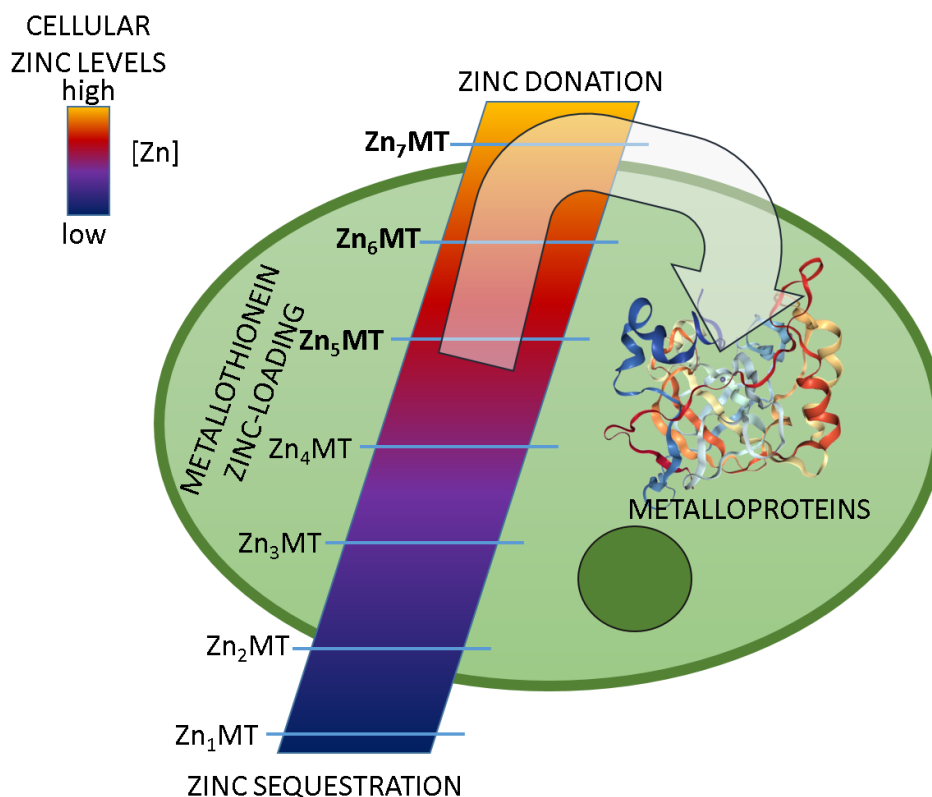


Figure 1-2 Donation of Zn(II) in Zn-MT to apo carbonic anhydrase

Zn(II)₅₋₇MT, the most labile ions in terms of the stepwise binding constants, are the first metals donated to carbonic anhydrase. This figure is adapted from T. B. J. Pinter and M. J. Stillman (2015).²⁸

1.1.1.2 Cadmium and Heavy Metal Toxicity

Without a doubt, the initial discovery of MT as a Cd-binding protein presented a bias towards its perceived role in heavy metal detoxification. MTs are excellent at accumulating toxic heavy metals. Soft heavy metals like Hg(II) and Cd(II) bind to MT *in vivo*, which induces the synthesis of new MT protein. Accumulation of MT in response to elevated metal ion concentrations, combined with its association with these ions, indicates a role in the sequestration of any excess metal ion.²⁹ Importantly, heavy, toxic metal ions including, but not limited to, Hg(II), Cd(II), Pb(II), As(III), Pt(II), Pd(II), Rh (I,II), only are present in the body as a result of external intake. These soft heavy metals have no

known biological role. Man-made industrial practices as described above have literally dug up these metals and through consumerism, introduced these metals into the ecosystem of the Earth's surface, with the nightmare scenario being a catastrophic pollution event (for example, Aznalcóllar Disaster, Donana Park, Spain³⁰). These electron-rich d-block metals displace natively bound essential metals (e.g. Zn(II), Cu(I)), destroying enzymatic activity, or disrupting biological structures, often irreversibly. The presence of these metal ions can also establish a pro-oxidant environment, where redox reactions and resulting reactive oxygen species can affect cellular and genetic structures.³¹

The induction of MT synthesis has been correlated to external Cd(II) and Cu(I) tolerance in both a variety of cultured cells and animal studies.³² Heavy metals like Hg(II) and Mn(II) are known to accumulate in thiol rich fractions of cells in marine fish.³ Use of trace metal analysis of fish to understand the extent of pollution in a marine source is based on the idea of bioaccumulation. During the life of a fish, metals accumulate within their body and are neither metabolized nor excreted. Biomagnification is a related principle that extends bioaccumulation through the predators of the food chain; those at the top of the food chain consume not only the metals of those within the fish of the rung below, but also the fish that was consumed by that fish, and the fish below that, etc.

Animal studies show that after exposure, Cd(II) binds to albumin in the blood plasma, and is transported to the liver.¹¹ Initially, Cd(II) levels rise in the liver as a result. The arrival of Cd(II) in the liver signals MT synthesis, which chelates the Cd(II) to form Cd-bound MT (Cd-MT), which in turn, circulates the body via blood plasma towards the kidneys.¹⁰ In mammals, the small molecular weight (MW) of Cd-MT allows it to be filtered by the proximal tube of the glomerulus, excreted through the renal system and exits the body in urine. Unfortunately, this process is not rapid. Cd-MT can be reabsorbed by the tubular cells, and subsequently release relatively large concentrations of Cd(II) upon Cd-MT degradation, leading to renal damage. Friberg et al. reported that the half-life of Cd(II) in the blood on the order of hundreds of days, and several years to decades in the kidneys.¹¹

High levels of Cd-MT in the urine are markers for toxicity, as was established in Japan following the mass "Itai-Itai Disease" outbreak from Cd(II) poisoning caused by malpractices of Mitsui Mining & Smelting Co. Itai-Itai disease is one of the Four Major

Pollution Diseases of Japan.³³ Industrial waste from the smelting plant entered the Jinzu River Basin, where downstream citizens relied on the river ecosystem to provide fish, fresh water, and irrigation for rice crops. Over time, crippling physiological effects related to the poisoned ecosystem became evident in the affected population. Side effects included brittle bones, and severe renal damage with Cd-MT prevalent as a urinary marker for the affliction.³⁴

More recently, similar damage to other ecosystems occurred both in Japan²³ and Canada²⁴ from industrial mercury waste,^{35,36} which became incorporated in the marine ecosystem including fish that were essential to the local diet. This caused the severe neurological effects of Minamata disease in the affected population.

1.2 Metallothioneins are Ubiquitous

The metallothionein family is remarkable in that it appears that every phylum in Life has an MT or MT-like protein involved in metal regulation. About one-third of its short, ~61 amino acid sequence comes from phylogenetically conserved cysteine regions. These cysteines, often in the sequence as -C-C-, -C-X-C- or -C-X-X-C- repeat regions, have soft, reactive thiolates involved in metal binding, but do not form disulfide bonds natively. MTs are present in all mammalian tissues, with more pronounced expression in the liver, kidney, brain, and during fetal development.³⁷ These proteins exist in the cytosol and in the nucleus, as well as in extracellular fluids like bile, plasma, and urine.³⁸

MTs are unorthodox in their high metal loading capabilities, and their promiscuous nature: one protein molecule is capable of multiple and variable stoichiometric metal binding.¹³ Class 1 MTs do not form a single, specific metal -loaded species, unless through strictly controlled metal exposure. We see this heterogeneous binding property in the simultaneous binding of Zn(II), Cu(I), and Cd(II) in a single protein molecule. Because of these wildly adaptive behaviors, the biological role of MT was a subject of great debate in the years following its discovery.³⁹ Was it involved in detoxification? Could MT reactivate apo-enzymes? Why could MT be induced by such a variety of external agents?

The discovery of other low MW, cysteine rich proteins demonstrated their evolutionary necessity, but through natural divergence, the purpose and functions have become optimized by their amino acid structure. These sulfur rich metal binding proteins are given the family name of, “metallothioneins,” and are divided among 3 class types, based on their similarities of their cysteine homologies.

Class 1 MT: polypeptide with a highly conserved sequence: cysteine residues are congruent with those in the equine renal cortex sequence (e.g. mammalian, vertebrate)

Class 2 MT: polypeptide that is also rich in cysteine residues, though not entirely in the same location as equine renal cortex. (e.g. fungi, plant, invertebrate)

Class 3 MT atypical, non-translationally synthesized metal thiolate polypeptides e.g. cadystins, phytochelatin

Vertbrate MTs

```
MDP-NCSEST GGSCHCTSSK AAKNCKKTSK KKS■CCS■CCPV GCSKCAQGGVC KGAAD-----R■CTCCA MT1 M. musculus (P02802)
MDP-NCSCAA GDSCHCAGSK KCKRCKKTSK KKS■CCS■CCPV GCAKCAQGGIC KGASD-----R■CSCCA MT2 H. sapiens (P02795)
MDPETCPPT GGSCHCSDKC KCKGCKKTK KKS■CCS■CCPA GCEKCAKDVIC KGEGAKAE AER■CS■CCQ MT3 M. musculus (P28184)
MDPETCPPT GGSCHCSDKC KCKGCKKTK KKS■CCS■CCPA GCEKCAKDVIC KGEGAKAE --R■CS■CCQ MT3 R. norvegicus (P37361)
MMDPGECHMS GGI■CHCGDNC KCTTCKKTK RKS■CCB■CCPP GCAKCAQGGIC KGGSD-----R■CSCCA MT4 C. lupus familiaris (Q9TUI5)
```

Figure 1-3 Mammalian MT isoforms

Representative single amino acid code sequences of mammalian MTs. Conserved cysteine motifs highlighted with black. Sequences obtained from the UniProt Database, with the respective protein ID in parenthesis.

Within each class, there are 4 major isoforms characterized by their cysteine topology (e.g. MT1, MT2, MT3, MT4, Figure 1-3, Figure 1-4), that represents a protein category within a species' MT gene expression. A representative sequence of mammalian MTs representing each isoform is shown in Figure 1-4. These isoforms themselves may have sub-isoforms (e.g. MT1A,-1B, -1C etc.). These sub-isoforms exhibit single residue variation in their amino acid sequence that affects the charge of the overall protein. This leads to the question of whether sequence-specific MT in higher level eukaryotes expressing these multiple MT genes have their own have specific metal binding properties. The majority of the studies described in this Thesis concern Class 1 MTs, with the experiments performed utilizing recombinant human metallothionein 1a.

1.2.1 Human Metallothioneins

Human metallothioneins are understandably the most relatable of the vertebrate MTs. Humans MTs are divided into four main subtypes, and each display slightly varied characteristics.

UniProt ID - Human	N-	β	α	-C							
P04731 MT-1A	MDPNCS	ATG GSC	CTGSGCKKE	CKCTSCK KSC	CCSCPPMS	CAKCAQGGIC	KGASEK	SCC A			
P07438 MT-1B	MDPNCS	MTT GGS	CACAGS	CKKE	CKCTSCKKC	CCSCPPVGG	AKAQQGVCKGSSEK	CRCCA			
P04732 MT-1E	MDPNCS	CAT GGS	CTCAGS	CKKE	CKCTSCKKS	CCSCPPVGG	AKAQQGVCKGASEK	SCCA			
P04733 MT-1F	MDPNCS	AA GVS	CTCAGS	CKKE	CKCTSCKKS	CCSCPPVGG	AKAQQGVCKGASEK	SCCD			
P13640 MT-1G	MDPNCS	AA GVS	CTCASS	CKKE	CKCTSCKKS	CCSCPPVGG	AKAQQGVCKGASEK	SCCA			
P80294 MT-1H	MDPNCS	AA GVS	CTCAGS	CKKE	CKCTSCKKS	CCSCPPVGG	AKAQQGVCKGASEK	SCCA			
P02795 MT-2A	MDPNCS	AAG DS	CTCAGSCK	CKE	CKCTSCK	KSC	CCSCPPVGG	CAKCAQGGIC	KGASDK	SCC A	
P25713 MT3	MDPETCP	PS GGS	CTCADSC	KCEGCK	CTSCK	KKS	CCSCPPA	ECEKCAKDCV	CKGGEAAEAE	AEK	SCCQ
P47944 MT4	MDPRECV	GMS GGI	CMGDNC	KCTTCN	KTY	WKS	CCPCPP	GCAKCAQGGIC	CKGSDK	SCC	CP

Figure 1-4 Human MT1 and MT2 protein sequence

Single amino acid code sequences of human MT isoforms 1-4 displaying MT1 with its multiple sub-isoforms. Cysteine residues are highlighted in black. Sequences obtained from the UniProt Database, with the respective protein ID preceding the isoform.

MT1 and MT2 are the major isoforms present in all species but are highly expressed in the liver and kidneys. These isoforms are generally found *in vivo* bound to Zn(II) and some Cd(II). While MT2 is expressed homogenously, MT1 can exist in several subisoforms as shown in Figure 1-4. MT 3 is expressed in the brain and is known to favour Cu(I)/Zn(II) binding. This particular isoform has been linked to mitigation of protein misfolding and aggregation in neural cells, leading to neurodegenerative diseases. MT 4 is expressed in squamous epithelial cells, which line the outside of organs to afford external protection.

Along with their metal binding properties, MTs are associated with oxidative stress remediation. Compared to glutathione, another prominent cellular antioxidant, MT is shown to have a twenty times greater protective power against peroxide radical damage.^{40, 41} This makes MT an indirect player in many roles of cellular regulation, and protection against generic cellular damage, sparking interest especially in MTs role in diseases, aging, and drug resistance.

1.3 Structural Elements of Metallothioneins

Protein structure defines its function. This is a dogma that is difficult to apply to the flexible nature of MT. The structural properties of MTs are enigmatically elusive; the most easily observable form being the fully metallated MTs. Complete metallation forms the two characteristic metal-thiolate clusters; an observable feature that can be readily identified using a number of instrumental techniques, once it has completely formed. Even with full metallation, crystallization of MT has proven hard. In many proteins, their secondary structural features provide stability such that crystals can be isolated and structurally analyzed, but with MT this is not the case. To our knowledge, just one X-ray diffraction study is reported for mammalian MT, that is, for Cd,Zn-MT1 from rat liver.⁴² The structural parameters were greatly extended by ¹H NMR studies subsequent to this report.⁴³ The presence of a two domain structure in mammalian MT was established from ^{111/113}Cd NMR studies pioneered by the Armitage group, starting in 1980. The ¹H NMR and X-ray diffraction results were discussed together in a single paper giving great detail to the protein structure and linker region.⁴³

MT is a cytoplasmic protein and relies heavily on the solution environment for the native structure it adopts. MT *in vivo* is not fully metallated. Cd₇MT and Zn₇MT are not easily found, unless under extreme Cd(II) or Zn(II) exposure. Conversely, the metal-free apo-protein, or partially metallated protein long eluded isolation, until Maret and workers reported the use of Förster Resonance Energy Transfer (FRET) imaging to establish the presence of free thiols in MT.⁴⁴⁻⁴⁶ This new discovery led to a significant paradigm shift: what was originally believed to be fully holo (fully metallated) was now known to exist in a partially metallated state. Therefore, metallation of MT is a post-translational modification.⁴⁷ The MT structure is significantly more dynamic and variegated than traditional elucidation techniques could determine.

1.3.1 Metal-Induced Structure

The formation of the many metal-thiolate bonds in MT is the driving force for its subsequent folding and structural order. MT has few hydrophobic residues, implying that the major intramolecular forces at play are electrostatics, hydrogen bonding, and the key

element: formation of the metal-thiolate bond in tetrahedral beads,⁴⁸ as we continue in our discussion below. The stepwise metallation sequence itself, has revealed most unusual binding site properties for a protein, in that the metal induced folding depends on the metal loading status. Early spectroscopic studies involving MT metal binding focused on finding the stoichiometry at which the observed signal for metallation became saturated. This provided in essence, a “frozen” state that could be examined for its properties. Thus the idea of “magic numbers” based on the stoichiometry of signal saturation was popularized for defining the metal binding properties of MT.⁴⁹ These golden numbers were identified with the metals that had been found in MTs of living organisms, including Zn(II), Cd(II), Cu(I), and Hg(II). These metals were studied extensively for their possible role in MT’s function. For the purpose of this Chapter we will refer to these as the classical metals. As we will see further in the Chapter, metals that do not belong in this category or are encased in coordination complexes do not follow these magic numbers. These metals are never found physiologically. Their metal binding chemistries are governed by the flexibility of the MT protein, and the geometry of the incoming metal complex. We will describe these metals as non-traditional, when we discuss their metallation of MTs further below.

1.3.2 Non-Traditional Metallation of Metallothioneins

All cells have a basal level of MT expression. Increased protein production can be induced by external pressures, such as oxidation, or the presence of heavy metals as described above. In certain cancer types, MT expression has been correlated to developed resistance against therapeutic action. MT can break down metal complexes to their metal ion. Platinum based drugs and other cytotoxic agents face this drug resistance, which has been associated with an increase in gene expression or protein production of MT, particularly in cancerous cells. The combination of the abhorrent and uncontrolled growth of cancerous cells plus the ability to increase production of this multi-protective peptide provides a formidable defense against chemotherapeutic agents. As we will discuss further, the acidic conditions of a cancerous cell⁵⁰ promotes the protective effect of MT, particularly against the electron rich transition metals being used in these medicines.

Because of their propensity to bind soft d^{10} metals (e.g. the aforementioned Cu(I), Zn(II), Cd(II), Pt(II) etc.), MTs are suspected of playing a role in the developed resistance to cisplatin and as such, the protein's ability to possibly bind any metal has been of interest when considering therapeutic agents that can withstand this resistance.

As we will see in Chapter 2, the general metallation mechanism *in vivo* involves tetrahedral cysteine M(II) coordination, with the onset of clusters at high metal loading or a lower pH environment. We can see a variety of different coordination behaviors with M(I), e.g. Cu(I) can bind MT with a variety of metal stoichiometries (6, 12, 20), and each of these may involve different coordination modes. With 6 mol. eq. of Cu(I), a Cu_6S_9 cluster forms. With 12-13 mol. eq., a combination of a Cu_6 and Cu_7 cluster forms. In both cases, trigonal coordination was assigned. However, at 20 eq. of Cu(I), the metal conformation requires digonal cysteine thiolate coordination. The reaction with Cu(I) shows the great degree of flexibility that MT binding can take on, and that *in vitro*, we can push the envelope of possible binding modes to explore *what could happen*. The flexible nature of hydrogen bonding in MT allows for a variety of unexpected interactions to occur. For example, N and O donors are known to be involved in binding some metals and may tune the soft/hard nature of the chelating MT.

In the following section we describe the mechanism of this metal sequestration, how the structures adopted from the metallation relates to MT function, and how the resulting protein depends on the conditions involved.

1.4 Techniques Used in this Thesis

1.4.1 Expression and Purification of Recombinant Human Metallothionein 1a

Model species are “models” because they have rapid production times and can be observed easily. What grows faster than bacteria? Recombinant expression involves employing bacterial machinery to over express translation of a desired protein, in our case MT. This technique is ideal for plant and human MTs, as *Escherichia coli* can grow in large quantities with short life cycles and faster growth periods, without the need for

animal decapitation. The technique used in this Thesis was developed by Peter Kille and Ian Watt at Cardiff university.⁵¹ The general procedure is summarized as:

Complementary DNA (cDNA) of the metallothionein mRNA is cloned into a plasmid. Typical plasmids will also include coding for proteins “tags” or short amino acid sequences that can assist in protein purification that are later removed. Other important elements of the plasmid include a transcriptase, a resistance marker to aid in cell selection, and an inducible repressor (such as the Lac I repressor) to induce expression. Once these plasmids are prepared, they are transformed, or transferred into the host *E. coli* cells.

These cells now carry a resistance to the antibiotic defined in its plasmid sequence, and we can take advantage of antibiotics to ensure the growth of only the transformed cells. A small preparation is made on LB Agar plates with the antibiotic kanamycin, according to the protocol in Figure 1-5(Left). These cells are inoculated in a liquid LB Broth culture (prepared according to the protocol in Figure 1-5(Right) and grown until they reach a “lag phase” (the bacterial growth plateau), at which point the maximum number of viable cells is present. In the case of the Lac I repressor, Isopropyl β -D-1-thiogalactopyranoside (IPTG) turns on this repressor and is added externally to initiate MT expression.

A difficulty with metalloprotein overexpression is the maintenance of structure upon synthesis, as once formed, proteins are vulnerable to protease and other regulatory actions. To properly isolate large quantities of the induced protein, extra metal is added to the medium to prevent protein degradation by the bacterial proteases. The cells are then harvested usually by centrifugation and can be kept frozen in a glycerol solution prior to purification.

To purify the protein from the bacteria, the cells must be lysed with high pressure. Generally, with the addition of that protein tag, described earlier, the desired protein can be isolated using a chromatographic column that complements the protein tag properties. The extra residues are then removed with a protease reaction. In the case of the MT produced in the Stillman Group, the 15 amino acid S-tag is attached to the N-terminus.⁵²

The recombinant human MT1A used in the experiments described in this Thesis were all prepared using the following method:

Preparation of Recombinant Human Metallothionein I: Recombinant human metallothionein I (rh-MT1) was expressed in BL21(DE3) *E. coli* cells that were transformed using a pET-29a plasmid containing an S-tag for protein stability during the purification. The cells were grown in LB broth with 0.5 mL 50 mg/mL kanamycin. MT expression was induced with IPTG and metallated with CdSO₄ (Figure 1-5). Cells were lysed using a cell disruption system (Constant Systems, UK), and then centrifuged to separate the MT- containing supernatant from unwanted cellular components. Further purification was performed using High Performance Liquid Chromatography (HPLC, Dionex UltiMate 3000, Thermo Fischer Scientific). Elution through a 5 mL HiTrap SP HP ion exchange column was achieved using 10 mM tris(hydroxymethyl)aminomethane (Tris-HCl) at pH 7.4 (Fisher) was monitored by UV-visible absorption (Cary UV 50 Bio, Varian, Toronto) at the characteristic Cd-MT wavelengths of 300-200 nm. Fractions that contained metallated MT were collected, and the S-tag removed using a Thrombin CleanCleave™ Kit (Sigma Aldrich). The thrombin resin beads were recovered, regenerated, and stored for later use. The purified MT protein was evacuated and purged with Argon prior to storage in -80°C, with individual experimental preparations as further described in each Chapter.

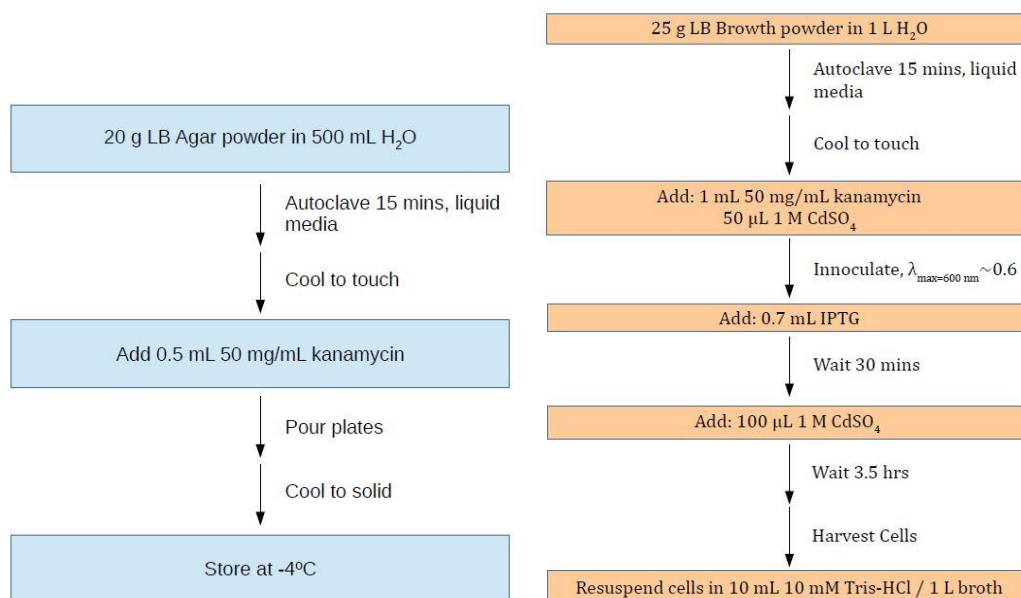


Figure 1-5 LB agar and LB broth preparation

LB agar (Left) and LB broth (Right) preparation instructions for the preparation of kanamycin-resistant, human MT expressing E. coli cells.

1.4.2 Spectroscopic Methods

Spectroscopic analysis of metallothioneins has been generally restricted to UV-visible absorption, Circular Dichroism (CD), and proton and metal Nuclear Magnetic Resonance (NMR) techniques. This is because the nd^{10} metals that traditionally are used *in vitro* and are recovered from MTs *in vivo*, exhibit only ligand-to-metal-charge-transfer (LMCT) in the absorption spectrum and the peptide, with its absence of aromatic amino acids, exhibits a very restricted band envelope below 220 nm. In addition, the lack of native secondary or tertiary structure for the apo-MT means that the CD spectrum in the absence of metals, is also uninformative. In a sense, this absence of spectroscopic signatures for the apo-protein has allowed the metallation reaction to be followed readily from changes in the absorption spectrum centred on the LMCT band of the specific metal, for example, at 250 nm for Cd-MT. In parallel with the increase in absorption, and red shifted from the apo-MT edge at 220 nm, is the development of CD spectral properties related to the metal-induced folding of the peptide backbone. This technique is used especially in Chapters 4 and 5.

1.4.2.1 Absorption Spectroscopy

Bioinorganic complexes can exhibit spectral properties arising from charge transfer absorption bands that are characteristic of certain bonds, such as the one for $S \rightarrow Cd$ described above.⁵³ Comparing isosbestic changes in absorption patterns during metal titrations provides important information on metal binding stoichiometries of MT.⁵⁴ Care must be taken to avoid the interference of buffers and metals to exclude side reactions; and significantly, to avoid oxidative conditions due to the sulfur rich nature of MTs.

1.4.2.2 Circular Dichroism Spectroscopy

The absorption of circularly polarized light of the CD experiment is modified by the presence of chiral environments. The structural properties of α helices and β pleated

sheets commonly found in proteins exhibit specific CD spectral signatures. These spectral features can be used to analyze the consequences of structural modifications in proteins. The MT peptide, however, does not adopt well-formed secondary or tertiary structural elements, and as a result, the CD spectrum for apo-MT is devoid of these spectral signatures. However, metal binding to apo-MT imparts metal-induced structural properties, which results in strong CD spectral envelopes in the LMCT region. These CD envelopes arise from metal-induced chiral environments, and are stoichiometrically dependent, allowing the quantitation of the metal-induced structural properties of the metallated MT.⁴⁸ These spectroscopic properties are useful for monitoring structural changes during metal titrations. Good examples have been reported for titrations of MT with Ag(I), Au(I), Cu(I), Pt(II), Cd(II), and Co(II).⁵⁵

Prior to the common use of native ESI-MS, the changes in the CD spectral envelopes provided by far the greatest detail about the structural properties of the MT peptide. This is because for there to be significant changes in the CD spectrum there had only to be an absorption band related to the metal that was sensitive to a major influence of the coordination geometry on the structure of the metallated MT.^{53,56} The focus on the use of CD spectroscopy was specifically important for the metallation of MT because of the number of metals that bind in almost identical environments, meaning that the absorption chromophore does not distinguish between each metal. It is not possible to resolve changes that takes place as a function of the metal bound. This issue became most apparent when the use of native ESI-MS was common and metallation titrations became available, showing a wide distribution of species during titration for each mol. eq. added except for saturation.²⁷

1.4.3 Electrospray Ionization Mass Spectrometry (ESI-MS)

Mass spectrometers ionize species in a solution and separate those ions based on their mass. All mass spectrometers (Figure 1-6A) have the following components: (a) sample inlet ionization source, (b) ion optics, (c) mass analyzer and ion detector, (d) data analyzer, and (e) vacuum pump system.⁵⁷ There are many methods of ionization possible, but the method most useful for metalloprotein studies uses direct sample solution infusion into an electrospray ionization atmospheric interface. The sample solution is passed

through a fine, highly charged capillary, which results in charged molecules in solution either from the ionization of the solvent or from a redox reaction directly with the molecule. The central feature of the ESI-MS approach is that the wet droplets of protein must rapidly dry to form the ionized protein efficiently Figure 1-6(B). High temperature N_2 gas evaporates the solvent until nothing remains but the charged molecular ion. There are two common mass analyzers: (i) quadrupole and (ii) time-of-flight (TOF).⁵⁸ Recently, a third mass analyzer based on the quantized ion trap has become an emerging player (Orbitrap™).⁵⁹ For a wider range of mass speciation in metalloproteins and with greater resolution, the TOF is most useful, because it has a wider and almost linear range of detection allowing a greater variety of metallated species to be analyzed. The charged particles are accelerated through a time-of-flight mass analyzer; all ions are given the same kinetic energy but are then separated by their different distributions of mass. The charge distribution of the protein species leaving the atmospheric interface is not singular; rather a multiplet of charged species exists. The range of the multiplet can be from two or three charges to up to 25 components. It is now generally accepted that the charge distribution depends on the surface area that will contain the charged ions, which, for positive, protonated, species will be diagnostic for the extent of the instantaneous folding or unfolding of the protein under the solution conditions.^{60, 61} This multiplet consists therefore, of several m/z species where m is the mass of the protein plus the number of protons and z is the total charge introduced by the number of protons bound. The deconvolution of the series of multiplet masses, knowing their charge, can be determined mathematically to give the parent protein mass. This is illustrated in Figure 1-7. The structural power of this requirement is that as the surface area increases (for e.g. with a denaturant or by unfolding) the multiplet number increases. This provides a fine measure of the degree of folding under any solution conditions that exceeds the typical quantitation of folding provided by the CD experiment described earlier. The specific structures involved though, have not been associated to date, with the different multiplets observed. I will describe the value of this experimental technique below when I discuss

the structural properties of apo-MT.

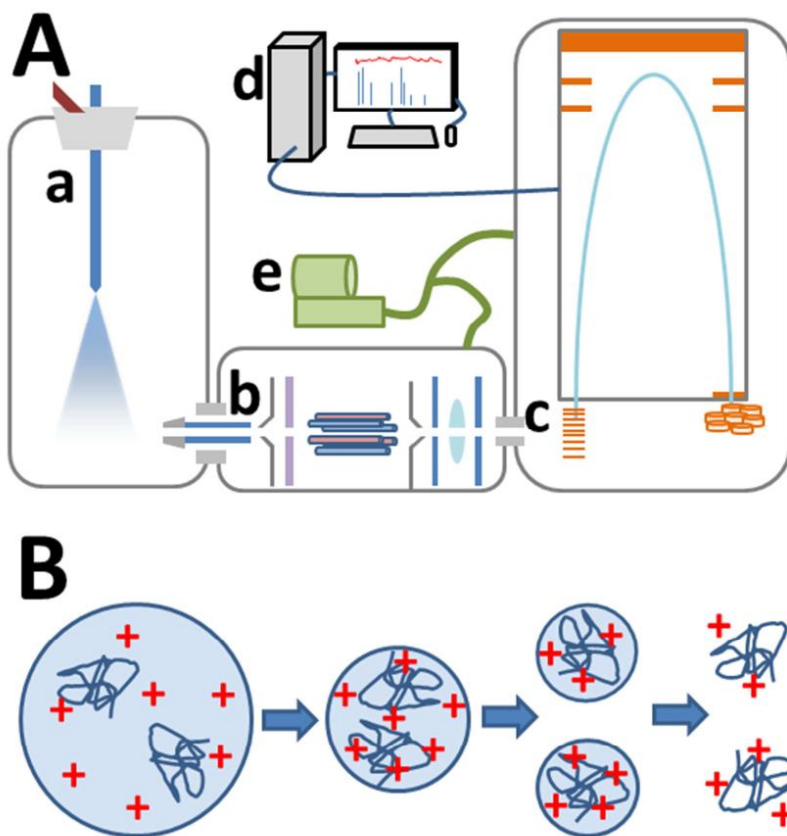


Figure 1-6 An ESI-TOF-MS and its ionization mechanism

A) Schematic of a basic ESI-MS instrument. B) As the analyte solution droplets move through the charged capillary, the surface tension of the solution becomes overcome by the repulsive force of the charged particles, known as a "Coulombic explosion."⁶²

An analytical method like this can precisely describe the composition of a protein mixture, showing the masses of all the individual components. Data from native ESI-MS experiments can be used to account for the species in an averaged spectroscopic signal by defining the individual contributions. ESI-MS methods have been used widely in drug-protein interaction studies, enzymatic reactions, and elucidative applications.

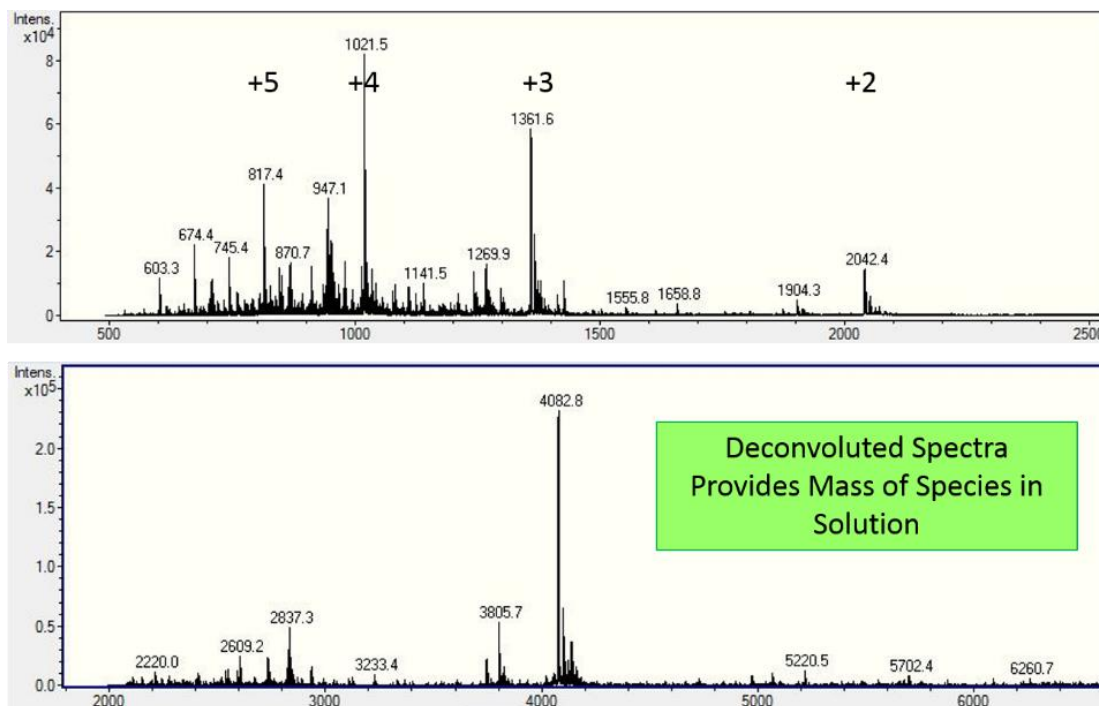


Figure 1-7 Charge state and deconvoluted mass spectra

Apo α -MT fragment at pH 2. Screenshot of the acquired spectrum window in the Bruker DataAnalysis 4.2 software with the m/z spectra shown top with major charge states +5, +4, +3, +2, labelled, with the bottom showing the deconvoluted spectrum showing the mass in Da of the species resolved from the m/z spectra.

1.4.3.1 Electrospray Ionization Mass Spectrometry (ESI-MS) in MT studies

Fenselau's group was a leader in the realm of ESI-MS analysis of metallothioneins. At the time in the early 1990's, mass spectrometry was being recognized as a high resolution technique for analysing protein complexes.⁶³ Fenselau and coworkers used ESI-MS to identify the many partially metallated species of MT that accompany metal titration, while showing the ease of use especially in the case of direct solution infusion. Their work highlighted the delicacies of the pH environment in metallation, suggesting the pH dependence of cooperativity that is now widely understood,⁶⁴ while also demonstrating the power of ESI-MS in drug—protein complex analysis.⁶⁵ They pioneered work in cysteine alkylation studies using therapeutic alkylating agents to probe the structure of MT, which we will expand on further in this section. With Fenselau and others now

illustrating the ease with which ESI-MS can be used to analyze solution samples, Lobinski introduced the idea of coupling techniques for high resolution metal binding analysis.⁶⁶ Since ESI-MS allows for direction infusion of the sample, attaching a high performance liquid chromatography (HPLC) system with an acidification column prior to ESI analysis allowed for the absolute identification of rabbit liver MT isoforms and subisoforms, that could previously only be postulated through chromatographic separation. ESI-MS then took off as the best way to quantify metallation of MTs, and was used to compare different MT species,⁶⁷ compare polymorphisms in plant MTs,⁶⁸ and to further question the cluster formation properties of MTs.⁶⁹

Structural studies with MS using Cysteine Modification by Alkylation

Because of its cysteine rich structure, MT is prone to react with alkylating agents. This was postulated as a method of drug induced resistance by Fenselau, who used alkylating therapeutic agents like chlorambucil, melphalan, and dexamethasone to probe the cysteine structure.^{64, 65, 70-72} These alkylating methods were also used to demonstrate the effects of alkylation on metal ion flux between enzymes, as these therapeutic agents reacted in small stoichiometric ratios without dissociating seven divalent metals, but that modification did increase rates of Zn(II) donation to apo CA, suggesting that the modification had distorted the native structure.⁶⁵ Depending on the size and charge density of the alkylating agent, differential binding patterns could be resolved, and used to infer structural information.⁶⁵ For instance, the smaller alkylating agents penetrate and bind free cysteines differentially based on their solvent exposed surface area. This is combined with ESI-MS to show that the structure of the protein may define the metallation mechanism (cluster vs. bead, described in Chapter 2) that dominates metallation. These alkylating reactions show that not only are the cysteine residues buried within the protein structure, but also that they are differentially accessible by solvent. It supported the idea that not all 7 binding sites can be considered equal, emphasising that the pseudo first order generalizations of these early MT studies were not adequate assumptions.

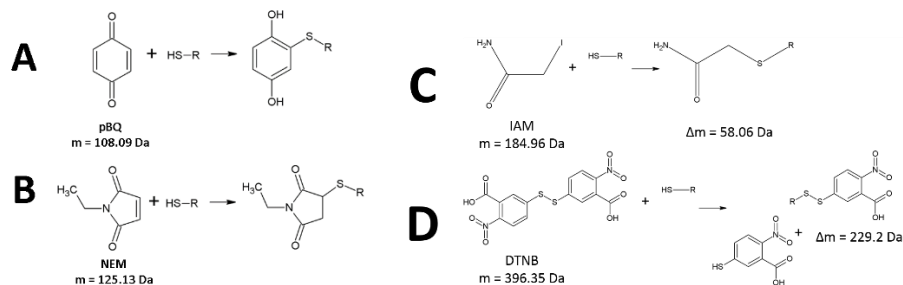


Figure 1-8 Various cysteine alkylating agents

Reactions of various small alkylating agents with free thiols. (A) the reaction of para-benzoquinone. (B) the reaction of n-ethyl maleimide. (C) the reaction of iodoacetamide. (D) the reaction with 5,5'-Disulfanediyldis(2-nitrobenzoic acid).

As we have seen in the variety of metallation reactions that MT can partake in, the richness of its cysteine thiols imparts great reactivity. These thiolates can act as nucleophiles in substitution reactions. For instance Ellman's Reagent (5,5'-disulfanediyldis(2-nitrobenzoic acid), DTNB, Figure 1-8(D)), has been historically used to quantify thiols in solution, with stoichiometric reaction depicted in the Figure 1-8 above.⁷³ Iodoacetamide (IAM, Figure 1-8(C)) is used as well, but it benefits from a small spatial size, allowing it to fully penetrate most protein structures. *Para*-benzoquinone (pBQ, Figure 1-8(A)) is a useful agent that is easy to prepare but is photo-reactive and works best below neutral pH. This is a difficulty when trying to analyze proteins at neutral, physiological pH. N-ethyl maleimide (NEM, Figure 1-8(B)) can work under those conditions, albeit it is not as small and penetrating as IAM. Depending on the conditions used, the alkylation is so favourable that it can displace native bound metals. Regardless, both pBQ and NEM (Figure 1-8A, B) differentially bind MT and provide information about the solution structure under controlled conditions. Their differential mass spectrometric profiles of species distribution can give clues about the shape of the protein solvent surface. This technique and its related principles are used to analyze the native structure of apo-MT in Chapter 2, and to probe Rh-bound MT in Chapter 5.

1.4.3.2 ESI-MS for Quantitative Analysis of Stepwise Metallation

The binding constants of each metallation event depict the metal donation properties of MT. With the advent of ESI-MS, quantitative studies involving metal titrations into MT

could be equilibrated and measured with ESI-MS to find the resulting equilibrium constants K , from the relative intensities of the products.

Kinetic rate constant determination

Another advantage with ESI-MS is the ability to monitor reactions in real time up to hours (or however long the sample solution lasts at a particular flow rate). With MT however, the metallation is generally rapid and complete before the dead time of the instrument. As such, the kinetic analysis of metallation to MTs was mostly constrained to inferring results from competition reactions.

Ngu et al. took advantage of the differential rates of metallation depending on metal type, using arsenic metallation of MT.⁷⁴ As(III) is known to bind *in vitro* to MT with a maximum stoichiometry of As_6MT . This binding is slow enough that it can be monitored using ESI-MS and was used as a model for the metallation by more naturally found Zn(II) and Cd(II). The highly detailed time-dependent, temperature-resolved results show that the each metallation event is faster than its subsequent metallation event ($k_1 > k_2$ and so on). This is true for both the whole protein and the metallation of the individual domains, shown in Figure 1-9.

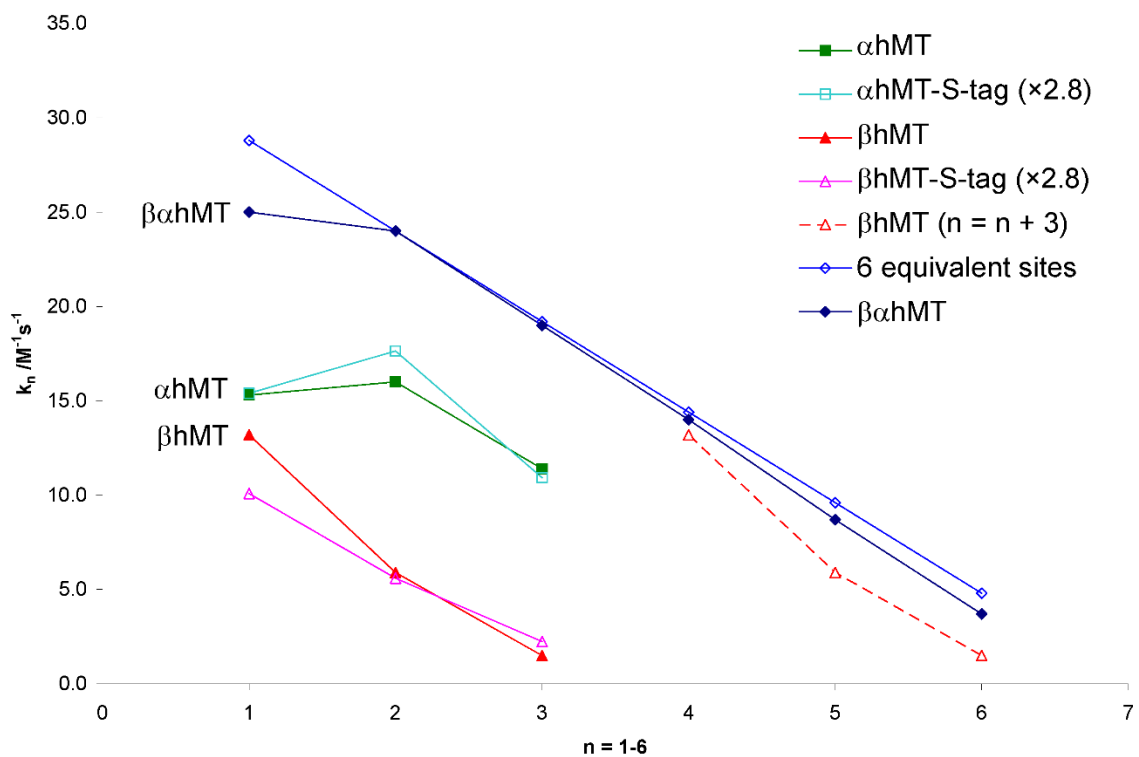
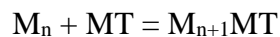


Figure 1-9 Decreasing rate constants shown in the stepwise metallation of $\beta\alpha$ MT and its individual domains.

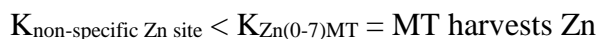
Comparison of the rate constants calculated from the time-resolved ESI-MS measurements for As^{3+} -metallation of β hMT, α hMT, and $\beta\alpha$ hMT, the trend in rate constant values for six equivalent sites where $k_1 = 28.8 M^{-1}s^{-1}$ and the rate constants reported for β hMT-S-tag and α hMTS-tag. The red dashed line represents rate constant data for the β hMT redrawn with the value of n shifted by three to illustrate the similarity to the rate constant trend for the final three As^{3+} binding to $\beta\alpha$ hMT. Reproduced from Ngu et al.⁷⁴ Copyright 2008 American Chemical Society.

Equilibrium Constant determination

The early studies of MT were focused on observed optical signals, but now the focus resides on numerically assigning properties to MTs to distinguish isoforms and their specific functions. Historically, the metallation reaction of MT can be described as a bimolecular reaction with metals binding at a single rate with a single binding constant.



This simplification of the metallation mechanism was to compensate for the lack of detail in the instrumental method. Often the metallation reaction was complete within the dead time of the instrument, resulting in an apparent cooperative reaction. Because metals like Cd(II), Zn(II), and Cu(I) bind so rapidly, the individual steps cannot be visualized. However, the lability of Zn(II) and Cu(I) bound to MT is linked to the thermodynamic stability of the bond and this defines MT's metal donation properties. As the metallation reaction progresses, the last metals to bind have the weakest binding affinity. If the binding affinity of the last metallation reaction of MT is close to the binding constant for a protein's Zn(II) binding site, metal donation to the apoenzyme occurs. Otherwise, the MT harvests Zn(II) from sites with lower K_F than it. As such, these numerical values are requisite for understanding MT's metallation and metal donation processes.^{20, 28}



1.4.4 Computational Studies of Metallothionein

Because protein structures are not limited to the rigid dimensions defined by their crystal structure, the dynamic nature of proteins is hard to visualize. Computer simulations and molecular dynamics (MD) can predict what might happen to a truly dynamic protein system on small timescales (fs to ps). In the case of MT, studies on the fluxional apo structure showed the position of the cysteines in the native structure prior to metallation, as a model for the *de novo* synthesized protein. By doing so with MD, we can also watch the energy of the system until it reaches a minimum, resting state. A combination of molecular mechanics (MM) and MD were used by Rigby et al. to watch the effect on protein folding that each M(II) metallation event imparted on the structure. This showed the metal dependent folding mechanism emphasized the importance of the native apo structure. The study showed that initially, cysteines were partially solvent exposed, and as metallation progressed, the metal cysteine bonds coalesced into the protein center. When

the reverse (demetallation) was performed, the cysteines moved to the exterior of the protein chain.⁷⁵ This structural rearrangement is evident in the models of Rh₂MT in Chapter 5. The early ESI-MS work by Fenselau identified alkylating agents that reacted readily and selectively with MT. To determine the position of the cysteine residues involved in the selective alkylation, the eight most solvent accessible cysteines were simulated bound to drug molecules and the energies and distances were compared, identifying Cys 33 and Cys 48 as the most favourable for complexation,⁷⁰ giving information on metal binding sites.

The challenge with applying computational chemistry to metallothioneins actually begins when metallating the protein. The complexity of transition metals is still computationally expensive compared to simple MM, MD, or Newtonian based calculations. In order to consider the electronic effects of orbitals, Time Dependent Density Functional theory is used to apply models for forces that are present with the diffuse electronic orbitals of d-block metals. This is because the inclusion of the d and higher orbitals introduces electron movements that are not included in the MM theory and creates complications when calculating structures. A way to deal with this is by both defining a fixed geometry and assuming it, or separating the sections involved in the calculations. However this greatly limits the affordable calculations that can be performed. Returning to the concept of models and modelling reactions, the binding of glutathione, a small peptide with a cysteine thiolate, is used to mimic a single thiolate binding event in the metallation of MT, as is discussed in Chapter 6.

1.5 Scope

To understand the possible binding mechanisms of xenobiotic metals *in vivo*, it is necessary to first understand what we have now defined as traditional metal binding to MT.

In Chapter 2, I provide an overview of the metallation of M(II) to MTs by exploring millisecond timescale reactions of Cd(II) binding to apo-MT. Particularly, the partially metallated forms are of interest as they are the most probabilistic form of the protein *in*

vivo, and as they are known to exist in multiple conformations, either terminally bound or in complex metal thiolate networks involving bridging cysteines between the metals.

With the onset of xenobiotic metal pollution and metal-based therapy (e.g., platinum group metals), it is necessary to consider how these foreign metals bind to MT *in vivo*. It is often the clustering pattern of metals in MTs that give structural features, but in the case of these non-physiologically relevant metals, binding is anything but characteristic. It is through these reactions with xenobiotic metals that the flexible nature of MT metal chelation can be tested, as the world is approaching exposure to heavy metal pollution unimaginable before.

Currently, the best model of the physiological effects of non-natural metals comes from metal-therapeutics testing. These tests involve strictly controlled exposure and well documented effects. By testing the metal defense protein MT with these xenobiotic complexes, we understand our own physiological metal defense and the mechanism behind developed drug resistance.

In Chapter 3, using cisplatin, I unravel the rapid initial reaction pathway for MT with cisplatin, that is believed to be involved in developing cisplatin resistance. The results show the step by step destruction of cisplatin, and ligand displacement by the MT's cysteine thiolates.

Following the studies with cisplatin, in Chapters 4 and 5, we explore a platinum alternative, dirhodium(II) tetraacetate, in a model study with the β domain fragment of MT followed by a study with the whole protein. Through this reaction we see the sequential destructive chemistry clearly with the loss of all 4 acetate ligands, but in this complexation geometry, the metal-metal bond remains intact. This bond strength is analyzed with molecular modelling studies employing GSH and $\text{Rh}_2(\text{OAc})_4$, using TD-DFT methods in Chapter 6, to observe the electronic interactions and to investigate the origin of the spectroscopic signal.

Finally, in Chapter 7, we summarise the findings of this Thesis exploring non-traditional metallation of metallothioneins, by introducing some examples of xenobiotic metals in therapeutic use, and reviewing their reactions with metallothioneins.

1.6 References

1. P. Przybyłowski and A. Wilczyńska, Honey as an environmental marker, *Food Chem.*, 2001, **74**, 289-291.
2. K. M. Chan, Metallothionein: potential biomarker for monitoring heavy metal pollution in fish around Hong Kong, *Marine Poll. Bull.*, 1995, **31**, 411-415.
3. M. Roch, J. McCarter, A. Matheson, M. Clark and R. Olafson, Hepatic metallothionein in rainbow trout (*Salmo gairdneri*) as an indicator of metal pollution in the Campbell River system, *Can. J. Fish Aquat. Sci.*, 1982, **39**, 1596-1601.
4. P. J. Burke, Metal footprint linked to economy, *Nat. Geosci.*, 2018, **11**, 224.
5. P. P. M. Mejame, Y. M. Kim, D. S. Lee and S.-R. Lim, Effect of technology development on potential environmental impacts from heavy metals in waste smartphones, *J. Mater. Cycles Waste Manag.*, 2018, **20**, 100-109.
6. M. Sahan, M. A. Kucuker, B. Demirel, K. Kuchta and A. Hursthouse, Determination of Metal Content of Waste Mobile Phones and Estimation of Their Recovery Potential in Turkey, *Int. J. Environ. Res. Public Health*, 2019, **16**, 887.
7. P. J. Sadler, in *Advances in Inorganic Chemistry*, Elsevier, 1991, vol. 36, pp. 1-48.
8. I. Arany and R. L. Safirstein, "Cisplatin nephrotoxicity" presented in part at the Seminars in Nephrology, 2003.
9. B. Vallee, Zinc: biochemistry, physiology, toxicology and clinical pathology, *Biofactors*, 1988, **1**, 31-36.
10. L. Friberg, Cadmium and the kidney, *Environ. Health Perspect.*, 1984, **54**, 1.
11. G. F. Nordberg, Historical perspectives on cadmium toxicology, *Toxicol. Appl. Pharmacol.*, 2009, **238**, 192-200.
12. M. Margoshes and B. L. Vallee, A cadmium protein from equine kidney cortex, *J. Am. Chem. Soc.*, 1957, **79**, 4813-4814.
13. J. H. Kägi, *Metallothionein II: Proceedings of the «Second International Meeting on Metallothionein and Other Low Molecular Weight Metalbinding Proteins»*, Zürich, August 21–24, 1985, Birkhäuser, 2014.

14. M. P. Richards and R. J. Cousins, Isolation of an intestinal metallothionein induced by parenteral zinc, *Biochem. Biophys. Res. Commun.*, 1977, **75**, 286-294.
15. C. C. McCormick, M. P. Menard and R. J. Cousins, Induction of hepatic metallothionein by feeding zinc to rats of depleted zinc status, *Am. J. Physiol. - Endoc. M.*, 1981, **240**, E414-E421.
16. D. Durnam and R. Palmiter, Transcriptional regulation of the mouse metallothionein-I gene by heavy metals, *J. Biol. Chem.*, 1981, **256**, 5712-5716.
17. A. Pattanaik, C. F. Shaw III, D. H. Petering, J. Garvey and A. J. Kraker, Basal metallothionein in tumors: widespread presence of apoprotein, *J. Inorg. Biochem.*, 1994, **54**, 91-105.
18. R. Heuchel, F. Radtke, O. Georgiev, G. Stark, M. Aguet and W. Schaffner, The transcription factor MTF-1 is essential for basal and heavy metal-induced metallothionein gene expression, *EMBO J.*, 1994, **13**, 2870-2875.
19. B. Jasani and K. Schmid, Significance of metallothionein overexpression in human tumours, *Histopathology*, 1997, **31**, 211-214.
20. A. Drozd, D. Wojewska, M. D. Peris-Díaz, P. Jakimowicz and A. Krężel, Crosstalk of the structural and zinc buffering properties of mammalian metallothionein-2, *Metallomics*, 2018, **10**, 595-613.
21. A. O. Udom and F. O. Brady, Reactivation in vitro of zinc-requiring apo-enzymes by rat liver zinc-thionein, *Biochem. J.*, 1980, **187**, 329-335.
22. W. Maret, K. S. Larsen and B. L. Vallee, Coordination dynamics of biological zinc "clusters" in metallothioneins and in the DNA-binding domain of the transcription factor Gal4, *Proc. Natl. Acad. Sci. U.S.A.*, 1997, **94**, 2233-2237.
23. J. W. Ejnik, A. Muñoz, E. DeRose, C. F. Shaw and D. H. Petering, Structural consequences of metallothionein dimerization: solution structure of the isolated Cd₄- α -domain and comparison with the holoprotein dimer, *Biochemistry*, 2003, **42**, 8403-8410.
24. Y. Hathout, K. J. Reynolds, Z. Szilagyi and C. Fenselau, Metallothionein dimers studied by nano-spray mass spectrometry, *J. Inorg. Biochem.*, 2002, **88**, 119-122.
25. K. H. Falchuk, in *Molecular and cellular effects of nutrition on disease processes*, Springer, 1998, pp. 41-48.
26. J. Ejnik, C. F. Shaw III and D. H. Petering, Mechanism of cadmium ion substitution in mammalian zinc metallothionein and metallothionein α domain: Kinetic and structural studies, *Inorg. Chem.*, 2010, **49**, 6525-6534.

27. T. B. Pinter, G. W. Irvine and M. J. Stillman, Domain selection in metallothionein 1a: Affinity-controlled mechanisms of zinc binding and cadmium exchange, *Biochemistry*, 2015, **54**, 5006-5016.
28. T. B. Pinter and M. J. Stillman, The zinc balance: Competitive zinc metalation of carbonic anhydrase and metallothionein 1A, *Biochemistry*, 2014, **53**, 6276-6285.
29. M. Webb, in *Metallothionein II*, Springer, 1987, pp. 109-134.
30. D. Pain, A. Sanchez and A. Meharg, The Donana ecological disaster: contamination of a world heritage estuarine marsh ecosystem with acidified pyrite mine waste, *Sci. Total Environ.*, 1998, **222**, 45-54.
31. K. S. Kasprzak and G. S. Buzard, The role of metals in oxidative damage and red ox cell-signaling der angement, *Mol. Biol. Toxicol. Metals*, 2000, **477**.
32. D. M. Templeton and M. G. Cherian, in *Methods in enzymology*, Elsevier, 1991, vol. 205, pp. 11-24.
33. K. Tsuchiya, Causation of Ouch-ouch disease (Itai-Itai Byo)-an introductory review, *Keio J. Med.*, 1969, **18**, 195-211.
34. H. Baba, K. Tsuneyama, M. Yazaki, K. Nagata, T. Minamisaka, T. Tsuda, K. Nomoto, S. Hayashi, S. Miwa and T. Nakajima, The liver in itai-itai disease (chronic cadmium poisoning): pathological features and metallothionein expression, *Modern Pathol.*, 2013, **26**, 1228.
35. M. Harada, Minamata disease: methylmercury poisoning in Japan caused by environmental pollution, *Crit. Rev. Toxicol.*, 1995, **25**, 1-24.
36. T. Takeuchi, M. Frank, P. V. Fischer, C. S. Annett and M. Okabe, The outbreak of Minamata disease (methyl mercury poisoning) in cats on Northwestern Ontario reserves, *Environ. Res.*, 1977, **13**, 215-228.
37. I. Bremner, in *Metallothionein II*, Springer, 1987, pp. 81-107.
38. I. Bremner, R. Mehra and M. Sato, in *Metallothionein II*, Springer, 1987, pp. 507-517.
39. U. Weser and H.-J. Hartmann, in *Methods in enzymology*, Elsevier, 1991, vol. 205, pp. 274-278.
40. P. J. Thornalley and M. Vašák, Possible role for metallothionein in protection against radiation-induced oxidative stress. Kinetics and mechanism of its reaction with superoxide and hydroxyl radicals, *BBA - Protein Struct. M.*, 1985, **827**, 36-44.

41. M. Sato and I. Bremner, Oxygen free radicals and metallothionein, *Free Radic. Biol. Med.*, 1993, **14**, 325-337.
42. K. Melis, D. Carter, C. Stout and D. Winge, Single crystals of cadmium, zinc metallothionein, *J. Biol. Chem.*, 1983, **258**, 6255-6257.
43. W. Braun, M. Vasak, A. Robbins, C. Stout, G. Wagner, J. Kägi and K. Wüthrich, Comparison of the NMR solution structure and the x-ray crystal structure of rat metallothionein-2, *Proc. Natl. Acad. Sci. U.S.A.*, 1992, **89**, 10124-10128.
44. Y. Yang, W. Maret and B. L. Vallee, Differential fluorescence labeling of cysteinyl clusters uncovers high tissue levels of thionein, *Proc. Natl. Acad. Sci. U.S.A.*, 2001, **98**, 5556-5559.
45. H. Haase and W. Maret, A differential assay for the reduced and oxidized states of metallothionein and thionein, *Anal. Biochem.*, 2004, **333**, 19-26.
46. S.-H. Hong, Q. Hao and W. Maret, Domain-specific fluorescence resonance energy transfer (FRET) sensors of metallothionein/thionein, *Protein Eng. Des. Sel.*, 2005, **18**, 255-263.
47. K. E. R. Duncan, T. T. Ngu, J. Chan, M. T. Salgado, M. E. Merrifield and M. J. Stillman, Peptide folding, metal-binding mechanisms, and binding site structures in metallothioneins, *Exp. Biol. Med.*, 2006, **231**, 1488-1499.
48. K. E. R. Duncan and M. J. Stillman, Metal-dependent protein folding: metallation of metallothionein, *J. Inorg. Biochem.*, 2006, **100**, 2101-2107.
49. D. E. Sutherland and M. J. Stillman, The “magic numbers” of metallothionein, *Metallomics*, 2011, **3**, 444-463.
50. I. F. Tannock and D. Rotin, Acid pH in tumors and its potential for therapeutic exploitation, *Cancer Res.*, 1989, **49**, 4373-4384.
51. P. Kille, D. R. Winge, J. L. Harwood and J. Kay, A plant metallothionein produced in *E. coli*, *FEBS Lett*, 1991, **295**, 171-175.
52. R. T. Raines, M. McCormick, T. R. Van Oosbree and R. C. Mierendorf, in *Methods in enzymology*, Elsevier, 2000, vol. 326, pp. 362-376.
53. W. Lu and M. J. Stillman, Mercury-thiolate clusters in metallothionein. Analysis of circular dichroism spectra of complexes formed between. alpha.-metallothionein, apometallothionein, zinc metallothionein, and cadmium metallothionein and mercury (2+), *J. Am. Chem. Soc.*, 1993, **115**, 3291-3299.
54. M. J. Stillman, A. Y. Law, W. Cai and A. J. Zelazowski, in *Metallothionein II*, Springer, 1987, pp. 203-211.

55. M. J. Stillman, A. S. Zelazowski, J. Szymanska and Z. Gasyna, Luminescent metallothioneins: Emission properties of copper, silver, gold and platinum complexes of MT, *Inorganica Chim. Acta*, 1989, **161**, 275-279.
56. M. J. Stillman, A. R. Green, Z. Gui, D. Fowle and P. A. Presta, in *Metallothionein IV*, Springer, 1999, pp. 23-35.
57. J. B. Fenn, M. Mann, C. K. Meng, S. F. Wong and C. M. Whitehouse, Electrospray ionization for mass spectrometry of large biomolecules, *Science*, 1989, **246**, 64-71.
58. B. Domon and R. Aebersold, Mass spectrometry and protein analysis, *Science*, 2006, **312**, 212-217.
59. R. H. Perry, R. G. Cooks and R. J. Noll, Orbitrap mass spectrometry: instrumentation, ion motion and applications, *Mass Spectrom Rev.*, 2008, **27**, 661-699.
60. I. A. Kaltashov and A. Mohimen, Estimates of protein surface areas in solution by electrospray ionization mass spectrometry, *Anal. Chem.*, 2005, **77**, 5370-5379.
61. P. Kebarle and M. Peschke, On the mechanisms by which the charged droplets produced by electrospray lead to gas phase ions, *Anal. Chim. Acta.*, 2000, **406**, 11-35.
62. I. A. Kaltashov and R. R. Abzalimov, Do ionic charges in ESI MS provide useful information on macromolecular structure?, *J. Am. Soc. Mass Spectrom.*, 2008, **19**, 1239-1246.
63. J. A. Loo, R. R. O. Loo, H. R. Udseth, C. G. Edmonds and R. D. Smith, Solvent-induced conformational changes of polypeptides probed by electrospray-ionization mass spectrometry, *Rapid. Commun. Mass. Spectrom.*, 1991, **5**, 101-105.
64. X. Yu, M. Wojciechowski and C. Fenselau, Assessment of metals in reconstituted metallothioneins by electrospray mass spectrometry, *Anal. Chem.*, 1993, **65**, 1355-1359.
65. J. Zaia, D. Fabris, D. Wei, R. L. Karpel and C. Fenselau, Monitoring metal ion flux in reactions of metallothionein and drug-modified metallothionein by electrospray mass spectrometry, *Protein Sci.*, 1998, **7**, 2398-2404.
66. R. Lobinski, H. Chassaing and J. Szpunar, Analysis for metallothioneins using coupled techniques, *Talanta*, 1998, **46**, 271-289.
67. P. M. Gehrig, C. You, R. Dallinger, C. Gruber, M. Brouwer, J. H. Kägi and P. E. Hunziker, Electrospray ionization mass spectrometry of zinc, cadmium, and

- copper metallothioneins: evidence for metal-binding cooperativity, *Protein Sci.*, 2000, **9**, 395-402.
68. H. Chassaigne and R. Lobinski, Polymorphism and identification of metallothionein isoforms by reversed-phase HPLC with on-line ion-spray mass spectrometric detection, *Anal. Chem.*, 1998, **70**, 2536-2543.
 69. L. T. Jensen, J. M. Peltier and D. R. Winge, Identification of a four copper folding intermediate in mammalian copper metallothionein by electrospray ionization mass spectrometry, *J. Biol. Inorg. Chem.*, 1998, **3**, 627-631.
 70. Z. Szilágyi and C. Fenselau, Molecular dynamics simulation of metallothionein-drug complexes, *Drug Metab. Dispos.*, 2000, **28**, 174-179.
 71. X. Yu, Z. Wu and C. Fenselau, Covalent sequestration of melphalan by metallothionein and selective alkylation of cysteines, *Biochemistry*, 1995, **34**, 3377-3385.
 72. J. Zaia, L. Jiang, M. S. Han, J. R. Tabb, Z. Wu, D. Fabris and C. Fenselau, A binding site for chlorambucil on metallothionein, *Biochemistry*, 1996, **35**, 2830-2835.
 73. J. Ejniak, J. Robinson, J. Zhu, H. Försterling, C. F. Shaw III and D. H. Petering, Folding pathway of apo-metallothionein induced by Zn^{2+} , Cd^{2+} and Co^{2+} , *J. Inorg. Biochem.*, 2002, **88**, 144-152.
 74. T. T. Ngu, A. Easton and M. J. Stillman, Kinetic analysis of arsenic– metalation of human metallothionein: significance of the two-domain structure, *J. Am. Chem. Soc.*, 2008, **130**, 17016-17028.
 75. K. E. Rigby, J. Chan, J. Mackie and M. J. Stillman, Molecular dynamics study on the folding and metallation of the individual domains of metallothionein, *Proteins: Struct., Funct., Bioinf.*, 2006, **62**, 159-172.

Chapter 2

2 Understanding Cd²⁺ Binding Mechanisms and its Relation to the Intrinsically Disordered Structure of Metallothioneins*

The 20-cysteine mammalian metallothioneins are considered to be central to the homeostatic control of the essential metals Zn(II) and Cu(I) and, as part of their partially metal-loaded status, play a role in reversing oxidative stress.¹ Native apo-MT does not adopt a well-known structural motif, being described as a random-coil or intrinsically-disordered. Conclusions reached from a combination of ESI-mass spectral charge states, As(III) metallation of apo-MT at low pH, from molecular dynamic calculations and from metallation of the α -domain fragment, suggest that in fact the native apo-MT adopts a structure that is highly efficient towards metallation at physiological pH. The results in this Chapter show that the initial (M<5) Cd(II) metallation at physiological pH takes place to rapidly form structures based on isolated Cd(SCYS)₄ units, beads. At pH 5, cysteine bridged Cd₄(SCYS)₁₁ clusters form. The ESI-mass spectral profile of cysteine modified apo-MT at physiological pH shows that it is folded, whereas in the presence of 3 M guanidinium hydrochloride, the apo-MT is unfolded. Stopped-flow kinetic studies of the Cd(II) metallation show that the reaction is much slower for the denatured vs. the native apo-MT for formation of either beads or clusters. Metallation is slower for the formation of clusters than the formation of beads. These results are the first to quantify the presence of structure in native apo-MT in terms of the critical metallation properties. The implications of this study suggest that disruption of apo-MT structure due to ageing or other agents will negatively impact the metallation process for essential metals.

2.1 The Native Structure of Metallothionein

Essential metals are critical to Life's processes. Metals that disrupt these processes are considered toxic. Therefore, Life requires control of metal ions for necessary function, employing regulatory control agents like metallothioneins (MT). MTs are a family of cysteine-rich, low molecular weight proteins that coordinate, and, therefore, isolate a

*A version of this chapter has been published:

Metallomics DOI:10.1039/C8MT00347E Citation: *Metallomics*, 2019, Advance Article. Copyright 2019 Royal Society of Chemistry.

Reproduced with permission from: D. L. Wong, N. C. Korkola, and M. J. Stillman.

variety of free metal ions. Despite the critical involvement of MTs in Zn(II) and Cu(I) homeostasis, their stepwise metallation mechanisms are poorly understood. Since MT's discovery in 1957, as a Cd-containing protein,² much research has focused on the metal saturated, two-domain structure of Cd₇MT and Zn₇MT. When it was reported that MT natively exists predominantly in either the reduced apo (metal free, no S-S) state, or the partially metallated states,³⁻⁵ interest was spurred about the metallation mechanism and the true structure of native MT *in vivo*.^{4, 6-14}

Information about the apo-MT structure has remained mysteriously vague. Labelled as “random coil,” “globular,” or “intrinsically disordered,” the structure of partially metallated MTs have been historically difficult to elucidate due to the lack of secondary structures, little to no aromatic residues, extreme sensitivity to oxidation, and dependence on solution phase interactions. MT is unique in that progressive metallation imparts a major increase in the ordered structure.¹⁵ Initially, at physiological pH, the divalent metal ions bind tetrahedrally to terminal cysteinyl thiolates as isolated beads, which with further metallation, progress to the formation of metal-thiolate clusters, involving metal-bridging cysteine thiols.¹⁶ The traditional, two-domain, dumbbell-like structure is formed only upon full metallation with 7 divalent metals at physiological pH.

Extensive advances have been made in studying partially metallated and metal-free MTs, including *in vivo* fluorescence detection,^{5, 17} molecular dynamic simulations,^{18, 19} collision induced denaturation,²⁰ and mass spectrometric methods.^{14, 21} The work in this Chapter builds on recent investigations involving denaturation,²² cysteine modification¹² and mass spectrometry,^{6, 23-25} in conjunction with stopped-flow kinetic analysis to provide new detail about the first metallation steps that take place as a function of the structural status of the apo-MT. The structures adopted initially by *de novo* apo-MT are critical to the subsequent metallation steps and define the complete metallation pathway. These early metallation steps are vital to the function of MTs *in vivo*.

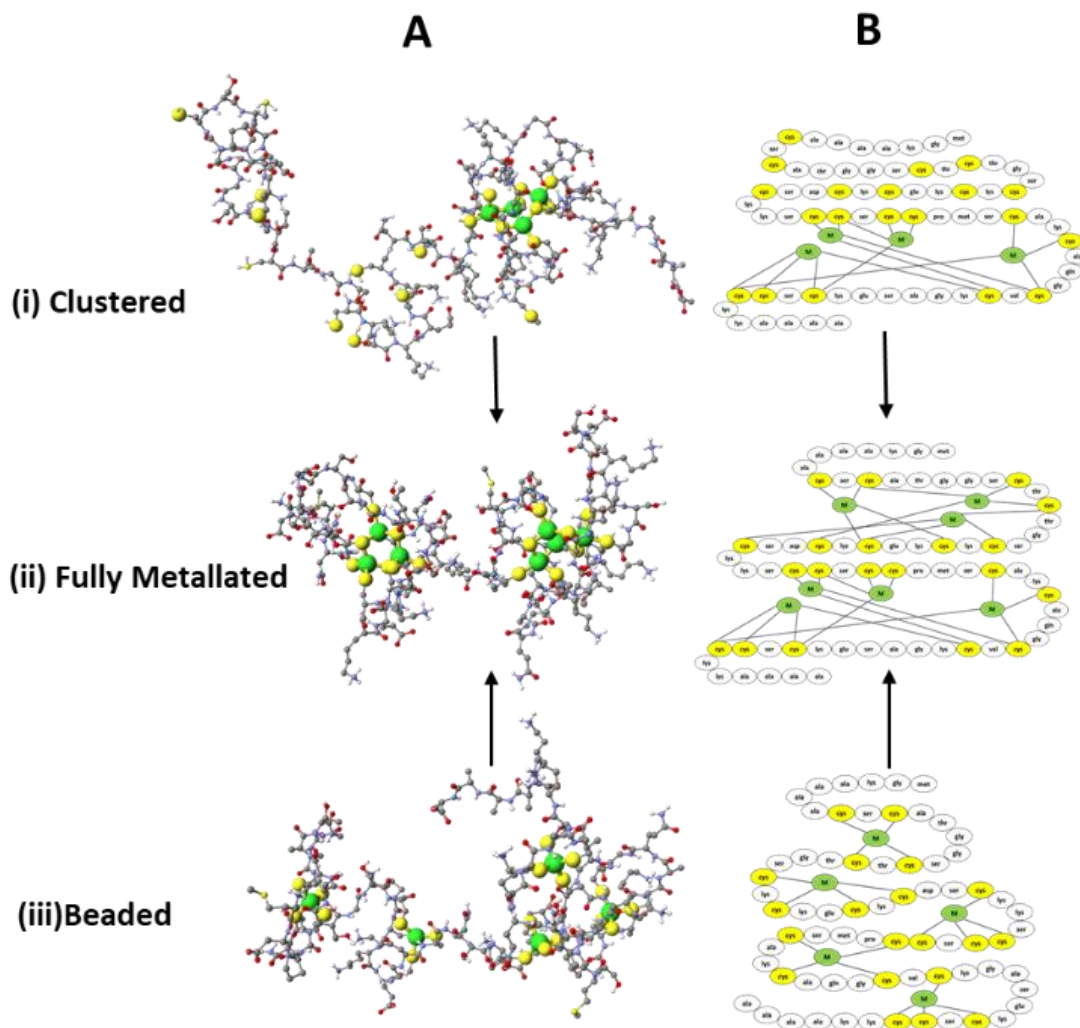


Figure 2-1 The many structures of metallothionein.

(A) Conceptual structures for (i) the Cd_4 cluster in the α domain, (ii) the fully metallated structure, and (iii) 5 terminally-bound (beaded) $Cd(II)$ displaying no domain structure based on MM3 molecular models and (B) sequence and connectivity diagrams of fully metallated β MT and the two partially metallated pathways. Calculations and image from N. C. Korkola, reproduced with permission from the Royal Society of Chemistry.²⁶

The confirmation of the presence of apo-MT *in vivo* has cemented the fact that metallation is a post-translational modification. The connectivities of bridging cysteines take place across the domain, Figure 2-1B (i) and (ii), and, as a result, these metal-bonds can only be formed once the protein is fully synthesized. Therefore, the initial states of

metallation are of great interest for the purpose of determining the properties and influence of the structure adopted by metal free MTs.

From studies reported specifically over the last two years by Irvine et al.,^{8, 16} two distinct, pH dependent, metal binding pathways or mechanisms are at play. Initially, and especially for $M \leq 3$, the formation of “beads” involving terminally bound cysteines is dominant, especially for Zn(II) above pH 6 and Cd(II) above pH 7. The native MT protein structure under the beaded pathway can accommodate a maximum of 5 M(II), with the 20 cysteines tetrahedrally coordinating each metal, Figure 2-1(iii). MT adopts a “single domain” type globular structure, where the lack of bridging cysteines results in no true binding domain as described previously.^{16, 27, 28} Figure 2-1 shows these two major conformations that MTs flexibly adopt at specific points during metallation. The ball-and-stick models are displayed Figure 2-1A and the peptide sequence in Figure 2-1B, and Figure 2-1(i) show the structure of the Cd_4S_{11} cluster that forms favourably in the α -domain.

At metallation levels of $M =$ “magic number 4”^{1, 11, 12, 20, 29, 30} and higher, the pathway adopted involves cooperative coalescence to a metal-thiolate cluster. This is now a thermodynamically stable, M_4S_{cys11} cluster formed in the C-terminal α domain,³¹ and increases the stability of the MT peptide against protease digestion. The conditions for selecting the dominant pathway are pH, temperature, and metal concentration and the selection is element dependent. The effects of the dominating pathway can be seen in the speciation of the metallated products using ESI-MS methods.

The rapid stepwise metallation of MTs has been difficult to observe. Due to the spectroscopically silent nature of native Zn(II)MT, Cd(II) is used as a spectroscopic probe because of its $S \rightarrow Cd(II)$ ligand to metal charge transfer (LMCT) that is at 250 nm; this is well clear of protein-based absorbance because of the absence of aromatic residues. Initial kinetic reports of MT metallation focused on rates of demetallation, or rates of metallation of the C-terminal α -domain of this protein.^{14, 31} The α -domain is an 11-cysteine fragment that contains the M_4S_{11} , thermodynamically stable, adamantane-like, metal-thiolate cluster. The β -domain (“ β -MT”) is a smaller, 9 cysteine peptide fragment that forms a cluster when saturated (M_3S_9) but is more labile than the α -fragment. The α

domain has been studied previously by our group, with results that show that the metallation kinetics are influenced by the apo-MT structure, and is flexible enough to accommodate 5 M(II) in forced conditions.⁷ While studying the isolated domains gives valuable information regarding individual cysteine coordination,³¹ it is now understood that the isolated domains behave differently than the intact protein.^{17, 27, 32, 33}

In this Chapter, the rates of the metallation by Cd(II) of the native $\beta\alpha$ MT protein in solution are reported and discussed to understand how changes in the apo structure influence the metal-binding pathways. The rate of the early steps in the Cd(II) metallation of apo- $\beta\alpha$ MT depends on the folded state of the MT, and the metallation structure that results. By using denaturing agents at physiological pH, and at pH values that favour either beaded (pH ~8) or cluster formation (pH ~5), stopped-flow kinetic methods provide the binding rate for the Cd(II) metallation. The extent of folding under these conditions is obtained from the ESI-mass spectral data using cysteine modification methods. The results show that the metallation rate at physiological pH is 10 times faster than at pH 5 for both the folded and the denatured protein. Metallation involving cluster formation is slower than bead formation. These results indicate that at physiological pH, MT is a highly efficient scavenger of Cd(II) and can employ its 20 cysteines with flexible binding. The metallation properties for partially metallated Cd-MTs at both pH extremes, which would mimic the pathways adopted specifically for zinc binding, are described below. By selecting conditions that are known to favour either of the two pathways, and confirmed using ESI-MS, the rates of metallation of the beaded pathway vs. the cluster pathway can be compared. The outcomes of these experiments provide evidence that at physiological pH, apo-MT adopts a specific native structure that is optimized for metallation.

2.2 Experimental Methods

2.2.1 Solution Preparation

Ammonium formate (J.T. Baker) and tris(hydroxymethyl)aminomethane-HCl (Tris-HCl) (Sigma-Aldrich) buffers were prepared by dissolving solid crystals into DI water to make a final concentration of 10 mM. The solution was then pH adjusted to 2.80, 5, 6, 7, 7.4, 7.5, or 8 using HCl and NH₄OH. KCl (Fisher) was added to the ammonium formate

buffer used in stopped flow studies to final concentration of 200 mM to maintain a constant ionic strength.

50 mg/mL Kanamycin (Teknova), 1 M isopropyl β -D-1-thiogalactopyranoside (IPTG) (Fisher), and 1 M CdSO₄ (J.T. Baker) for cell growth were prepared by dissolving the appropriate amount of solid reagent in DI water. 10 mM solutions of *N*-ethylmaleimide (NEM) (Eastman) and Cd(OAc)₂ (Acros) were made by mixing solid crystals into the ammonium formate buffer of the desired pH for the experiment. KCl was added to the Cd(OAc)₂ solution used in stopped flow studies to a concentration of 200 mM. 8 M guanidinium chloride (GdmCl) was prepared by mixing solid GdmCl crystals (Omnipur) and KCl to make 200 mM in the case of stopped flow experiments with ammonium formate buffer. The mixture was gently heated until all the solid crystals had dissolved. The solution was allowed to cool and was then pH adjusted to the desired pH of 5, 6, 7, 7.4, 7.5, and 8 using HCl and NH₄OH. CdOAc₂ solutions at concentrations of 5, 10, 12.5, 15, 20, and 25 μ M for use in stopped flow reactions were prepared by diluting the stock 10 mM Cd(OAc)₂ solution with the appropriate amount of ammonium formate buffer and GdmCl at the desired pH of 5, 6, 7, 7.4, 7.5, or 8 for a final denaturant concentration of 4 M.

Preparation of apo-MT with pH adjustment

A 1-2 mL solution of Cd₇MT was thawed under a vacuum and demetallated by buffer exchange using a pH 2.80 ammonium formate buffer, and then raised using ammonium formate buffer of the desired sample pH of 5, 6, 7, 7.4, 7.5, or 8.

Mass spectrometric (MS) studies of the apo-MT structure were carried out using samples prepared with a Millipore centrifuge filter tube with a cut-off of 3kDa. The MT and low pH buffer were centrifuged at 4000 rpm for 30 minutes twice. The 10 mM ammonium formate buffer at pH 7.4 was then added along with a drop of concentrated ammonium hydroxide. The buffer exchange was performed under the same conditions as the demetallation 3-4 times. The pH of the flow-through was tested after each spin. For MS studies of the partial metallation of MT, the protein was demetallated using a PD-10 (GE Healthcare) size exclusion column with pH 2.80 ammonium formate buffer. The protein

was centrifuged once at 4000 rpm for 30 minutes and then run down another column at pH 5 or 8 to raise the pH. The MT was then centrifuged again for 30 minutes at the same speed as before. For stopped-flow studies, the MT was demetallated using the PD-10 column with the pH 2.80 ammonium formate buffer. It was then put down another PD-10 column with the buffer of pH 5, 6, 7, 7.5, or 8. The pH of the resulting protein solution was tested.

The concentration of the apo-MT was determined by metallating a small portion of the sample with excess $\text{Cd}(\text{OAc})_2$ and measuring the absorbance of the $S \rightarrow \text{Cd}(\text{II})$ LMCT band at 250 nm. Beer's law was used to calculate the concentration using the molar extinction coefficient of fully metallated $\beta\alpha\text{MT}$ of $\epsilon = 89000 \text{ cm}^{-1}$.

For MS studies of the apo protein, the apo-MT sample was split into 2 vials. One of the vials was denatured by adding 8 M GdmCl to make a final concentration of 3 M. The other was left in its native state. The appropriate amount of 10 mM NEM solution was added to both samples to equal 10 molar equivalents compared to the MT concentration. The denatured solution was buffer exchanged by dialysis in 10 mM ammonium formate buffer at pH 7.4 for 2 hours to remove the GdmCl, as its signal would dominate the mass spectrum. Since the NEM was now covalently bound to the cysteine residues, the buffer exchange does not affect the distribution of the modifications.

For the MS studies of the stepwise metallation of MT, the protein samples at pH 5 and pH 8 were metallated with the appropriate amount of $\text{Cd}(\text{OAc})_2$ to give approximately 0.5, 1.5, 4, 5, and 6 molar equivalents of Cd(II) per protein for the solutions at pH 5, and 1, 2.5, and 5 molar equivalents for the pH 8 samples. The exact equivalents of Cd(II) added were calculated using the average of all the species present in the spectra.

For stopped-flow kinetics studies, the protein samples were diluted with 10 mM ammonium formate buffer adjusted to pH 5, 6, 7, 7.5, or 8 and 8 M GdmCl to result in a final solution of 5 μM MT with either 0, 1, 2, or 4 M of GdmCl. KCl was added to give a final concentration of 200 mM KCl to keep the ionic strength of the solution constant. It is important to note that the rate of metallation of native apo-MT was compared to the rate in the presence of 5 M chloride ions and in the presence of sucrose matching the

viscosity of 5 M GdmCl. This was to confirm that the presence of the chloride ions in GdmCl did not interfere with the cadmium and the viscosity of the GdmCl did not affect the rate of metallation.

2.2.2 Mass Spectral Studies

Mass spectra were collected on a MicroTOF ESI mass spectrometer (Bruker, Toronto). The parameters were as follows: Capillary: 4200 V, end plate offset: 500 V, dry gas: 8.0 L/min, dry temperature: 100°C, capillary exit: 180.0 V, Skimmer 1: 22.0 V, hexapole 1: 22.5 V, hexapole RF: 600.0 V, skimmer 2: 22.0 V, lens 1 transfer: 88.0 μ s, lens 1 pre-pulse storage: 23.0 μ s, mass range: 500-4000 m/z, flow rate: 10 μ L/min. The spectra were averaged over 2 minutes.

2.2.3 Stopped Flow Studies

An SFM-300 instrument (BioLogic, France), Figure 2-2, was used to rapidly mix and transfer the reagents to a cuvette with a 10 mm path length and 1 mm aperture. The reaction was observed with a MOS 250 spectrophotometer and the resulting kinetic traces were recorded using BioKine software. This reaction was performed at 10 °C.

Apo-MT, ammonium formate buffer of the desired pH, and Cd(OAc)₂ were loaded into syringes 1, 2, and 3, respectively. First, 500 μ L of buffer was shot at a flow rate of 5 mL/s to clean the cuvette and to confirm the baseline level. Then, 160 μ L each of apo-MT and Cd(OAc)₂ were shot at a flow rate of 8 mL/s. These were mixed and reached the cuvette with a dead time of 1.9 ms. After 20 ms mixing time, the hard stop was closed and the reagents were allowed to react in the cuvette. The reaction was monitored through the LMCT band at 250 nm and recorded every 500 μ s for a total of 2 s. This process was repeated at least three times to give an average of multiple traces. The standard deviation over multiple kinetic traces for each set of experimental conditions was 10 %.

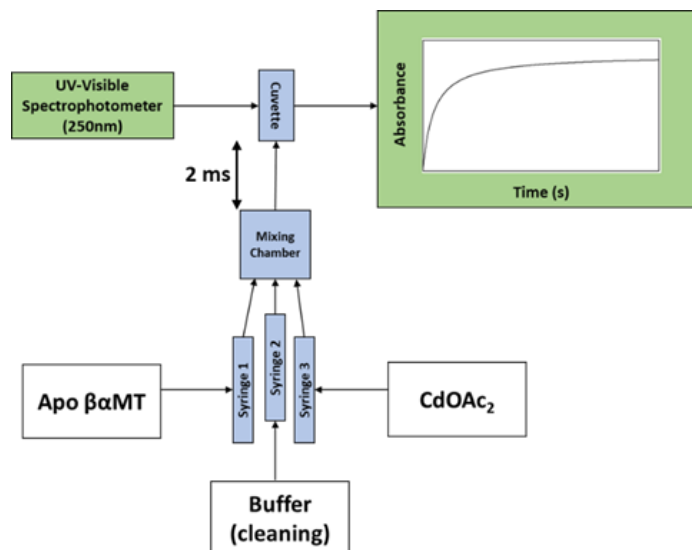


Figure 2-2 A schematic of the SFM apparatus.

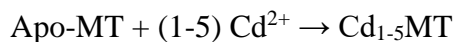
The three syringes are shown with their respective reagents along with their path to the mixing chamber and then the cuvette. The lowest achievable dead time from the mixer to the cuvette is approximately 2 ms. Image from N. C. Korkola, reproduced with permission from the Royal Society of Chemistry.²⁶

2.2.4 Fitting of the Kinetic Traces

The data were not transformed from absorbance to concentration units due to the multi-product nature of the final solution. The partially metallated MT form a distribution of species, each of which would have its own specific molar extinction coefficient. These coefficient values have not been determined for the individual species, and is further clouded by the averaging of the absorption signal. Therefore, Beer's Law could not be used to determine the concentration of the product. It should be noted that the rate constants reported by this method are only relative, as the concentration must be known to find the absolute values.

The fitting program GEPASI version 3.30³⁴ was used to fit the experimental kinetic traces and find the relative rate constants. The metallation reaction was treated as a single bimolecular step as shown below. Although the acquired traces in reality consisted of multiple overlapping bimolecular reactions, it was not possible to resolve these as the overall reaction was close to the dead time of the instrument. The simplified single

bimolecular reaction that encompasses all the metallation steps resulted in an appropriate fit for this complicated kinetic mechanism.



Two different methods were used in combination to fit the traces. The Nelder and Mead (Simplex) method was used until the sum of squares reached a constant value and then the Levenberg-Marquardt was used until the final solution was found.

2.2.5 Molecular Modelling

The clustered, beaded, and fully metallated MT structures were modelled using Scigress 6.0 (Fujitsu, Poland).³⁵ The sequence shown in Figure 2-1 (B) was input into the software. The geometry of the MT was optimized to the lowest energy level using the MM3 procedure. The lowest energy conformation was then found by running the MD (MM3) procedure to create multiple random conformations over a time of 5000 ps. The procedure was run under low temperature conditions of 5 K to simulate the hydrogen-bonded native protein and high temperature conditions of 1000 K to mimic the denatured conformation. The dielectric was set at 78, the van der Waals cut-off distance at 9 Å, and the van der Waals interaction update rate at 50. The output frequency was 200 steps and the refresh rate was 100 steps.

2.3 Results

2.3.1 Denaturation of MT with Guanidinium Hydrochloride

The extent of unfolding of the apo-MT in the presence of the 3 M reversible denaturant GdmCl was probed by adding N-ethyl maleimide (NEM) to covalently and irreversibly modify solvent exposed cysteine residues. The denaturant was then removed, and the resulting modified protein was examined using ESI-MS at pH 7.4. Figure 2-3, A shows that the speciation profile of NEM binding to the apo-MT displays preferred modification under physiological pH in the absence of denaturant. This spectral profile drastically changes in the presence of 3 M GdmCl, Figure 2-3, B, where the alkylated species has a Normal distribution profile.

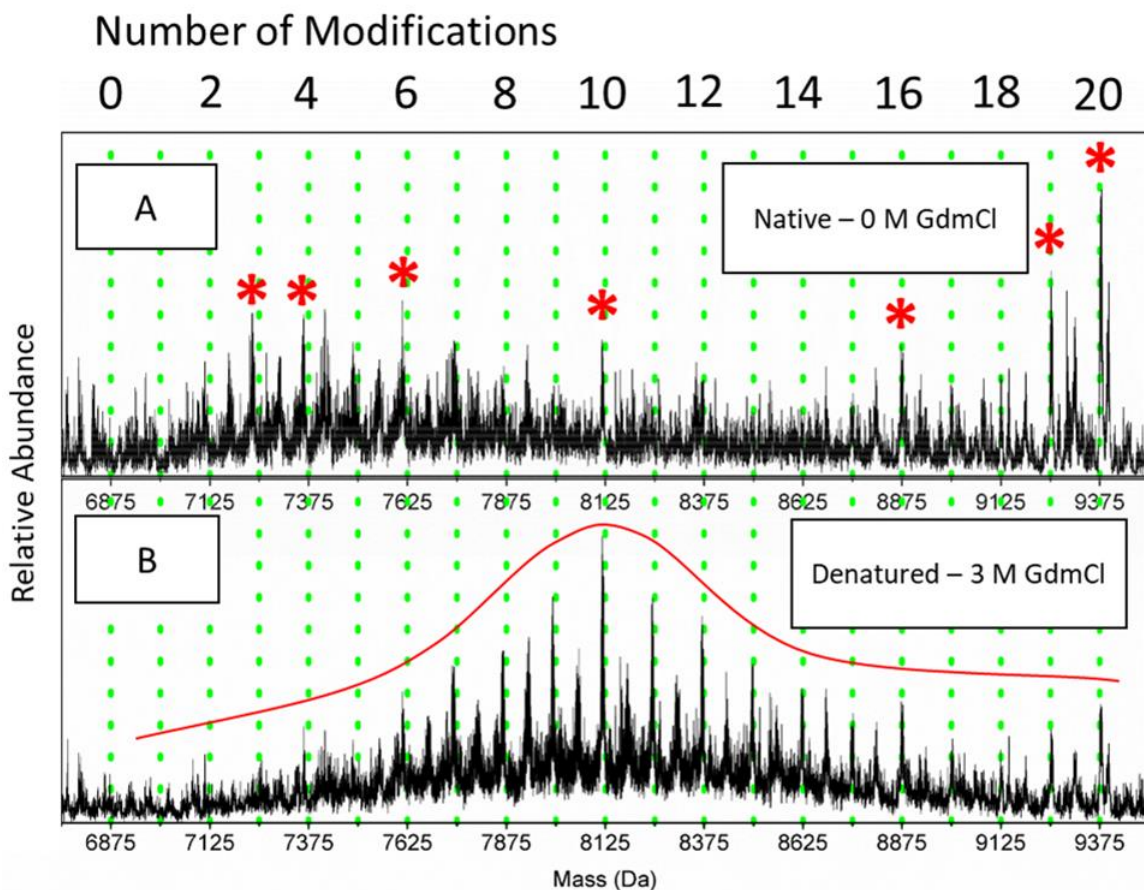


Figure 2-3 Native and denatured MT modified by NEM

Deconvoluted ESI mass spectra of (A) native apo-MT at pH 7.4 and (B) apo-MT denatured with 3 M GdmCl at pH 7.4, both modified with 10 molar equivalents of NEM. MT in the native environment (A) shows a cooperative modification pattern, while the denatured protein (B) shows a modification distribution resembling a Normal curve. Data and image from N. C. Korkola, reproduced with permission from the Royal Society of Chemistry.²⁶

The series of stopped flow kinetic absorbance traces number Figure S1-5 are used to create the plots of Figure 2-4.

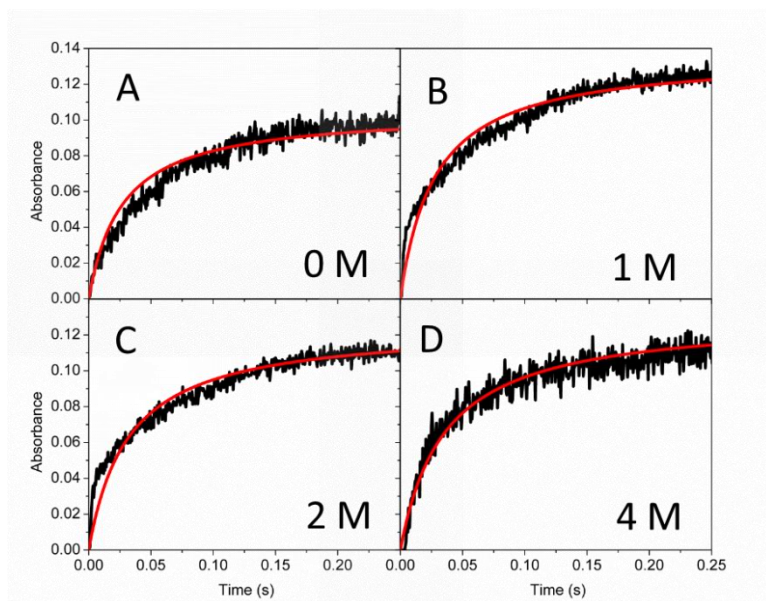


Figure S1. The kinetics traces of the binding of 2.5 eq. of Cd to apo-MT at pH 5 in the presence of increasing amounts of GdmCl at concentrations of A) 0 M, B) 1 M, C) 2 M, and D) 4 M. Data and image from N. C. Korkola, reproduced with permission from the Royal Society of Chemistry.²⁶

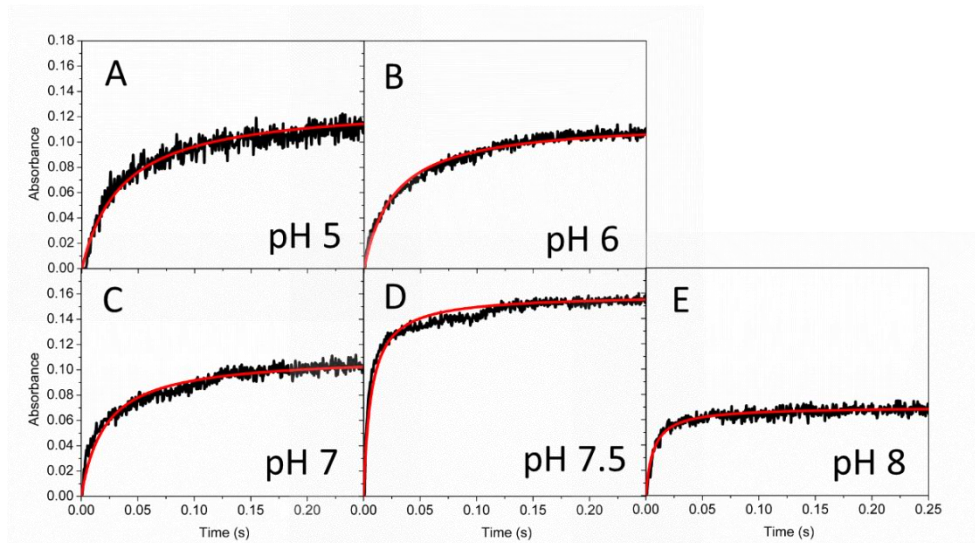


Figure S2. The kinetics traces of the binding of 2.5 eq. of Cd to apo-MT in the presence of 4 M GdmCl at pH A) 5, B) 6, C) 7, D) 7.5, and E) 8. Data and image from N. C. Korkola, reproduced with permission from the Royal Society of Chemistry.²⁶

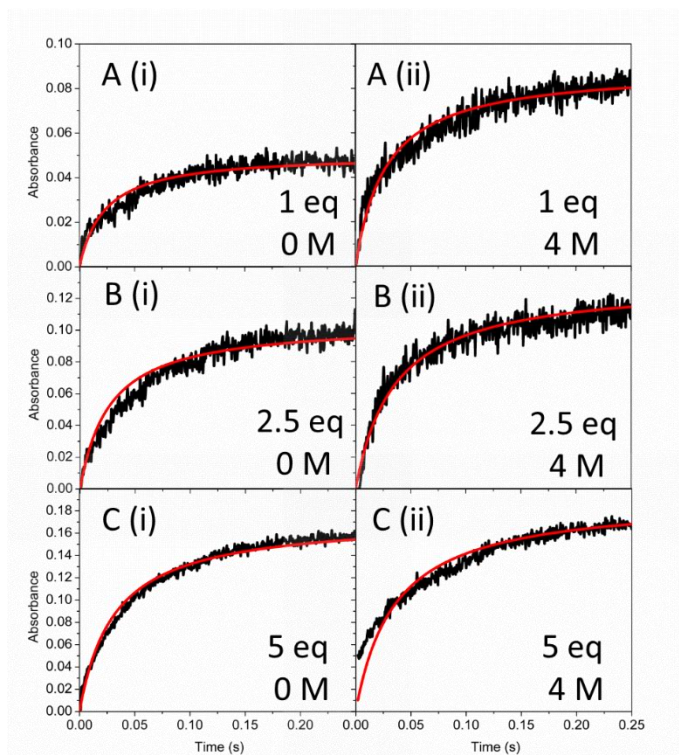


Figure S3. The kinetics traces of the binding of apo-MT to A) 1, B) 2.5, and C) 5 equivalents of cadmium at pH 5 and in the presence of (i) 0 M and (ii) 4 M of GdmCl. Data and image from N. C. Korkola, reproduced with permission from the Royal Society of Chemistry.²⁶

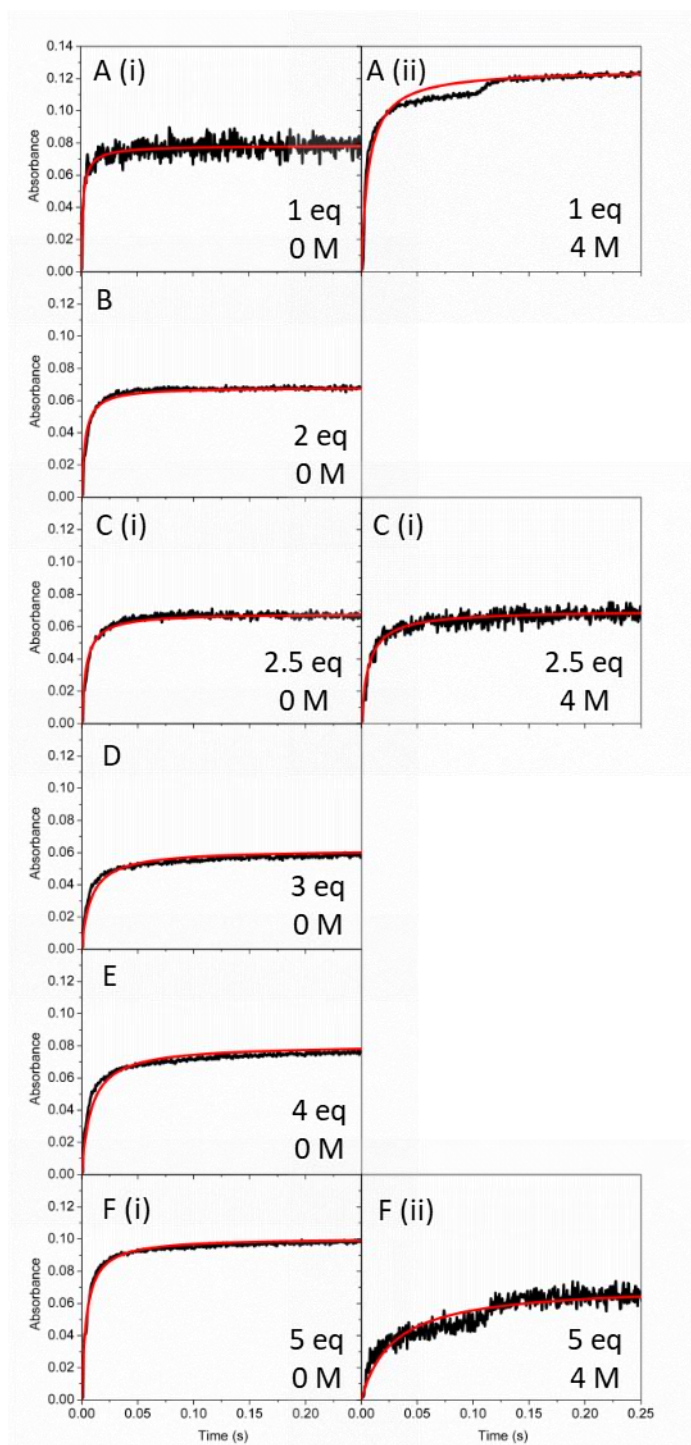


Figure S4. The kinetics traces of the binding of apo-MT to A) 1, B) 2, C) 2.5, D) 3, E) 4, and F) 5 equivalents of cadmium at pH 8 and in the presence of (i) 0 M and (ii) 4 M of GdmCl. Data and image from N. C. Korkola in reference,²⁶ reproduced with permission from the Royal Society of Chemistry.

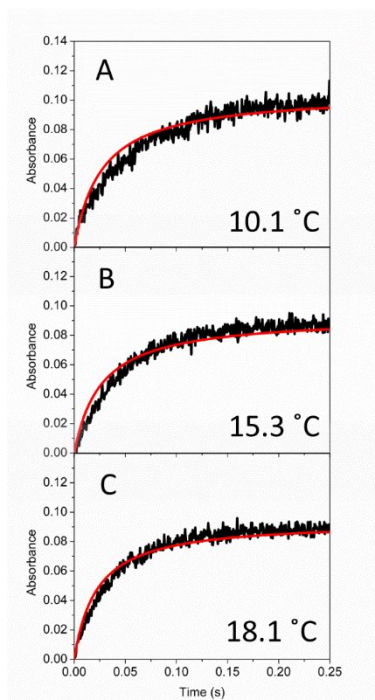


Figure S5. The kinetics traces of the binding of 2.5 eq. of Cd to apo-MT at pH 5 and with no denaturant at temperatures of A) 10.1 °C, B) 15.3 °C, and C) 18.1 °C. Data and image from N. C. Korkola, reproduced with permission from the Royal Society of Chemistry.²⁶

2.3.2 Relative k_{obs} Decreases with Increasing Denaturant at pH 5 and Fixed Metal Status

Figure S1 shows the change in absorbance at 250 nm for the reaction of apo-MT with a fixed 2.5 mol. eq. of Cd(OAc)₂ and increasing concentrations of GdmCl, at pH 5. The relative k_{obs} values are shown in Figure 2-4. The rate of metallation decreases as a function of increasing denaturant concentration.

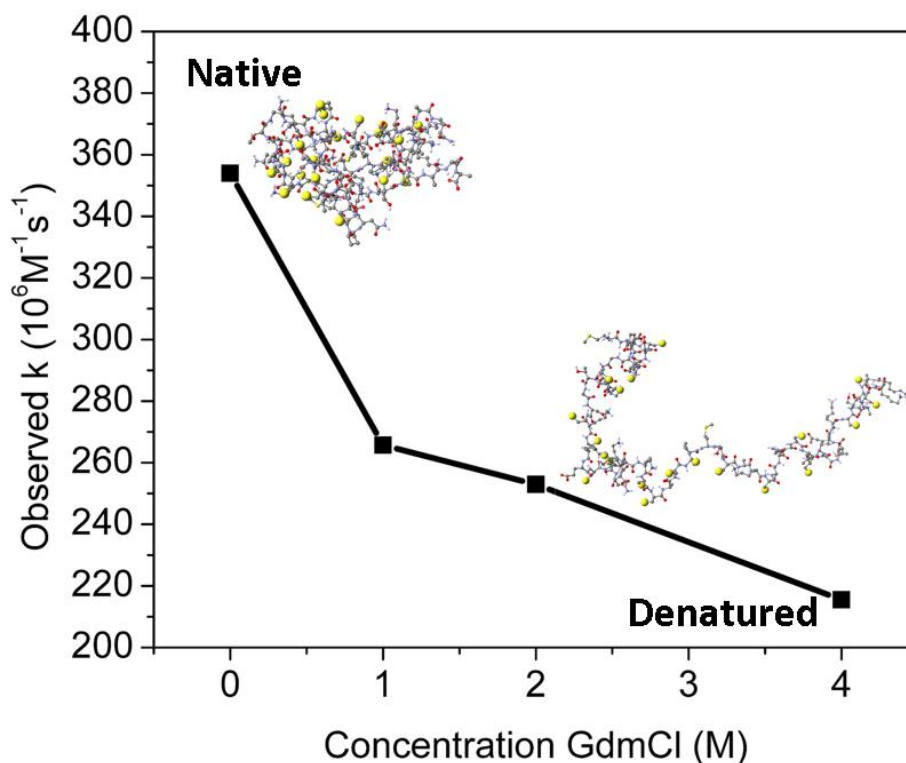


Figure 2-4 Plot of the observed rate constant as a function of GdmCl concentration. Apo-MT was reacted with 2.5 mol. eq. of $\text{Cd}(\text{OAc})_2$ with increasing concentration of denaturant, at pH 5. At this pH, the resulting product would be the $[\text{Cd}_4\text{S}_{11}]^{3-}$ cluster. The rate of metallation slows down as MT unfolds. Data and image from N. C. Korkola, reproduced with permission from the Royal Society of Chemistry.²⁶

2.3.3 The Cd(II) Metallation Rate is pH Dependent

The pH dependence of metallation was determined using stopped flow kinetic methods for the reaction of the apo-MT with 2.5 mol. eq. of $\text{Cd}(\text{OAc})_2$, with no denaturant present. The choice of 2.5 mol. eq. was because the dominating metallation pathway (beads or clusters) is readily apparent in the mass spectral data with this level of partial metallation. The metallation of apo-MT by Cd(II) is rapid at physiological pH ($3633 \times 10^6 \text{ mol}^{-1} \text{ s}^{-1}$), but the rate decreases sharply as the pH is lowered ($354 \times 10^6 \text{ mol}^{-1} \text{ s}^{-1}$), as seen in Figure 2-5.

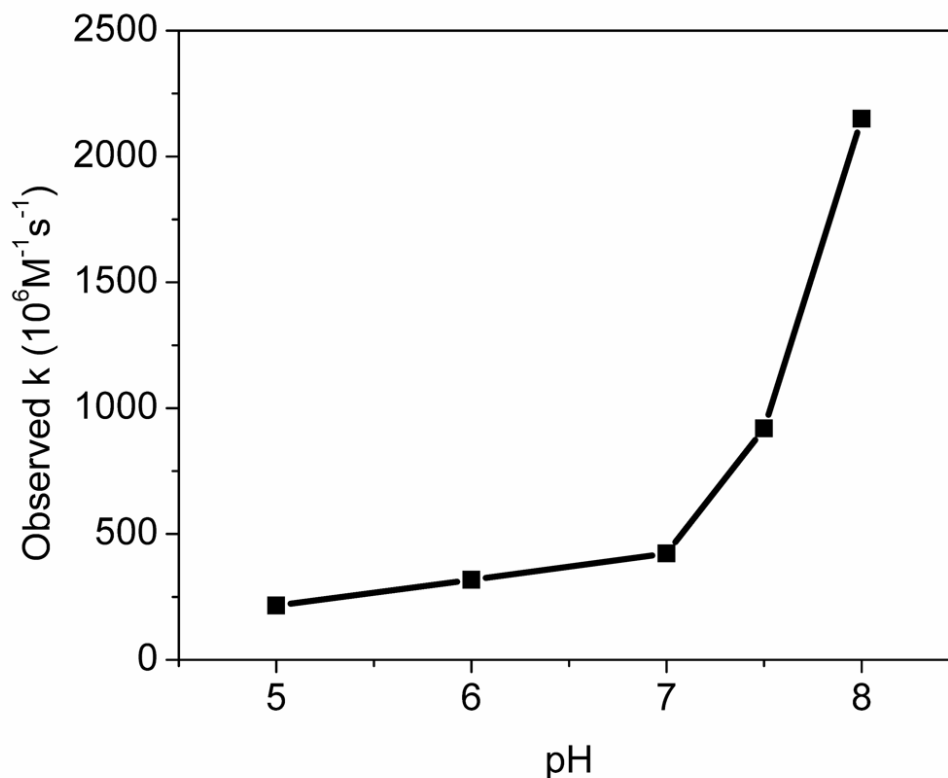


Figure 2-5 Relationship between observed rate constant k of the reaction of native apo-MT

Apo-MT was reacted with 2.5 mol. eq. Cd(II) at pH 5, 6, 7, 7.5, and 8, in the presence of 4 M GdmCl. The product at each pH can be determined from Figure 2-6 and Figure 2-7. At pH 5 the resulting product would be the $[\text{Cd}_4\text{S}_{11}]^{3-}$ cluster. At pH 8 the resulting product would be a series of $[\text{Cd}_1\text{S}_4]^{2-}$ beads. Data and image from N. C. Korkola, reproduced with permission from the Royal Society of Chemistry.²⁶

The mass spectral data shown in Figure 2-6 and Figure 2-7 detail the speciation profiles at the extremes of the pH range used in Figure 2-5 above. The two metallation pathways manifest in different patterns of species abundance. The spectra taken at both pH 5 and 8, with 1, 2.5, and 5 mol. eq. of Cd(II) added show differing speciation at the 2.5 and 5 mol.

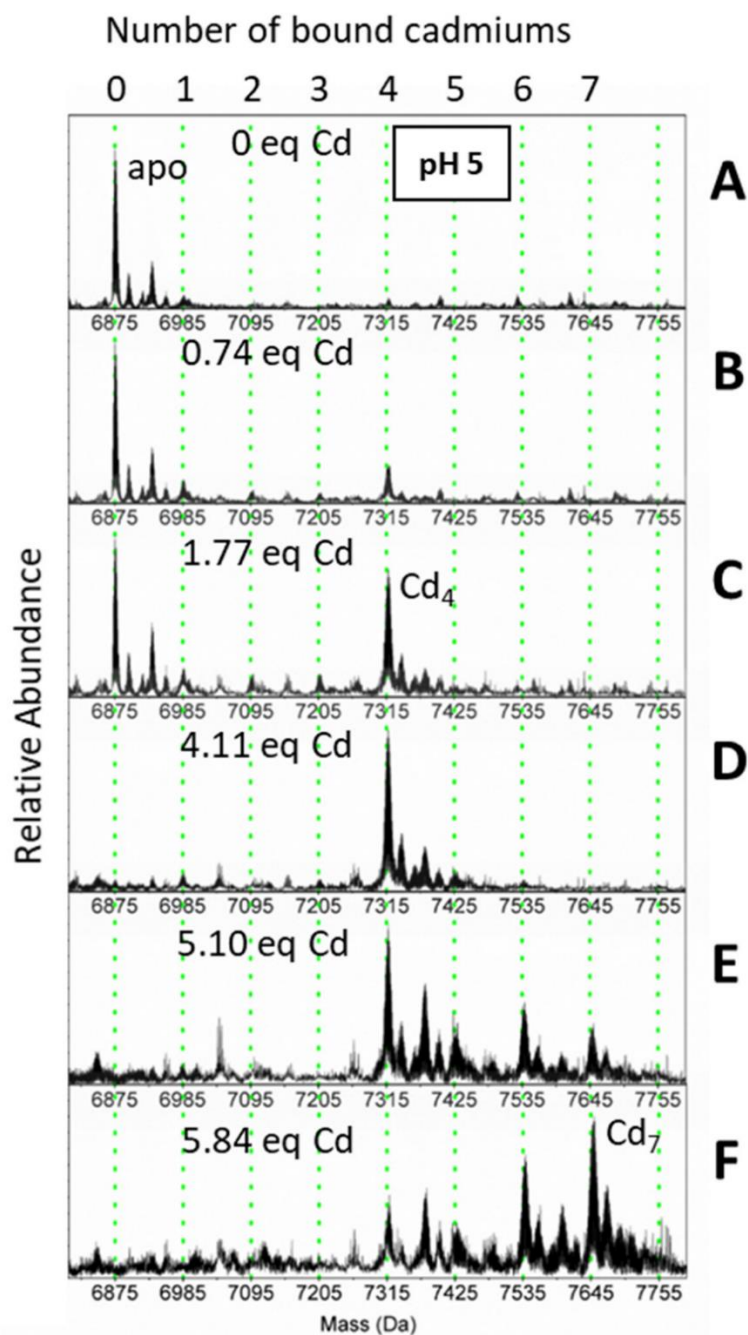


Figure 2-6 ESI mass spectra for the Cd(II) titration of apo-MT at pH 5. Deconvoluted ESI mass spectra at pH 5 of the partially metallated MT species using (A) 0, (B) 0.74, (C) 1.77, (D) 4.11, (E) 5.10, and (F) 5.84 mol. eq. of cadmium. The Cd_4 cluster is favoured at low equivalence and the fully metallated Cd_7 species is favoured upon adding higher amounts of cadmium. Data and image from N. C. Korkola, reproduced with permission from the Royal Society of Chemistry.²⁶

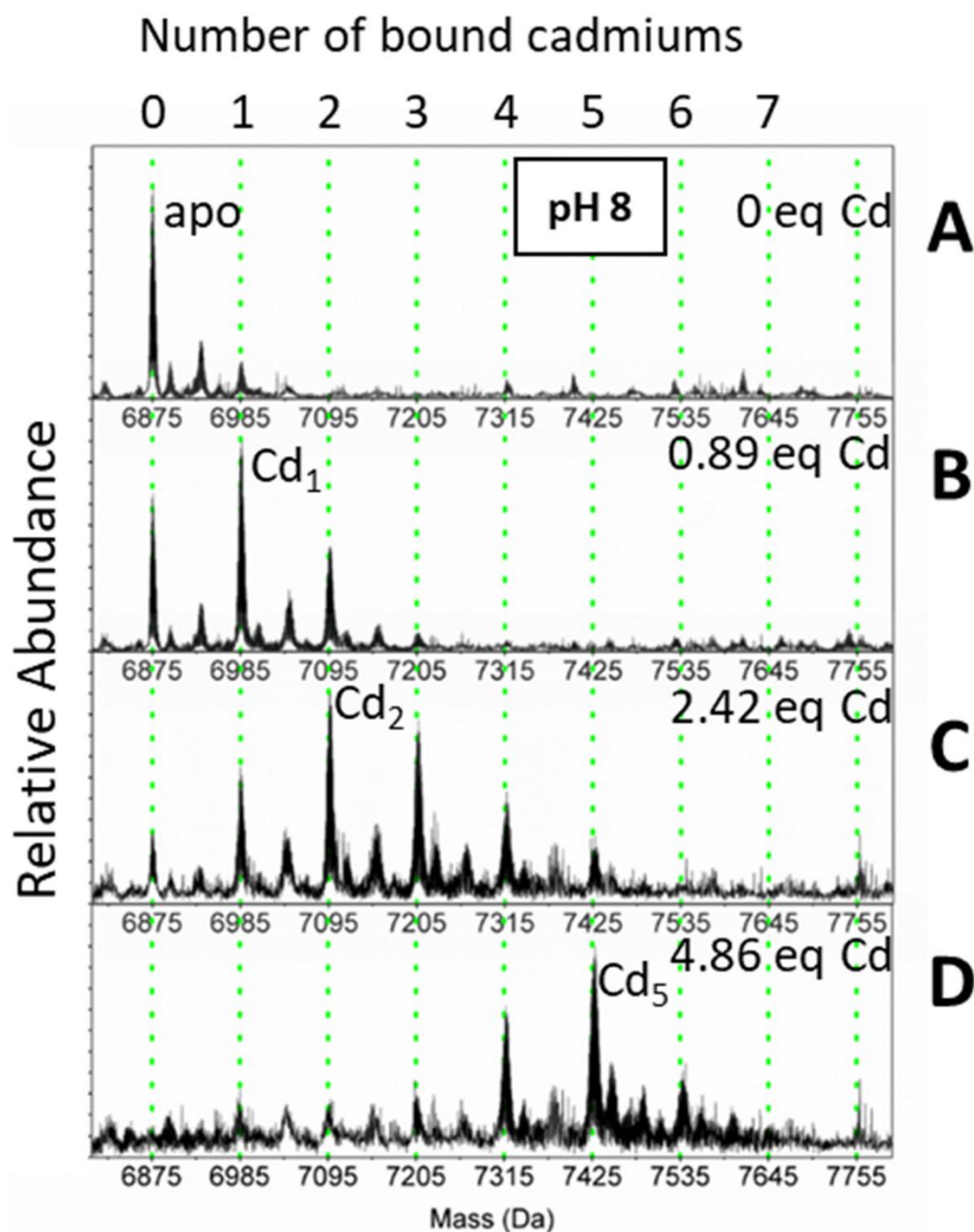


Figure 2-7 ESI mass spectra for the Cd(II) titration of apo-MT at pH 8. Deconvoluted ESI mass spectra at pH 8 of the partially metallated MT species using (A) 0, (B) 0.89, (C) 2.42, and (D) 4.86 mol. eq. of cadmium. The species display a Normal distribution pattern centered around the molar equivalents of cadmium added. Data and image from N. C. Korkola, reproduced with permission from the Royal Society of Chemistry.²⁶

eq. point, where at pH 5, a strong preference for the clustered Cd₄MT species is observed, Figure 2-6. In the case of the pH 8 (Figure 2-7) metallation pathway, a Normal distribution is observed, indicating the statistical formation of beaded products.

To test if the presence of denaturant affected either the cluster pathway (pH 5) or the beaded pathway (pH 8), or both, the metallation rates were measured for apo-MT binding to 2.5 mol. eq. Cd(OAc)₂ under 0 M (no denaturant) and 4 M GdmCl conditions. Figure 2-8 shows the results for four unique conditions: **A**) pH 5 and no denaturant, **B**) pH 5 with 4 M GdmCl, **C**) pH 8 with no denaturant, and **D**) pH 8 with 4 M GdmCl. The rate constants k_{obs} for A-D are: 354, 325, 3633, and 2150 ($10^6 \text{ M}^{-1} \text{ s}^{-1}$) respectively, which are shown comparatively in Figure 2-9.

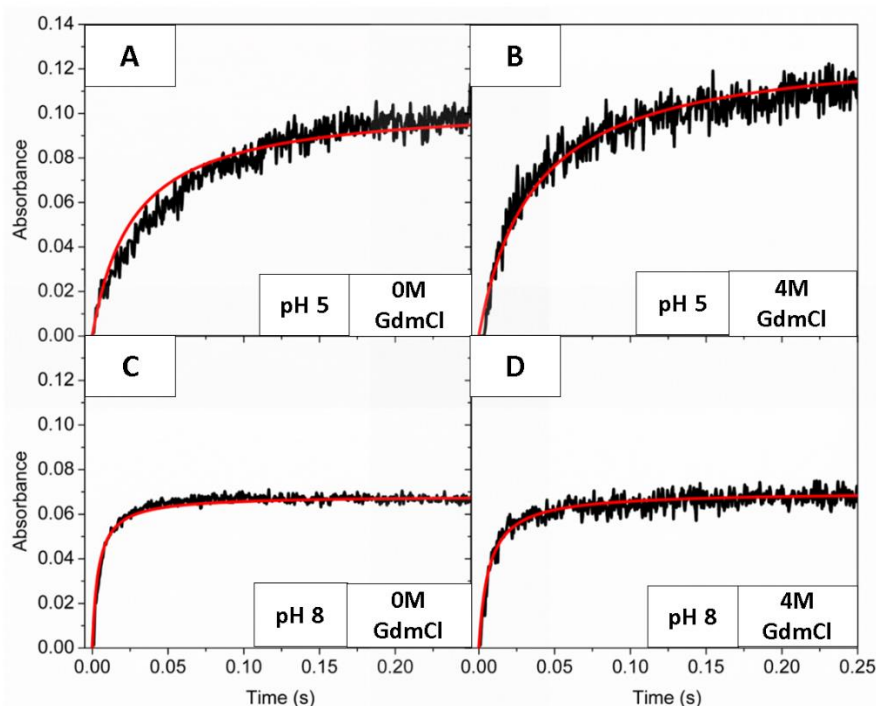


Figure 2-8 Kinetic absorption traces of MT metallation

Kinetic traces of the metallation of 2.5 mol. eq. of cadmium to apo-MT under conditions of (A) pH 5 and no denaturant, (B) pH 5 and 4 M of GdmCl, (C) pH 8 and no denaturant, and (D) pH 8 and 4 M of GdmCl. The traces show that the beaded pathway at pH 8 proceeds much faster than the clustered pathway at pH 5 and that denaturant slows down both pathways Data and image from N. C. Korkola, reproduced with permission from the Royal Society of Chemistry.²⁶

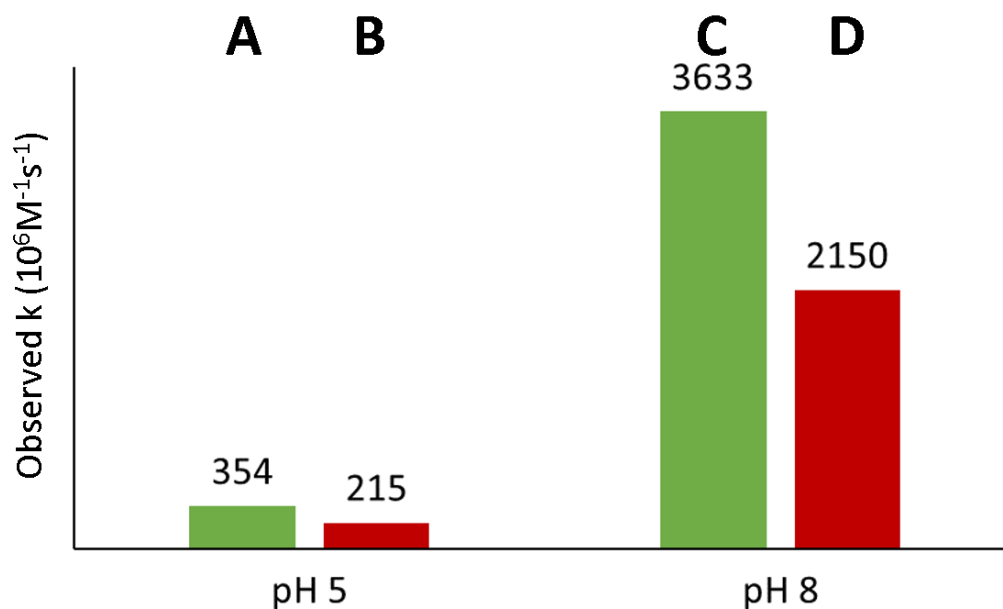


Figure 2-9 Comparison of rate constants

Bar graph representation showing the observed rate constants of the metallation with 2.5 mol. equivalents of cadmium (A) pH 5 and no denaturant, (B) pH 5 and 4 M of GdmCl, (C) pH 8 and no denaturant, and (D) pH 8 and 4 M of GdmCl. The effect of the denaturant is much less pronounced than that of the pH environment. Data and image from N. C. Korkola, reproduced with permission from the Royal Society of Chemistry.²⁶

2.3.4 Relative k_{obs} Decreases with Increasing Metallation

Figure 2-10 shows the relative k_{obs} values of the reaction of a fixed concentration of apo-MT with increasing Cd(II) mol. eq. at pH 5 (Figure 2-10A) and pH 8 (Figure 2-10B). In both cases, in the absence of denaturant (black dashed line), the relative k_{obs} rate decreases as a function of the increase in the number of Cd(II) bound. In the presence of denaturant (4 M GdmCl, red dotted line), the overall rates at both pHs are reduced. At pH 5, there is an approximately 50% reduction in the rate, but continues to follow a decreasing trend with metallation. At pH 8 on the other hand, the denaturant dramatically reduces the metallation rate.

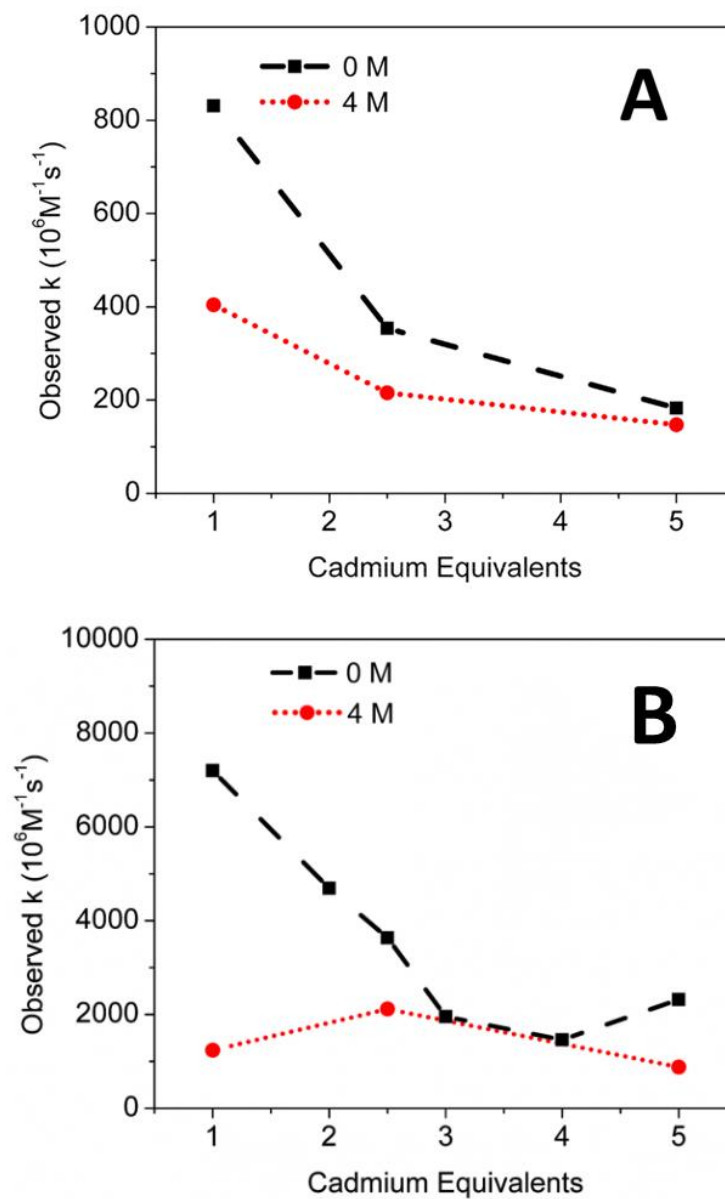


Figure 2-10 Cadmium equivalence vs. observed metallation rate k
 Plots showing the relationship between the observed rate constant and mol. equiv. of cadmium added at (A) pH 5 and (B) pH 8, both with denaturant (red dotted line) and without denaturant (black dashed line). The observed rate slows down as MT binds increasing numbers of cadmium ions. Data and image from N. C. Korkola, reproduced with permission from the Royal Society of Chemistry.²⁶

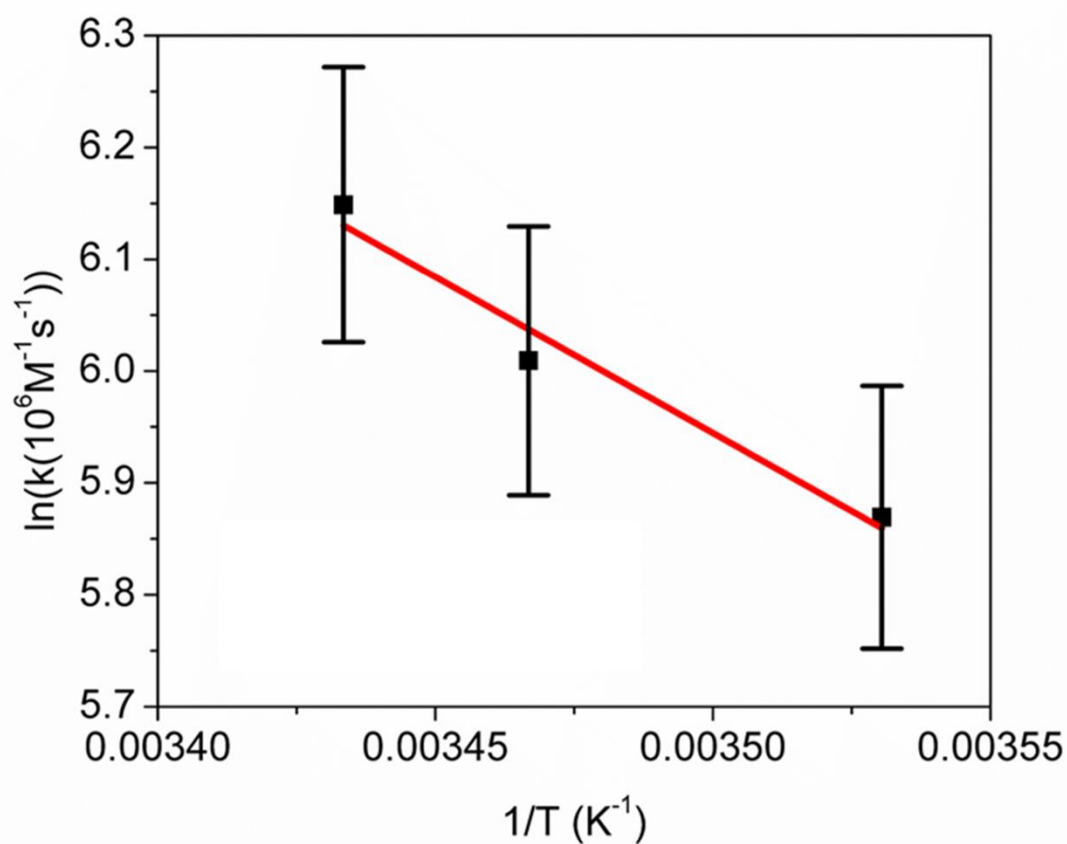


Figure 2-11 Arrhenius plot for Cd(II) metallation of MT

Arrhenius plot displaying the dependence of the observed rate constant on temperature.

The natural logarithm of the observed rate constant has a linear relationship to the inverse temperature: $y = -2791.4x + 15.71$, $R^2 = 0.9375$. Data and image from N. C.

Korkola, reproduced with permission from the Royal Society of Chemistry.²⁶

2.3.5 Metallation is Temperature Dependent

The relative k_{obs} for the metallation of apo-MT with 2.5 mol. eq. of Cd(OAc)₂ at pH 5 were determined at 10.1, 15.3, and 18.1 °C, with the resulting Arrhenius plot shown in Figure 2-11. The reaction rate slows as the temperature decreases, with a calculated activation energy E_A of 232 kJ/mol with an Arrhenius constant of 16. The rate of reaction at 25 °C and above was too fast for the instrumentation.

2.4 Discussion

2.4.1 Does Native Apo-MT have a Folded Structure?

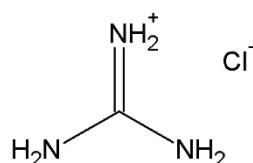
Defining the structure of apo-MT is difficult. It is clear that metallation results in metal-induced folding, such that the metal-saturated product (M(II)) exists with two, well-defined binding domains.³⁶ However, these domains do not exist in the absence of the metal, unlike most metalloproteins. Circular dichroism spectroscopy can typically be used to assess the degree or extent of 2° structure in a protein, from the characteristic CD spectral profiles between 190 and 230 nm. However, no such spectral properties exist in apo-MTs because of the absence of any defined folding. Mass spectrometry offers an alternative and to some extent, a more precise measure of the degree of denaturation associated with unfolding from the charge state manifold. Generally, when employing mass spectrometry to probe changes in the protein structure as a function of an external event, one examines the charge state envelope, its central number, and its spread to assess the change in protein-solvent accessibility. With metallothioneins, their limited size reduces the magnitude of changes in the charge state distribution, making this a less precise method of tracking protein structure, compared to, for example, myoglobin (~17000 Da). For greater sensitivity, cysteine alkylating agents, for example NEM or pBQ as described in Chapter 1, provide detailed evidence of solvent accessible cysteines as a function of increasing denaturant concentrations.^{6, 23} The use of GdmCl as a denaturant allows protein denaturation without affecting the pH of the solution.

The data in Figure 2-3 showed that the apo-MT structure is dramatically and significantly affected by the presence of denaturant. The two profiles have been described previously in terms of the structural origins that would result in cysteine modification profiles with such differences. The explanation that fits the experimental environment was described first by Irvine et al. in 2014 for the structures of apo- α -MT fragment.⁷ Considering the reaction as having simply run out of the NEM, the spectrum obtained is a snapshot of the reaction, frozen by the lack of sufficient modifier. NEM covalently alkylates with the free cysteinyl thiols in the MT protein to form a mass change readily discernible in the mass spectrum. Irvine et al. have demonstrated that the more unfolded or solvent accessible the protein is, the more Normal the distribution of the resulting modified species.^{24, 37} If the

protein were folded with only a certain set of cysteines being solvent accessible, this would be visualized in the ESI mass spectrum as a strong preference for a certain number of alkylations. For the experimental conditions required in the rest of this Chapter, the data show that 3 M GdmCl effectively unfolds apo-MT without altering the pH of the solution, allowing elucidation of pH dependent metallation pathways, as is described below.

2.4.2 Metallation Slows in the Presence of Denaturant

Both heat and acidity have been shown to be effective denaturants of MT.^{7, 8, 22, 23}



Scheme 2-1 Guanidinium chloride CH_6ClN_3

However, due to the pH dependence of MT's chelation properties, GdmCl (Scheme 2-1) was chosen so that the pH would not be affected by addition of denaturant. GdmCl is a chaotropic agent that denatures by disrupting hydrogen bonding.³⁸ The MT sequence contains few hydrophobic residues, suggesting that hydrogen bonds and electrostatic interactions are solely responsible for the overall stabilization of the protein in the metal free state.¹⁸ Previously reported molecular dynamics results showed that the hydrogen bond network in metal-saturated MT is largely retained upon complete demetallation, but increases upon stepwise, sequential, demetallation because the structure becomes more folded.^{15, 18}

Figure 2-4 shows that even with the cluster structure, that the unfolded peptide metallates more slowly. This result is coincident with previous results reported for just the apo α -MT metallated with excess Cd(II) in 2015 by Irvine et al.⁷ pH 5 was chosen specifically for the series of experiments described in Figure 2-4 as it ensures the dominance of the Cd₄S₁₁ cluster.

2.4.3 pH Changes the Dominant Metal Binding Pathway: Cluster Formation at pH 5 is Slower than Bead Formation at pH 8

Irvine et al. have demonstrated the pH dependence for Zn(II) and Cd(II) metallation, and that the pathway adopted at different pHs can be confirmed by observing the metallated species in the ESI-mass spectrum.¹⁶ Acidic conditions promote the cluster pathway for both metals, as shown in the low pH MS data for Cd(II), Figure 2-6. At physiological pH, both Cd(II) and Zn(II) bind in a beaded fashion up to 5 M(II) ions bound, as shown in the MS data for Cd(II) metallation, Figure 2-7. Figure 2-7 clearly shows the expected stepwise progression of the speciation as a function of Cd(II) mol. eq. There is no preference at this pH for the Cd₄S₁₁ clusters. The rate of metallation was obtained as function of pH. However, Cd(II) switches to the cluster pathway at a much higher pH compared to Zn(II). Zn(II) generally follows the tetrahedral terminal bead pathway over this pH range, with the cluster pathway only playing a role at a pH <5.1.¹⁶ In the case of Cd(II), cluster pathways can begin to dominate at a pH <7, which indicates the major influence a small change in pH can have on metal binding structures. This is pertinent to the discussion of metal anticancer therapeutics in the acidic condition of the tumor cell, which would promote MT to form stable metal-thiolate clusters, impeding drug delivery and efficacy.³⁹

In Figure 2-5, the pH range 5-8 encompasses a change in metallation product for the 2.5 mol. eq. of Cd(II) of clusters at pH 5 and beads at pH 8. Because the trend in rate constant follows almost exactly the trend in % terminal binding as a function of pH reported by Irvine et al.,¹⁶ cluster formation (pH 5) is dramatically slower than bead formation (pH 8). The mass spectral data shown in Figure 2-6 and Figure 2-7, indicate that for the solutions used in the stopped-flow in Figure 2-8A and B, the metallation products are dominated by Cd₄S₁₁ cluster formation in the α domain. For Figure 2-8C and D The increase from pH 5 to pH 8 increased the observed metallation rate tenfold in both cases, with the pH 8, native apo-MT, beaded metallation pathway, remaining the most rapid of the four conditions, Figure 2-9. It should be noted that in Figure 2-8, the plateaus of the kinetic traces do not all end at the same y-value. This is due to instrument variability, caused by measuring at 250 nm which is close to the detection limit. Normalizing the curves to end

at the appropriate y-values according to Beer's Law results in the same trends presented here.

2.4.4 Why is Terminal Cysteine Coordination Faster than Cluster Formation?

The formation of terminally bound metal beads is shown to be fast in Figure 2-5. This could be because although there is no defined structure for the cysteines: (i) the ESI mass spectral modification data, Figure 2-3, (ii) the modification data provided by Irvine et al.,^{6,23} and (iii) the previous molecular dynamics results, together support a structure for the apo-MT that involves non-specific folding optimized for metallation. Beaded metallation requires the concerted binding of 4 cysteine thiols at a time to M(II). The folded apo-MT structure orients the cysteines in close proximity such that the beads are formed rapidly. The cysteines that are most solvent exposed and have the most reduced energy upon metallation may well be metallated first.^{12, 18, 19, 40, 41}

In the case of cluster formation, this is a highly organized process with very specific cysteines involved in bridging arrangements resulting in the most energy minimized structure. The kinetic data show that this large-scale organization occurs at a slower rate than that of the beaded pathway, presumably due to the requirement of such precise cysteine coordination.

2.4.5 Rate as a Function of Metal Loading

k_{obs} decreases with sequential metallation, with the initial metals having the highest values. The last binding sites to be occupied are the slowest, as a reflection of a decrease in available sites. This is reflected widely across all metal species, as previously shown with time-dependent ESI-mass spectral data with Cd(II),¹⁶ As(III),⁴² and Cu(I).⁴³ A sequential increase in K_f is generally associated with the formation of a stable cluster, if $M > 1$, as has been shown in the titration of Cu(I)₁₋₂₀MT,⁴³ As₁₋₆MT,^{11, 12, 36} and notably with Cd₄S₁₁ and Co₄S₁₁ clusters in the α domain.

2.4.6 Temperature Dependence of Metallation

Petering et al.⁴¹ and Stillman et al.³⁰ have reported the temperature dependence of the metal lability in metallothioneins. The interprotein exchange of Zn(II) between carbonic anhydrase is much more rapid at 37 ° C than at 25 °C.⁴¹ The intraprotein exchange of Cd(II) and Zn(II) between domains can be followed readily with circular dichroism spectroscopy at temperature extremes.³⁰ The initial metallation reactions studied in this paper are also temperature dependent, as shown in Figure 2-11. There is an upper limit, as shown by Irvine et al, who used heat assisted denaturation at 94°C to demonstrate temperature dependent denaturation.²²

2.4.7 Metallation of Unfolded Apo-MT is Slower than Native Folded MT

The results of Figure 2-4, Figure 2-5, Figure 2-8, and Figure 2-9 show that the disruption of the apo-MT structure affects the rate of both the bead and cluster formation. pH influences the dominant pathway, but each pathway does have an optimal structure required for efficient metallation. Other structure impeding agents present in the cellular environment may cause similar disruption to the metallation process. Being particularly sensitive to sulphur oxidation, oxidized MT manifests in the formation of disulphide bridges, which will greatly disrupt the delicate and highly specific metal-thiolate organization of the native MT.

Does the apparent lack of formal structure for the native apo-MT have an impact on metallation rates? The use of a well-studied denaturant together with well understood structural metal-thiolate products (beads up to 5 Cd(II) at neutral pH and up, cluster formation below pH 6) meant that the single variable being tested was the extent of folding of the apo-MT. The data in Figure 2-8 and Figure 2-9 clearly answer this question. The metallation rate for Cd(II) is always faster in the absence of a denaturant. At physiological pH (choosing pH 8 to eliminate cluster formation) the folded apo-MT (absent denaturant), metallated over 50% faster than the unfolded (with denaturant). This same trend is the case at pH 5.

On a similar vein, these results demonstrate the effect of misfolding on the efficient function of a native protein. A common source of protein damage occurs as a result of oxidation. MT plays a role in both the protection and repair of oxidative damage.⁴⁴⁻⁴⁶ Oxidation and protein misfolding are thought to be one of the causes of cellular ageing, with a build-up of misfolded proteins and metal ions aggregating in the lysosome.⁴⁷ There is increasing evidence that MT plays a protective role in metal aggregation limitation, such as in the reduction of amyloid plaques in neurodegenerative diseases.⁴⁸⁻⁵⁰ With its multitude of reduced cysteine residues, MT can repair oxidative damage through the formation of disulphide bonds. This oxidation would greatly reduce MTs metal binding efficacy and place the cell at risk for dysfunctional regulation. A build-up of these misfolded products could result in differentiating cell conditions, such as decrease in pH, thus altering the activity of MT metallation to promote stable cluster formation.

MTs are well known for their stable metal-thiolate clusters, that protect the MT from oxidation and protease digestion.^{51, 52} From an evolutionary standpoint, MTs adaptive role in metallation and oxidative protection makes it a key player against ageing. Its ubiquity across all phyla cements this idea. Species specific amino acids may also impart fine-tuned structural influences to optimize efficiency in particular organisms, for which the reader is courteously directed to selected references comparing plant and mammalian MTs.⁵³⁻⁵⁵

2.5 Conclusions

The metallation of MT is a post-translational modification that is dependent on the cellular environment, particularly pH and metal loading status. In lower pH environments, such as hypoxic or tumorous cells, clustering pathways would predominate, especially in the presence of toxic Cd(II). This is relevant towards developed metallodrug resistance that some cancer types exhibit: MT of these cancerous cells is capable under these conditions of binding soft metals in a stable metal-thiolate cluster, minimizing cellular damage. At physiological pH, the evidence from the experiments reported in this Chapter, suggest that apo-MT adopts a compact folded structure, with cysteines oriented for facile metallation, indicated by the higher metallation rate. Folded apo-MT forms these very specific structures during the stepwise metallation process. Further studies are needed to

investigate how these structures change when the protein has been damaged as a result of misfolding or binding to a foreign or xenobiotic metal.

2.6 References

1. D. E. Sutherland and M. J. Stillman, The “magic numbers” of metallothionein, *Metallomics*, 2011, **3**, 444-463.
2. M. Margoshes and B. L. Vallee, A cadmium protein from equine kidney cortex, *J. Am. Chem. Soc.*, 1957, **79**, 4813-4814.
3. A. Pattanaik, C. F. Shaw III, D. H. Petering, J. Garvey and A. J. Kraker, Basal metallothionein in tumors: widespread presence of apoprotein, *J. Inorg. Biochem.*, 1994, **54**, 91-105.
4. D. H. Petering, J. Zhu, S. Krezoski, J. Meeusen, C. Kiekenbush, S. Krull, T. Specher and M. Dughish, Apo-metallothionein emerging as a major player in the cellular activities of metallothionein, *Exp. Biol. Med.*, 2006, **231**, 1528-1534.
5. Y. Yang, W. Maret and B. L. Vallee, Differential fluorescence labeling of cysteinyl clusters uncovers high tissue levels of thionein, *Proc. Natl. Acad. Sci. U.S.A.*, 2001, **98**, 5556-5559.
6. G. W. Irvine and M. J. Stillman, Residue Modification and Mass Spectrometry for the Investigation of Structural and Metalation Properties of Metallothionein and Cysteine-Rich Proteins, *Int. J. Mol. Sci.*, 2017, **18**, 913.
7. G. W. Irvine, K. E. Duncan, M. Gullons and M. J. Stillman, Metalation kinetics of the human α -metallothionein 1a fragment is dependent on the fluxional structure of the apo-protein, *Chem. Eur. J.*, 2015, **21**, 1269-1279.
8. G. W. Irvine, Doctorate, The University of Western Ontario, 2017.
9. K. B. Nielson and D. Winge, Order of metal binding in metallothionein, *J. Biol. Chem.*, 1983, **258**, 13063-13069.
10. K. B. Nielson, C. Atkin and D. Winge, Distinct metal-binding configurations in metallothionein, *J. Biol. Chem.*, 1985, **260**, 5342-5350.
11. J. Byrd and D. R. Winge, Cooperative cluster formation in metallothionein, *Arch. Biochem. Biophys.*, 1986, **250**, 233-237.
12. J. Ejniak, J. Robinson, J. Zhu, H. Försterling, C. F. Shaw III and D. H. Petering, Folding pathway of apo-metallothionein induced by Zn^{2+} , Cd^{2+} and Co^{2+} , *J. Inorg. Biochem.*, 2002, **88**, 144-152.

13. S.-H. Chen, L. Chen and D. H. Russell, Metal-induced conformational changes of human metallothionein-2A: A combined theoretical and experimental study of metal-free and partially metalated intermediates, *J. Am. Chem. Soc.*, 2014, **136**, 9499-9508.
14. S.-H. Chen, W. K. Russell and D. H. Russell, Combining chemical labeling, bottom-up and top-down ion-mobility mass spectrometry to identify metal-binding sites of partially metalated metallothionein, *Anal. Chem.*, 2013, **85**, 3229-3237.
15. K. E. R. Duncan and M. J. Stillman, Metal-dependent protein folding: metallation of metallothionein, *J. Inorg. Biochem.*, 2006, **100**, 2101-2107.
16. G. W. Irvine, T. B. Pinter and M. J. Stillman, Defining the metal binding pathways of human metallothionein 1a: balancing zinc availability and cadmium seclusion, *Metallomics*, 2016, **8**, 71-81.
17. S.-H. Hong, Q. Hao and W. Maret, Domain-specific fluorescence resonance energy transfer (FRET) sensors of metallothionein/thionein, *Protein Eng. Des. Sel.*, 2005, **18**, 255-263.
18. K. E. Rigby, J. Chan, J. Mackie and M. J. Stillman, Molecular dynamics study on the folding and metallation of the individual domains of metallothionein, *Proteins: Struct., Funct., Bioinf.*, 2006, **62**, 159-172.
19. K. E. R. Duncan and M. J. Stillman, Kinetic and molecular dynamics studies on the metal-dependent folding of metallothionein (MT), *FASEB J.*, 2006, **20**, A501-A501.
20. S. Dong, N. D. Wagner and D. H. Russell, Collision-Induced Unfolding of Partially Metalated Metallothionein-2A: Tracking Unfolding Reactions of Gas Phase Ions, *Anal. Chem.*, 2018, **90**, 11856-11862.
21. S.-H. Chen and D. H. Russell, How closely related are conformations of protein ions sampled by IM-MS to native solution structures?, *J. Am. Soc. Mass Spectrom.*, 2015, **26**, 1433-1443.
22. G. W. Irvine, N. Korkola and M. J. Stillman, Isolated domains of recombinant human apo-metallothionein 1A are folded at neutral pH: a denaturant and heat-induced unfolding study using ESI-MS, *Biosci. Rep.*, 2018, BSR20180592.
23. G. W. Irvine, M. Santolini and M. J. Stillman, Selective cysteine modification of metal-free human metallothionein 1a and its isolated domain fragments: Solution structural properties revealed via ESI-MS, *Protein Sci.*, 2017, **26**, 960-971.
24. G. W. Irvine, K. L. Summers and M. J. Stillman, Cysteine accessibility during As³⁺ metalation of the α - and β -domains of recombinant human MT1a, *Biochem. Biophys. Res. Commun.*, 2013, **433**, 477-483.

25. G. W. Irvine and M. J. Stillman, Chromatographic separation of similar post-translationally modified metallothioneins reveals the changing conformations of apo-MT upon cysteine alkylation by high resolution LC-ESI-MS, *BBA - Proteins Proteom.*, 2018, **1866**, 589-601.
26. D. L. Wong, N. C. Korkola and M. J. Stillman, Kinetics of competitive Cd²⁺ binding pathways: the realistic structure of intrinsically disordered, partially metallated metallothioneins, *Metallomics*, 2019.
27. D. E. Sutherland and M. J. Stillman, Challenging conventional wisdom: single domain metallothioneins, *Metallomics*, 2014, **6**, 702-728.
28. T. B. Pinter and M. J. Stillman, The zinc balance: Competitive zinc metalation of carbonic anhydrase and metallothionein 1A, *Biochemistry*, 2014, **53**, 6276-6285.
29. M. Good, R. Hollenstein, P. J. Sadler and M. Vasak, Cadmium-113 NMR studies on metal-thiolate cluster formation in rabbit cadmium (II) metallothionein: Evidence for a pH dependence, *Biochemistry*, 1988, **27**, 7163-7166.
30. M. Stillman, W. Cai and A. Zelazowski, Cadmium binding to metallothioneins. Domain specificity in reactions of alpha and beta fragments, apometallothionein, and zinc metallothionein with Cd²⁺, *J. Biol. Chem.*, 1987, **262**, 4538-4548.
31. J. Ejnik, C. F. Shaw III and D. H. Petering, Mechanism of cadmium ion substitution in mammalian zinc metallothionein and metallothionein α domain: Kinetic and structural studies, *Inorg. Chem.*, 2010, **49**, 6525-6534.
32. T. B. Pinter and M. J. Stillman, Putting the pieces into place: Properties of intact zinc metallothionein 1A determined from interaction of its isolated domains with carbonic anhydrase, *Biochem. J.*, 2015, **471**, 347-356.
33. T. B. Pinter, G. W. Irvine and M. J. Stillman, Domain selection in metallothionein 1a: Affinity-controlled mechanisms of zinc binding and cadmium exchange, *Biochemistry*, 2015, **54**, 5006-5016.
34. P. Mendes, GEPASI: a software package for modelling the dynamics, steady states and control of biochemical and other systems, *Bioinformatics*, 1993, **9**, 563-571.
35. FQS Poland, Scigress Molecular Modeling Software, 6.0.0, 2016. Retrieved from http://www.fqs.pl/chemistry_materials_life_science/products/scigress.
36. D. Winge and K.-A. Miklossy, Domain nature of metallothionein, *J. Biol. Chem.*, 1982, **257**, 3471-3476.
37. G. W. Irvine and M. J. Stillman, Topographical analysis of As-induced folding of α -MT1a, *Biochem. Biophys. Res. Commun.*, 2013, **441**, 208-213.

38. B. Ibarra-Molero, V. V. Loladze, G. I. Makhatadze and J. M. Sanchez-Ruiz, Thermal versus guanidine-induced unfolding of ubiquitin. An analysis in terms of the contributions from charge– charge interactions to protein stability, *Biochemistry*, 1999, **38**, 8138-8149.
39. D. L. Wong and M. J. Stillman, Capturing platinum in cisplatin: kinetic reactions with recombinant human apo-metallothionein 1a, *Metallomics*, 2018, **10**, 713-721.
40. K. E. R. Duncan, T. T. Ngu, J. Chan, M. T. Salgado, M. E. Merrifield and M. J. Stillman, Peptide folding, metal-binding mechanisms, and binding site structures in metallothioneins, *Exp. Biol. Med.*, 2006, **231**, 1488-1499.
41. J. Ejniak, A. Muñoz, T. Gan, C. F. Shaw III and D. Petering, Interprotein metal ion exchange between cadmium-carbonic anhydrase and apo-or zinc-metallothionein, *J. Biol. Inorg. Chem.*, 1999, **4**, 784-790.
42. T. T. Ngu, A. Easton and M. J. Stillman, Kinetic analysis of arsenic– metalation of human metallothionein: significance of the two-domain structure, *J. Am. Chem. Soc.*, 2008, **130**, 17016-17028.
43. J. S. Scheller, G. W. Irvine, D. L. Wong, A. Hartwig and M. J. Stillman, Stepwise copper (I) binding to metallothionein: a mixed cooperative and non-cooperative mechanism for all 20 copper ions, *Metallomics*, 2017, **9**, 447-462.
44. P. J. Thornalley and M. Vašák, Possible role for metallothionein in protection against radiation-induced oxidative stress. Kinetics and mechanism of its reaction with superoxide and hydroxyl radicals, *BBA - Protein Struct. M.*, 1985, **827**, 36-44.
45. B. Ruttkay-Nedecky, L. Nejdl, J. Gumulec, O. Zitka, M. Masarik, T. Eckschlager, M. Stiborova, V. Adam and R. Kizek, The role of metallothionein in oxidative stress, *Int. J. Mol. Sci.*, 2013, **14**, 6044-6066.
46. N. Chiaverini and M. De Ley, Protective effect of metallothionein on oxidative stress-induced DNA damage, *Free Radic. Res.*, 2010, **44**, 605-613.
47. S. Reeg and T. Grune, Protein oxidation in aging: does it play a role in aging progression?, *Antioxid. Redox. Sign.*, 2015, **23**, 239-255.
48. J. Durand, G. Meloni, C. Talmard, M. Vašák and P. Faller, Zinc release of Zn₇-metallothionein-3 induces fibrillar type amyloid- β aggregates, *Metallomics*, 2010, **2**, 741-744.
49. G. Meloni, V. Sonois, T. Delaine, L. Guilloureau, A. Gillet, J. Teissié, P. Faller and M. Vašák, Metal swap between Zn₇-metallothionein-3 and amyloid- β -Cu protects against amyloid- β toxicity, *Nat. Chem. Biol.*, 2008, **4**, 366.

50. E. Atrián-Blasco, A. Santoro, D. L. Pountney, G. Meloni, C. Hureau and P. Faller, Chemistry of mammalian metallothioneins and their interaction with amyloidogenic peptides and proteins, *Chem. Soc. Rev.*, 2017, **46**, 7683-7693.
51. D. R. Winge, in *Methods in enzymology*, Elsevier, 1991, vol. 205, pp. 438-447.
52. J. S. Calvo, V. M. Lopez and G. Meloni, Non-coordinative metal selectivity bias in human metallothioneins metal-thiolate clusters, *Metallomics*, 2018.
53. E. Freisinger, Structural features specific to plant metallothioneins, *J. Biol. Inorg. Chem.*, 2011, **16**, 1035-1045.
54. C. A. Blindauer, Advances in the molecular understanding of biological zinc transport, *Chem. Commun.*, 2015, **51**, 4544-4563.
55. M. Capdevila and S. Atrian, Metallothionein protein evolution: a miniassay, *J. Biol. Inorg. Chem.*, 2011, **16**, 977-989.

Chapter 3

3 Capturing Platinum in Cisplatin: Kinetic Reactions with Recombinant Human apo-Metallothionein 1a*

3.1 Introduction

The prolonged use of cis-diamminedichloroplatinum(II) (cisplatin), a powerful chemotherapeutic, can incur chemoresistance in cancers during treatment, reducing the chance of therapeutic success. Metallothioneins (MTs) are suspected of metaldrug interference via ligand removal and metal sequestration. The mechanistic details and reactions rates k_{obs} for the systematic deconstruction of cisplatin by apo-human MT are reported and analyzed from mass spectral data.

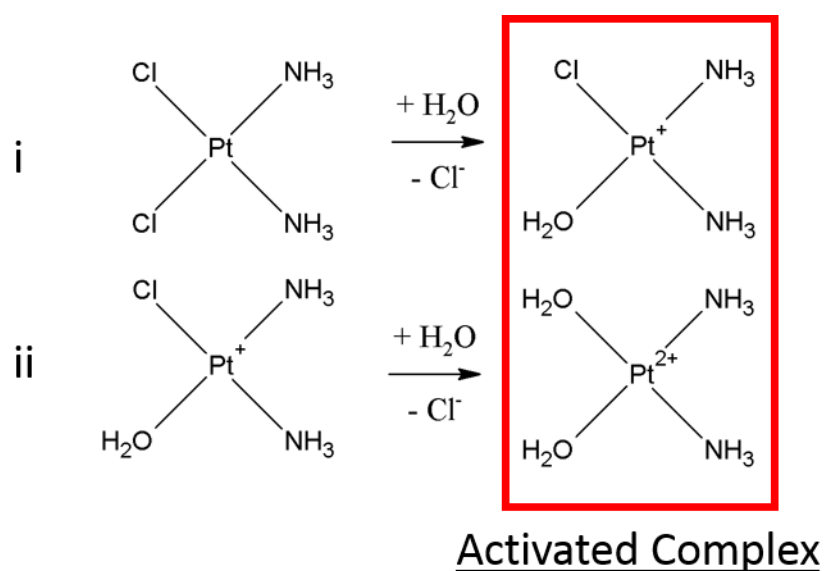
In order to understand pre-target resistance in metallo-chemotherapeutics it is necessary to investigate the mechanisms responsible for metal-protein binding reactions. Cisplatin, a popular and extremely effective anti-cancer drug, is the focus of worldwide interdisciplinary investigations into emerging chemoresistance and metabolic toxicology in cancers. This present paper focuses on monitoring the abrupt and disruptive reaction involving a major cellular thiol source, metallothionein, with cisplatin. MT is implicated as a metal sink that may be also involved in nephrotoxicity. Time-dependent, solution-phase, ESI-MS was used to monitor the destruction of the cisplatin molecule. Kinetic analysis provided the reaction rates for the individual steps from the initial binding of the complete molecule, through extrusion of the ligands, and final accumulation of isolated Pt(II) bound to metallothionein.

3.1.1 Cisplatin: A Standard Treatment for Cancer

Since its discovery by Rosenberg in 1978, cis-diamminedichloroplatinum(II) (more commonly known as cisplatin) has been used as a potent anti-cancer agent for the treatment of testicular, ovarian, head and neck, bladder, colorectal, and lung cancers.¹⁻⁴ As a metaldrug, cisplatin can act upon several biochemical pathways to trigger cell death. For instance, with its soft, transition metal core, cisplatin is capable of readily binding the free thiols of glutathione and metallothioneins, reducing the cell's facility to

**A version of this chapter has been published:
Metallomics, 10(5), 713-721 (2018). Copyright 2018 Royal Society of Chemistry
Reproduced with permission from: D. L. Wong, and M. J. Stillman.*

respond to oxidative stress.^{1, 2, 5-9} Binding to glutathione (GSH) can instigate efflux from the cell via MRP1 and MRP2, removing this thiol source from the cell.¹⁰⁻¹² Similarly, by binding to free thiols near the active site of enzymes, cisplatin can disrupt cell function.^{13, 14} However, its most well-known method of action is through the creation of DNA adducts triggering mitochondrial apoptosis and cell death.



Scheme 3-1 *Cisplatin and the aquation reaction involved in its initial entrance to the body. Reproduced from D. L. Wong and M. J. Stillman with permission from the Royal Society of Chemistry.*¹⁵

Upon administration in the body, cisplatin becomes an active form through aquation reactions where the chloride ligands are spontaneously exchanged with water, as described in Scheme 3-1, above.^{16, 17} This results in a complex that reacts readily with endogenous nucleophilic groups, like the free thiols mentioned above, or, in particular, the guanine N7 site on purines in DNA.^{2, 18} Multiple reactions can occur for each Pt(II) core of the cisplatin, resulting in inter- and intra- strand crosslinking of DNA, disrupting transcription and translation. It should be noted that in fact, very little (1%) of the intracellular cisplatin binds to nuclear DNA.¹⁹ Clearly, DNA damage is not the only cytotoxic pathway at play, as cisplatin also exerts toxic effects on enucleated cells.²⁰

3.1.2 Metallothionein and Drug Resistance

While initially effective in many cancer types, chemoresistance to cisplatin can develop with prolonged treatment.^{21, 22} Increased expression of cellular thiols GSH and MT have both been implicated in these resistance mechanisms but they are believed to be independently induced.²³ Kelley et al. remarked that there was a noticeable increase in cellular MT levels in several cancer lines treated with cisplatin and antineoplastic agents melphalan, and chlorambucil.²⁴ It has also been suggested that MT is an obstacle in the treatment of the ovarian cancer A2780CR cell lines that are cisplatin resistant. Work from Surowiak et al. suggests that nuclear MT expression levels increase with cisplatin treatment, which may be correlated with the diminished overall clinical response.²² The direct correlation between cellular MT and chemoresistance is not clear cut for all cancer types, as shown by Woo et al, nuclear and cellular MT levels vary greatly across cancer types, and this subcellular compartmentalization of MT plays a role in its metal response.²³ While the relationship between MT expression and developed cisplatin resistance is unclear, the correlation between the two has been suggested as a possible biomarker for resistance. As such, the connection between the two has been the focus of gene expression and metallomics studies.²⁵

As described extensively in Chapters 1 and 2, MTs are a family of ubiquitous, low molecular weight (6-8 kDa), cysteine-rich, metal binding proteins that most notably play a role in Zn(II) and Cu(I) homeostasis, heavy metal detoxification, and response to oxidative stress.^{7, 26-30} MTs are capable of creating a variety of metal-thiolate cluster structures using 20 cysteine thiolates.²⁹⁻³³ The involvement of MTs in cisplatin resistance is suggested to be due to their property of binding a wide array of soft, d-block, xenobiotic metals, such as Cd(II), Hg(II), As(III), and Pb(II), as well as those of therapeutic interest, like Bi(III), Au(I), Ag(I), and Pt(II), among others.^{27, 28, 34-37} MTs act to sequester toxic metals for excretion, which in the case of cisplatin, can lead to renal side effects associated with treatment.³⁸

MT binding with cisplatin has been studied intensely due to its association with developed cisplatin resistance. Reactions showing remetallation of Zn-MT and Cd-MT by Pt(II) demonstrate the strong affinity of the cysteine thiol for the Pt(II).^{6, 39-47} MT 1 and

MT 2 are capable of binding up to 7 Pt(II), mimicking the stoichiometry of the two-domain binding structure of native Zn₇-MT and Cd₇-MT.⁴⁸ The Stillman group has previously demonstrated low temperature (77 K) emissive properties of Pt-bound MT,³⁵ a property of metal-thiolate cluster formation.

Extensive kinetic analysis of the metallation of metallothionein by cisplatin has been performed by Hagrman et al. involving spectroscopic methods.⁶ Mimicking chemical conditions of the cell, their study involved monitoring *in vitro* the loss of cisplatin over the course of full metallation of metallothionein. As expected, the Pt-MT product has none of the ancillary ligands of the original cisplatin molecule. Hagrman et al. note that there is a delay in the observed signal, indicating that initial reactions may be occurring that are not detectable under the conditions used.⁶ A limitation of optical techniques is the averaging of all the signals, which masks the individual mechanistic details in these early stages of the reaction.

3.1.3 Biological Significance

Many of the *in vitro* methods described above utilize widely available rabbit liver or rat liver metallothioneins, which often come in mixtures of isoforms, metallated with Zn(II) or Cd(II), or as a mixed metal species. Using recombinant human metallothionein expressed in *Escherichia coli* provides isoform-pure recombinant human MT 1a. MT regulation is influenced by the presence of xenobiotic metals, like Bi(III), Au(I) and Pt(II), and as such, apo-MT will be synthesized by the cell in response to the presence of these metals.^{33, 36, 49} Indeed, several reports now confirm the presence of apo-MT *in vivo* in large quantities.⁵⁰⁻⁵³ This perspective indicates that the metallation of MTs is a post-translational modification. Therefore, the properties of the reaction between apo-MT1a and cisplatin are investigated using the high species resolution of ESI-MS. The time-dependence of this early reaction involving the deconstruction of the cisplatin complex can be monitored at this resolution. This provides insight on the interactions between MT and complex chemotherapeutic complexes, as opposed to the free ion metallation studies of MT performed previously. The benefit of applying ESI-MS is the availability of high-resolution snapshots of solution-phase intermediates throughout the course of the

reaction. With this, the initial reaction that Hagrman et al. and Pattanaik et al. suggest exist but have not yet characterized the speciation involved can be identified.^{6, 46}

The following Chapters involving the aggressive reaction of human MT with dirhodium(II) tetraacetate raised the question whether MTs might react similarly with the most important and effective metal-based anticancer drug, cisplatin. In the reaction with the dirhodium(II) tetraacetate, the MT bound the complete molecule and in a stepwise fashion competed for the possible binding sites with its numerous cysteinyl thiols until only the [Rh-Rh]⁴⁺ core remained encapsulated by the protein. The high resolution capabilities of ESI-mass spectral data displayed each of the stepwise species formed during the reaction, showing the systematic destruction of the dirhodium(II) tetraacetate.⁵⁴ A similar destructive effect was demonstrated by MT upon antimetastatic Ru(II)-arene complexes.⁵⁵

The experiments reported in this Chapter leverage the exquisite power of the ESI-MS technique to interrogate the products formed initially between MT and cisplatin. In this manner, the early mechanistic details will become clear, allowing the determination of the structural aspects of cisplatin that lead to MT deactivation. The goal of this work is to determine the identity of the initial Pt-based species that bind to the MT, and then to elucidate the subsequent reaction pathways of the Pt-based species while debilitatingly immobilized in the MT. Unlike previous reports, the mechanism explored in this work involves the metallation by each individual cisplatin molecule to form the Pt-MT product. To avoid the complexity of a distribution of metallated species in partially-metallated MTs,^{31, 56, 57} The apo-MT with its 20 uncoordinated cysteines was chosen as a model for the uncoordinated cysteines in partially metallated MT. The results may be used to guide design of metallodrug structures that are resistant to this MT-thiolate destructive chemistry.

3.2 Experimental Methods

Recombinant human metallothionein 1a were produced and purified according to previously described methods with the sequence

GSMGKAAAACSCATGGCTCTGSCKCKECKCNSCKKSCCSCCPMSCAKCAQGC

VCKGASEKSCCKKAAAA.^{56, 58, 59} This recombinant sequence has mutations (T27N and I51V) compared with the native human MT1a for purposes of overexpression in *E. coli*. The metallation properties of this recombinant isoform (MT1a) has been shown in spectroscopic studies from the Stillman Group to behave similarly to mammalian MTs, for example, rabbit liver MT2A.^{60, 61} The purified Cd-bound MT1a was demetallated by acidification (pH<2) and the resulting free Cd(II) in solution were removed by centrifugal filtration (Amicon Ultra-4 3000 Da MWCO). Protein concentration was calculated by remetallating a measured aliquot with CdSO₄ and determining the A_{max} at the 250 nm shoulder characteristic of the LMCT of Cd-S bonds ($\epsilon = 89,000 \text{ L mol}^{-1} \text{ cm}^{-1}$).

Solutions of cisplatin (Sigma) were prepared in DI water well ahead of time to allow for aquation. Aliquots containing cisplatin equivalent to ~ 3 mol. eq. of the apo-MT were added to the apo-MT solution (20 mM ammonium formate buffer, Fluka, pH 7.0) immediately prior to mass spectral data acquisition using a MicroTOF II (Bruker Daltonics, Toronto). All solutions were at room temperature and thoroughly deaerated using vacuum evacuation followed by Ar saturation. NaI was used as the calibrant. Spectra were collected in positive ion mode, as a function of time following mixing. The settings used are described in Chapter 1.

The averaged spectra and data analysis were carried out using the Bruker Data Analysis 4.2 program. The resulting spectral data were normalized, and the dominant species identified by mass. The identified species and their abundance data were grouped and input into GEPASI,^{62, 63} a biochemical kinetics simulator, as the reactions defined in Scheme 2 in the Results and Discussion section. The four reaction rate constants, k_{1-4} , were defined as irreversible mass action, and the k 's and concentrations were limited by user-defined parameters.

3.3 Results and Discussion

The time-dependent deconvoluted mass spectral data recorded during the reaction of cisplatin with apo-metallothionein 1a experimental data are shown in Figure 3-1, and in block form Figure 3-2. In the Apo panel of Figure 3-2, the black bar represents the Apo-MT abundance at the beginning of the reaction. By one minute (A) each of the species

found at the end of the reaction can be discerned. The speciation is grouped in terms of MT involved in Pt_1 complexes (red, “ Pt_1 Group”), Pt_2 complexes (blue, “ Pt_2 Group”), Pt_3 complex (green), and Pt_4 complex (pink). The mass spectral data are rich in detail about the many species involved in the initial binding of cisplatin to the MT. There are two ways of describing the data shown in Figure 3-2: (i) Either by the time-dependence of the individual groups, based on the number of Pt(II) bound to the protein ($x = 1-4$), (ii) or based on the appearance of species at each time point (A – F). The kinetic analysis, to be described below, is based on the 4 groups, but not the individual speciation within the groups. At this point, the focus is directed to describing the change in speciation for each individual platinum bound (Figure 3-1 A-F).

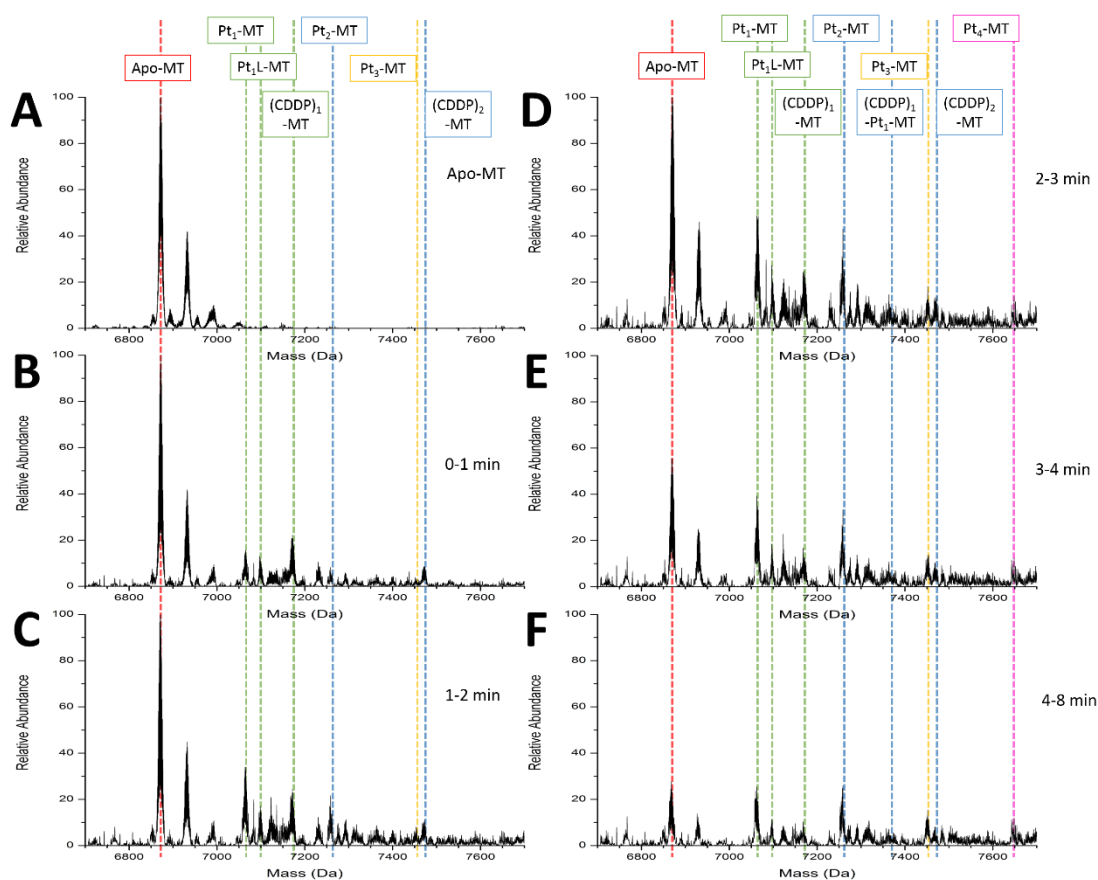


Figure 3-1 ESI mass spectra following the reaction of cisplatin with apo-MT1a.

The apo-MT peak is highlighted by the red dashed line. Platinated species are coloured according to the number of Pt(II) atoms contained, with its associated partially ligated (Pt_xL -MT) or fully ligated $((CDDP)_x$ -MT) species sharing the same colour. MT bound to Pt_1 represented with green dashed lines. MT bound to Pt_2 represented with blue dashed

lines. MT bound to Pt₃ represented with yellow dashed lines. MT bound to Pt₄ represented with pink dashed lines. Reproduced from D. L. Wong and M. J. Stillman with permission from the Royal Society of Chemistry.¹⁵

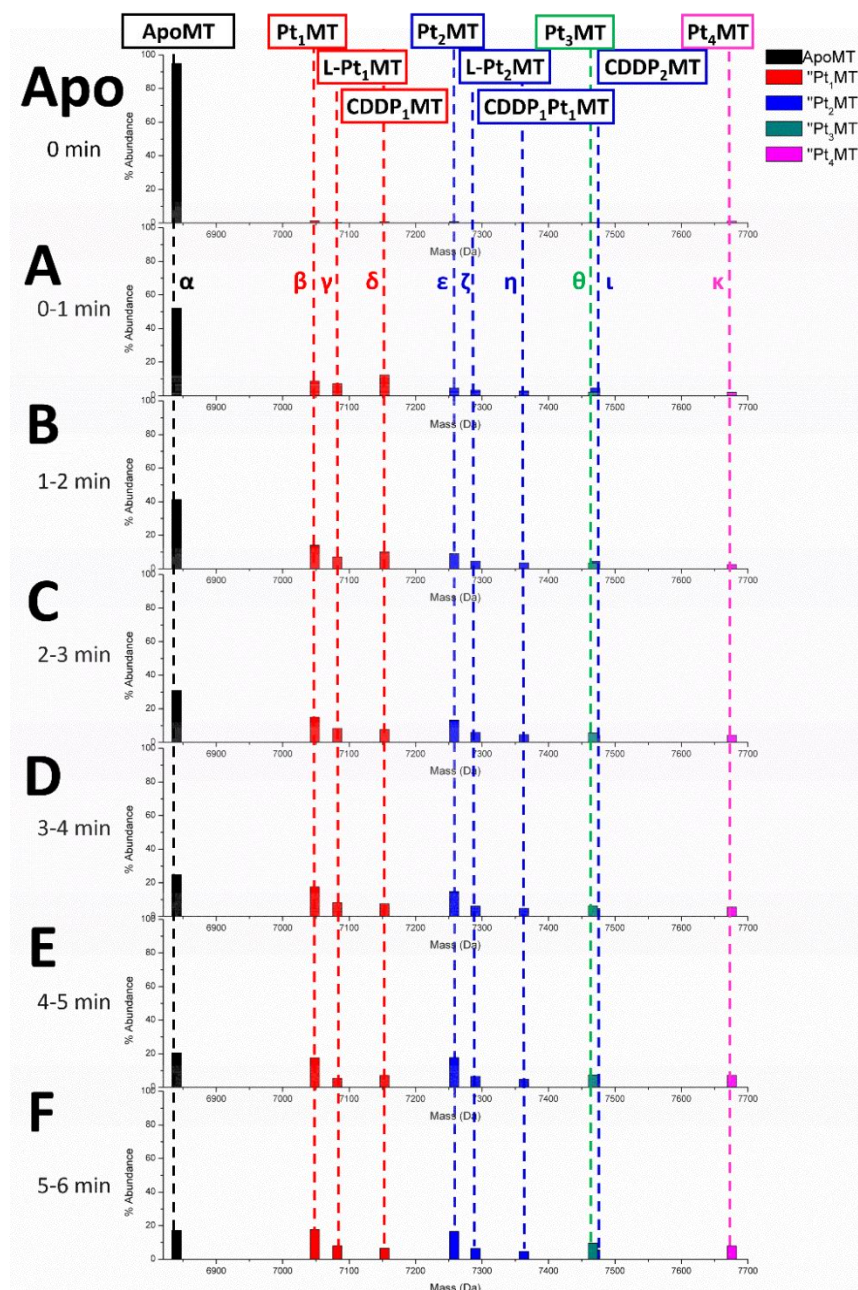


Figure 3-2 ESI mass spectra following the reaction of cisplatin with apo-MT1a in bar graph representation.

The apo-MT peak is highlighted by the black bar. Platinated species are coloured according to the number of Pt(II) atoms contained, with its associated partially ligated (L-Pt-MT) or fully ligated (CDDP-MT) species sharing the same colour. MT bound to Pt₁

represented with red. MT bound to Pt₂ represented with blue. MT bound to Pt₃ represented with green. MT bound to Pt₄ represented with pink. Reproduced from D. L. Wong and M. J. Stillman with permission from the Royal Society of Chemistry.¹⁵

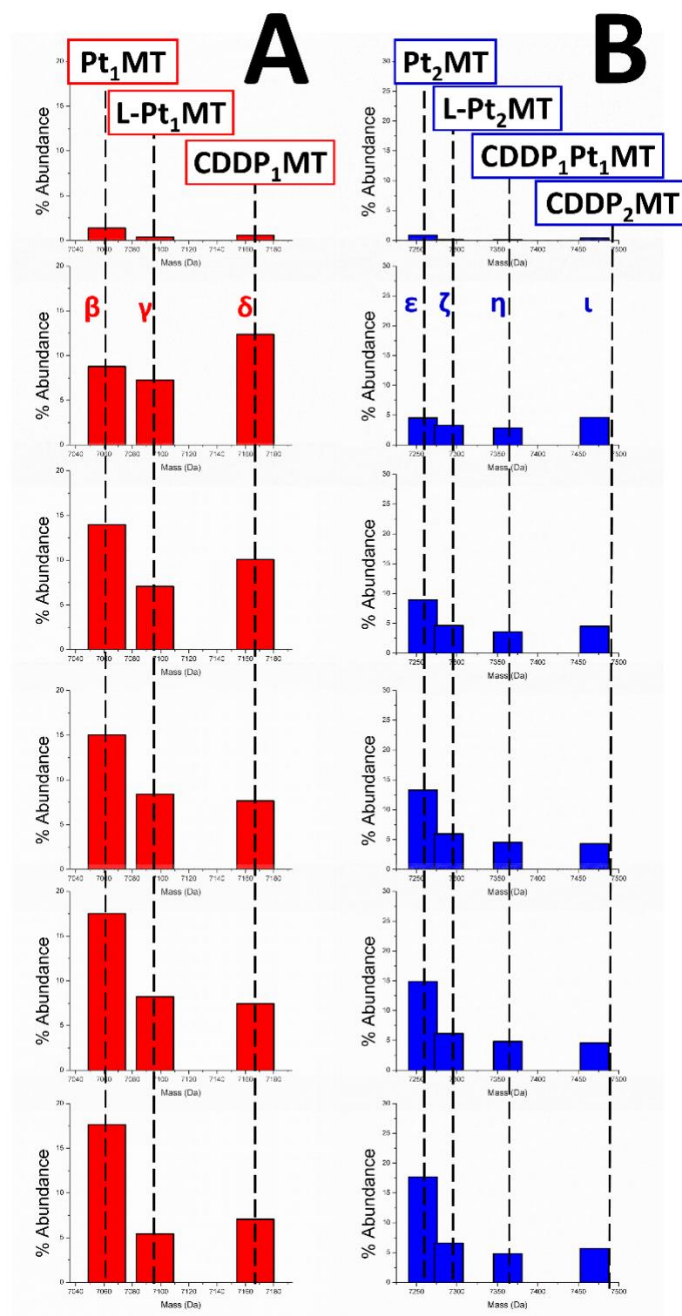


Figure 3-3 Detailed ESI mass spectral data of CDDP₁MT and CDDP₂MT
Detailed comparison of mass spectral data for the “Pt₁ Group” (Red, left) and “Pt₂ Group” (Blue, Right). The selected panels are from the frames shown in Figure 3-1A-F.

*The overall cisplatin molecule deconstruction is observed from the overall decrease of the “CDDP” species and the overall increase of the “Pt” species. Reproduced from D. L. Wong and M. J. Stillman with permission from the Royal Society of Chemistry.*¹⁵

In Figure 3-2A, within the red Pt₁ group, the whole CDDP is bound to the MT, and over time to F, it loses its ligands, forming Pt₁, which is seen in greater detail in Figure 3-3A. The intermediate in this pathway reaction can be seen as the peak labelled LPt₁-MT, where the ligand (L) can be either (2 NH₃) or Cl¹⁻, but this cannot be distinguished because of the overlap in the masses of these species. However, due to the nature of the ESI-MS experiment, L is most likely to be NH₃ from the ammonium formate buffer, and due to the favourable loss of the Cl¹⁻ as shown in Scheme 3-1. Returning to Figure 3-2A, the Pt₂ species (blue) can be formed from both CDDP₁Pt₁-MT and CDDP₂ species. However, by F, the Pt₂MT dominates, again illustrated more clearly in Figure 3-3. Returning once more to Figure 3-2A, under the concentration conditions at this stage of the initial reaction, only the Pt₃MT and Pt₄MT species are observed, but these species grow in abundance as the reaction proceeds, to F. To summarize the time-dependence of the data, there is clear evidence that two complete CDDP molecules bind to MT, and that these two molecules degrade to the sequestered metal core. In F, the dominant species are Pt₁MT, Pt₂MT, Pt₃MT, and Pt₄MT. The Pt_x-MT species without any ligands are the final products of each metallation event. The coexistence of Pt₁₋₄MT is not an unusual observation for mechanisms that are not cooperatively driven.^{31, 57, 58, 64, 65}

Each of the individual species can be seen at the 3-4 minute point, Figure 3-2D. i) β, Pt₁MT, appearing as expected at 7062.7 Da, α, Apo-MT at 6868.8 Da. This mass difference corresponds to the mass of cisplatin molecule. ii) γ, L-Pt₁MT at 7096.8 Da, iii) δ, CDDP₁-MT 7167.8 Da, iv) ε, Pt₂MT at 7258.7 Da, v) ζ, L-Pt(Pt)MT 7290.8 vi) η, CDDP₁Pt₁MT at 7363.7, vii) θ, Pt₃MT 7453.7, viii) ι, CDDP₂MT at 7470.7, and ix) κ, Pt₄MT 7648.5 Da. MT species of Pt > 4 could not be distinguished from noise. The M₄S₁₁ stoichiometry is a well-known structure involving metal-thiolate cluster formation that occurs in other divalent metals.^{27, 57, 66-68}

Figure 3-3 show the time-dependent change in the Pt₁ group (A, red) and Pt₂ group (B, blue) taken from panels A-F in Figure 3-2. In Figure 3-3A, the initially bound CDDP

degrades to L-Pt₁MT and then to Pt₁MT. In the Pt₂ group there are two reactants that can form the Pt₂MT species: CDDP₁Pt₁MT and CDDP₂MT. Both of these are seen at 7363.7 and 7470.7 Da, respectively. The time-dependence data again show that the encapsulated core, Pt₂MT, is the product.

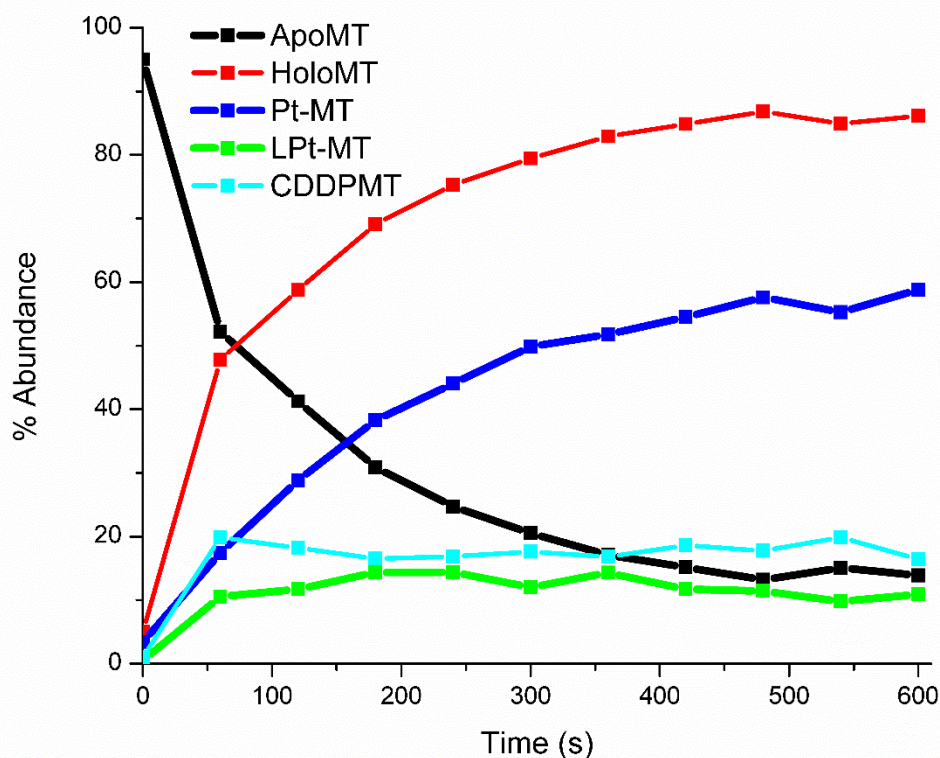


Figure 3-4 Experimental speciation abundance over time

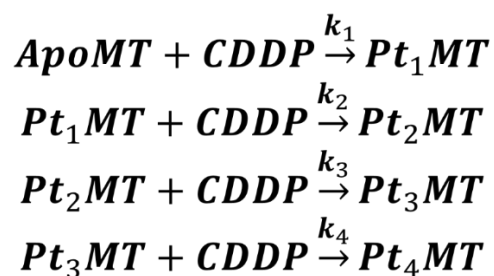
Abundance speciation data over time taken from the experimental mass spectral data.

Apo-MT species are represented with black. The holoMT species (red) represents the sum of Pt_xMT species (blue), ligated Pt species LPt_xMT (green), and MT species with a whole cisplatin molecule bound, CDDP_xMT (cyan). Reproduced from D. L. Wong and M. J.

Stillman with permission from the Royal Society of Chemistry.¹⁵

The time-dependence of the mass-spectral data is used to quantify the reaction mechanism shown in Equation 3-1. The resolving power of ESI-mass spectrometer allows monitoring this reaction in higher detail than has been possible previously. In particular, the time-resolved spectra shows the emergence and subsequent loss of the intermediate

species, as well as the composition of the intermediates that reach a steady state. However, the 9 species present make the kinetic analysis extremely challenging. In Figure 3-4, the metal-free species, Apo-MT (Black), decreases over the course of the reaction, as it begins to sequester the cisplatin in solution. All the resulting metallated species are summed and reported in Figure 3-4 as Holo-MT (Red). Holo-MT represents the sum of all the many sub-species that form as cisplatin is deconstructed while bound within the MT. The specific components are i) the majority final products Pt_x -MT where $x=1-4$, contains the sequestered and deactivated platinum core that is no longer a functional chemotherapeutic (Figure 3-4: Blue); and ii) the ligated species, LPt_x MT (Figure 3-4: Green) and $CDDP_x$ MT (Figure 3-4: Cyan) are intermediate species in much lower abundance than those of Pt_x -MT, and achieve a steady state over the course of the reaction.



Equation 3-1 Bimolecular reaction equations for the metallation of MT by CDDP
*Simplified reaction pathway. Products grouped according to its Pt stoichiometry, with the reaction rates k representing the summation of the overall observed rate of the individual species. Reproduced from D. L. Wong and M. J. Stillman with permission from the Royal Society of Chemistry.*¹⁵

An unusual observation during the metallation reaction of MT with cisplatin (Figure 3-2) was that the observed mass corresponds to the dichlorinated cisplatin. This was unexpected given the time allowed for aquation to occur. However, the observation of the chloride ion in the cisplatin molecule that is bound within the MT clearly delineates the starting point of the subsequent deconstruction of the cisplatin. For instance, distinguishing between the amine groups and water ligands in the aquated cisplatin would be difficult by MS due to protein band broadening, but the loss of the chloride ligands is clearly observed with the resulting significant mass difference. While this chlorinated

speciation is not likely the physiologically observed form of cisplatin, its appearance in these mass spectra provides information that can be used in the development of the deconstruction reaction pathway.

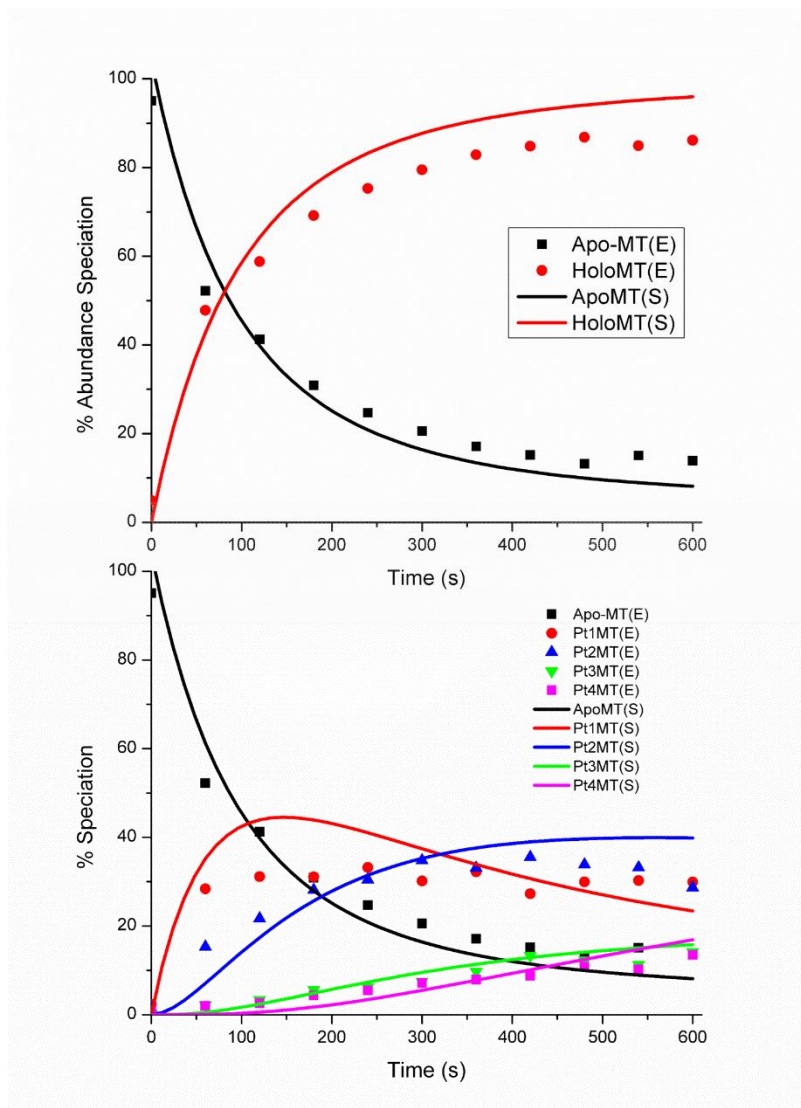


Figure 3-5 Experimental and simulated relative speciation abundance

Experimental data (markers, labelled (E) in legend) and the fitted time dependent reaction (smooth lines, labelled (S) in the legend) of speciation abundance. The top spectra show the Apo-MT and HoloMT speciation, where HoloMT represents the sum of the respective metallated species shown in the bottom spectra. Reproduced from D. L. Wong and M. J. Stillman with permission from the Royal Society of Chemistry.¹⁵

The presence of so many individual intermediate species can make kinetic analysis difficult by standard fitting methods. Using GEPASI, a biochemical pathway simulator, the observed kinetic rates can be simulated by fitting each of the metallation rate laws for cisplatin binding to MT to the experimental data.^{62, 63} For the experimental data, we use the time dependence of the abundance of each species in the ESI mass spectral data. To simplify the overall process, reactions involving the CDDP-MT, CDDP-Pt-MT, and L-Pt-MT intermediate species were grouped based on their total Pt:MT stoichiometry (eg: Pt₁MT, Pt₂MT, Pt₃MT, Pt₄MT) (Equation 3-1), as described for Figure 3-2. The observed rate constants were then derived from the experimental data for each group (Table 3-1). The four consecutive rate law equations modelled the experimental data using the initial concentrations. Taking into account the errors in experimental MS abundancies, the fitted k values are quite reasonable, with % standard deviations below 22%. The errors for the formation for Pt₄MT are large because the abundancies are low as it is the final step in the mechanism. The analysis also shows that the reaction is still in progress at the 600 s time point.

Figure 3-5, top, summarizes the fitting results. Apo-MT reacts rapidly with cisplatin to form HoloMT, with more than 50% of the metallation occurring in the first 100 s. Figure 3-5, bottom, shows the individual components of the HoloMT that were fitted with the k values shown in Table 3-1. These four k values are the rate constants for the steps by which individual Pt_xMT (x = 1-4) form. They encompass ligand substitution by the MT cysteine thiolates until only the Pt(II) core is left.

Table 3-1 Fitted reaction rate k values from experimental mass spectral data. *Reproduced from D. L. Wong and M. J. Stillman with permission from the Royal Society of Chemistry.*

15

<u>Parameter</u>	<u>Value (/10⁻⁶)</u>	<u>Std. Deviation</u>
k ₁	34	6%
k ₂	23	6%
k ₃	14	11%
k ₄	28	21%

The kinetic analysis provides details of the initial pathways by which metallothionein interacts with the incoming cisplatin. The complexity of the reaction, indicated by the similarity in the rate constants, arises from multiple overlapping consecutive pathways, as noted in previous studies.^{6,46} However, the ESI-MS data provides the time-dependent concentration of each of these initial species. The kinetic analysis provides the quantitative data to support the speciation sequence in the binding of cisplatin to MT to form eventually the PtMT product. The first example of a complete analysis of the metallation mechanism of MT was reported for As(III) binding using time- and temperature-dependent MS data.³⁴ The results of presented in this Thesis allows the concentration of any of the 10 cisplatin-MT intermediate species to be calculated at any time following mixing, starting with only the initial concentrations of Apo-MT and cisplatin. It is interesting to note that Hagrman et al. reported a similar magnitude k value for their overall reaction of apo-metallothionein with cisplatin.⁶

These ESI-mass spectral methods can be employed in the investigation of pharmacodynamics of drug metabolism in other biological or clinical applications. With respect to the interaction of MT with cisplatin as discussed above, it is important to comment on the toxic effects of the metabolism and excretion of cisplatin through the proximal renal tubules. It is now commonplace to induce metallothionein in the kidneys using Bi(III) to reduce the tubular damage from the excretion of cisplatin metabolites.⁶⁹ For instance, with relevance to Pt-based chemotherapeutics, platinum analogues including carboplatin and oxaliplatin, employ alternative ligand structures to deter chemoresistance mechanisms and toxic metabolite formation to reduce these symptoms.

3.4 Conclusion

This destructive property of MT towards transition metal complexes reported here with cisplatin emphasize the role of MT as a major player in pre-target resistance. The role of MT in metal metabolism and excretion coupled with the strength of binding to Pt(II), demonstrates the route in which renal damage occurs is likely similar to that of Cd-MT described in Chapter 1. Evidence of long term platinum persistence in individuals treated with platinum anticancer treatments,⁷⁰ indicates that the metabolism of Pt(II) is a long process and chronic exposure would exacerbate this effect. When considering that the

heightened reactivity of MT and related thiols with trans-diamminedichloroplatinate(II) (transplatin) makes it unable to exact cytotoxic effects, it is clear that the character of the ligand on the metal greatly influences treatment success. The importance of the design of a thiol-resistant drug necessary to negate this resistance pathway. High resolution ESI-MS is a means to quantify metabolic products following metallodrug administration, and provides a sophisticated approach for identifying specific metabolic pathways.

3.5 References

1. L. Galluzzi, L. Senovilla, I. Vitale, J. Michels, I. Martins, O. Kepp, M. Castedo and G. Kroemer, Molecular mechanisms of cisplatin resistance, *Oncogene*, 2012, **31**, 1869-1883.
2. Z. H. Siddik, Cisplatin: mode of cytotoxic action and molecular basis of resistance, *Oncogene*, 2003, **22**, 7265-7279.
3. S. Dasari and P. B. Tchounwou, Cisplatin in cancer therapy: molecular mechanisms of action, *Eur. J. Pharmacol.*, 2014, **740**, 364-378.
4. K. Mellish, L. Kelland and K. Harrap, In vitro platinum drug chemosensitivity of human cervical squamous cell carcinoma cell lines with intrinsic and acquired resistance to cisplatin, *Br. J. Cancer*, 1993, **68**, 240.
5. J. C. Dabrowiak, J. Goodisman and A.-K. Souid, Kinetic study of the reaction of cisplatin with thiols, *Drug Metab. Dispos.*, 2002, **30**, 1378-1384.
6. D. Hagrman, J. Goodisman, J. C. Dabrowiak and A.-K. Souid, Kinetic study on the reaction of cisplatin with metallothionein, *Drug Metab. Dispos.*, 2003, **31**, 916-923.
7. P. J. Thornalley and M. Vašák, Possible role for metallothionein in protection against radiation-induced oxidative stress. Kinetics and mechanism of its reaction with superoxide and hydroxyl radicals, *BBA - Protein Struct. M.*, 1985, **827**, 36-44.
8. P. D. Sadowitz, B. A. Hubbard, J. C. Dabrowiak, J. Goodisman, K. A. Tacka, M. K. Aktas, M. J. Cunningham, R. L. Dubowy and A.-K. Souid, Kinetics of cisplatin binding to cellular DNA and modulations by thiol-blocking agents and thiol drugs, *Drug Metab. Dispos.*, 2002, **30**, 183-190.
9. L. Cubo, M. Groessl, P. J. Dyson, A. G. Quiroga, C. Navarro-Ranninger and A. Casini, Proteins as Possible Targets for Cytotoxic trans-Platinum (II) Complexes with Aliphatic Amine Ligands: Further Exceptions to the DNA Paradigm, *ChemMedChem*, 2010, **5**, 1335-1343.

10. A. Boumendjel, A. Florin and J. Boutonnat, Reversal agents of multidrug resistance mediated by multidrug resistance-associated proteins (MRPs), *ABC Transporters and Multidrug Resistance*, 2009, 261-288.
11. G. D. Kruh and M. G. Belinsky, The MRP family of drug efflux pumps, *Oncogene*, 2003, **22**, 7537.
12. E. M. Leslie, R. G. Deeley and S. P. Cole, Multidrug resistance proteins: role of P-glycoprotein, MRP1, MRP2, and BCRP (ABCG2) in tissue defense, *Toxicol. Appl. Pharmacol.*, 2005, **204**, 216-237.
13. L. Messori and A. Merlino, Cisplatin binding to proteins: a structural perspective, *Coord. Chem. Rev.*, 2016, **315**, 67-89.
14. L. Messori and A. Merlino, Cisplatin binding to proteins: molecular structure of the ribonuclease A adduct, *Inorg. Chem.*, 2014, **53**, 3929-3931.
15. D. L. Wong and M. J. Stillman, Capturing platinum in cisplatin: kinetic reactions with recombinant human apo-metallothionein 1a, *Metallomics*, 2018, **10**, 713-721.
16. B. Lippert, *Cisplatin: chemistry and biochemistry of a leading anticancer drug*, John Wiley & Sons, 1999.
17. M. Sooriyaarachchi, G. N. George, I. J. Pickering, A. Narendran and J. Gailer, Tuning the metabolism of the anticancer drug cisplatin with chemoprotective agents to improve its safety and efficacy, *Metallomics*, 2016, **8**, 1170-1176.
18. P. M. Takahara, A. C. Rosenzweig, C. A. Frederick and S. J. Lippard, Crystal structure of double-stranded DNA containing the major adduct of the anticancer drug cisplatin, *Nature*, 1995, **377**, 649.
19. V. M. Gonzalez, M. A. Fuertes, C. Alonso and J. M. Perez, Is cisplatin-induced cell death always produced by apoptosis?, *Mol. Pharmacol.*, 2001, **59**, 657-663.
20. A. Mandic, J. Hansson, S. Linder and M. C. Shoshan, Cisplatin induces endoplasmic reticulum stress and nucleus-independent apoptotic signaling, *J. Biol. Chem.*, 2003, **278**, 9100-9106.
21. R. Schilder, L. Hall, A. Monks, L. Handel, A. Fornace, R. Ozols, A. Fojo and T. Hamilton, Metallothionein gene expression and resistance to cisplatin in human ovarian cancer, *Int. J. Cancer*, 1990, **45**, 416-422.
22. P. Surowiak, V. Materna, A. Maciejczyk, M. Pudełko, E. Markwitz, M. Spaczyński, M. Dietel, M. Zabel and H. Lage, Nuclear metallothionein expression correlates with cisplatin resistance of ovarian cancer cells and poor clinical outcome, *Virchows Arch.*, 2007, **450**, 279-285.

23. E. S. Woo, A. Monks, S. C. Watkins, A. S. Wang and J. S. Lazo, Diversity of metallothionein content and subcellular localization in the National Cancer Institute tumor panel, *Cancer Chemother. Pharmacol.*, 1997, **41**, 61-68.
24. S. L. Kelley, A. Basu, B. A. Teicher, M. P. Hacker, D. H. Hamer and J. S. Lazo, Overexpression of metallothionein confers resistance to anticancer drugs, *Science*, 1988, **241**, 1813-1815.
25. T. Gansukh, P. Donizy, A. Halon, H. Lage and P. Surowiak, In vitro analysis of the relationships between metallothionein expression and cisplatin sensitivity of non-small cellular lung cancer cells, *Anticancer Res.*, 2013, **33**, 5255-5260.
26. E. Atrián-Blasco, A. Santoro, D. L. Pountney, G. Meloni, C. Hureau and P. Faller, Chemistry of mammalian metallothioneins and their interaction with amyloidogenic peptides and proteins, *Chem. Soc. Rev.*, 2017, **46**, 7683-7693.
27. D. E. Sutherland and M. J. Stillman, The “magic numbers” of metallothionein, *Metallomics*, 2011, **3**, 444-463.
28. T. T. Ngu and M. J. Stillman, Metal-binding mechanisms in metallothioneins, *Dalton Trans.*, 2009, 5425-5433.
29. C. A. Blindauer, in *Binding, Transport and Storage of Metal Ions in Biological Cells*, 2014, pp. 606-665.
30. E. Freisinger, Structural features specific to plant metallothioneins, *J. Biol. Inorg. Chem.*, 2011, **16**, 1035-1045.
31. J. S. Scheller, G. W. Irvine, D. L. Wong, A. Hartwig and M. J. Stillman, Stepwise copper (I) binding to metallothionein: a mixed cooperative and non-cooperative mechanism for all 20 copper ions, *Metallomics*, 2017, **9**, 447-462.
32. C. A. Blindauer, Advances in the molecular understanding of biological zinc transport, *Chem. Commun.*, 2015, **51**, 4544-4563.
33. J. D. Otvos, D. H. Petering and C. F. Shaw, Structure—Reactivity Relationships of Metallothionein, a Unique Metal-Binding Protein, *Comment Inorg. Chem.*, 1989, **9**, 1-35.
34. T. T. Ngu, A. Easton and M. J. Stillman, Kinetic analysis of arsenic– metalation of human metallothionein: significance of the two-domain structure, *J. Am. Chem. Soc.*, 2008, **130**, 17016-17028.
35. M. J. Stillman, A. S. Zelazowski, J. Szymanska and Z. Gasyna, Luminescent metallothioneins: Emission properties of copper, silver, gold and platinum complexes of MT, *Inorganica Chim. Acta*, 1989, **161**, 275-279.

36. W. Bernhard, M. Good, M. Vašák and J. H. Kägi, Spectroscopic studies and characterization of metallothioneins containing mercury, lead and bismuth, *Inorganica Chim. Acta*, 1983, **79**, 154-155.
37. I. Bertini, C. Luchinat, L. Messori and M. Vasak, Proton NMR studies of the cobalt (II)-metallothionein system, *J. Am. Chem. Soc.*, 1989, **111**, 7296-7300.
38. D. M. Townsend, M. Deng, L. Zhang, M. G. Lopus and M. H. Hanigan, Metabolism of cisplatin to a nephrotoxin in proximal tubule cells, *J. Am. Soc. Nephrol.*, 2003, **14**, 1-10.
39. A. J. Żelazowski, J. S. Garvey and J. D. Hoeschele, In vivo and in vitro binding of platinum to metallothionein, *Arch. Biochem. Biophys.*, 1984, **229**, 246-252.
40. B. Zhang and W. Tang, Kinetics of the reaction of platinum (II) complexes with metallothionein, *J. Inorg. Biochem.*, 1994, **56**, 143-153.
41. M. Knipp, Metallothioneins and platinum (II) anti-tumor compounds, *Curr. Med. Chem.*, 2009, **16**, 522-537.
42. B. Zhang, W. Tang, S. Gao and Y. Zhou, Platinum binding to metallothionein. Analysis of circular dichroism spectra of complexes formed between metallothionein and platinum from cis- and trans-diamminedichloroplatinum, *J. Inorg. Biochem.*, 1995, **58**, 9-19.
43. A. V. Karotki and M. Vašák, Reaction of human metallothionein-3 with cisplatin and transplatin, *J. Biol. Inorg. Chem.*, 2009, **14**, 1129-1138.
44. M. Knipp, A. V. Karotki, S. Chesnov, G. Natile, P. J. Sadler, V. Brabec and M. Vašák, Reaction of Zn₇Metallothionein with cis- and trans-[Pt (N-donor)₂Cl₂] anticancer complexes: trans-PtII complexes retain their N-donor ligands, *J. Med. Chem.*, 2007, **50**, 4075-4086.
45. R. Mandal, R. Kalke and X. F. Li, Mass spectrometric studies of cisplatin-induced changes of hemoglobin, *Rapid. Commun. Mass. Spectrom.*, 2003, **17**, 2748-2754.
46. A. Pattanaik, G. Bachowski, J. Laib, D. Lemkuil, C. Shaw, D. Petering, A. Hitchcock and L. Saryan, Properties of the reaction of cis-dichlorodiammineplatinum (II) with metallothionein, *J. Biol. Chem.*, 1992, **267**, 16121-16128.
47. A. Kraker, J. Schmidt, S. Krezoski and D. Petering, Binding of cis-dichlorodiammine platinum (II) to metallothionein in Ehrlich cells, *Biochem. Biophys. Res. Commun.*, 1985, **130**, 786-792.
48. D. C. Lemkuil, D. Nettesheim, C. F. Shaw and D. H. Petering, Reaction of Cd₇-metallothionein with cis-dichlorodiammine platinum (II), *J. Biol. Chem.*, 1994, **269**, 24792-24797.

49. T. T. Ngu, S. Krecisz and M. J. Stillman, Bismuth binding studies to the human metallothionein using electrospray mass spectrometry, *Biochem. Biophys. Res. Commun.*, 2010, **396**, 206-212.
50. A. Pattanaik, C. F. Shaw III, D. H. Petering, J. Garvey and A. J. Kraker, Basal metallothionein in tumors: widespread presence of apoprotein, *J. Inorg. Biochem.*, 1994, **54**, 91-105.
51. M. Apostolova, P. Bontchev, C. Nachev and I. Sirakova, Apometallothionein in rat liver, *J. Chromatogr. B Biomed. Sci. Appl.*, 1993, **620**, 191-197.
52. D. H. Petering, J. Zhu, S. Krezoski, J. Meeusen, C. Kiekenbush, S. Krull, T. Specher and M. Dughish, Apo-metallothionein emerging as a major player in the cellular activities of metallothionein, *Exp. Biol. Med.*, 2006, **231**, 1528-1534.
53. Y. Yang, W. Maret and B. L. Vallee, Differential fluorescence labeling of cysteinyl clusters uncovers high tissue levels of thionein, *Proc. Natl. Acad. Sci. U.S.A.*, 2001, **98**, 5556-5559.
54. D. L. Wong and M. J. Stillman, Destructive interactions of dirhodium (II) tetraacetate with β metallothionein rh1a, *Chem. Commun.*, 2016, **52**, 5698-5701.
55. A. Casini, A. Karotki, C. Gabbiani, F. Rugi, M. Vařák, L. Messori and P. J. Dyson, Reactivity of an antimetastatic organometallic ruthenium compound with metallothionein-2: relevance to the mechanism of action, *Metallomics*, 2009, **1**, 434-441.
56. G. W. Irvine, T. B. Pinter and M. J. Stillman, Defining the metal binding pathways of human metallothionein 1a: balancing zinc availability and cadmium seclusion, *Metallomics*, 2016, **8**, 71-81.
57. G. W. Irvine and M. J. Stillman, Cadmium binding mechanisms of isolated domains of human MT isoform 1a: Non-cooperative terminal sites and cooperative cluster sites, *J. Inorg. Biochem.*, 2016, **158**, 115-121.
58. D. P. Jayawardena, I. U. Heinemann and M. J. Stillman, Zinc binds non-cooperatively to human liver metallothionein 2a at physiological pH, *Biochem. Biophys. Res. Commun.*, 2017, **493**, 650-653.
59. J. Chan, Z. Huang, I. Watt, P. Kille and M. J. Stillman, Characterization of the conformational changes in recombinant human metallothioneins using ESI-MS and molecular modeling, *Can. J. Chem.*, 2007, **85**, 898-912.
60. W. Lu and M. J. Stillman, Mercury-thiolate clusters in metallothionein. Analysis of circular dichroism spectra of complexes formed between. α -metallothionein, apometallothionein, zinc metallothionein, and cadmium metallothionein and mercury (2+), *J. Am. Chem. Soc.*, 1993, **115**, 3291-3299.

61. M. J. Stillman, D. Thomas, C. Trevithick, X. Guo and M. Siu, Circular dichroism, kinetic and mass spectrometric studies of copper (I) and mercury (II) binding to metallothionein, *J. Inorg. Biochem.*, 2000, **79**, 11-19.
62. P. Mendes, Biochemistry by numbers: simulation of biochemical pathways with Gepasi 3, *Trends Biochem. Sci.*, 1997, **22**, 361-363.
63. P. Mendes, GEPASI: a software package for modelling the dynamics, steady states and control of biochemical and other systems, *Bioinformatics*, 1993, **9**, 563-571.
64. D. E. Sutherland and M. J. Stillman, Noncooperative cadmium (II) binding to human metallothionein 1a, *Biochem. Biophys. Res. Commun.*, 2008, **372**, 840-844.
65. D. E. Sutherland, K. L. Summers and M. J. Stillman, Noncooperative metalation of metallothionein 1A and its isolated domains with zinc, *Biochemistry*, 2012, **51**, 6690-6700.
66. D. E. Sutherland, K. L. Summers and M. J. Stillman, Modeling the Zn 2+ and Cd 2+ metalation mechanism in mammalian metallothionein 1a, *Biochem. Biophys. Res. Commun.*, 2012, **426**, 601-607.
67. T. B. Pinter and M. J. Stillman, Putting the pieces into place: Properties of intact zinc metallothionein 1A determined from interaction of its isolated domains with carbonic anhydrase, *Biochem. J.*, 2015, **471**, 347-356.
68. I. Bertini, C. Luchinat, L. Messori and M. Vasak, Proton NMR spectra of the Co₄S₁₁ cluster in metallothioneins: a theoretical model, *J. Am. Chem. Soc.*, 1989, **111**, 7300-7303.
69. E. R. Tiekink, Antimony and bismuth compounds in oncology, *Crit. Rev. Oncol. Hematol.*, 2002, **42**, 217-224.
70. G. Rentschler, I. Rodushkin, M. Cerna, C. Chen, F. Harari, R. Harari, M. Horvat, F. Hrubá, L. Kasparová and K. Koppová, Platinum, palladium, rhodium, molybdenum and strontium in blood of urban women in nine countries, *Int. J. Hyg. Environ. Health*, 2018, **221**, 223-230.

Chapter 4

4 Destructive Interactions of Dirhodium(II) Tetraacetate with β Metallothionein rh1a*

4.1 Introduction

Metallo drugs have a long and successful history in curing many different classes of disease; for example, cisplatin for testicular cancer, sodium aurothiomalate for rheumatoid arthritis, Li salts for psychological disorders, and Bi salts for gastrointestinal distress.^{1,2} Challenges in the development of new metallopharmaceuticals include overcoming the cellular metal defences protecting the target. Metal-chelating gate-keeper proteins can result in dramatically decreased drug efficacy. The experiments in this Chapter report that one such gate-keeping protein, metallothionein, both binds dirhodium acetate, a potential anticancer metallo drug, and sequentially strips off the acetate ligands reducing the complex to just a thiolate-coordinated dirhodium core. This reaction may indicate a possible mechanism for a cellular metallo drug resistance pathway.

Metallothioneins (MTs) are sulfur rich proteins that bind a variety of metals including toxic metals and those of medicinal interest. Current metallo drug designs aim to overcome these defences, for example using non-platinum compounds, like the robust series of half-sandwich arene Ru(II) anti-cancer compounds.³⁻⁵ While the over-expression of the cysteine-rich MT has been correlated to drug resistance,^{6,7} there is very little direct, quantitative evidence of the mechanism that may be involved in the proposed interactions. In addition, there have been no reports of the subsequent fate of the metallo drug following its interaction with MT. Studies with cisplatin have provided some insight into the rates of metal ion isolation as seen in the previous Chapter,^{8,9} but much more detailed information on the mechanism of destruction of the metal complex by the MT through ligand exchange is needed. Using dirhodium(II) tetraacetate as a model complex this ligand exchange can be observed with four identical ligands, while featuring a central metal-metal bond.

**A version of this chapter has been published
Chemical Communications, 52(33), 5698-5701. (2016). Copyright 2016 Royal Society of Chemistry.
Reproduced with permission from: D. L. Wong, and M. J. Stillman.*

4.1.1 Dirhodium(II) Tetraacetate as a Model Chemotherapeutic Complex

Metal-metal bonded dirhodium carboxylate complexes have gained interest as an alternative to classical platinum anti-cancer compounds.¹⁰ Dirhodium complexes are 18 electron systems when the two axial positions are capped by solvent, with octahedral coordination of the rhodium metals. Ground work studies have shown high *in vivo* antitumor activity of $\text{Rh}_2(\text{O}_2\text{CR})_4$ (R = Me, Et, Pr) against L1210 tumors, Ehrlich ascites, and the sarcoma 180 and P388 tumor lines,¹¹ as well as the ability to bind DNA and inhibit protein synthesis in a manner akin to cisplatin.¹² Current research has extended the applications of rhodium compounds to medical imaging and protein labelling, but the significant antitumor characteristics of these rhodium complexes remain of great interest.¹³⁻¹⁶ However, the dirhodium carboxylates are particularly sensitive to sulfur coordination from cysteines in biomolecular targets.^{17, 18} This is significant because MT may stand in the way as a formidable defence for cancerous cells due to the tendency of cysteine coordination of any incoming metal. Herein, preliminary studies involving the remarkable and systematic deconstruction of dirhodium(II) tetraacetate ($\text{Rh}_2(\text{OAc})_4$), a compound with anti-tumor activity, by the β -domain fragment of human metallothionein 1a, are reported and discussed.

4.1.2 Electrospray Ionization Mass Spectrometry (ESI-MS)

ESI-MS is a powerful technique that allows for the quantitative visualization of a reaction as it progresses. In particular, mass spectrometry is especially effective in monitoring drug-protein binding reactions, as it is able to provide information regarding intermediate species as they develop in real time.^{19, 20} ESI mass spectral data can be used in the characterization of species formed in a reaction by providing kinetic and stoichiometric details. When combined with UV-visible absorption and circular dichroism spectroscopic information, binding sites and changes of protein structure as a result of metal binding can be determined. These techniques provide a simple, yet information-rich method for assessing the viability of a preliminary study. While *in vivo* studies may be suited for determining mobility and target binding site information in a cell, the high detail of the *in vitro* studies shown here provide the mechanistic insight required to understand the

protective function that MT may perform in such drug resistant cancer forms. In this study, ESI-MS, UV-visible absorption and circular dichroism spectroscopy, together with molecular dynamics calculations were employed to monitor the binding reaction of $\text{Rh}_2(\text{OAc})_4$ with apo- β -MT.

4.2 Experimental Methods

Preparation of recombinant human Metallothionein1a

Preparation of isolated MT domain fragments followed previously reported methods.²¹ The amino acid sequence for the isolated domain used in this study was based on the recombinant human MT1a 38-residue β -MT domain fragment sequence (MGKAAAACSC ATGGSTCTG SCKCKECKCN SCKKAAAA). Each of the corresponding DNA sequences was inserted as an N-terminal S-tag fusion protein into pET29a plasmids and individually expressed in *E. coli* BL21(DE3) with cadmium-supplemented growth medium, as described in Chapter 1. The protein was expressed and purified as the cadmium saturated form for stability. All purified protein solutions were evacuated and saturated with argon to impede cysteine oxidation.

Preparation of apo- β -Metallothionein

Cadmium was removed from the purified, isolated MT domains by acidifying the protein solutions to pH 2.7. The protein was desalted and buffer exchanged with argon-saturated deionized water, returned to neutral pH, and concentrated using Millipore Amicon Ultra-4 centrifuge filter units (3 kDa MWCO). Protein concentrations of the final, pH-adjusted apo- β -MT solutions were determined by cadmium remetalation of small fractions of each protein monitored using UV-visible absorption (Cary 50, Varian Canada): ϵ_{250} values of Cd_3 - β -MT is $36000 \text{ M}^{-1} \text{ cm}^{-1}$.²² Protein solutions were diluted to a final concentration of $10 \mu\text{M}$.

Preparation of $\text{Rh}_2(\text{OAc})_4$ solutions

Stock solutions of $500 \mu\text{M}$ dirhodium(II) tetraacetate (Sigma-Aldrich) were freshly prepared in deionized water, evacuated and argon saturated. The MT cysteine concentration was determined and two-fold excess of $\text{Rh}_2(\text{OAc})_4$ was added to the MT solution and mixed immediately prior to MS acquisition. The room-temperature UV-

visible and circular dichroism (CD) spectra of the solutions were also measured following $\text{Rh}_2(\text{OAc})_4$ saturation.

Electrospray Ionization Mass Spectrometry, UV- Visible and Circular Dichroism Absorption

A Bruker Micro-TOF II instrument (Bruker Daltonics, Toronto, ON) operated in positive ion mode was used to collect the data. NaI was used as an external calibrant. The settings are the same as those described in Chapter 1. The spectra were collected continuously over 1 hr and time slices were deconvoluted using the Maximum Entropy algorithm of the Bruker Compass DataAnalysis software package.

A Cary 50 (Varian, Canada) was used to collect UV-visible absorption data from the visible region. A Jasco J810 spectropolarimeter was used to collect CD spectral data. The following scan parameters were used: step scan; range, 800-200 nm; data pitch, 1 nm; bandwidth, 0.5 nm; response, 1 s.

Molecular Dynamics Calculations

A minimized structure of the 38-residue Cd_3 - β -MT1a domain fragment was used (Scigress 6.0.0 MM3/MD method with augmented force field; Fujitsu Poland) to test if the Rh_2^{4+} core could be reasonably coordinated by 8 of the 9 cys of the β -MT1a. The three Cd^{2+} ions were deleted from the original structure and the Rh_2^{4+} core inserted using cysteine thiolate connections that were in close proximity to the 8 x/y ligand positions on the Rh_2^{4+} core. The alignment of the core was locked to stop rotation about the Rh-Rh bond. The molecular dynamics calculation was carried out for 200 ps at an average temperature of 355 K with 2 fs steps using a dielectric of 78.5. The initial structure relaxed immediately then was stable.

4.3 Results

ESI mass spectra were recorded continuously over 60 min following the mixing of $(\text{Rh}_2(\text{OAc})_4)$ with apo- β -MT in water. Six representative mass spectra extracted at different times from the 60 minute collection are shown in Figure 4-1. The spectral data were averaged over 15 seconds meaning that the average data point time is 7.5 s from the

start of the averaging in each spectrum resulting in data at 7.5, 37.5, 52.5, 67.5, 95.0 and 127.5 s.

Apo- β -MT is recognizable at a mass of ~ 3751 Da (track A), with the metallated species resulting in a series of higher mass species (tracks D-H). The metallated Rh_2 - β -MT has a mass of ~ 3952 Da (track D), with each Rh replacing four of the cysteine thiol protons, which, we propose, results in an octahedral geometry for each Rh(II) in the dirhodium core, retaining its Rh-Rh bond. The remarkable feature of this binding reaction is that the data show, in sequence, the systematic removal of each of the four acetate groups, whose mass initially starts at ~ 4193 Da (track H) and with each acetate removal being noted at peaks $M = \sim 4136$ (track G), 4081 (track F), and 4016 Da (track E), respectively. The released acetates in solution likely form surface adducts to positively charged amino acids (such as lysine) in the remaining MT, with these adducted species identified by a mass difference of 59 Da, and in proportional amount to the formation of Rh_2 - β -MT. There was no other source of acetate in the solution. The time-dependent data indicate that loss of the acetates is faster than the initial interaction because the partially-ligated Rh-MT complexes with 2, 3 or 4 acetates are in very low proportional concentration (tracks F-H) compared with the mono-acetate and Rh_2^{4+} core (track D). The overall binding rate can be seen from the decline in apo- β -MT abundance. As the Rh_2^{4+} core binds to the MT, the remaining apo- β -MT diminishes so that by 127.5 s almost none remains (tracks A-C).

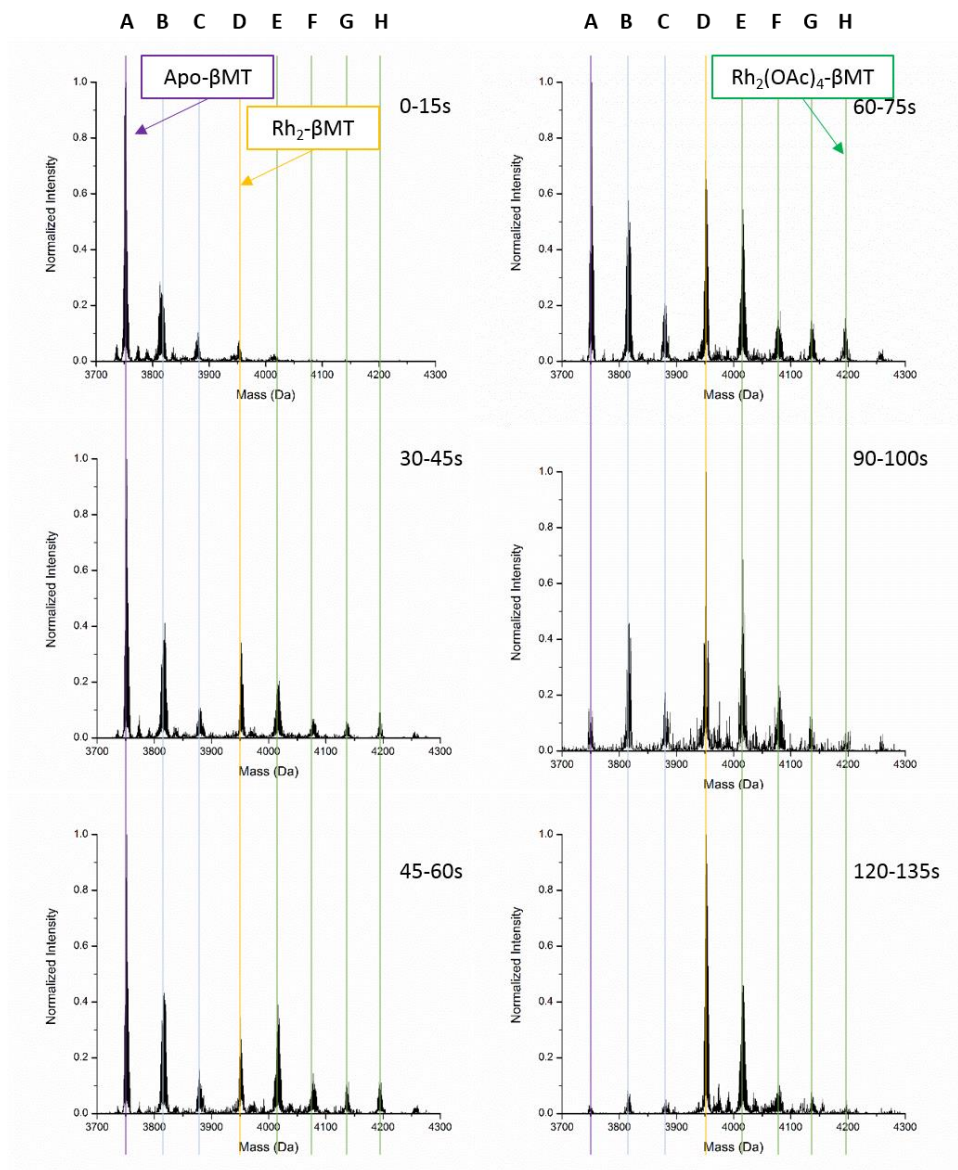


Figure 4-1 Deconvoluted time-dependent ESI-mass spectra recorded following the mixing of apo- β -MT with excess $\text{Rh}_2(\text{OAc})_4$ at pH 7.3. The vertical axis shows the normalized intensity; the horizontal axis shows the mass in Da. Data were averaged for 15 seconds starting at 0, 30, 45, 60, 90 and 120 s from a data set collected over 60 minutes. The apo- β -MT is marked in track A, the final product with the Rh_2^{4+} bound is marked by track D. Track identifiers: A) Apo- β -MT; mass 3751. B) Apo(OAc) $_1$ - β -MT; 3811. C) Apo(OAc) $_2$ - β -MT; 3875. D) Rh_2 - β -MT; 3951. E) $\text{Rh}_2(\text{OAc})_1$ - β -MT; 4013. F) $\text{Rh}_2(\text{OAc})_2$ - β -MT; 4075. G) $\text{Rh}_2(\text{OAc})_3$ - β -MT; 4136. H) $\text{Rh}_2(\text{OAc})_4$ - β -MT; 4192. Reproduced from D. L. Wong and M. J. Stillman, with permission from the Royal Society of Chemistry.²³

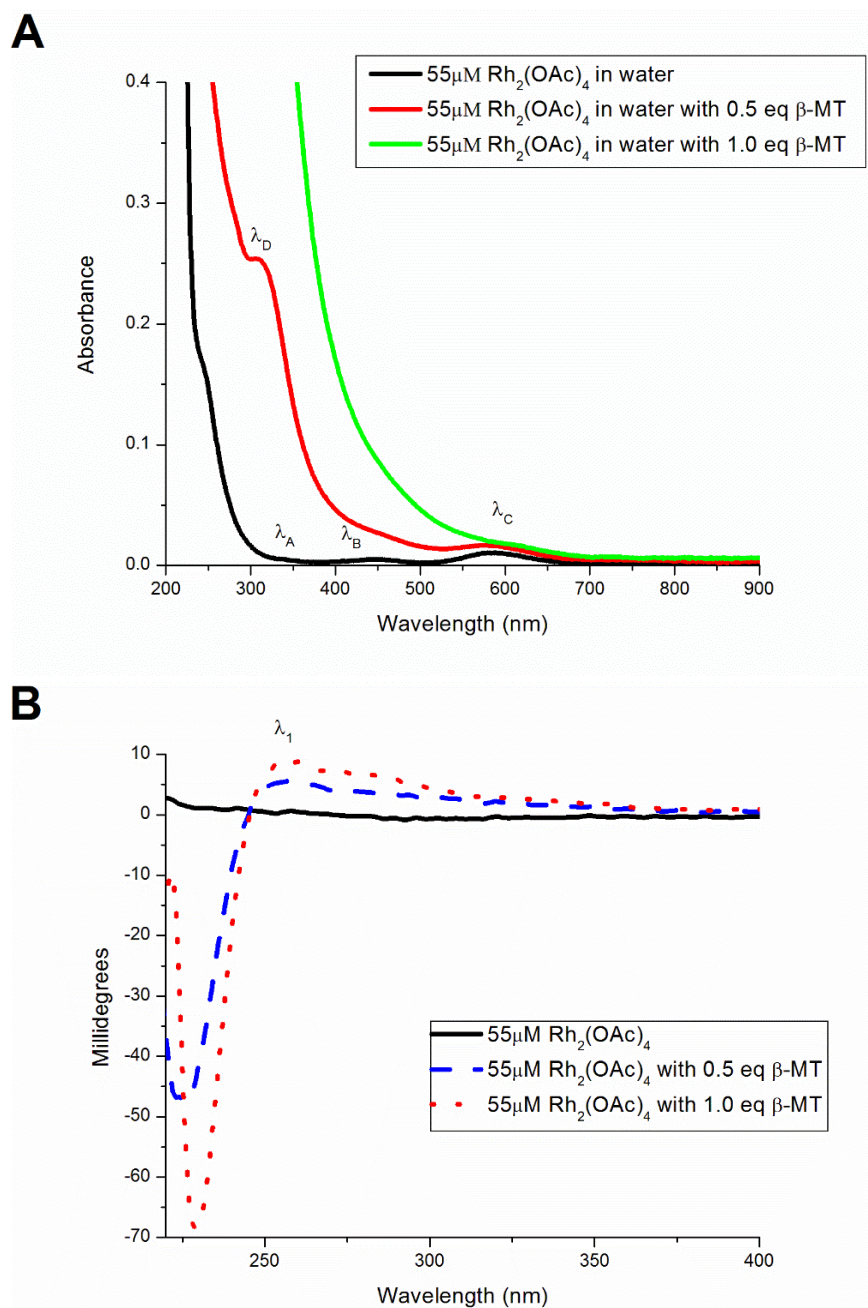


Figure 4-2 Absorption and CD spectra of the reaction of Rh₂(OAc)₄ and β -MT
UV-visible absorption spectra (A) and circular dichroism spectra (B) of a 55 μ M Rh₂(OAc)₄ solution in water with 0.5 and 1.0 mol. eq. of apo- β -MT added. Figure 4-2A. Spectral assignments: $\lambda_A = 350$ nm; σ (H₂O) \rightarrow σ^ (Rh₂). $\lambda_B = 455$ nm; π^* (Rh₂) \rightarrow σ^* (Rh-O). $\lambda_C = 580$ nm; π^* (Rh₂) \rightarrow σ^* (Rh₂). $\lambda_D = 350$ nm; σ (S) \rightarrow σ^* (Rh₂). Figure 4-2B. Spectral assignments: $\lambda_1 = 255$ nm, a new band appearing upon Rh₂(OAc)₄ binding.*

*Reproduced from D. L. Wong and M. J. Stillman, with permission from the Royal Society of Chemistry.*²³

The UV-visible absorption spectra recorded with 0.5 and 1 mol. eq. of $\text{Rh}_2(\text{OAc})_4$ added to the apo- β -MT showed appearance of bands near 3250 nm associated with a change in color from blue to yellow (Figure 4-2A). The Rh-Rh metal-metal bond was indicated by the band near 580 nm that only slightly blue shifted, as reported by others regarding rhodium axial coordination by solvents.¹⁸

The circular dichroism spectra show a new band forming near 255 nm that only appears as a result of the protein binding to the $\text{Rh}_2(\text{OAc})_4$ (Figure 4-2B).

The ESI-mass spectral data together with the absorption spectral data, support our proposal that the $\text{Rh}_2(\text{OAc})_4$ complex is bound as the Rh_2^{4+} core after each of the acetate bridging ligands is released and replaced by pairs of cysteinyl thiolates from the MT. In this mechanism, the thiolates displace the acetates stepwise, allowing the Rh-Rh bond to survive. However, the proposal does require a test of whether the Rh_2^{4+} core could exist within the peptide using a reasonable folding motif achievable from the 9 cysteines of the apo- β -MT fragment. To test this, an energy minimized structure of $\text{Cd}_3\beta\text{-MT1a}$ was used to establish a typical host volume.²⁴ Using the $\text{Rh}_2(\text{OAc})_4$ complex structure as a starting point, the deleted 3 Cd^{2+} ions in the protein binding site and inserted the Rh_2^{4+} core aligned by the acetates. The alignment was locked as the MM3 system has no information about the electronic structure of the Rh_2^{4+} metal-metal bond requirement. The 8 coordination points for the 8 x/y aligned thiolate ligands are defined in the electronic structure as being eclipsed. There are two further z-axis coordination points frequently used by solvents.¹⁸ The cysteinyl thiolate alignments following deletion of the three Cd^{2+} ions were used to guide bond formation to the Rh_2^{4+} core. The MD calculation trajectory showed that the peptide backbone realigned within 10 ps, indicating that the Rh_2^{4+} core required very little rearrangement to use the volume previously occupied by the 3 Cd^{2+} ions. Figure 4-3 shows the space filling representation and the ribbon alignment of the orientation at 200 ps. No significant change in the energy was observed for over 170 ps. The ribbon (Figure 4-3, right) shows that the peptide encapsulates the Rh_2^{4+} core. Emission data from Cu^+ binding studies to metallothioneins support the proposal that

when the MT peptide binds using all the cysteines in a cluster that there is little access to the solvent,²⁵ so water was not included in the binding region. The ribbon depiction of the peptide orientation in Cd₃-β-MT was virtually the same as shown in Figure 4-3, confirming that replacement of the three Cd²⁺ ions by the Rh₂⁴⁺ core did not require major reorientation of the cysteines. The structure in Figure 4-3 is a hypothetical model designed to indicate the possible conformational changes necessary for the 38-amino acid, 9 cysteine apo-β-MT to bind the Rh₂⁴⁺ core.

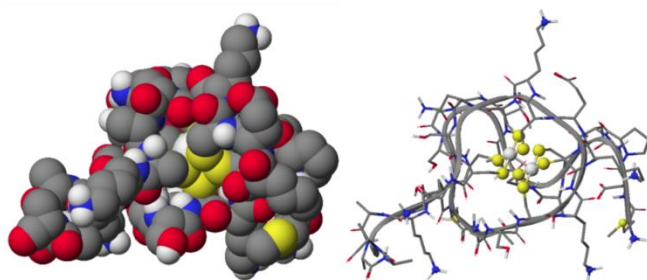


Figure 4-3 Molecular Dynamics structure for Rh₂-bound β-MT.

Results of a molecular dynamics calculation where the Rh₂⁴⁺ core was inserted into the apo-β-MT1a binding site. The calculation was carried out for 200 ps at an average temperature of 355 K with a dielectric constant set to the 78.5 of water. The yellow spheres are cysteinyl thiolates while the white spheres (right) are the two Rh²⁺ ions. The intention of this calculation was to examine if the Rh₂⁴⁺ core could bind using 8 cys S without major change to the normal conformation. Reproduced from D. L. Wong and M. J. Stillman, with permission from the Royal Society of Chemistry.²³

4.4 Conclusion

This Chapter introduces investigations of the simplest dirhodium carboxylate, dirhodium(II) tetraacetate (Rh₂(OAc)₄), and its deconstruction *in vitro* by the human MT1a β-domain fragment of the metal-defence protein, MT. Metallothioneins have a well-documented chemistry of scavenging toxic metals that enter the cell. Our group and others have suggested that this property can contribute to greatly reduced efficacies for metal-based drugs. In the reaction described in this Chapter, the four metal-coordinated acetates are replaced stepwise by the more aggressive cysteinyl thiolates of the metallothionein. The protein wraps around the rhodium complex, maintaining the Rh-Rh

bond, bringing the cysteinyl thiolates closer to the interior core. To further investigate this metallation mechanism, studies continue with the full length, two-domain MT, in the following Chapter.

4.5 References

1. P. J. Dyson, Metal-based Drugs, *Aust. J. Chem.*, 2010, **63**, 1503-1504.
2. K. D. Mjos and C. Orvig, Metallo drugs in medicinal inorganic chemistry, *Chem. Rev.*, 2014, **114**, 4540-4563.
3. A. Casini, A. Karotki, C. Gabbiani, F. Rugi, M. Vašák, L. Messori and P. J. Dyson, Reactivity of an antimetastatic organometallic ruthenium compound with metallothionein-2: relevance to the mechanism of action, *Metallomics*, 2009, **1**, 434-441.
4. P. Nowak-Sliwinska, J. R. van Beijnum, A. Casini, A. A. Nazarov, G. Wagnieres, H. van den Bergh, P. J. Dyson and A. W. Griffioen, Organometallic ruthenium (II) arene compounds with antiangiogenic activity, *J. Med. Chem.*, 2011, **54**, 3895-3902.
5. Z. Almodares, S. J. Lucas, B. D. Crossley, A. M. Basri, C. M. Pask, A. J. Hebden, R. M. Phillips and P. C. McGowan, Rhodium, iridium, and ruthenium half-sandwich picolinamide complexes as anticancer agents, *Inorg. Chem.*, 2014, **53**, 727-736.
6. P. A. Andrews, M. P. Murphy and S. B. Howell, Metallothionein-mediated cisplatin resistance in human ovarian carcinoma cells, *Cancer Chemother. Pharmacol.*, 1987, **19**, 149-154.
7. M. Kartalou and J. M. Essigmann, Mechanisms of resistance to cisplatin, *Mutat. Res.-Fund. Mol. Mech. Mut.*, 2001, **478**, 23-43.
8. D. Hagrman, J. Goodisman, J. C. Dabrowiak and A.-K. Souid, Kinetic study on the reaction of cisplatin with metallothionein, *Drug Metab. Dispos.*, 2003, **31**, 916-923.
9. M. Knipp, A. V. Karotki, S. Chesnov, G. Natile, P. J. Sadler, V. Brabec and M. Vašák, Reaction of Zn₇Metallothionein with cis- and trans-[Pt (N-donor)₂Cl₂] anticancer complexes: trans-PtII complexes retain their N-donor ligands, *J. Med. Chem.*, 2007, **50**, 4075-4086.
10. A. Erck, E. Sherwood, J. Bear and A. Kimball, The metabolism of rhodium (II) acetate in tumor-bearing mice, *Cancer Res.*, 1976, **36**, 2204-2209.

11. R. Howard, T. Spring and J. Bear, The interaction of rhodium (II) carboxylates with enzymes, *Cancer Res.*, 1976, **36**, 4402-4405.
12. A. M. Angeles-Boza, H. T. Chifotides, J. D. Aguirre, A. Chouai, P. K.-L. Fu, K. R. Dunbar and C. Turro, Dirhodium (II, II) complexes: molecular characteristics that affect in vitro activity, *J. Med. Chem.*, 2006, **49**, 6841-6847.
13. Z. Majer, S. Bősze, I. Szabó, V. G. Mihucz, A. Gaál, G. Szilvályi, G. Pepponi, F. Meirer, P. Wobrauschek and N. Szoboszlai, Study of dinuclear Rh (II) complexes of phenylalanine derivatives as potential anticancer agents by using X-ray fluorescence and X-ray absorption, *Microchem. J.*, 2015, **120**, 51-57.
14. G. Gasser, I. Ott and N. Metzler-Nolte, Organometallic anticancer compounds, *J. Med. Chem.*, 2010, **54**, 3-25.
15. K. Sorasaenee, P. K.-L. Fu, A. M. Angeles-Boza, K. R. Dunbar and C. Turro, Inhibition of transcription in vitro by anticancer active dirhodium (II) complexes, *Inorg. Chem.*, 2003, **42**, 1267-1271.
16. A. Dorcier, W. H. Ang, S. Bolano, L. Gonsalvi, L. Juillerat-Jeannerat, G. Laurency, M. Peruzzini, A. D. Phillips, F. Zanobini and P. J. Dyson, In vitro evaluation of rhodium and osmium RAPTA analogues: the case for organometallic anticancer drugs not based on ruthenium, *Organometallics*, 2006, **25**, 4090-4096.
17. F. Pruchnik and D. Dus, Properties of rhodium (II) complexes having cytostatic activity, *J. Inorg. Biochem.*, 1996, **61**, 55-61.
18. R. Głaszczka, J. Jaźwiński, B. Kamiński and M. Kamińska, Adducts of rhodium (II) tetraacylates with methionine and its derivatives: ^1H and ^{13}C nuclear magnetic resonance spectroscopy and chiral recognition, *Tetrahedron Asymmetry*, 2010, **21**, 2346-2355.
19. Ü. Laskay, C. Garino, Y. Tsybin, L. Salassa and A. Casini, Gold finger formation studied by high-resolution mass spectrometry and in silico methods, *Chem. Commun.*, 2015, **51**, 1612-1615.
20. A. Jacques, C. Lebrun, A. Casini, I. Kieffer, O. Proux, J. M. Latour and O. Sénéque, Reactivity of Cys₄ zinc finger domains with gold (III) complexes: insights into the formation of “gold fingers”. *Inorg. Chem.*, 2015, **54**, 4104-4113.
21. T. B. Pinter, G. W. Irvine and M. J. Stillman, Domain selection in metallothionein 1a: Affinity-controlled mechanisms of zinc binding and cadmium exchange, *Biochemistry*, 2015, **54**, 5006-5016.
22. K. L. Summers, D. E. Sutherland and M. J. Stillman, Single-domain metallothioneins: Evidence of the onset of clustered metal binding domains in Zn-rhMT 1a, *Biochemistry*, 2013, **52**, 2461-2471.

23. D. L. Wong and M. J. Stillman, Destructive interactions of dirhodium (II) tetraacetate with β metallothionein rh1a, *Chem. Commun.*, 2016, **52**, 5698-5701.
24. K. E. Rigby, J. Chan, J. Mackie and M. J. Stillman, Molecular dynamics study on the folding and metallation of the individual domains of metallothionein, *Proteins: Struct., Funct., Bioinf.*, 2006, **62**, 159-172.
25. M. T. Salgado, K. L. Bacher and M. J. Stillman, Probing structural changes in the α and β domains of copper-and silver-substituted metallothionein by emission spectroscopy and electrospray ionization mass spectrometry, *J. Biol. Inorg. Chem.*, 2007, **12**, 294-312.

Chapter 5

5 Metallothionein: an Aggressive Scavenger– The Metabolism of Rhodium(II) Tetraacetate ($\text{Rh}_2(\text{OAc})_4$)*

5.1 Heavy Metal Pollution from Anthropogenic Sources

With the turn of the millennium, sales of consumer products produced with xenobiotic metallic elements have increased globally. Examples of these metals are: Ti, Pb, Ni, and Sn in cosmetics,¹⁻⁶ Sn, Ni, and rare earth elements in electronic cigarettes,⁷⁻⁹ Cd in batteries, Hg in lamps, As in older microchips, and Platinum Group Metals (PGM's, Pd, Pt, Rh, Ru, Os, Ir) in jewelry , and widely in the automotive industry.¹⁰⁻¹³ In addition, occupational exposure and environmental pollution can occur as a direct result of metal mining and refining.^{14, 15} These metals have no known physiological role, and with multiple routes of exposure, pose an unknown and largely unavoidable risk to human health. In the case of metallotherapeutics incorporating a range of rare metals (e.g. Au, Ag, Pt, Pd, Rh, and others), humans are directly exposed to acute concentrations. This increase in mobilization of these rare metals results in widespread human exposure, spreading from concentrated points and diffusing across the globe.

The physiological response to these rare metals relies on the body's own protective response mechanisms to metals. Because of their nucleophilicity and metal scavenging ability, biological thiols like metallothioneins (MTs) and glutathione are involved in toxic metal resistance, whether directly or due to a downstream response triggered by metal exposure. Reports of these platinum group metals in urban environments and prevalence and accumulation in marine life near industrial runoff indicates the impending omnipresence and perturbation to daily life.^{16, 17} This may be reflected in the increased expression of MTs and the documented accumulation of PGMs initiated in a wide variety of marine, shellfish, seaweed and plant MTs, to changes in mineral environment. This metal accumulation in organisms can be used as a natural marker for environmental toxicity.¹⁸⁻²² Regardless, while the introduction of such foreign metals trigger an apparent defensive response, renal toxicity can still occur (e.g. Cd in MT, Itai-Itai disease). The long-term storage of Cd by MT in the kidneys raises the question about whether these

**A version of this chapter has been published:*

ACS Omega, 3(11), 16314-16327. (2018) Available with open access from the American Chemical Society, 2018.

Reproduced with permission from: D. L. Wong, and M. J. Stillman.

xenobiotic metals will follow this pathway and bioaccumulate. For instance, platinum levels persist in the blood of women many years after their anticancer treatment.²³

As a consequence of this growing threat, it is important to understand the reaction of MTs with metals that humans and the natural world are now becoming increasingly exposed to.

5.2 Exposure to Xenobiotic Metals from Therapeutics

Since the discovery of platinum based anti-cancer drugs, developed chemoresistance in certain cancer types has been associated with increased expression of MT.²⁴⁻²⁷ MTs can interfere with a chemotherapeutic agent before it can reach its desired target, or act in converse to its desired cytotoxic effect. Cellular thiols like glutathione and MT are correlated to expression in resistant cancers, although their direct causation to resistance is unclear. MT expression levels are affected by a variety of stress inducers^{18, 25, 27-37} including metal therapeutics, e.g. Au and Ag nanoparticles,³⁸⁻⁴⁰ and Pd, Pt, and Rh particles airborne through mining and industrial exposure.¹⁵ Cisplatin resistance and its relationship with MT's aggressive metal binding behavior is the focus of much research.⁴¹⁻⁴⁶ MTs are rich in highly reactive cysteine thiolates, which are suspected of being involved in the interference of platinum drugs. The many stress inducers of MT may easily cause upregulation of the protein following a dosage of platinum drugs. This trend has been identified by looking at MT mRNA expression and cellular MT levels in a variety of cisplatin resistant cell lines compared to their parent lines.^{24, 38, 45, 46} In medicine, new metallocomplexes show promising results in clinical trials, many of them consisting of PGMs and related metals.⁴⁷ This present study focuses on this new realm of "non-traditional metallation" to draw attention to the mechanism behind the metallation of xenobiotic metals to mammalian metallothioneins.

In this study, the global issue is the specific exposure of humans to a xenobiotic metal complex, where the clearest examples come from well-defined cytotoxic agents. The anti-tumor agent and common chemical catalyst dirhodium(II) tetraacetate ($\text{Rh}_2(\text{OAc})_4$) and its binding reactions to MT is the focus of the study described here.

5.3 Cytotoxic Dirhodium(II) Tetraacetate as a Model Metal Complex

The discovery of cisplatin in 1978 opened exploration of the cytotoxicity of metal-based complexes for cancer treatment.⁴⁸⁻⁵⁰ As described in Chapter 4, dirhodium(II) carboxylates are one of the classes of complexes of interest for their therapeutic and cytotoxic activity.⁵¹⁻⁵³ Similar to cisplatin, these dimeric compounds also cause disruption of DNA replication and transcription, as well as creating DNA adducts and crosslinking.⁵⁴⁻⁵⁸ Most notably, these anti-tumor dirhodium complexes irreversibly bind free cysteinyl thiols, inhibiting thiol-dependent enzymes.^{51, 53, 59} Unlike other amino acids, the reaction of cysteines with these rhodium complexes results in a breakdown of the carboxylate cage structure by thiolate replacement of the O donor ligands.^{52, 58} Their sensitivity to sulfur coordination from cysteines in biomolecular targets means rhodium(II) carboxylates can also act as radiosensitizers by depleting cellular thiol sources, lowering the cell's ability to respond to oxidative stress.^{59, 60} Current research has extended the applications of rhodium compounds to medical imaging, radioactive isotope therapy, photodynamic therapy, and protein labelling, but the significant antitumor characteristics of these rhodium complexes remain of great interest.^{59, 60}

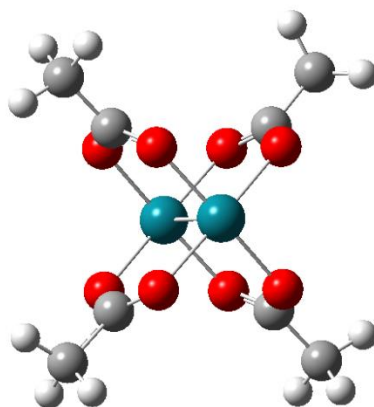


Figure 5-1 Ball-and-stick representation of $(\text{Rh}_2(\text{OAc})_4)$.

Teal represents Rh, red represents O, grey represents C, white represents H. Reproduced from D. L. Wong and M. J. Stillman. Copyright 2018 American Chemical Society.⁶¹

Dirhodium(II) tetraacetate ($\text{Rh}_2(\text{OAc})_4$), Figure 5-1, is the simplest of the dirhodium(II) carboxylates. $\text{Rh}_2(\text{OAc})_4$ is used widely as a synthetic catalyst in many organic reactions, a unique form of occupational exposure. It is used in many chemical synthesis reactions, such as catalysis of C-H, X-H insertion, and aromatic cycloaddition, with a relatively high solubility in aqueous solutions compared to Cu(II) acetate. $\text{Rh}_2(\text{OAc})_4$ and related dirhodium complexes have demonstrated significant anti-tumor activity; $\text{Rh}_2(\text{OAc})_4$ administered to mice dramatically decreased the size of tumors.⁵¹⁻⁵³ Tumor growth was inhibited by the interruption of DNA replication and protein transcription. Exhaled $^{14}\text{CO}_2$ from ^{14}C labelled $\text{Rh}_2(\text{OAc})_4$ indicated that the complex was decomposed within the organism. Urine analysis showed ~1% of the Rh was excreted, indicating that the remaining rhodium irreversibly bound to its target and accumulated. However, the exact target of $\text{Rh}_2(\text{OAc})_4$ activity is unknown, and toxic renal side effects were high.⁵¹⁻⁵³

Because these dirhodium(II) carboxylates are uniquely sensitive to cysteine binding, MT is a likely binding target. Another major cellular thiol, glutathione, was found to rapidly form adducts with $\text{Rh}_2(\text{OAc})_4$ both aerobically and anaerobically.^{62, 63} If cytotoxicity by $\text{Rh}_2(\text{OAc})_4$ involves DNA adduct formation, or inhibition of specific enzymes, then MT would be acting as a pre-target interference source. Alternatively, if the cytotoxicity involves the depletion of cellular thiols, then MT would be the desired target. This can provide beneficial information for the design of future chemotherapeutics.

5.4 Scope and Application of Results

To prepare for the inevitable increased exposure of humans to xenobiotic metal complexes from many sources, it is of vital importance to understand their physiological chemistry. For the success of metal-based chemotherapeutics, it is imperative to understand drug metabolism and resistance mechanisms. The strong correlation between cellular thiol induction and chemoresistance requires the study of the metal binding pathways to the key thiol molecules, especially ubiquitous metallothioneins. In this Chapter, the work from Chapter 4 is extended. The systematic and rapid deconstruction of the tetraacetate ligands in $\text{Rh}_2(\text{OAc})_4$, and the robust Rh_2 binding by the 20 cysteines in apo- $\beta\alpha\text{MT}$ is reported. The metallation speciation was modelled using semi-quantitative electrospray ionization mass spectrometry (ESI-MS) data to obtain relative K_f values. The

results and their impact on the cytotoxic and environmental effects of the bioconjugation of MT and dirhodium complexes are discussed.

5.5 Experimental Methods

Preparation of Apo-MT

Recombinant human metallothionein 1a (rh- β MT 1a, referred when used in this study as “MT” unless specified otherwise) was overexpressed with an S-tag in *Escherichia coli*.

The S-tag was removed and the MT purified according to previously described methods.^{64, 65} The cleaved construct has the sequence GSMGKAAAACSCATGGGCTCTGSKCKECKCNSCKKSCCSCCPMSCAKCAQGCVCKGASEKCSCCA KKA AAAA.

This construct contains two mutations when compared with the human MT 1A sequence archived on UniProt protein database, T27N and I51V. These mutations are commonly found in other mammalian MTs including other human isoforms (as seen in Chapter 1, Figure 1-5), and are not involved in metallation reactions of the cysteinyl thiolates.⁶⁶ The purified Cd-bound MT1a was demetallated by acidification (pH<2) and the resulting free Cd(II) in solution were removed by centrifugal filtration (Amicon Ultra-4 3000 Da MWCO). Protein concentration was calculated by remetallating a measured aliquot with CdSO₄ and determining the A_{\max} at the 250 nm shoulder characteristic of the LMCT band of Cd-S bonds ($\epsilon = 89,000 \text{ L mol}^{-1} \text{ cm}^{-1}$).⁶⁷

UV-visible absorption and circular dichroism spectroscopy

UV-visible absorption and circular dichroism (CD) spectral data were acquired on a Cary UV Bio50 and JASCO J-810 Spectropolarimeter, respectively. Solutions were evacuated and backfilled with Ar gas prior to data collection, and measured in a sealed, 1 cm x 1 cm quartz cuvette.

ESI-MS Studies

Solutions of Rh₂(OAc)₄ (Sigma Aldrich) were prepared in deoxygenated, argon aerated, DI water. Aliquots containing known molar equivalents were added to the apo-MT solution immediately prior to mass spectral data acquisition using a MicroTOF II (Bruker

Daltonics, Toronto). All solutions were at room temperature and thoroughly deaerated using vacuum evacuation followed by Ar saturation. NaI was used as the calibrant. Spectra were collected in positive ion mode, as a function of time following mixing. The settings used are described in Chapter 1. The averaged spectra and data analysis were carried out using the Maximum Entropy application in Bruker Data Analysis 4.2 program. The resulting spectral data were normalized and the dominant species identified by mass.

Cysteine Modification by p-benzoquinone and n-ethyl maleimide

10 mM stock solutions of p-benzoquinone (pBQ) and N-ethyl maleimide (NEM) were dissolved in 10% v/v methanol in water and the solution vials wrapped in aluminum foil to protect from photochemical degradation. Aliquots of the modifiers were added to protein samples containing Rh₂, Rh₄, and Rh₆MT, and mass spectral data of the resulting products were obtained to identify the species present. The modifier was titrated to excess, until the mass spectra no longer changed between additions.

Molecular Dynamics Models of Rh₂MT, Rh₄MT, and Rh₆MT Structures

Molecular modelling calculations were carried out using Scigress Version 6.0.0 (Fujitsu Poland Ltd.). Structures, modelling parameters and sequence information were adapted from previously reported Cd₇MT and As₆MT models to build the Rh₂MT models.^{64, 68, 69} In brief, the Cd(II) ions were deleted and replaced with Rh(II) prior to Molecular Mechanics calculations (MM3). Molecular Dynamics calculations were carried out at 300 K for 500 ps using the dielectric constant for water of 78.5. Metal thiolate structures in the alpha domain were based on bridging thiol arrangements in Cd₇MT.

Methodology

Spectroscopic and mass spectral studies provide the identity of the binding moiety and detailed speciation data. The mass spectral data were simulated computationally to determine the stepwise equilibrium constants. Cysteine modification was used initially to determine the metallation stoichiometry by quantifying the number of cysteines not involved in binding the Rh₂(OAc)₄. However, these results directed the research focus towards understanding the protein structural changes in metallation, using molecular

dynamics modelling and mass spectral titrations under unfolded conditions. Altogether, these experiments fully document the metallation process by which xenobiotic dirhodium(II) tetraacetate is accumulated by MT.

5.6 Results

5.6.1 Metallation Reactions of MT with $\text{Rh}_2(\text{OAc})_4$: Optical Spectroscopic Properties

Figure 5-2, top, shows the UV-visible absorption spectral data for the titration of apo-MT with increasing mole equivalents of $\text{Rh}_2(\text{OAc})_4$ added. Significantly, the UV-visible absorption data show an increased absorption at ~ 300 nm, corresponding to the well-known cysteine $\text{S} \rightarrow \text{Rh}$ LMCT band. Similar absorption is also observed with glutathione, cysteine, methionine, and other biological thiols.^{62, 63, 70-74} This LMCT band is very strong and the transition from the blue of the metal solution to the yellow of the protein-bound product can be followed readily with the naked eye.

The CD spectra in Figure 5-2, bottom, shows the titration of increasing mol. eq. of $\text{Rh}_2(\text{OAc})_4$. The apo-MT spectra is shown in blue. Unlike the UV-visible absorption spectra, there is no significant change in the spectra with increasing $\text{Rh}_2(\text{OAc})_4$.

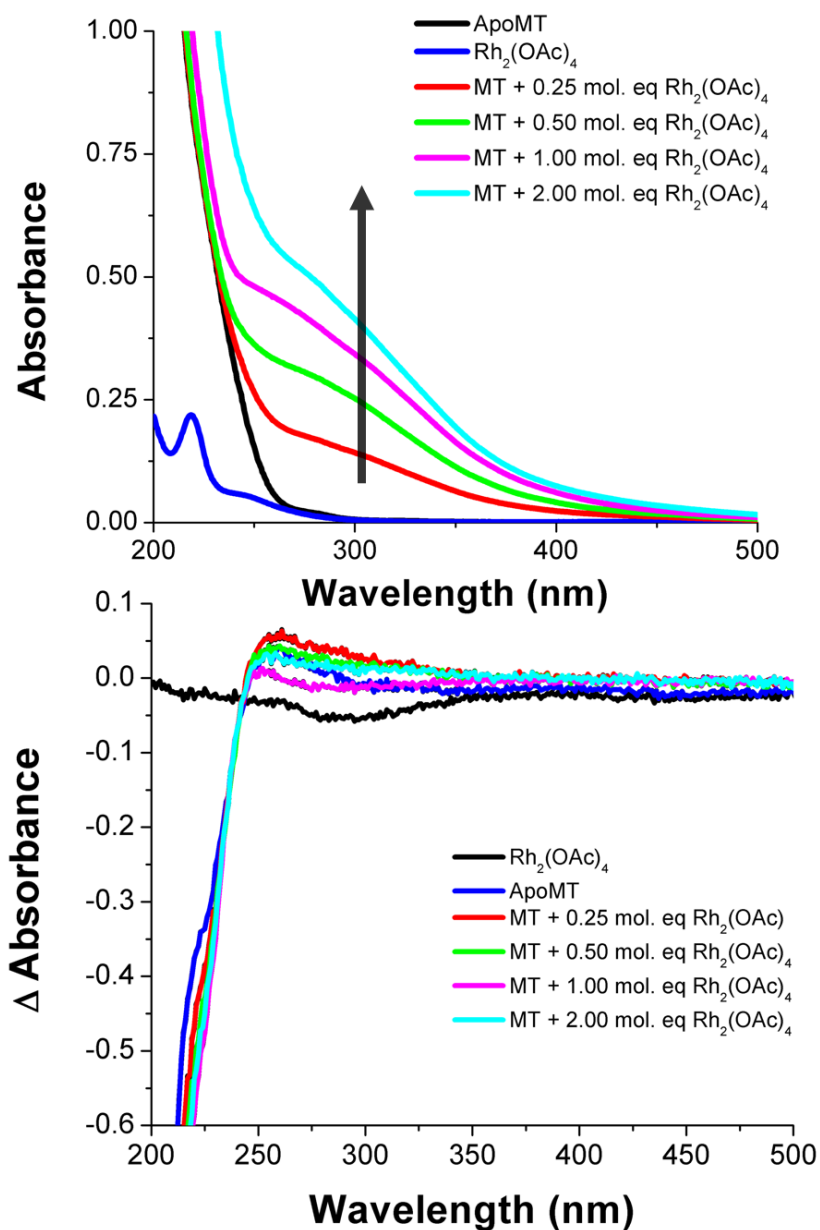


Figure 5-2 Spectroscopic results of the Rh₂(OAc)₄ into MT titration

UV-visible absorption (top) and circular dichroism (bottom) spectra for a titration with increasing molar equivalents of Rh₂(OAc)₄. The arrow indicates the direction of increased [Rh₂(OAc)₄]. The S→Rh LMCT band increases in absorbance at ca. 300 nm. Reproduced from D. L. Wong and M. J. Stillman. Copyright 2018 American Chemical Society.⁶¹

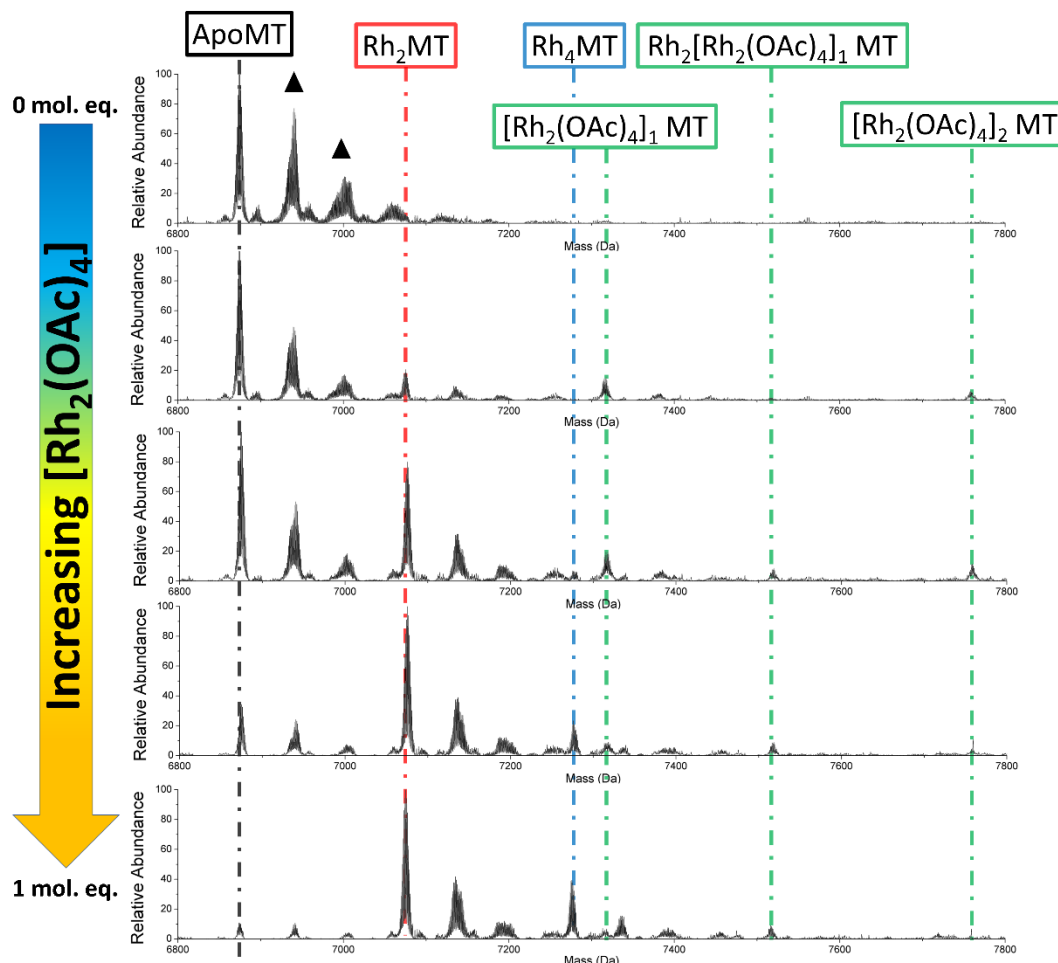


Figure 5-3 Initial deconstruction of $\text{Rh}_2(\text{OAc})_4$ by apo-MT observed with ESI – MS. Stepwise addition of 0.0 to 1.0 mol. eq. of $\text{Rh}_2(\text{OAc})_4$ to apo-MT. Major species are indicated by dashed lines: black for apo-MT, red for Rh_2MT , blue for Rh_4MT and green for species bound to at least one complete $\text{Rh}_2(\text{OAc})_4$ molecule. Carboxymethylated MT species are mass shifted by $\sim 60\text{Da}$ and are represented with a triangle. Reproduced from D. L. Wong and M. J. Stillman. Copyright 2018 American Chemical Society.⁶¹

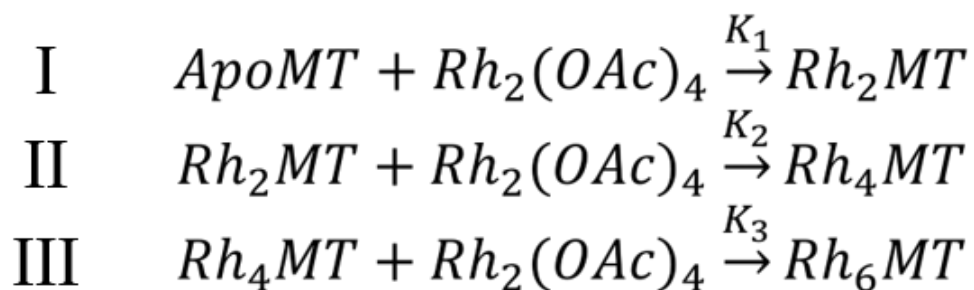
5.6.2 Initial Deconstruction of $\text{Rh}_2(\text{OAc})_4$ by Apo-MT: Rapid Displacement of the Tetraacetate Ligands

Figure 5-3 shows a series of ESI-mass spectra as a function of increasing molar ratio of $\text{Rh}_2(\text{OAc})_4$:MT (from 0 to 1 mol. eq.). The data shown in Figure 5-3 provide a snapshot of speciation at very low molar ratios during the early stages of apo-MT (6875 Da)

metallation. As previously demonstrated with cisplatin,⁷⁵ the apo-MT rapidly (within the dead time of the instrument) engulfs the incoming Rh₂(OAc)₄ molecule (441.99 Da), then systematically shreds the ligands from the metal complex until only the Rh-Rh core is sequestered within its thiolate binding site. The mass spectral data show the presence of the incoming complete complex, and the final isolated Rh₂ core bound to the MT. The protein species with masses of 7316, 7517, and 7758 Da are representative of Rh₂(OAc)₄-MT, Rh₂(Rh₂(OAc)₄)-MT, and (Rh₂(OAc)₄)₂-MT, respectively. These dominant masses gradually diminish as the reaction inside the MT proceeds, until the masses of the final products of Rh₂MT and Rh₄MT, at 7074 and 7273 Da, respectively, dominate. The change in mass coincides with the mass differences between the lost acetate moieties from the Rh₂(OAc)₄ bound protein species, where each acetate group has a mass of 59.04 Da.

5.6.3 Accumulation of Rh₂: Formation of Rh₂MT, Rh₄MT, and Rh₆MT

The formation of Rh₂-metallated MT products can be described by three stepwise bimolecular reactions, as shown in Scheme 5-1. Each metallation event begins with encapsulation of the whole molecule, followed by rapid deconstruction of the ligand structure to the dirhodium core. The metallation continues with formation of the ligand-stripped Rh₄MT (7273 Da) and Rh₆MT (7473 Da). Figure 5-4 shows a series of stepwise metallation reactions as from 0.0 - 2.0 mol. eq. of Rh₂(OAc)₄ were added to apo-MT under equilibrium binding conditions. The major product of the reaction is Rh₄MT, which forms rapidly, with a small amount of Rh₆MT.



Scheme 5-1 Proposed bimolecular, stepwise metallation reactions for Rh₂(OAc)₄ binding to apo-MT.

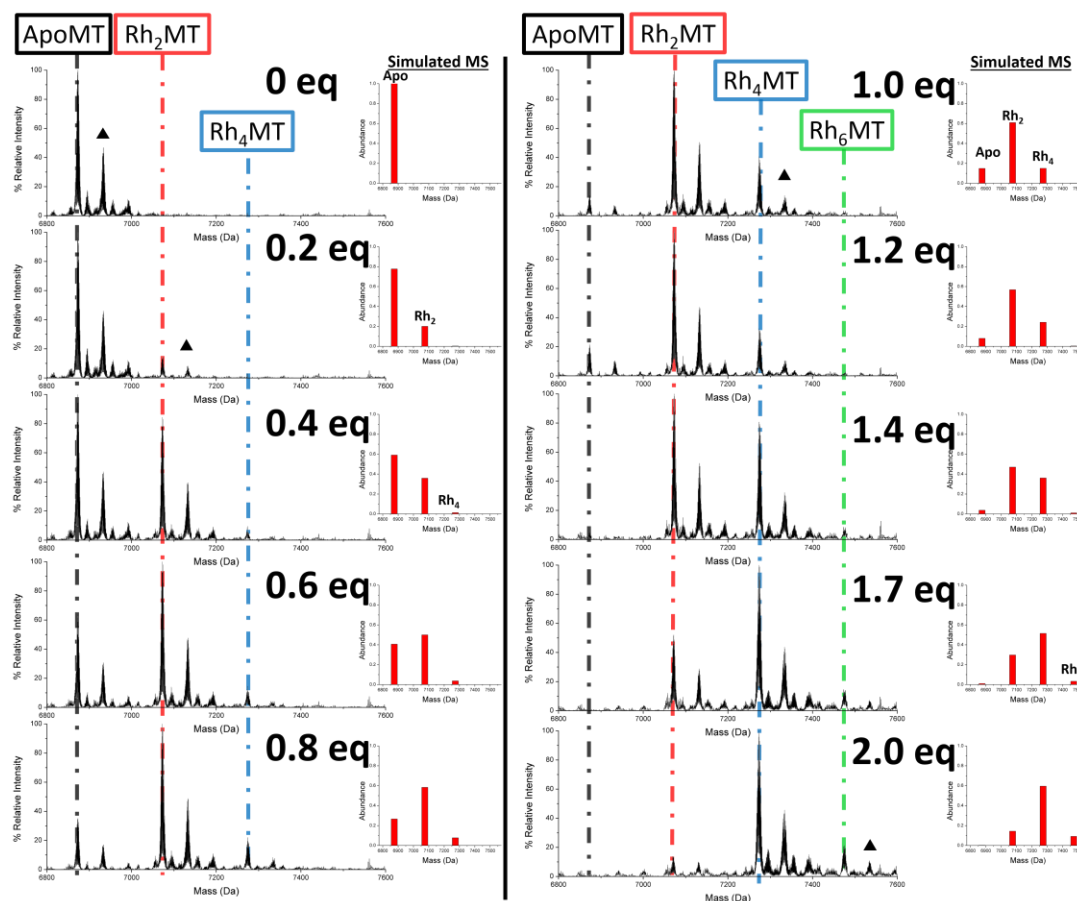


Figure 5-4 ESI mass spectral data recorded during the titration of apo-MT with aliquots 0.0 to 2.0 mol. eq. $\text{Rh}_2(\text{OAc})_4$.

The major species are indicated by dashed lines: black for apo-MT; red for Rh_2MT ; blue for Rh_4MT ; and green for Rh_6MT . The inset bar graphs on the right of each spectra shows simulated mass spectral data based on the model described in Figure 5-5, using K_f values in Table 5-1. Carboxymethylated MT species are mass shifted by ~ 60 Da and are represented with a triangle and are not included in the simulation. Reproduced from D. L. Wong and M. J. Stillman. Copyright 2018 American Chemical Society.⁶¹

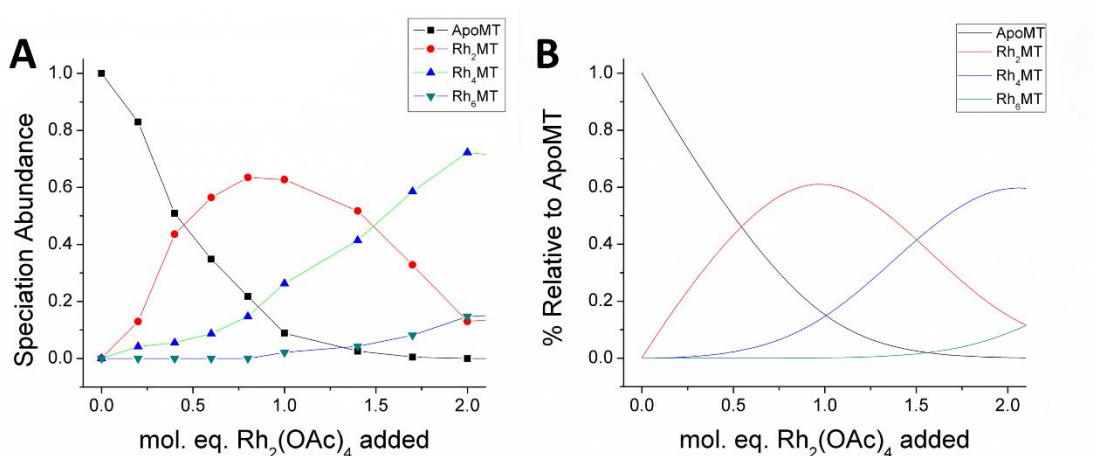


Figure 5-5 Experimental and simulated speciation abundance

Experimental mass spectral speciation abundance data (A, left) and simulated data (B, right) calculated from the fitted relative K_f values (Table 1). Reproduced from D. L. Wong and M. J. Stillman. Copyright 2018 American Chemical Society.⁶¹

5.6.4 Modeling the Reaction: Determination of Relative Binding Constants (K_f)

Using the Hyperquad Simulation Speciation (HYSS)⁷⁵ software, the mass spectral abundances associated with these reactions were modelled based on the concentrations and mole equivalences of the $\text{Rh}_2(\text{OAc})_4$ added, using the equations in Scheme 5-1. The three relative K values (shown in Table 5-1) were calculated so that the simulated model matched the experimental data, Figure 5-4. The calculated abundances were used to simulate the mass spectra as seen in the red bar graph Figure 5-4 insets. The simulated mass spectra closely match the experimental MS data over the course of the titration.

Figure 5-5A shows the experimental speciation data extracted from Figure 5-4. The sequence of speciation clearly follows a typical non-cooperative metallation mechanism⁷⁶ in which Rh_2MT forms, followed by Rh_4MT , followed by Rh_6MT . The fitted results, in Figure 5-5B, match the experimental data closely, and provide the relative binding constants as shown in Table 5-1.

Table 5-1 Relative equilibrium binding constants for the reaction of $\text{Rh}_2(\text{OAc})_4$ with Apo-MT

$\text{MT}(\text{Rh}_2)_n$	Log β	Log K_f
1	4.22	4.22
2	7.22	3.00
3	8.89	1.67

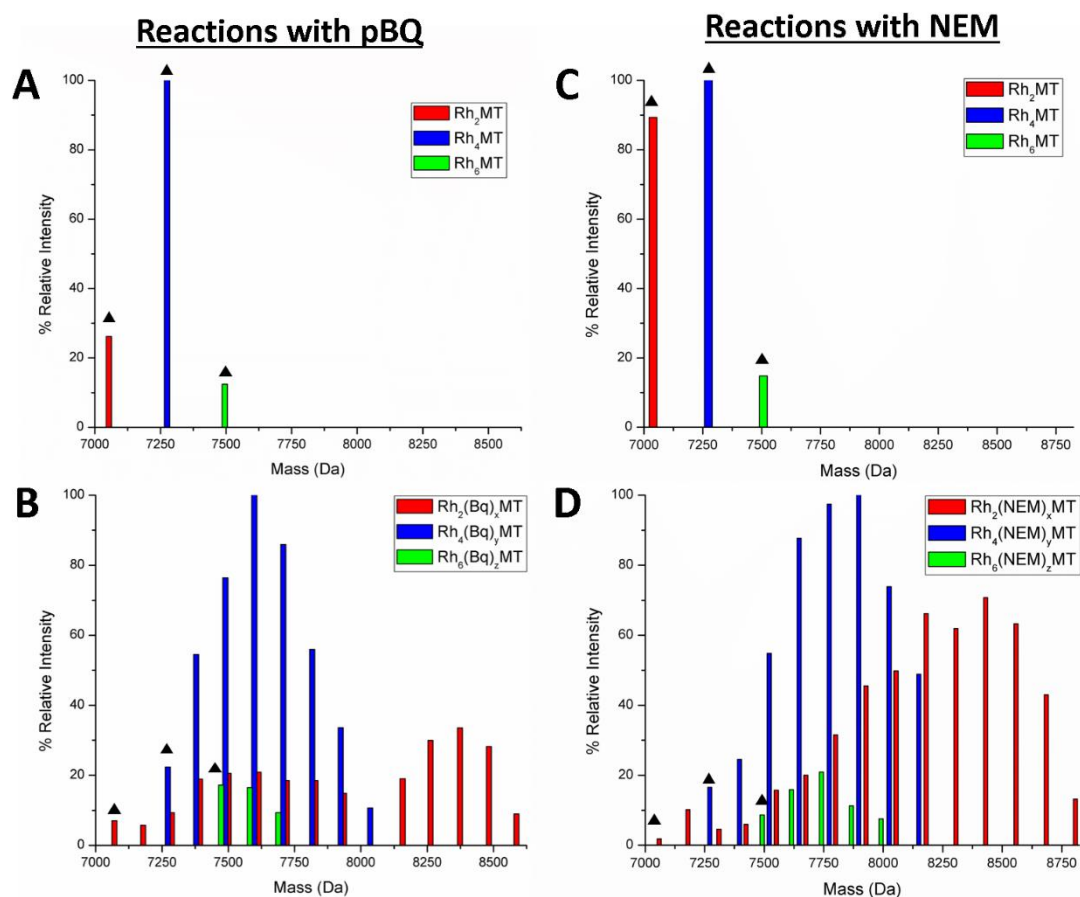


Figure 5-6 ESI-mass spectral data of modified and unmodified mixed Rh_2 metallated species

(A): non-modified Rh_2 -, Rh_4 -, and Rh_6 -MT, represented by a triangle. (B): solution in (A) following addition of p-BQ. (C): non-modified Rh_2 -, Rh_4 -, and Rh_6 -MT, represented by a triangle. (D): solution in C following addition of NEM. The experimental data are shown in bar graph representation. Persistent titrations to excess and long incubation times did not affect the resulting spectra indicating completed reaction. Rh_2MT species shown in red, Rh_4MT species in blue, and Rh_6MT species in green. Reproduced from D. L. Wong and M. J. Stillman. Copyright 2018 American Chemical Society.⁶¹

The data in Figure 5-6 show modification of MT containing Rh₂MT, Rh₄MT, and Rh₆MT by both pBQ (Figure 5-6, A, B, left half) and NEM (Figure 5-6, right half). The Rh₂MT, Rh₄MT, and Rh₆MT spectra measured prior to modification are shown in Figure 5-6, top (A and C). In B and D, these same species are present (identified by triangles) even though excess modifier was added. Both sets of modified species (Figure 5-6, lower) display a variety of Normal distributed species, as shown in Figure 5-6 in bar graph format. The experimental mass spectral data is shown below in Figure 5-7, but is represented in bar graph format in Figure 5-6 for clarity.

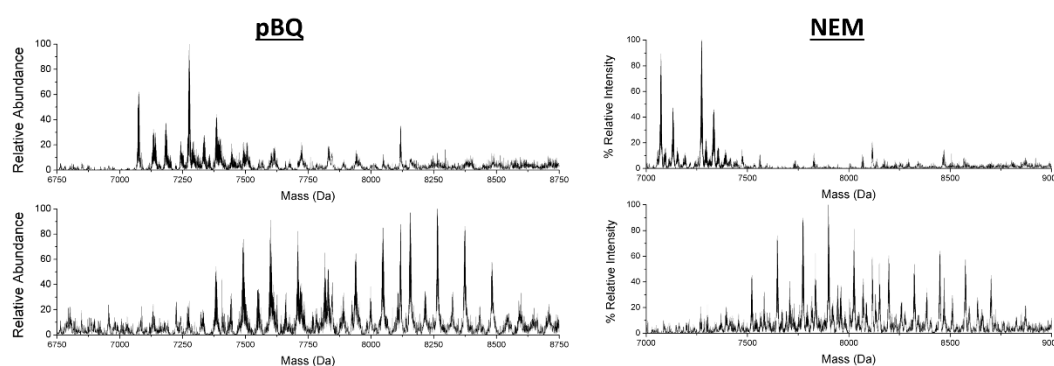


Figure 5-7 Mass spectral data of the alkylation of Rh₂-bound MT

ESI Mass spectral data collected for a mixture containing Rh₂MT, Rh₄MT, and Rh₆MT (top left and top right) and their subsequent modification by pBQ (bottom left) and NEM (bottom right). Reproduced from D. L. Wong and M. J. Stillman. Copyright 2018 American Chemical Society.⁶¹

As described by Irvine et al, cysteine accessibility can be understood by the distribution of cysteine modified species.⁷⁷ A Normal distribution represents statistically equal accessibility of the modifier to all available free cysteines. This means that the unbound cysteines are exposed. Therefore, the breadth or spread of the distribution tells us the number of available cysteines, and the shape of the distribution tells us if there is conformation specificity or equal accessibility of the free thiols. Figure 5-6B shows the distribution of the modified Rh₂(BQ)_xMT species (red bars). The data indicate the presence of two species, one with $x = 0-8$ free cysteines, and another with $x = 10-15$ free cysteines. This means that there are two distinct Rh₂MT products: one coordinating the Rh₂ with 12 cysteines, and the other coordinating the Rh₂ with 5 cysteines. This is harder

to distinguish at increased concentrations as the abundancies of the two distributions overlap each other, Figure 5-6D. The steep rise of the modified $\text{Rh}_4(\text{BQ})_y\text{MT}$ (blue) also displays a Normal distribution with $y = 0-7$ free cysteines. The formation of a modified $\text{Rh}_6(\text{BQ})_z\text{MT}$ species with $z = 0-4$ free cysteines also can be observed (green).

There is a small discrepancy between the number of modified cysteines observed using pBQ and NEM. This is likely due to the reaction occurring at physiological pH, at which pBQ is not as effective as NEM.⁷⁸ Therefore, our conclusions about the number of free cysteines for the metallated MT is based on the greatest number of NEM-modified cysteines for each Rh-bound complex.

5.6.5 Accumulation of $\text{Rh}_2(\text{OAc})_4$ in αMT : Evidence for Structure-Dependent Metallation

Figure 5-8 shows the time-dependent metallation of the single domain apo- αMT fragment at low pH (<2) with $\text{Rh}_2(\text{OAc})_4$. Over the time course of the reaction (44 minutes), species ranging from $[\text{Rh}_2(\text{OAc})_4]_1\text{-MT}$ to $[\text{Rh}_2(\text{OAc})_4]_6\text{-MT}$ are observed. This is completely different when compared with the results from the titration carried out at pH 7.4 with the two-domain protein (Figure 5-4).

These data show that the unfolded, loose structure caused by the high $[\text{H}^+]$ greatly increases cysteine accessibility to the incoming $\text{Rh}_2(\text{OAc})_4$ in this single domain fragment. In the presence of excess $\text{Rh}_2(\text{OAc})_4$, this manifests as two distinct reaction pathways: i) ligand replacement by thiolates following $\text{Rh}_2(\text{OAc})_4$ binding, as described for the whole protein above, and ii) proposed axial coordination of $\text{Rh}_2(\text{OAc})_4$ by cysteine. These two reaction pathways are outlined in Figure 5-8, right. The acidic conditions minimize the nucleophilicity of the cysteinyl thiols, and allow for the lower Cys:metal ratios to bind with metal ratios of up to 6 x $\text{Rh}_2(\text{OAc})_4$. Despite the observation of this “supermetallation,” the cysteine replacement of the tetraacetates still occurs albeit slower than at physiological pH.

In Figure 5-8, the key species identified are: apo- αMT , $[\text{Rh}_2(\text{OAc})_4]_1\text{-}\alpha\text{MT}$, $[\text{Rh}_2(\text{OAc})_4]_2\text{-}\alpha\text{MT}$, $[\text{Rh}_2(\text{OAc})_4]_3\text{-}\alpha\text{MT}$, $[\text{Rh}_2(\text{OAc})_4]_4\text{-}\alpha\text{MT}$, $[\text{Rh}_2(\text{OAc})_4]_5\text{-}\alpha\text{MT}$,

$[\text{Rh}_2(\text{OAc})_4]_6\text{-}\alpha\text{MT}$, $\text{Rh}_2[\text{Rh}_2(\text{OAc})_4]_1\text{-}\alpha\text{MT}$, $\text{Rh}_2[\text{Rh}_2(\text{OAc})_4]_2\text{-}\alpha\text{MT}$, $\text{Rh}_2[\text{Rh}_2(\text{OAc})_4]_3\text{-}\alpha\text{MT}$, $\text{Rh}_2[\text{Rh}_2(\text{OAc})_4]_4\text{-}\alpha\text{MT}$, $\text{Rh}_2[\text{Rh}_2(\text{OAc})_4]_5\text{-}\alpha\text{MT}$, Rh_2MT , and Rh_4MT .

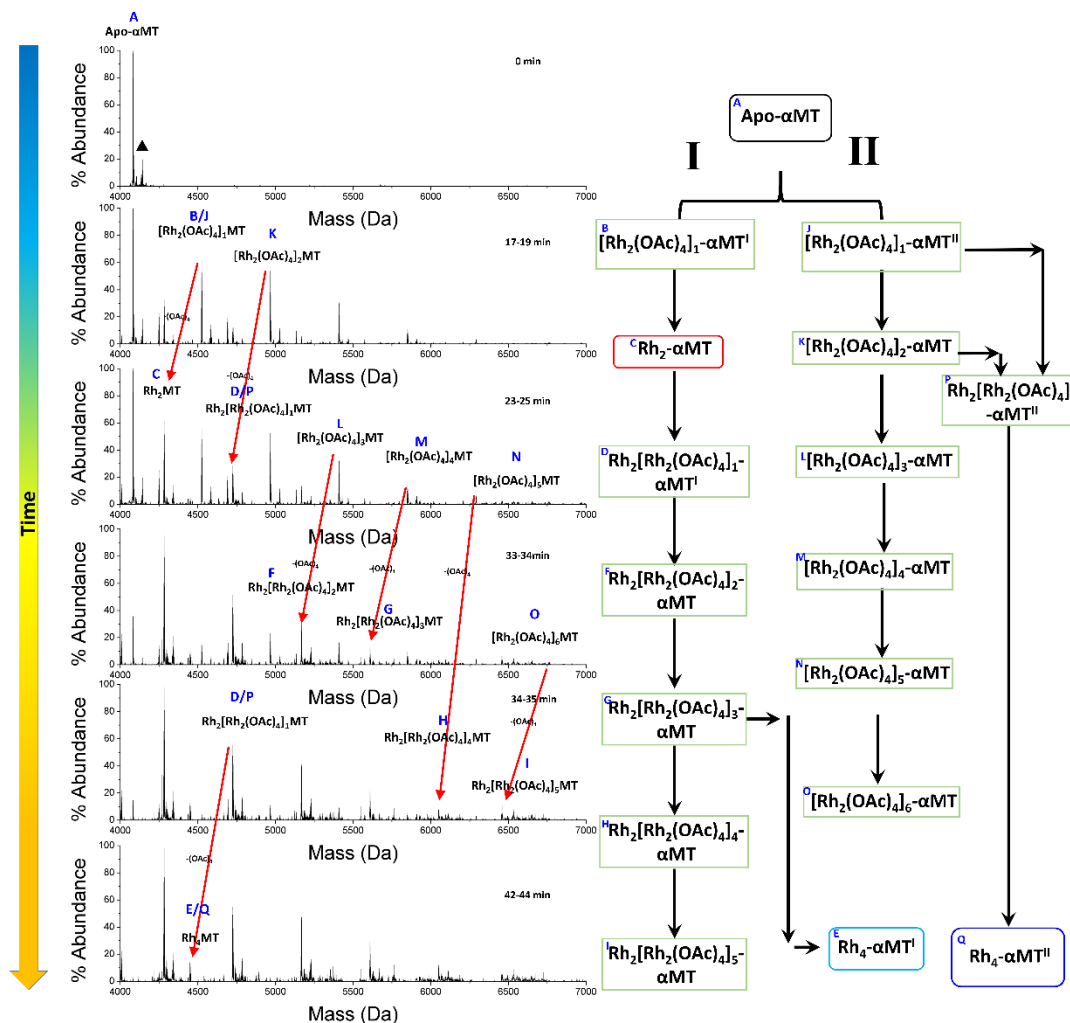


Figure 5-8 ESI mass spectral data of the low pH titration of $\text{Rh}_2(\text{OAc})_4$ into αMT
 (Left) Time-dependent mass spectral data of apo- αMT at low pH (<2), recorded over 44 minutes following addition excess $\text{Rh}_2(\text{OAc})_4$. Red arrows indicate mass shift resulting from the loss of $(\text{OAc})_4$. (Right) Labels for identifiable species in the mass spectral data and proposed formation pathways. Reproduced from D. L. Wong and M. J. Stillman. Copyright 2018 American Chemical Society.⁶¹

5.6.6 3D Models: Cysteine Accessibility throughout Metallation

Representative structures of apo-MT, Rh₂MT, Rh₄MT, and Rh₆MT are shown in Figure 5-9. Energy minimized geometries using MD for apo-MT, Rh₂MT, Rh₄MT, and Rh₆MT were constructed in Scigress 6.0.0 and geometry optimized using Molecular Mechanics (MM3) prior to Molecular Dynamics (MD) calculations at 300 K for 500 ps. These structures are shown in ball and stick format in Figure 5-9 and in full page format along with H-bond mapping in Appendix C.

The apo-MT model, Figure 5-9A, shows the structure of the non-metallated cysteines, and how MT orients itself with respect to metallation. The energy minimization of apo-MT results in a compact globular structure, in accordance with mass spectral studies at physiological pH.⁷⁹ The cysteine residues (-SH shown with yellow spheres in Figure 5-9) are oriented to the exterior when metal-free, but coalesce toward the interior of the protein when metal-bound. In the apo-MT structure, the backbone and cysteines arrange themselves in a similar fashion to a helix, with cysteines facing outward. This agrees with results from Irvine et al. and Rigby et al. that the cysteine solvent accessibility in the apo form facilitates metal binding.⁸⁰⁻⁸² The driving force for organized structural formation in mammalian metallothioneins is the metal-induced folding with each sequential M-SCYS chelation event.⁸⁰ Once bound to a metal, these cysteines become buried within the protein interior, shielding them from the cellular environment. The fully bound Rh₆MT (Figure 5-9H, "Rh_{2β4α}MT") shows this clearly. The configuration of the peptide backbone shows that MT wraps around the metal core upon binding. This effect is observed in the partially metallated Rh₂MT and Rh₄MT structures as well, in Figure 5-9. When the Rh₂ is bound to cysteines that nominally form a single domain (Figure 5-9, Rh_{2β}MT, Rh_{2α}MTI, Rh_{2α}MTII, Rh_{4α}MT), the metal-bound cysteines are buried, while the remaining metal-free cysteine maintain their external orientation. This reflects the globular protein structure seen in the apo-MT model, Figure 5-9A. However, these one-domain-bound MTs are fluxional and capable of further subsequent metallation. In contrast, for two-domain metal binding, like in the Rh_{2β2α}MTI, Rh_{2β2α}MTII, and Rh₆MT, a dumb-bell-like structure typical of M(II) ion metallation is obtained.⁸³ When both domains are bound, the

cysteine accessibility is greatly diminished. This accounts for the lower abundance of the Rh₆MT species in the mass spectral data.

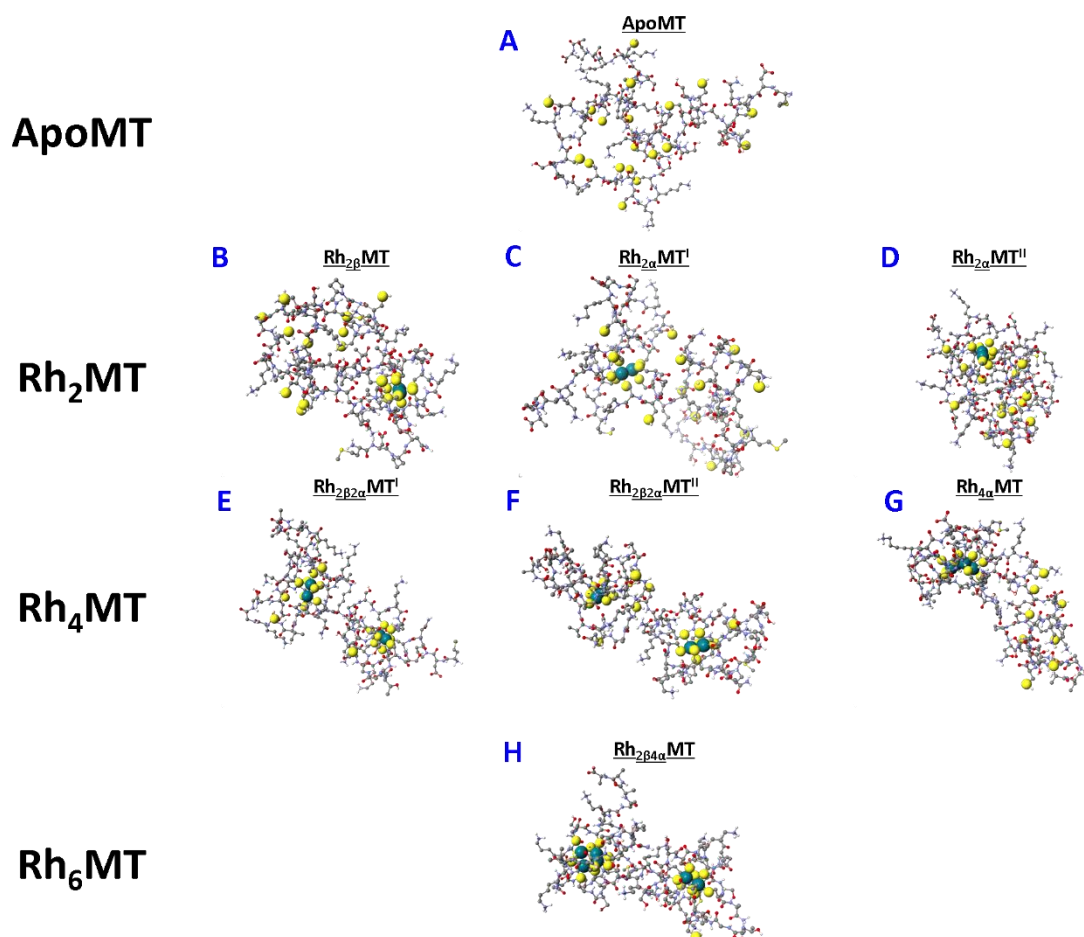


Figure 5-9 Energy minimized molecular dynamics models of apo-MT, Rh₂MT, Rh₄MT, and Rh₆MT.

Rh shown enlarged in teal, cysteines shown enlarged in yellow, C in gray, O in red, N in blue, H in white. Structures were constructed based on Cd₇MT structures from previously reports,^{10, 64, 68} using Scigress 6.0.0.⁸⁴ Details of the minimization are given in the text. Reproduced from D. L. Wong and M. J. Stillman. Copyright 2018 American Chemical Society.⁶¹

5.7 Discussion

5.7.1 Chronic Presence of Anthropogenic Pt, Pd, Rh (PGM's)

Platinum group metals have no biological role, and little is known about their long-term toxicity. Pd and Rh are naturally found alongside metallic Pt, therefore, their contamination is often mobilized by the same routes. With the use of these metals in catalytic converters in automobiles (to reduce volatile organic components), airborne PGM particulate is becoming a widespread route of exposure. Higher concentrations of these PGM's are related to higher traffic density.^{10, 13, 23, 85} Spreading from urban areas and carried by the winds, fine metal particulate (< 10 nm) enter the soil, water, and food chain, often being converted into inorganic complexes through ingestion, inhalation, or absorption through damaged skin.^{11, 13, 16, 86-90} Bacterial, organismal, and environmental transformations can convert inert metal species into reactive ones. With the number of automotive vehicles ever increasing, the biofixation of these metals makes them more bioavailable than ever before. The accumulation and biological effects of subclinical levels of these PGM's (in public areas like playgrounds, tramways, narrow streets) particularly in cities with dense populations and heavy traffic are of a concern for the future.^{10, 12, 13}

There are already several examples of anthropogenic PGMs affecting waterways and corresponding ecosystems near urban regions, detectable in Arctic ice cores, with documented metal levels increasing over several decades.⁸⁸⁻⁹² Varying soil and water conditions, such as pH, N and S availability, and temperature and precipitation levels can affect metal solubility, thereby accelerating permeation through the food chain.⁹³ Bacterial resistance and introduction of metals into the food chain results by biomethylation.⁹⁴ The Hg cycle, for example, causes bioaccumulation in fish and shellfish species, which magnifies through larger predators.⁹⁵

The cytotoxicity of these metals has been demonstrated in current and potential cancer metallodrugs, showing the danger of exposure in the form of their side effects. Although the long-term effects of sub-clinical levels of exposure are relatively unknown, it is concerning especially for vulnerable populations, like children.⁹⁶ These soft, heavy metals

are more likely to be accumulated by coordination with biological thiols and exhibit long biological half times, increasing the risk of nephrotoxicity. While other lighter or physiologically essential metals are recycled or excreted through the urine rapidly, heavy metals like Pt, and Cd can remain in the body for decades.

5.7.2 Binding Reactions of MT with Rh₂(OAc)₄: Explaining the Spectroscopic Results

As expected, the replacement of the acetate groups with cysteine thiols resulted in a strong absorbance at ~ 300 nm (Figure 5-2, top). This agrees with other spectroscopic studies involving biological thiols (cys, GSH for e.g.^{62, 63, 72-74, 97, 98}) and confirms the cysteine thiol as the binding moiety involved in the Rh₂ complexation.

In the case of the CD spectral data (Figure 5-2, bottom), it is surprising that no significant spectral intensities are observed during the titration of the full apo-MT. However, the lack of a distinct CD spectral intensity is likely due to the overlap from the presence of several structurally different species because the mass spectral and structural cysteine modification data indicate that the Rh₂(OAc)₄ has bound to the apo-MT. This contrast the results previously reported for Rh₂(OAc)₄ binding to the β-domain fragment, in which a single product is formed in a 1:1 fashion, producing a strong CD signal, as seen in Chapter 4.⁷⁰

5.7.3 Metallothionein: Non-Traditional Metallation and Metal Complex Deconstruction is Evident from the Mass Spectra

Mass spectrometry is especially helpful in identifying biological targets.⁹⁹ ESI-MS is a soft ionizing, high resolution, solution-phase technique that is ideally suited for tracking the metallation status of MT. The advantage of using ESI-MS is that it allows for confirmation of the presence of intermediate states in real time. These versatile properties have been widely exploited in Native ESI-MS,¹⁰⁰ allowing detailed kinetic and equilibrium studies of the metallation of MTs.^{65, 70, 76, 83, 100-109} The stoichiometric and structural information provided by the ESI method is particularly important for MT because the lack of typical protein features and its high sensitivity to oxidation makes

MT's protein structure difficult to observe with crystallography, NMR, or other structure elucidating methods.

The conditions for cooperative and non-cooperative bimolecular metallation of Zn(II), Cd(II), and Cu(I) to MT have been studied with consistent stoichiometric ratios identified primarily using ESI-MS, including traditional metallation to form stable cluster states $M(I)_6S_9$, $M(II)_3S_9$, $M(II)_4S_{11}$.^{65, 76, 83, 102-104, 110, 111} Binding coefficients can be accurately extracted from these data. The observed kinetic binding of Pt(II)₁₋₇ from cisplatin was first determined by chromatographic methods,¹¹² which were then enhanced by our ESI-MS modelling methods,⁴¹ a similar methodology to that applied to this current dirhodium study.

The metallation of Rh₂(OAc)₄ to apo-MT can be categorized as non-traditional metallation, because the binding of MT involves chelating Rh₂(OAc)₄ followed by disassembly of the initial metal complex by displacement of the original coordinated ligands. ESI-MS has been used to observe this destructive effect MT has with cisplatin, and Ru-based arene complexes⁴¹ This step-wise, sequential deconstruction of Rh₂(OAc)₄ has been reported previously with the single apo-β-domain fragment of MT1a. Under those conditions, one discernible product (Rh₂MT) is formed in a linear fashion.⁷⁰ In this present ESI-MS study, the full, two-domain protein has a higher sulfur availability (20 cysteines), which greatly increases the rate of reaction and the number of possible conformers (Rh₂MT, Rh₄MT, Rh₆MT) that can form. The ligand loss of the coordinating acetates and accumulation of the sequestered metal species shows that Rh₂(OAc)₄ does not survive intact when bound to MT. This emphasizes the destructive effect MTs can have on both chemotherapeutically related complexes and xenobiotic metals from environmental sources.

The presence of metal-thiolate (Zn(II), Cd(II), Cu(I)) clusters that form in higher ratios of these metals make MTs resistant to trypsin digestion.¹⁰⁵ However, it should be noted that As(III) binding is not considered to involve cluster formation. The As(III) bound to the isolated MT fragments form $M(III)_3S_9$ (α-domain), and $M(III)_3S_9$ (β-domain), and to the full protein forms $M(III)_6S_{18}$,¹¹¹ which means that the MT peptide flexibly accommodates a completely different style of binding than reported for the Group 12 M(II) ions. The

results of this Chapter show Rh₂ binding also does not follow traditional cluster formation of Zn(II), Cd(II), and Cu(I), instead binding to MT in a rigid manner. MT is unable to perform its usual metal relocation, as described in Chart 5-1. Therefore, a novel MT binding mode is now reported for Rh₂ in this study, which enforces the difference between the metallation of complexes and metal ions by the protein.

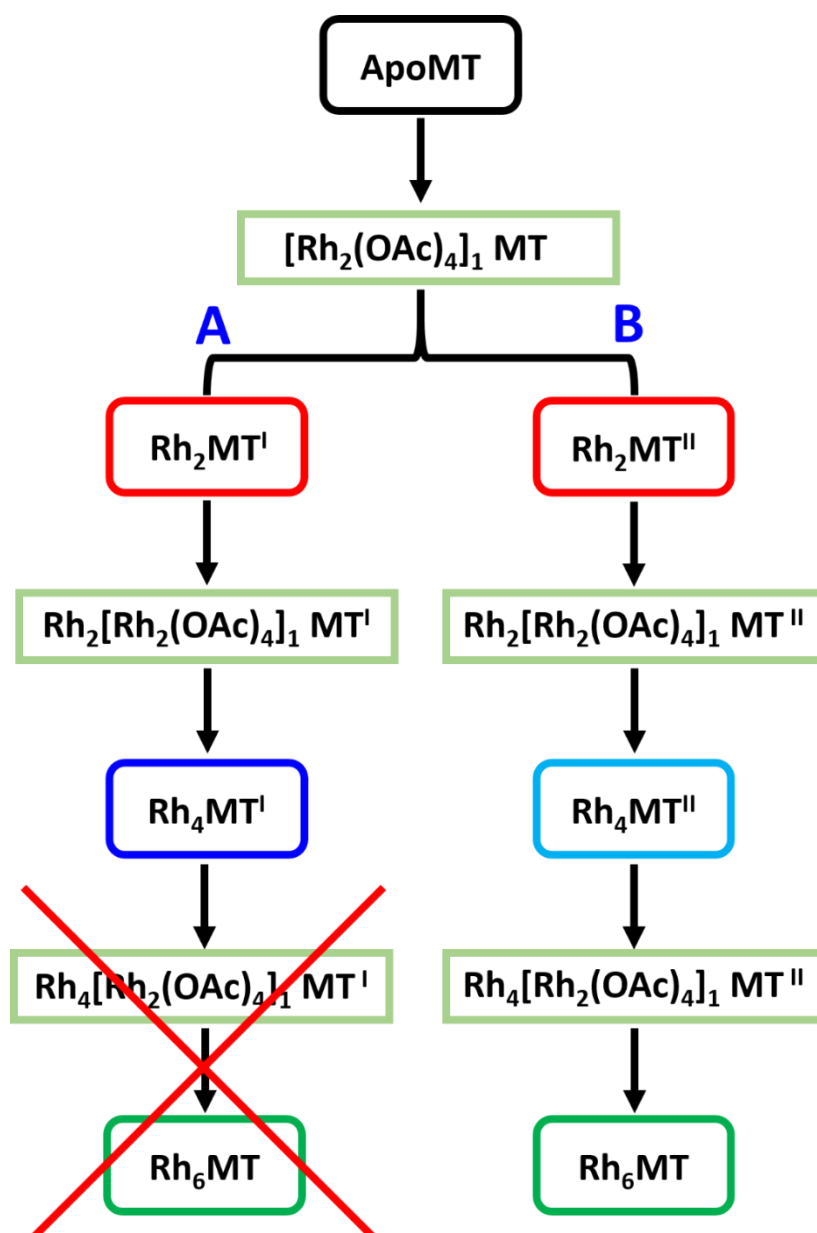


Chart 5-1 Proposed pathway for metallation of β MT 1a by Rh₂(OAc)₄ at physiological pH.

The two pathways shown apply to different configurations. Pathway A: Rh₂MT binds an additional Rh₂(OAc)₄ which is deconstructed, forming Rh₄MT of configuration I. No further metallation occurs at this point. Pathway B: Rh₂MT binds an additional Rh₂(OAc)₄ which is deconstructed, forming Rh₄MT involving a proposed alternate configuration II. This form can proceed to bind a further Rh₂(OAc)₄, producing Rh₆MT. Reproduced from D. L. Wong and M. J. Stillman. Copyright 2018 American Chemical Society.⁶¹

5.7.4 Structure-Dependent Metallation of Metallothioneins: Rigid Rh₂ Binding and Comparison of Binding Constants

The 2° and 3° structure of MT is only defined by metallation,⁸⁰ as it exhibits no 2° structural elements or aromatic residues. A broad distribution of metallated and metal-free MT species exist in the cell.^{65, 83, 103, 104, 113-115} Despite the sensitivity of the free cysteines to oxidation, fluorescence labelling has demonstrated the presence of metal free apo-MT in roughly equal quantities to holo-Zn-MT, both in the oxidized and reduced form.¹¹⁶ This confirms that metallation of MT is a post-translational modification that can only occur once the protein is fully synthesized, due to the cross-linking nature of metal-cysteine coordination that forms the metal-thiolate clusters. To better understand the metallation reaction, the fully demetallated apo-MT is used as the model for the partially metallated MTs expected *in vivo*.

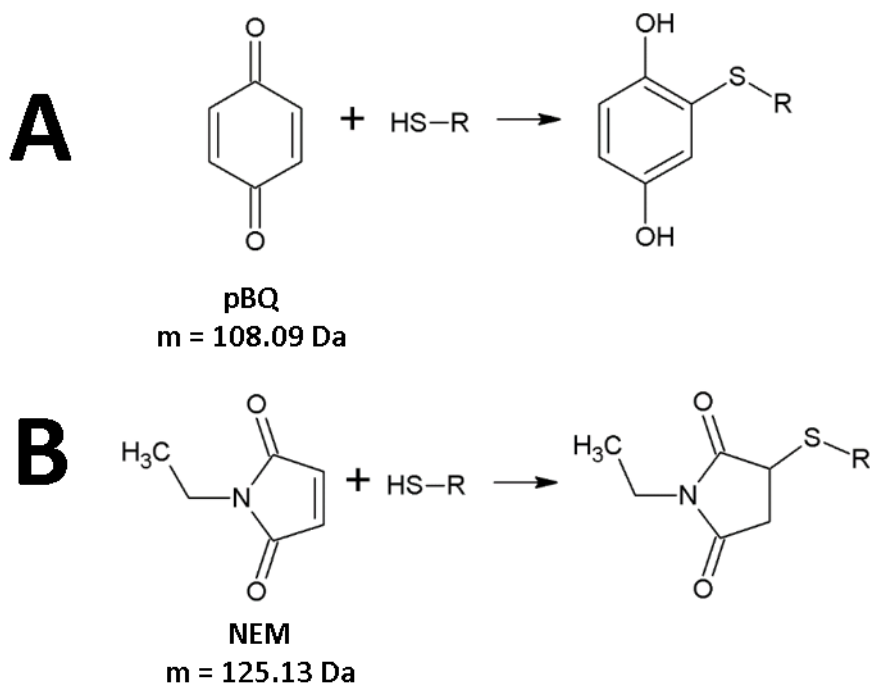
Metal binding to MT is generally fluxional such that the metal ions can move from site to site in search of the lowest thermodynamic product (for example, the well-known change in Cu(I)-MT emission signal when Cu(I) is titrated into Zn-MT 1A or Zn-MT 2A).¹¹⁷ In the case of the dimeric rhodium binding, the bound cysteines form multiple metallated species (Chart 1). The orientation of the initial metal binding in relation to the MT cysteines defines how the metallation proceeds. Due to the decreased abundance of Rh₄MT and Rh₆MT, the domain location and formation of Rh₂MT determines whether the metallation continue to Rh₆MT. The two distributions for the Rh₂(BQ)_xMT modified speciation data reflect these products. The decrease in relative log K_f's demonstrates its rigidity as metallation progresses (Table 5-1). Previous work with the single β domain fragment shows that the β-domain accommodates 1 Rh₂ moeity.⁷⁰ The 11 cysteines of the

alpha domain can accommodate the remaining 2Rh₂ if metallated efficiently (Chart 5-1, right pathway B). If not, the cysteines become too tangled to accommodate further metals (Chart 5-1, left pathway A).

It is evident that the magnitude of log K_f's cannot be directly compared between chemically different metals because of both different binding geometries, and the presence of competitive coordinating ligands. A comparison can only be made meaningfully between isomorphous metals. Due to the fluxional nature of the 20 cysteine thiols in MTs, metals with different oxidation states can form vastly different binding geometries. Just as Zn metallation of MT differs from Cd metallation, free metal ion accumulation in MT cannot be compared to the deconstructive process that MTs exert on ligated metal complexes. Complex deconstruction cannot be included in these values, as these are the final, observed, relative binding constants. This is important in comparing values, because this emphasizes the versatile nature of MT, in that there is no consistent metal binding site across metal families.

5.7.5 Solvent-Cysteine Accessibility and Protein Flexibility throughout Metallation

Typically, protein structural information can be obtained by analyzing the charge state distribution patterns in the mass spectral data. Due to the small size of MTs, this method is not as effective, especially to probe the apo-protein or partially metallated states. More recently, however, structural information about MT has been obtained through the reaction profiles of cysteine modifiers that take advantage of MT's cysteine rich structure. p-Benzoquinone (pBQ) and N-ethyl maleimide (NEM) are organic agents capable of binding covalently with free thiols, as shown in Scheme 5-2. Similarly to Ellman's Reagent (5,5'-dithiobis(2-nitrobenzoic acid), DTNB), this irreversible binding permits quantification of free thiols.^{77, 78, 103, 111, 118} This is observed as a predictable mass change, but in addition with respect to MT and its 20 cysteines, the modified speciation distribution can also provide information about the solvent accessibility of the cysteines.⁷⁸ This technique has been used to understand metallation of apo-MT through partially metallated and fully metallated Cu₆MT, Cu₁₃MT, Cu₂₀MT, and As₆MT.^{65, 103}



Scheme 5-2 Structure and reaction mechanism involved in the formation of covalent bonds between cysteine and modifiers pBQ (A, top) and NEM (B, bottom). Reproduced from D. L. Wong and M. J. Stillman. Copyright 2018 American Chemical Society.⁶¹

In this present study, both pBQ and NEM are used in conjunction with mass spectrometry to quantify the number of free cysteines and to probe the surface structure and the solvent accessibility of the partially metallated states of Rh₂MT, Rh₄MT, and Rh₆MT. Structural characteristics can be inferred from the reaction profile of modification observed in the mass spectral data.⁷⁷ As expected, the higher metallated Rh₄ and Rh₆ bound MT shows less solvent accessibility because of the lower spread of the p(BQ)-modified species. The most solvent accessible species, Rh₂MT, shows two distinct distributions, indicating that two metallated states are created. From the change in intensity for the higher metallated states, we can infer that only one of the observed Rh₂MT species is capable of further metallation, as described pictorially in Chart 5-1. This rigidity is reflected again with the lowered abundance of Rh₄MT and Rh₆MT, and in the decrease of the relative log K_f values showing that progressive metallation is less favorable.

3D structures constructed using MM/MD modelling techniques from previously reported AsMT^{119, 120} and Cd-MT^{64, 68} metallated forms were adapted to examine the possible metal thiolate constructs MT may adopt when bound to dirhodium cores. The absence of aromatic and hydrophobic residues, and the absence of mean that the driving force for protein folding is the cross-linking that results from the metallation of the cysteines, stabilized by hydrogen bond formation. As the cysteine modification results and the MD structures indicate, metal-free cysteine thiolates are found to be solvent accessible,⁷⁹ while holo cysteines are buried within the protein structure. MD calculations on the holo-Rh₆MT shows no change in the conformational geometry, demonstrating the holo-MT's rigid status.

The low pH experiment shows that while the unfolded, 9 cysteine apo- α MT can bind to the Rh₂(OAc)₄, it is unable to effectively displace the coordinating ligands of the complex. Instead, the unfolded peptide quickly binds to 1-6 Rh₂(OAc)₄ species (Figure 5-8), which occupies and locks the cysteine thiolates from other reactivity. Significantly, the MS data recorded at pH<2 demonstrates that Rh₂(OAc)₄ has a strong binding affinity, surpassing that of Cd, which is completely demetallated from MT at this pH. These low physiological pH, in which the more folded MT structure can orient its cysteines to displace the coordinated ligands more effectively than the unfolded protein.

The unusual malleability of MT, first reported for As(III) binding,¹¹¹ is clearly an additional characteristic property of MT. The many species seen in the Rh₂-binding mass spectral data imply multiple coordination possibilities for metal binding. This suggests that the “magic numbers” concept⁸³ prevalent in the literature does not apply to transition metal complexes.

The data reported here support the findings in Chapter 2 that the initial, intrinsically disordered, native MT structure at physiological pH can flexibly entrap metal complexes and is a necessary conformation to further react, deconstruct, and isolate the metal for storage.

5.8 Conclusions

This Chapter reports the reaction of a xenobiotic complex with MT as a test of the possible chelation properties of MTs with transition metal complexes. $\text{Rh}_2(\text{OAc})_4$, a robust synthetic catalyst, binds intact to the metal-free apo-MT. The tetraacetate ligands are rapidly removed upon binding by the folded MT at physiological pH, in a manner reported previously for cisplatin. The initial reaction of the apo-MT involves the displacement of tetraacetate groups by the cysteinyl thiolates. Where the first Rh_2 binds in the protein, which domain, governs the remaining space in which metallation can continue. This intermediate state can then proceed towards two structures, one of which allows the metallation of a third dirhodium moiety, forming Rh_6MT , the other pathway stops at Rh_4MT . These branching pathways were determined using complementary techniques of cysteine modification and mass spectrometry, together providing speciation data for equilibrium reaction modelling.

The increase in global exposure to anthropogenic xenobiotic metals demands updated understanding of the metabolic effects caused. Rh and PGMs are known to exert cytotoxic and nephrotoxic activity, through metabolic process that can increase the bioavailability. The experiments in this Thesis demonstrate the ease with which biological structures can greatly change the chemical activity of rhodium. A metal's persistence in ever changing chemical forms emphasizes the need for long-term study and caution for the continued utilization of these elements for human health.

Finally, of concern, the long term accumulation and storage of PGM's can provoke chronic toxic effects. Cd-bound MT has a reported half-life in the kidneys exceeding twenty years.¹²¹ Due to the firm and rigid binding of $\text{Rh}_2(\text{OAc})_4$ to MT, Rh would be expected to accumulate in a similarly dangerous manner. The heavy and widespread use of PGM's pose a risk that cannot be ignored, as history would remind us with the use of lead in gasoline and paints causing widespread toxic effects. This long-term storage is also applicable for these xenobiotic metals. The bioaccumulation of these metals can pose a significant health risk in the future.

5.9 References

1. M. Volpe, M. Nazzaro, R. Coppola, F. Rapuano and R. Aquino, Determination and assessments of selected heavy metals in eye shadow cosmetics from China, Italy, and USA, *Microchem. J.*, 2012, **101**, 65-69.
2. P. Gao, S. Liu, Z. Zhang, P. Meng, N. Lin, B. Lu, F. Cui, Y. Feng and B. Xing, Health impact of bioaccessible metal in lip cosmetics to female college students and career women, northeast of China, *Environ. Pollut.*, 2015, **197**, 214-220.
3. O. Al-Dayel, J. Hefne and T. Al-Ajyan, Human exposure to heavy metals from cosmetics, *Orient J. Chem.*, 2011, **27**, 1-11.
4. M. Marinovich, M. S. Boraso, E. Testai and C. L. Galli, Metals in cosmetics: An a posteriori safety evaluation, *Regul. Toxicol. Pharmacol.*, 2014, **69**, 416-424.
5. S. Borowska and M. M. Brzóška, Metals in cosmetics: implications for human health, *J. Appl. Toxicol.*, 2015, **35**, 551-572.
6. B. Bocca, A. Pino, A. Alimonti and G. Forte, Toxic metals contained in cosmetics: a status report, *Regul. Toxicol. Pharmacol.*, 2014, **68**, 447-467.
7. M. Badea, O. P. Luzardo, A. González-Antuña, M. Zumbado, L. Rogozea, L. Floroian, D. Alexandrescu, M. Moga, L. Gaman and M. Radoi, Body burden of toxic metals and rare earth elements in non-smokers, cigarette smokers and electronic cigarette users, *Environ. Res.*, 2018, **166**, 269-275.
8. M. Williams, A. Villarreal, K. Bozhilov, S. Lin and P. Talbot, Metal and silicate particles including nanoparticles are present in electronic cigarette cartomizer fluid and aerosol, *PLoS one*, 2013, **8**, e57987.
9. M. L. Goniewicz, J. Knysak, M. Gawron, L. Kosmider, A. Sobczak, J. Kurek, A. Prokopowicz, M. Jablonska-Czapla, C. Rosik-Dulewska, C. Havel, P. Jacob and N. Benowitz, Levels of selected carcinogens and toxicants in vapour from electronic cigarettes, *Tob. Control.*, 2014, **23**, 133-139.
10. C. L. Wiseman and F. Zereini, Airborne particulate matter, platinum group elements and human health: a review of recent evidence, *Sci. Total Environ.*, 2009, **407**, 2493-2500.
11. M. Moldovan, M. Palacios, M. Gomez, G. Morrison, S. Rauch, C. McLeod, R. Ma, S. Caroli, A. Alimonti and F. Petrucci, Environmental risk of particulate and soluble platinum group elements released from gasoline and diesel engine catalytic converters, *Sci. Total Environ.*, 2002, **296**, 199-208.
12. K. H. Ek, G. M. Morrison and S. Rauch, Environmental routes for platinum group elements to biological materials—a review, *Sci. Total Environ.*, 2004, **334**, 21-38.

13. K. Ravindra, L. Bencs and R. Van Grieken, Platinum group elements in the environment and their health risk, *Sci. Total Environ.*, 2004, **318**, 1-43.
14. J. O. Duruibe, M. Ogwuegbu and J. Egwurugwu, Heavy metal pollution and human biotoxic effects, *Int. J. Phys. Sci.*, 2007, **2**, 112-118.
15. M. Mauro, M. Crosera, C. Bianco, G. Adami, T. Montini, P. Fornasiero, M. Jaganjac, M. Bovenzi and F. L. Filon, Permeation of platinum and rhodium nanoparticles through intact and damaged human skin, *J. Nanoparticle Res.*, 2015, **17**, 253.
16. M. Mleczek, P. Niedzielski, P. Kalač, M. Siwulski, P. Rzymiski and M. Gąsecka, Levels of platinum group elements and rare-earth elements in wild mushroom species growing in Poland, *Food Addit. Contam. Part A Chem. Anal. Control Expo. Risk*, 2016, **33**, 86-94.
17. S. Zimmermann and B. Sures, Lessons learned from studies with the freshwater mussel *Dreissena polymorpha* exposed to platinum, palladium and rhodium, *Sci. Total Environ.*, 2018, **615**, 1396-1405.
18. G. K. Andrews, Regulation of metallothionein gene expression by oxidative stress and metal ions, *Biochem. Pharmacol.*, 2000, **59**, 95-104.
19. A. C. Cabral, J. Jakovleska, A. Deb, J. E. Penner-Hahn, V. L. Pecoraro and E. Freisinger, Further insights into the metal ion binding abilities and the metalation pathway of a plant metallothionein from *Musa acuminata*, *J. Biol. Inorg. Chem.*, 2018, **23**, 91-107.
20. K. M. Chan, Metallothionein: potential biomarker for monitoring heavy metal pollution in fish around Hong Kong, *Marine Poll. Bull.*, 1995, **31**, 411-415.
21. E. Freisinger, Plant MTs—long neglected members of the metallothionein superfamily, *Dalton Trans.*, 2008, 6663-6675.
22. V. Besada, J. M. Andrade, F. Schultze and J. J. González, Heavy metals in edible seaweeds commercialised for human consumption, *J. Mar. Syst.*, 2009, **75**, 305-313.
23. G. Rentschler, I. Rodushkin, M. Cerna, C. Chen, F. Harari, R. Harari, M. Horvat, F. Hrubá, L. Kasparová and K. Koppová, Platinum, palladium, rhodium, molybdenum and strontium in blood of urban women in nine countries, *Int. J. Hyg. Environ. Health*, 2018, **221**, 223-230.
24. S. L. Kelley, A. Basu, B. A. Teicher, M. P. Hacker, D. H. Hamer and J. S. Lazo, Overexpression of metallothionein confers resistance to anticancer drugs, *Science*, 1988, **241**, 1813-1815.

25. J. Hengstler, H. Pilch, M. Schmidt, H. Dahlenburg, J. Sagemüller, I. Schiffer, F. Oesch, P. Knapstein, B. Kaina and B. Tanner, Metallothionein expression in ovarian cancer in relation to histopathological parameters and molecular markers of prognosis, *Int. J. Cancer*, 2001, **95**, 121-127.
26. B. Desoize, Metals and metal compounds in cancer treatment, *Anticancer Res.*, 2004, **24**, 1529-1544.
27. V. Pekarik, J. Gumulec, M. Masarik, R. Kizek and V. Adam, Prostate cancer, miRNAs, metallothioneins and resistance to cytostatic drugs, *Curr. Med. Chem.*, 2013, **20**, 534-544.
28. J. Hardyman, J. Tyson, K. Jackson, C. Aldridge, S. Cockell, L. Wakeling, R. Valentine and D. Ford, Zinc sensing by metal-responsive transcription factor 1 (MTF1) controls metallothionein and ZnT1 expression to buffer the sensitivity of the transcriptome response to zinc, *Metallomics*, 2016, **8**, 337-343.
29. B. J. Murphy, G. K. Andrews, D. Bittel, D. J. Discher, J. McCue, C. J. Green, M. Yanovsky, A. Giaccia, R. M. Sutherland and K. R. Laderoute, Activation of metallothionein gene expression by hypoxia involves metal response elements and metal transcription factor-1, *Cancer Res.*, 1999, **59**, 1315-1322.
30. Y. Manso, G. Comes, J. C. López-Ramos, M. Belfiore, A. Molinero, M. Giralt, J. Carrasco, P. A. Adlard, A. I. Bush and J. M. Delgado-García, Overexpression of metallothionein-1 modulates the phenotype of the Tg2576 mouse model of Alzheimer's disease, *J. Alzheimers Dis.*, 2016, **51**, 81-95.
31. M. Sato and I. Bremner, Oxygen free radicals and metallothionein, *Free Radic. Biol. Med.*, 1993, **14**, 325-337.
32. M. Satoh, D. M. Kloth, S. A. Kadhim, J. L. Chin, A. Naganuma, N. Imura and M. G. Cherian, Modulation of both cisplatin nephrotoxicity and drug resistance in murine bladder tumor by controlling metallothionein synthesis, *Cancer Res.*, 1993, **53**, 1829-1832.
33. L. Endresen, A. Bakka and H. E. Rugstad, Increased resistance to chlorambucil in cultured cells with a high concentration of cytoplasmic metallothionein, *Cancer Res.*, 1983, **43**, 2918-2926.
34. J. Zaia, L. Jiang, M. S. Han, J. R. Tabb, Z. Wu, D. Fabris and C. Fenselau, A binding site for chlorambucil on metallothionein, *Biochemistry*, 1996, **35**, 2830-2835.
35. X. Yu, Z. Wu and C. Fenselau, Covalent sequestration of melphalan by metallothionein and selective alkylation of cysteines, *Biochemistry*, 1995, **34**, 3377-3385.

36. Y. Kondo, E. S. Woo, A. E. Michalska, K. A. Choo and J. S. Lazo, Metallothionein null cells have increased sensitivity to anticancer drugs, *Cancer Res.*, 1995, **55**, 2021-2023.
37. J. S. Lazo and B. R. Pitt, Metallothioneins and cell death by anticancer drugs, *Annu. Rev. Pharmacol.*, 1995, **35**, 635-653.
38. E. M. Luther, M. M. Schmidt, J. Diendorf, M. Epple and R. Dringen, Upregulation of metallothioneins after exposure of cultured primary astrocytes to silver nanoparticles, *Neurochem. Res.*, 2012, **37**, 1639-1648.
39. A. H. Ringwood, M. McCarthy, T. C. Bates and D. L. Carroll, The effects of silver nanoparticles on oyster embryos, *Mar. Environ. Res.*, 2010, **69**, S49-S51.
40. S. Renault, M. Baudrimont, N. Mesmer-Dudons, P. Gonzalez, S. Mornet and A. Brisson, Impacts of gold nanoparticle exposure on two freshwater species: a phytoplanktonic alga (*Scenedesmus subspicatus*) and a benthic bivalve (*Corbicula fluminea*), *Gold Bull.*, 2008, **41**, 116-126.
41. A. Casini, A. Karotki, C. Gabbiani, F. Rugi, M. Vašák, L. Messori and P. J. Dyson, Reactivity of an antimetastatic organometallic ruthenium compound with metallothionein-2: relevance to the mechanism of action, *Metallomics*, 2009, **1**, 434-441.
42. L. Galluzzi, L. Senovilla, I. Vitale, J. Michels, I. Martins, O. Kepp, M. Castedo and G. Kroemer, Molecular mechanisms of cisplatin resistance, *Oncogene*, 2012, **31**, 1869-1883.
43. L. Galluzzi, I. Vitale, J. Michels, C. Brenner, G. Szabadkai, A. Harel-Bellan, M. Castedo and G. Kroemer, Systems biology of cisplatin resistance: past, present and future, *Cell Death Dis.*, 2014, **5**, e1257.
44. E. Atrián-Blasco, A. Santoro, D. L. Pountney, G. Meloni, C. Hureau and P. Faller, Chemistry of mammalian metallothioneins and their interaction with amyloidogenic peptides and proteins, *Chem. Soc. Rev.*, 2017, **46**, 7683-7693.
45. P. Surowiak, V. Materna, I. Kaplenko, M. Spaczyński, M. Dietel, H. Lage and M. Zabel, Augmented expression of metallothionein and glutathione S-transferase pi as unfavourable prognostic factors in cisplatin-treated ovarian cancer patients, *Virchows Arch.*, 2005, **447**, 626-633.
46. P. Surowiak, V. Materna, A. Maciejczyk, M. Pudełko, E. Markwitz, M. Spaczyński, M. Dietel, M. Zabel and H. Lage, Nuclear metallothionein expression correlates with cisplatin resistance of ovarian cancer cells and poor clinical outcome, *Virchows Arch.*, 2007, **450**, 279-285.
47. U. Ndagi, N. Mhlongo and M. E. Soliman, Metal complexes in cancer therapy—an update from drug design perspective, *Drug. Des. Devel. Ther.*, 2017, **11**, 599.

48. N. P. Barry and P. J. Sadler, 100 years of metal coordination chemistry: from Alfred Werner to anticancer metallodrugs, *Pure Appl. Chem.*, 2014, **86**, 1897-1910.
49. B. Rosenberg, Anticancer activity of cis-dichlorodiammineplatinum (II) and some relevant chemistry, *Cancer Treat. Rep.*, 1979, **63**, 1433.
50. B. Rosenberg, Charles F. Ketrting prize. Fundamental studies with cisplatin, *Cancer*, 1985, **55**, 2303-2316.
51. J. Bear, J. H. Gray, L. Rainen, I. Chang, R. Howard, G. Serio and A. Kimball, Interaction of Rhodium (II) carboxylates with molecules of biologic importance, *Cancer Chemother. Rep.*, 1975, **59**, 611-620.
52. A. Erck, E. Sherwood, J. Bear and A. Kimball, The metabolism of rhodium (II) acetate in tumor-bearing mice, *Cancer Res.*, 1976, **36**, 2204-2209.
53. A. Erck, L. Rainen, J. Whileyman, I. Chang, A. Kimball and J. Bear, Studies of rhodium (II) carboxylates as potential antitumor agents, *Proc. Soc. Exp. Biol. Med.*, 1974, **145**, 1278-1283.
54. D. V. Deubel, Mechanism and Control of Rare Tautomer Trapping at a Metal–Metal Bond: Adenine Binding to Dirhodium Antitumor Agents1, *J. Am. Chem. Soc.*, 2008, **130**, 665-675.
55. A. M. Angeles-Boza, H. T. Chifotides, J. D. Aguirre, A. Chouai, P. K.-L. Fu, K. R. Dunbar and C. Turro, Dirhodium (II, II) complexes: molecular characteristics that affect in vitro activity, *J. Med. Chem.*, 2006, **49**, 6841-6847.
56. H. T. Chifotides and K. R. Dunbar, Interactions of metal–metal-bonded antitumor active complexes with DNA fragments and DNA, *Accounts Chem. Res.*, 2005, **38**, 146-156.
57. H. T. Chifotides, J. S. Hess, A. M. Angeles-Boza, J. R. Galán-Mascarós, K. Sorasaene and K. R. Dunbar, Structural evidence for monodentate binding of guanine to the dirhodium (II, II) core in a manner akin to that of cisplatin, *Dalton Trans.*, 2003, 4426-4430.
58. A. M. Angeles-Boza, P. M. Bradley, P. K.-L. Fu, S. E. Wicke, J. Bacsa, K. R. Dunbar and C. Turro, DNA binding and photocleavage in vitro by new dirhodium (II) dppz complexes: correlation to cytotoxicity and photocytotoxicity, *Inorg. Chem.*, 2004, **43**, 8510-8519.
59. N. Katsaros and A. Anagnostopoulou, Rhodium and its compounds as potential agents in cancer treatment, *Crit. Rev. Oncol. Hematol.*, 2002, **42**, 297-308.
60. E. B. Boyar and S. D. Robinson, Rhodium (II) carboxylates, *Coord. Chem. Rev.*, 1983, **50**, 109-208.

61. D. L. Wong and M. J. Stillman, Metallothionein: An Aggressive Scavenger—The Metabolism of Rhodium (II) Tetraacetate ($\text{Rh}_2(\text{CH}_3\text{CO}_2)_4$), *ACS Omega*, 2018, **3**, 16314-16327.
62. A. E. Garcia and F. Jalilehvand, Aerobic reactions of antitumor active dirhodium (II) tetraacetate $\text{Rh}_2(\text{CH}_3\text{COO})_4$ with glutathione, *J. Biol. Inorg. Chem.*, 2018, **23**, 231-239.
63. D. L. Wong, A. Zhang, A. S. Faponle, S. P. de Visser and M. J. Stillman, Glutathione binding to dirhodium tetraacetate: a spectroscopic, mass spectral and computational study of an anti-tumour compound, *Metallomics*, 2017, **9**, 501-516.
64. J. Chan, Z. Huang, I. Watt, P. Kille and M. J. Stillman, Characterization of the conformational changes in recombinant human metallothioneins using ESI-MS and molecular modeling, *Can. J. Chem.*, 2007, **85**, 898-912.
65. G. W. Irvine, T. B. Pinter and M. J. Stillman, Defining the metal binding pathways of human metallothionein 1a: balancing zinc availability and cadmium seclusion, *Metallomics*, 2016, **8**, 71-81.
66. J. Kägi and Y. Kojima, in *Metallothionein II*, Springer, 1987, pp. 25-61.
67. D. E. Sutherland, K. L. Summers and M. J. Stillman, Noncooperative metalation of metallothionein 1A and its isolated domains with zinc, *Biochemistry*, 2012, **51**, 6690-6700.
68. J. Chan, Z. Huang, M. E. Merrifield, M. T. Salgado and M. J. Stillman, Studies of metal binding reactions in metallothioneins by spectroscopic, molecular biology, and molecular modeling techniques, *Coord. Chem. Rev.*, 2002, **233**, 319-339.
69. T. T. Ngu and M. J. Stillman, Metal-binding mechanisms in metallothioneins, *Dalton Trans.*, 2009, 5425-5433.
70. D. L. Wong and M. J. Stillman, Destructive interactions of dirhodium (II) tetraacetate with β metallothionein rh1a, *Chem. Commun.*, 2016, **52**, 5698-5701.
71. P. Jakimowicz, L. Ostropolska and F. P. Pruchnik, Interaction of $[\text{Rh}_2(\text{O}_2\text{CCH}_3)_4(\text{H}_2\text{O})_2]$ and $[\text{Rh}_2(\text{O}_2\text{CCH}(\text{OH})\text{Ph})_2(\text{phen})_2(\text{H}_2\text{O})_2](\text{O}_2\text{C}-\text{CH}(\text{OH})\text{Ph})_2$ With Sulfhydryl Compounds and Ceruloplasmin, *Metal-based drugs*, 2000, **7**, 201-209.
72. F. Jalilehvand, A. Enriquez Garcia and P. Niksirat, Reactions of Antitumor Active Dirhodium (II) Tetraacetate $\text{Rh}_2(\text{CH}_3\text{COO})_4$ with Cysteine and Its Derivatives, *ACS Omega*, 2017, **2**, 6174-6186.
73. R. Głaszczka, J. Jaźwiński, B. Kamiński and M. Kamińska, Adducts of rhodium (II) tetraacylates with methionine and its derivatives: ^1H and ^{13}C nuclear magnetic resonance spectroscopy and chiral recognition, *Tetrahedron Asymmetry*, 2010, **21**, 2346-2355.

74. R. Głaszczka and J. Jaźwiński, In situ complexation of rhodium (II) tetracarboxylates with some derivatives of cysteine and related ligands studied by ^1H and ^{13}C nuclear magnetic resonance spectroscopy, *J. Coord. Chem.*, 2016, **69**, 3703-3714.
75. L. Alderighi, P. Gans, A. Ienco, D. Peters, A. Sabatini and A. Vacca, Hyperquad simulation and speciation (HySS): a utility program for the investigation of equilibria involving soluble and partially soluble species, *Coord. Chem. Rev.*, 1999, **184**, 311-318.
76. J. S. Scheller, G. W. Irvine and M. J. Stillman, Unravelling the mechanistic details of metal binding to mammalian metallothioneins from stoichiometric, kinetic, and binding affinity data, *Dalton Trans.*, 2018, **47**, 3613-3637.
77. G. W. Irvine and M. J. Stillman, Residue Modification and Mass Spectrometry for the Investigation of Structural and Metalation Properties of Metallothionein and Cysteine-Rich Proteins, *Int. J. Mol. Sci.*, 2017, **18**, 913.
78. W.-W. Li, J. Heinze and W. Haehnel, Site-specific binding of quinones to proteins through thiol addition and addition-elimination reactions, *J. Am. Chem. Soc.*, 2005, **127**, 6140-6141.
79. K. E. Rigby, J. Chan, J. Mackie and M. J. Stillman, Molecular dynamics study on the folding and metallation of the individual domains of metallothionein, *Proteins: Struct., Funct., Bioinf.*, 2006, **62**, 159-172.
80. K. E. R. Duncan and M. J. Stillman, Metal-dependent protein folding: metallation of metallothionein, *J. Inorg. Biochem.*, 2006, **100**, 2101-2107.
81. K. E. R. Duncan, T. T. Ngu, J. Chan, M. T. Salgado, M. E. Merrifield and M. J. Stillman, Peptide folding, metal-binding mechanisms, and binding site structures in metallothioneins, *Exp. Biol. Med.*, 2006, **231**, 1488-1499.
82. K. E. Rigby and M. J. Stillman, Structural studies of metal-free metallothionein, *Biochem. Biophys. Res. Commun.*, 2004, **325**, 1271-1278.
83. D. E. Sutherland and M. J. Stillman, The “magic numbers” of metallothionein, *Metallomics*, 2011, **3**, 444-463.
84. FQS Poland, Scigress Molecular Modeling Software, 6.0.0, 2016. Retrieved from http://www.fqs.pl/chemistry_materials_life_science/products/scigress.
85. J. Rinkovec, G. Pehneć, R. Godec, S. Davila and I. Bešlić, Spatial and temporal distribution of platinum, palladium and rhodium in Zagreb air, *Sci. Total Environ.*, 2018, **636**, 456-463.

86. C. Monti-Bragadin, M. Giacca, L. Dolzani and M. Tamaro, Mutagenic effects of rhodium (I) and ruthenium (II) organometallic complexes in bacteria, *Inorganica Chim. Acta*, 1987, **137**, 31-34.
87. F. Ajmone-Marsan and M. Biasioli, Trace elements in soils of urban areas, *Water Air Soil Pollut.*, 2010, **213**, 121-143.
88. C. Alméjida, M. Sharma, A. Cobelo-García, J. Santos-Echeandía and M. Caetano, Osmium and platinum decoupling in the environment: evidences in intertidal sediments (Tagus Estuary, SW Europe), *Environ. Sci. Technol.*, 2015, **49**, 6545-6553.
89. M. Sharma, in *Handbook of Environmental Isotope Geochemistry*, Springer, 2012, pp. 205-227.
90. C. Barbante, A. Veysseyre, C. Ferrari, K. Van De Velde, C. Morel, G. Capodaglio, P. Cescon, G. Scarponi and C. Boutron, Greenland snow evidence of large scale atmospheric contamination for platinum, palladium, and rhodium, *Environ. Sci. Technol.*, 2001, **35**, 835-839.
91. C. Chen, P. N. Sedwick and M. Sharma, Anthropogenic osmium in rain and snow reveals global-scale atmospheric contamination, *Proc. Natl. Acad. Sci. U.S.A.*, 2009, **106**, 7724-7728.
92. A. Kabata-Pendias, *Trace elements in soils and plants*, CRC press, 2010.
93. M. Sugita, The biological half-time of heavy metals, *Int. Arch. Occup. Environ. Health*, 1978, **41**, 25-40.
94. G. F. Nordberg, B. A. Fowler and M. Nordberg, *Handbook on the Toxicology of Metals*, Academic press, 2014.
95. J. M. Wood and H.-K. Wang, Microbial resistance to heavy metals, *Environ. Sci. Technol.*, 1983, **17**, 582A-590A.
96. A. V. Skalny, M. G. Skalnaya, A. R. Grabeklis, I. V. Zhegalova, E. P. Serebryansky, V. A. Demidov, E. V. Salnikova, M. S. Uzhentseva, Y. N. Lobanova and A. A. Skalny, Interactive effects of age and gender on levels of toxic and potentially toxic metals in children hair in different urban environments, *Int. J. Environ. Anal. Chem.*, 2018, 1-16.
97. L. Trynda and F. Pruchnik, Interaction of tetra- μ -acetatodirrhodium (II) with human serum albumin, *J. Inorg. Biochem.*, 1995, **58**, 69-77.
98. F. P. Pruchnik, Structure and reactivity of rhodium (II) complexes, *Pure Appl. Chem.*, 1989, **61**, 795-804.

99. M. Wenzel and A. Casini, Mass spectrometry as a powerful tool to study therapeutic metallodrugs speciation mechanisms: Current frontiers and perspectives, *Coord. Chem. Rev.*, 2017, **352**, 432-460.
100. A. J. Heck, Native mass spectrometry: a bridge between interactomics and structural biology, *Nat. Methods*, 2008, **5**, 927.
101. T. T. Ngu, S. Krecisz and M. J. Stillman, Bismuth binding studies to the human metallothionein using electrospray mass spectrometry, *Biochem. Biophys. Res. Commun.*, 2010, **396**, 206-212.
102. M. J. Stillman, D. Thomas, C. Trevithick, X. Guo and M. Siu, Circular dichroism, kinetic and mass spectrometric studies of copper (I) and mercury (II) binding to metallothionein, *J. Inorg. Biochem.*, 2000, **79**, 11-19.
103. J. S. Scheller, G. W. Irvine, D. L. Wong, A. Hartwig and M. J. Stillman, Stepwise copper (I) binding to metallothionein: a mixed cooperative and non-cooperative mechanism for all 20 copper ions, *Metallomics*, 2017, **9**, 447-462.
104. D. P. Jayawardena, I. U. Heinemann and M. J. Stillman, Zinc binds non-cooperatively to human liver metallothionein 2a at physiological pH, *Biochem. Biophys. Res. Commun.*, 2017, **493**, 650-653.
105. R. Wang, D. A. Sens, S. Garrett, S. Somji, M. A. Sens and X. Lu, The resistance of metallothionein to proteolytic digestion: An LC-MS/MS analysis, *Electrophoresis*, 2007, **28**, 2942-2952.
106. M. Knipp, Metallothioneins and platinum (II) anti-tumor compounds, *Curr. Med. Chem.*, 2009, **16**, 522-537.
107. G. W. Irvine, M. Santolini and M. J. Stillman, Selective cysteine modification of metal-free human metallothionein 1a and its isolated domain fragments: Solution structural properties revealed via ESI-MS, *Protein Sci.*, 2017, **26**, 960-971.
108. T. B. Pinter and M. J. Stillman, Kinetics of zinc and cadmium exchanges between metallothionein and carbonic anhydrase, *Biochemistry*, 2015, **54**, 6284-6293.
109. T. B. Pinter and M. J. Stillman, The zinc balance: Competitive zinc metalation of carbonic anhydrase and metallothionein 1A, *Biochemistry*, 2014, **53**, 6276-6285.
110. T. T. Ngu, M. D. Dryden and M. J. Stillman, Arsenic transfer between metallothionein proteins at physiological pH, *Biochem. Biophys. Res. Commun.*, 2010, **401**, 69-74.
111. G. W. Irvine, K. L. Summers and M. J. Stillman, Cysteine accessibility during As³⁺ metalation of the α - and β -domains of recombinant human MT1a, *Biochem. Biophys. Res. Commun.*, 2013, **433**, 477-483.

112. D. Hagerman, J. Goodisman, J. C. Dabrowiak and A.-K. Souid, Kinetic study on the reaction of cisplatin with metallothionein, *Drug Metab. Dispos.*, 2003, **31**, 916-923.
113. D. H. Petering, J. Zhu, S. Krezoski, J. Meeusen, C. Kiekenbush, S. Krull, T. Specher and M. Dughish, Apo-metallothionein emerging as a major player in the cellular activities of metallothionein, *Exp. Biol. Med.*, 2006, **231**, 1528-1534.
114. M. Apostolova, P. Bontchev, C. Nachev and I. Sirakova, Apometallothionein in rat liver, *J. Chromatogr. B Biomed. Sci. Appl.*, 1993, **620**, 191-197.
115. A. Pattanaik, C. F. Shaw III, D. H. Petering, J. Garvey and A. J. Kraker, Basal metallothionein in tumors: widespread presence of apoprotein, *J. Inorg. Biochem.*, 1994, **54**, 91-105.
116. Y. Yang, W. Maret and B. L. Vallee, Differential fluorescence labeling of cysteinyl clusters uncovers high tissue levels of thionein, *Proc. Natl. Acad. Sci. U.S.A.*, 2001, **98**, 5556-5559.
117. A. R. Green and M. J. Stillman, Mobility of copper in binding sites in rabbit liver metallothionein 2, *Inorg. Chem.*, 1996, **35**, 2799-2807.
118. R. A. Bednar, Reactivity and pH dependence of thiol conjugation to N-ethylmaleimide: detection of a conformational change in chalcone isomerase, *Biochemistry*, 1990, **29**, 3684-3690.
119. T. T. Ngu, A. Easton and M. J. Stillman, Kinetic analysis of arsenic– metalation of human metallothionein: significance of the two-domain structure, *J. Am. Chem. Soc.*, 2008, **130**, 17016-17028.
120. T. T. Ngu and M. J. Stillman, Metalation of metallothioneins, *IUBMB Life*, 2009, **61**, 438-446.
121. L. Friberg, M. Piscator, G. Nordberg and T. Kjellstrom, *Cadmium in the Environment*, CRC Press, Cleveland, 1974.

Chapter 6

6 Glutathione Binding to Dirhodium(II) Tetraacetate: a Spectroscopic, Mass Spectral and Computational Study of an Anti-Tumor Compound Bound to a Model Thiol*

6.1 Introduction

Intracellular thiols play an important role in metabolism.¹ Non-protein, sulfhydryl compounds aid in protection against oxidation, as well as in the safe detoxification of harmful or foreign agents through thioether formation.¹⁻⁴ This latter property may substantially reduce the efficacy of drug delivery pathways and, subsequently, the success of a drug, which can lead to drug resistance.⁵⁻¹¹ In particular, thiol-based resistance can be deleterious for metal-based chemotherapeutics, as the electron-rich thiolate favours binding to the soft, d-block metals commonly used in such pharmaceuticals, for example, Pt(II), and Au(I).¹⁰⁻¹²

Glutathione (GSH) is a tripeptide that is required in many metabolic cycles and is vital in cellular defence because of its cysteine thiol (Figure 6-1A).^{1, 2, 6, 9, 13} Intracellular concentrations of GSH can reach up to 10 mM, with its regulation and synthesis tightly controlled.^{2, 3} This cysteinyl thiol provides the main ordnance through which glutathione-based protective chemistry acts in guarding the cell against oxidative damage and conjugating metabolites for efflux.^{2, 3, 14} GSH is a common coenzyme and is also heavily involved in metabolic pathways such as glutathione peroxidases, reductases, and glutathione S-transferases.^{2, 6, 7, 15}

GSH S-transferases catalyse the combination of GSH with xenobiotic compounds for metabolism and excretion using the highly nucleophilic cysteinyl thiolate (GS⁻).² The predominance of GSH in the cell, coupled with its conjugation abilities, means that GSH is a major player in the destructive metabolism of therapeutic compounds, acting through conjugation as a means of drug resistance.^{3, 9, 11} Metal-based therapeutic compounds that are vulnerable to thiol chemistry can be structurally altered, and even deactivated, following reaction with intracellular GSH.^{8, 16, 17}

*A version of this chapter has been published:
Metallomics, 9(5), 501-516. (2017) Copyright 2017 Royal Society of Chemistry.
Reproduced with permission from: D. L. Wong et al.

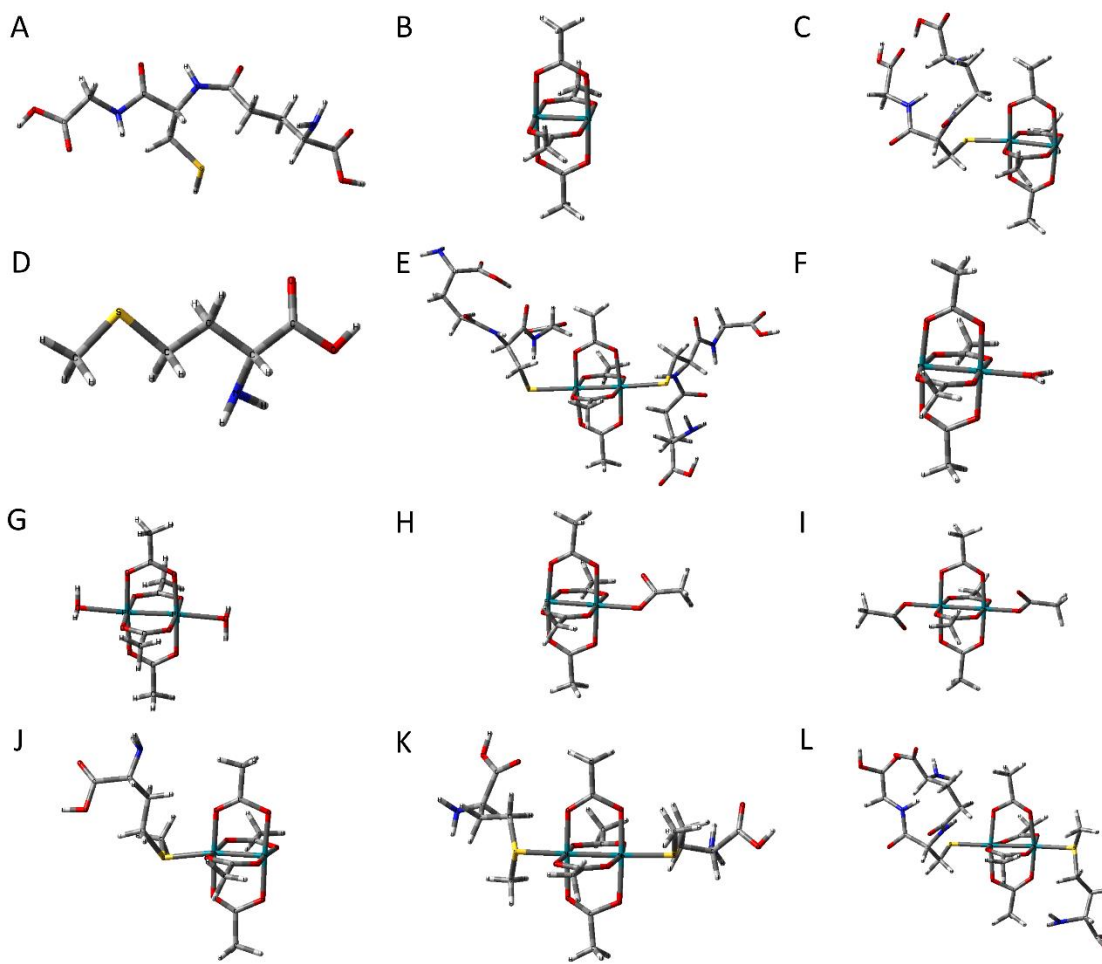


Figure 6-1 Structures described in Chapter 6

Structures of (A) glutathione (GSH), (B) $Rh_2(OAc)_4$, (C) $[Rh_2(OAc)_4(GS)]$, (D) methionine (Met), (E) $[Rh_2(OAc)_4(GS)_2]$, (F) $Rh_2(OAc)_4(H_2O)$, (G) $Rh_2(OAc)_4(H_2O)_2$, (H) $[Rh_2(OAc)_5]$, (I) $[Rh_2(OAc)_6]$, (J) $Rh_2(OAc)_4(Met)$, (K) $Rh_2(OAc)_4(Met)_2$, (L) $[Rh_2(OAc)_4(GS)(Met)]$. Colour coding: rhodium-turquoise, oxygen-red, sulfur-yellow, nitrogen-blue, carbon-grey, hydrogen-white. Calculations and image from A. Zhang in D. L. Wong *et al.*, reproduced with permission from the Royal Society of Chemistry.¹⁸

Glutathione reacts with large, soft, metals such as the toxic metals Cd(II), Hg(II), Pb(II), and As(III).¹⁹⁻²³ This tendency to bind soft metals also extends to the wide range of metals used in therapeutic complexes, for example, Ag(I), Bi(III), Pt(II) in cisplatin, and Au(I) in Auranofin.^{10, 12, 24-27} A marked increase in glutathione synthesis is often correlated with cisplatin resistance, such as the case in human ovarian cancers.^{10, 28, 29} This type of

protective chemistry is the basis for the co-administration of glutathione as a defence against renal toxicity in platinum-based chemotherapies.^{4, 14} There is evidence that the inhibition of glutathione synthesis reverses cisplatin resistance in some cancer types.³⁰⁻³² With an increase in the use of d-block metals as the key components of metallotherapeutic agents, it is critical to understand how this prominent defensive thiolate will interact with biologically-targeted metal complexes. Such interactions would likely reduce the efficacy of these metallodrugs.

Dirhodium(II) carboxylates and their derivatives are an emerging class of anti-tumor compounds that are described as exhibiting greater potency than cisplatin *in vitro*,³³⁻³⁹ as described in Chapter 4 and 5. However, significantly, with respect to possible cellular chemistry, rhodium(II) carboxylates bind strongly to sulfur containing compounds.^{33, 34, 36, 38, 40-42} Indeed, the propensity for these rhodium complexes to deplete intracellular thiols makes them especially useful as radiosensitizers^{43, 44}. Other classes of dirhodium carboxylates, such as the $\text{Rh}_2(\text{O}_2\text{CR})_4$ ($\text{R} = \text{Me}, \text{Et}, \text{Pr}$), display potent anti-tumor activity that stems from their ability to inhibit enzymes with sulfhydryl groups in their active sites^{34, 35, 45}. Dirhodium(II) tetraacetate (tetrakis(μ -acetato)dirhodium(II), hereby referred to as $\text{Rh}_2(\text{OAc})_4$, Figure 6-1B) is a bimetallic complex with four bridging acetate ligands bound in an octahedral geometry, with two empty axial sites usually coordinated by solvent molecules. This complex is capable of inhibiting DNA polymerase I and RNA polymerase, showing cytotoxic behaviour *in vivo* against L1210 tumors, Ehrlich ascites, and the sarcoma 180 and P388 tumor lines, as well as exhibiting DNA-binding in a manner similar to that of cisplatin^{35, 36, 46, 47} and is a suitable model complex for these therapeutic dirhodium carboxylates. However, because of the strong affinity for thiolate binding to the dirhodium(II) carboxylates' axial coordination sites, intracellular thiols like glutathione may prevent these rhodium-based therapeutics from reaching their intended target unchanged, especially with the Rh axial bioactive site remaining available. Axial coordination by the strongly binding thiolates will then block the intended activity.

Spectroscopic studies of glutathione binding to dirhodium tetraacetate and related compounds have been reported previously by Jakimowicz et al.⁴⁸ In the case of Jackimowicz et al., following the addition of molar equivalents of GSH to $\text{Rh}_2(\text{OAc})_4$, the

authors surmised that the stoichiometric ratio, GSH:Rh₂(OAc)₄, for the final conjugate was 2:1. Unfortunately, optical spectra provide limited information, as the spectral data results from an averaged signal of all the chromophores present. The determination of the stoichiometric ratio as a function of GSH is of critical importance in the assessment of dirhodium complexes with therapeutic properties, because chemistry that involves coordination to both axial sites would effectively block the therapeutic drug. With the resolving power of electrospray ionization mass spectrometry (ESI-MS), one is able to accurately describe the products formed in reactions of Rh₂(OAc)₄ with thiolates and determine whether this potentially therapeutic agent would likely survive attack by biological thiols.

This Chapter reports on the products formed following reaction of GSH with Rh₂(OAc)₄, as well as its competition with methionine-bound Rh₂(OAc)₄, to probe the fate of the rhodium complex after attack by the thiol and thioether groups, respectively. The reactions were studied *in vitro* using UV-visible and circular dichroism (CD) absorption spectroscopy, and electrospray-ionization mass spectrometry (ESI-MS). ESI-MS, which is now in this Thesis well established as an especially powerful as a technique for monitoring all possible intermediates formed in a reaction. Computational analysis by time-dependent density functional theory (TD-DFT) shows the extent of the overlap of both the linking acetates with the dirhodium d orbitals, and the major influence of the presence of water and thiolate axial ligands on all orbitals of the complex. The TD-DFT results explained the unexpected stoichiometric ratio of the glutathione products. These calculations show that the lowest energy absorption band blue-shifts with the addition of strong electron donors. The results described below show that GSH does attack the Rh₂(OAc)₄, but the stoichiometric ratio is 1:1 (Figure 6-1) unless there is large excess. If the drug complex was protected with the thioether of methionine (Figure 6-1D), the ESI-mass spectra show that GSH would eventually displace that group. However, unlike previously reported reactions with the cysteine-rich, human protein, metallothionein,⁴⁹ GSH did not disassemble the complex, leaving it intact, but with one of its axial reaction sites blocked. These results give detailed guidance for predicting the pharmacokinetics of potential metallodrugs and provide a mechanism by which the strongly binding GSH may be inhibited.

6.2 Experimental Methods

Solutions of 500 μM $\text{Rh}_2(\text{OAc})_4$ (Sigma Aldrich) and 10 mM glutathione (Fluka) in deionized water were deoxygenated under vacuum and backfilled with argon gas. For the UV-visible (Varian Cary 50 UV-visible Spectrophotometer) and circular dichroism (CD) (Jasco 810 Spectropolarimeter (Jasco, New Jersey, USA)) spectroscopic measurements, aliquots of 0, 0.5, 1.0, 1.5, 2.0, and 2.5, mol. eq. (and additionally, 3.0, and 4.0 mol. eq. for the UV-visible absorption spectra) of GSH were added to an argon-backfilled quartz cuvette sealed with a septum cap containing the dirhodium solution, with the data recorded after each addition. For the first ESI-MS data collection (Figure 6-4), excess reduced glutathione was added to a 500 μM $\text{Rh}_2(\text{OAc})_4$ solution in water at pH 3.0, and the mass spectral data were collected in positive ion mode; in the second series (Figure 6-4), solutions with 500 μM $\text{Rh}_2(\text{OAc})_4$ were titrated with 1.0, 1.5, and 2.5 mol. eq. 500 μM GSH in 1 mM NH_4OAc buffer at pH 7.4, recorded in both positive and negative ion mode. A Bruker Micro-TOF II instrument (Bruker Daltonics, Toronto, ON) operated in both positive and negative ion mode was used to collect the data. NaI was used as an external calibrant. The following settings were used: scan, m/z 50–3000; rolling average, 2; nebulizer, 2 bar; dry gas, 80°C at a rate of 8.0 L/min; capillary, 4000 V; end plate offset, -500 V; capillary exit, 175 V; skimmer 1, 30.0 V; skimmer 2, 23.5 V; hexapole RF, 800 V.

For the reactions with methionine followed by competition with GSH, solutions of 500 μM $\text{Rh}_2(\text{OAc})_4$, 10 mM DL-methionine (Sigma), and 10 mM glutathione in deionized water were deoxygenated under vacuum and backfilled with argon gas. The changes in the $\text{Rh}_2(\text{OAc})_4$ solution were monitored following the addition of 2 mol. eq. of methionine using UV-visible absorption spectroscopy, followed by a subsequent addition of 2 mol. eq. of GSH. ESI-mass spectra were taken after each addition using the negative ion mode. The settings were similar to those described previously.

$\text{Rh}_2(\text{OAc})_4$, $\text{Rh}_2(\text{OAc})_4(\text{H}_2\text{O})_2$, $[\text{Rh}_2(\text{OAc})_4(\text{GS})(\text{H}_2\text{O})]^-$, and $[\text{Rh}_2(\text{OAc})_4(\text{GS})_2]^{2-}$, models were drawn using the Scigress Modelling Software.⁵⁰ GS represents the deprotonated glutathione moiety. Ground-state geometry optimization and TD-DFT calculations were performed using the Gaussian G09 program,⁵¹ using the CAM-B3LYP functional. The 6-

31G(d,p) basis set was used for all atoms except for Rh, and the LANL2DZ basis set was used for Rh atoms. The TD-DFT calculations were carried out on the minimized geometry in single point mode, with 100 excited states calculated using the CAM-B3LYP functional, the 6-31G(d,p) basis set for all atoms except for Rh, and the LANL2DZ basis set for the Rh atoms.

6.3 Results and Discussion

6.3.1 UV-Visible and Circular Dichroism Spectroscopy Following the Colourful Reaction of Glutathione with $\text{Rh}_2(\text{OAc})_4$

The reaction of GSH with $\text{Rh}_2(\text{OAc})_4$ was followed with UV-visible absorption spectroscopy (Figure 6-2) and CD spectroscopy (Figure 6-3). With the introduction of glutathione, a new absorption shoulder appears at approximately 353 nm (Figure 6-2) which has been assigned to a $\text{S}(\sigma) \rightarrow \text{Rh}(\sigma^*)$ LMCT characteristic of sulfur coordination to dirhodium carboxylates.^{45, 48} A similar band has been previously reported for the spectrum of $\text{Rh}_2(\text{OAc})_4$ coordinated to the cysteine-rich protein, metallothionein.⁴⁹ discussed below, the assignment is better described as resulting from a mixture of molecular orbitals (MO) involving both the Rh-Rh MOs and the thiolate orbitals. The rapid change in spectral properties was observable with the naked eye, as the solution changed from sky blue to golden yellow as the titration progressed. This was expected as a result of the development of absorbance below 400 nm, which was much more intense than the weaker 589 nm absorption characteristic of the metal-metal-bond. The band at 448 nm has been assigned to $\text{Rh}_2(\pi^*) \rightarrow \text{Rh}-\text{O}(\sigma^*)$ transitions of the tetraacetate ligands,^{45, 48} which will be expanded on in the computational results below. The band at 589 nm represents the $\text{Rh}_2(\pi^*) \rightarrow \text{Rh}_2(\sigma^*)$ transition of the metal-metal single bond, which persists throughout the addition of the GSH and, therefore, shows that the Rh-Rh single bond is still intact following thiolate coordination. Only water was used as the solvent for these spectroscopic studies as others, like acetonitrile, involve coordinating moieties that can drastically alter spectroscopic results.

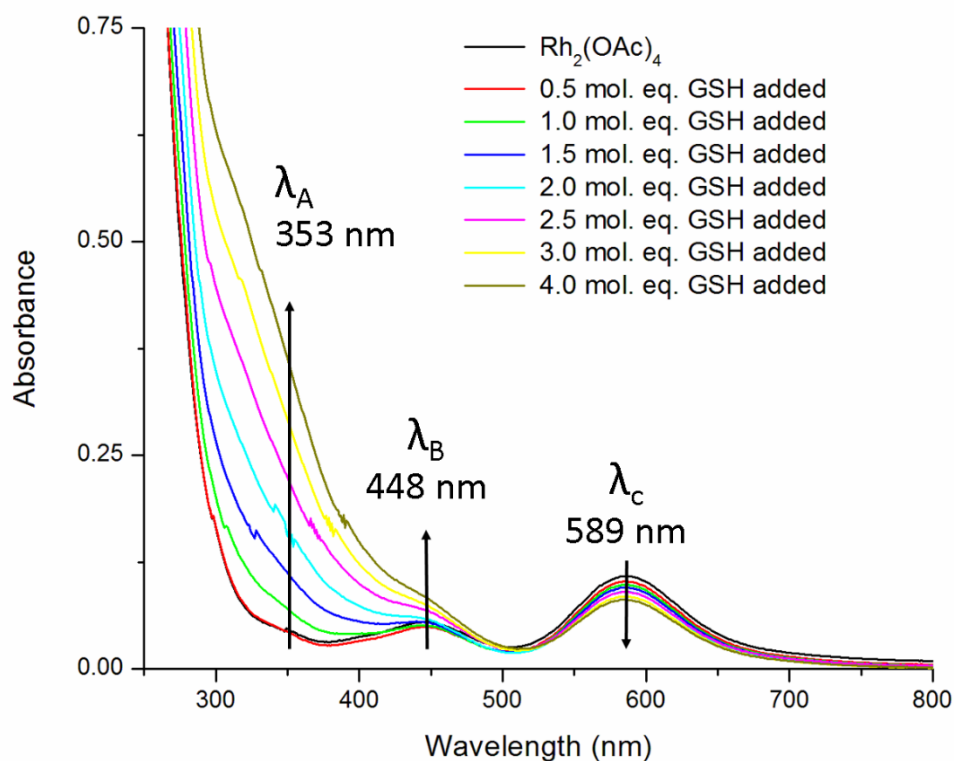


Figure 6-2 UV-visible absorption spectra of 500 μM $\text{Rh}_2(\text{OAc})_4$ with aliquots of reduced GSH added at pH 3.0 in deionized water.

λ_A : $S(\sigma) \rightarrow \text{Rh}(\sigma^*)$ LMCT at 353 nm. λ_B : $\text{Rh}_2(\pi^*) \rightarrow \text{Rh}-\text{O}(\sigma^*)$ at 448 nm. λ_C : $\text{Rh}_2(\pi^*) \rightarrow \text{Rh}_2(\sigma^*)$ at 589 nm. The arrows show the direction of change in absorbance with an increasing amount of GSH present. Reproduced from D. L. Wong et al., reproduced with permission from the Royal Society of Chemistry.¹⁸

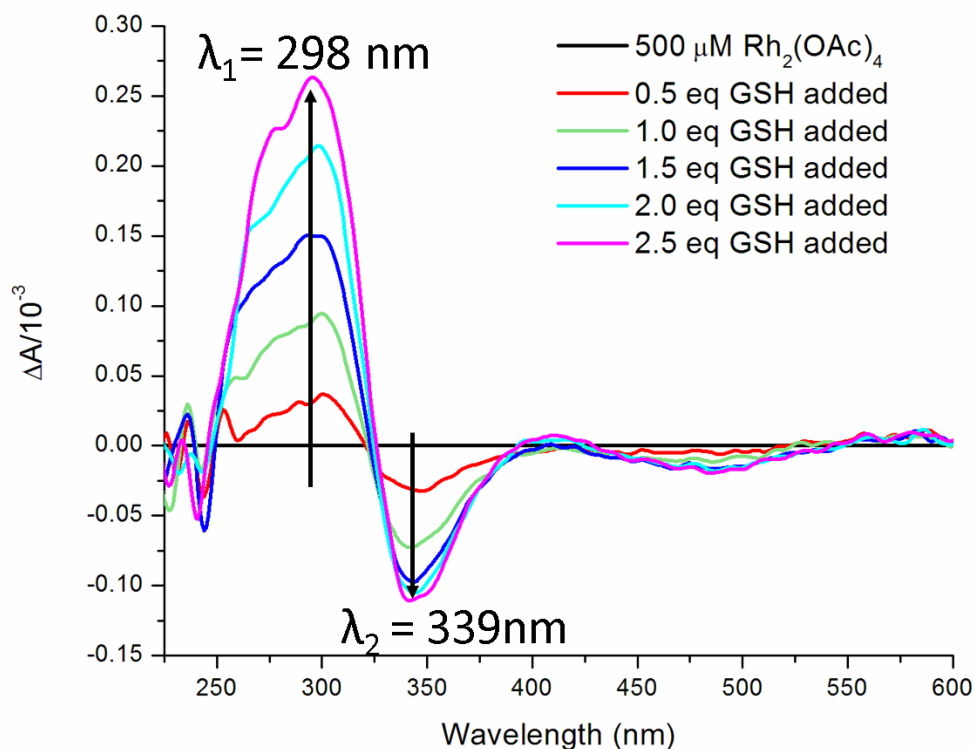


Figure 6-3 CD spectral results of glutathione reacting with $\text{Rh}_2(\text{OAc})_4$. Circular dichroism spectra of $500 \mu\text{M}$ $\text{Rh}_2(\text{OAc})_4$ following addition of 0, 0.5, 1.0, 1.5, 2.0, and 2.5 mol. eq. aliquots of 10 mM reduced GSH added. The arrows show the direction of change in absorbance with increasing amount of GSH present. GSH does not absorb in the region shown. Reproduced from D. L. Wong *et al.*, reproduced with permission from the Royal Society of Chemistry.¹⁸

The CD spectra shows that $\text{Rh}_2(\text{OAc})_4$ is achiral, as expected (black line, Figure 6-3). However, with the introduction of GSH, two new bands appear, a maximum at 298 nm (marked as λ_1) and a minimum at 339 nm (marked as λ_2), with a crossover point between 325 and 330 nm. The development of the strong CD spectrum with the coordination of GSH indicates that a chiral structure is formed upon binding GSH to the dirhodium complex. The arrows show the change in chiral signal over the course of the titration. Similar CD spectral changes have been reported previously for reactions of GSH with Cu(I) and Cd(II).⁵² There was little to no CD intensity under the metal-metal-bond band

at 589 nm. This was not unexpected, as the transition dipoles obtained from the computational results below are located away from the chirality introduced by the GSH.

6.3.2 Analysis by Electrospray Ionization Mass Spectrometry

An inherent property of mass spectrometry is the creation of charged species for their detection. All the masses in the spectra correspond to the charged species.

Spectra taken at pH 3.0 of $\text{Rh}_2(\text{OAc})_4$ with excess reduced glutathione show the presence of mono- and di-glutathione adducts (Figure 6-4). The ESI-mass spectral data shows that the reaction creates a mixture of species: (i) glutathione polymers (at 615.1, 922.2 (A), and 1229.3 (C) m/z, Figure 6-4); and (ii) deprotonated glutathione coordination of the $\text{Rh}_2(\text{OAc})_4$ forming $[(\text{GS})\text{Rh}_2(\text{OAc})_4]$, $[(\text{GS})_2\text{Rh}_2(\text{OAc})_4]$, and $[(\text{GS})_3\text{Rh}_2(\text{OAc})_4]$ at below 1% relative intensity (at 749.9 (star, Figure 6-4), 1056.0 (star, Figure 6-4), and 1364.1 m/z (D, Figure 6-4)). The two most prominent conjugates are those of a single deprotonated glutathione-bound complex, $[\text{GS}-\text{Rh}_2(\text{OAc})_4]$ (Figure 6-1C), and that of a double deprotonated di-glutathione-bound complex, $[(\text{GS})_2-\text{Rh}_2(\text{OAc})_4]$ (Figure 6-1E). With the accuracy of the ESI-MS experiment, it is observed that the masses of these two new complexes differ from the sum of the individual components by one and two protons, respectively, indicating that a proton is lost to form the binding moiety. Coupled with the optical spectroscopic data, we identify the cysteine sulfur as being the donor atom from the GSH that is involved. The GS^- binds to the vacant axial position of $\text{Rh}_2(\text{OAc})_4$ that is generally coordinated by solvent, as is confirmed by similar studies concerning dirhodium complexes.^{38, 40}

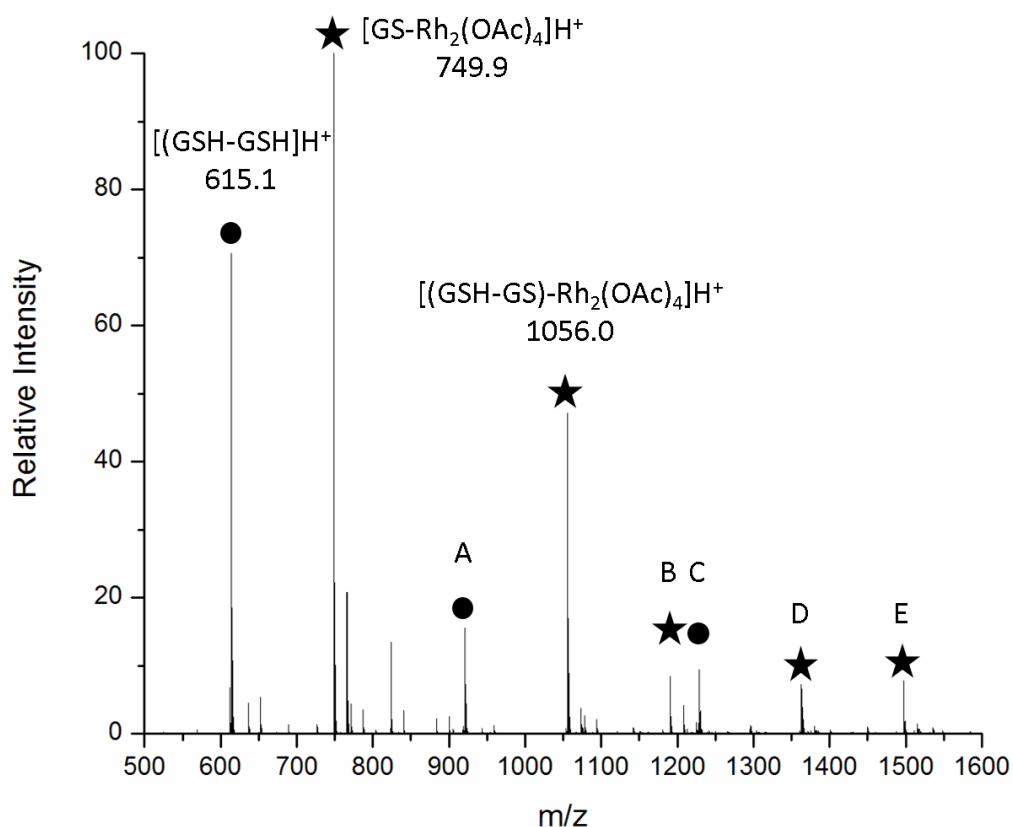


Figure 6-4 Low pH reaction of $\text{Rh}_2(\text{OAc})_4$ with GSH

ESI – mass spectra of $500 \mu\text{M}$. $\text{Rh}_2(\text{OAc})_4$ with excess reduced glutathione added, at pH 3.0 in deionized water. Taken in the positive ion mode. The circles identify GSH-related complexes, where A = $(\text{GSH})_3$ at 922.2 m/z , C = $(\text{GSH})_4$ at 1229.3 m/z and the stars indicate $\text{Rh}_2(\text{OAc})_4$ -related complexes, where B = $(\text{GS})[\text{Rh}_2(\text{OAc})_4]_2$ at 1191.8 m/z , D = $(\text{GS})_3\text{Rh}_2(\text{OAc})_4$ at 1364.1 m/z and E = $(\text{GS})_2\text{-}[\text{Rh}_2(\text{OAc})_4]_2$ at 1498.9 m/z . (Note that in the positive ion mode the complexes will be oxidized in the ionization process so the masses correspond to the complexes with correct charges, but are observed as the monocation). Reproduced from D. L. Wong et al., reproduced with permission from the Royal Society of Chemistry. ¹⁸.

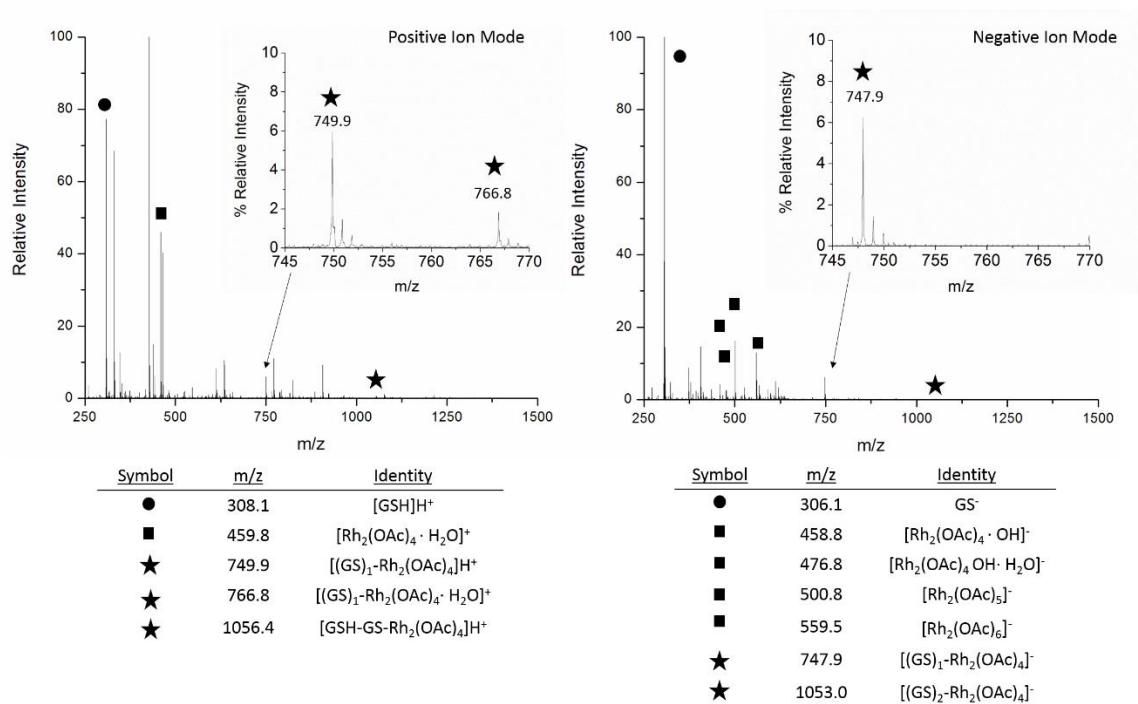


Figure 6-5 Reaction of Rh₂(OAc)₄ with GSH at physiological pH

ESI-Mass spectra of 500 μM Rh₂(OAc)₄ with 2.5 mol. eq. 500 μM GSH added, in 1 mM NH₄OAc buffer at pH 7.4, recorded in both positive (left) and negative (right) ion mode. The insets show detail of the mono-adduct glutathione-rhodium complex region at near 750 m/z for both polarities. The individual peaks are assigned in the tables. (Note that in the positive ion mode the complexes will be oxidized in the ionisation process so the masses correspond to the complexes with correct charges, but are observed as the monocation.) Reproduced from D. L. Wong et al., reproduced with permission from the Royal Society of Chemistry.¹⁸

To test the possibility of conjugation under a more physiologically relevant environment, the reaction was carried out using 500 μM Rh₂(OAc)₄ with 2.5 mol. eq. GSH added in 1 mM NH₄OAc at pH 7.4, Figure 6-5. Under these conditions, glutathione remains largely unbound at 308.1 m/z in the positive ion mode (further denoted as “+ mode”), and 306.1 m/z in the negative ion mode (further denoted as “- mode”). The main Rh₂(OAc)₄ species observed are the mono-aquated products (Figure 6-1F) at 459.8 m/z (+ mode), or 458.8 m/z in the negative ion mode, where the bis-aquated (Figure 6-1G), mono-acetate (Figure

6-1H) and bis-acetate coordinated species (Figure 6-1I) are also observed at 476.8, 500.8, and 559.5 m/z. At a relative intensity of under 10%, the glutathione mono-adduct product is observable at 749.9 m/z (+ mode), and 747.9 m/z (- mode), corresponding to a complex involving a deprotonated glutathione and the $\text{Rh}_2(\text{OAc})_4$. Very little di-glutathione adduct product was observed, at 1056.4 m/z (+ mode) and 1053.0 m/z (- mode), both at less than 1% relative abundance, with virtually none of the possible tri-adduct detected.

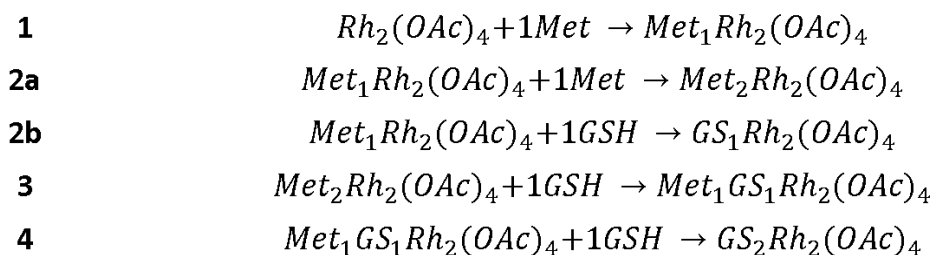
These quantitative results provide evidence for the exact products made in solution, and their relative abundancies viewed in both positive and negative ion mode. It is clear that the strong absorption band reported by Jakimowicz et al. should not be assigned to a 2:1 GSH: $\text{Rh}_2(\text{OAc})_4$ stoichiometry, rather the product formed in that study was likely 1:1. The computational results below provide an interpretation of the appearance of the strong absorption below 400 nm following coordination with thiolates.

At this point, it has been established that GSH binds as a deprotonated peptide to the $\text{Rh}_2(\text{OAc})_4$ axial positions, forming the mono-adduct at 749.9 m/z (+ mode). The combination of mass spectral data and the absorption and CD spectra suggest that the tetraacetate linkers are intact and that the Rh-Rh single bond persists. To address the structures of the proposed products, the structure of the singly-bound, and doubly-bound glutathione- $\text{Rh}_2(\text{OAc})_4$ complexes were constructed in the Scigress Modelling Software and their geometries optimized prior to molecular orbital (MO) calculations using TD-DFT methods, described below.

6.3.3 Competition by Glutathione for the Axially-Coordinated Methionine in $\text{Rh}_2(\text{OAc})_4(\text{Met})$

In Chapter 4 and 5, the studies with metallothionein suggested axial coordination of the dirhodium core by the cysteinyl thiolates was the initiating reaction prior to complex deconstruction, because the additional cysteines in the protein bound in the place of the O-donors of the tetraacetate ligands.⁴⁹ As discussed above, cellular resistance can be associated with thiol coordination of the active sites of metallodrugs. Blocking these axial positions of the metallodrug with weak nucleophiles should introduce a defense against cellular resistance due to steric effects impeding the attack by strong nucleophiles. The

question arises how best to protect the complex against fast attack by such agents as metallothionein and GSH. The use of a weaker binding ligand, such as the thioether of methionine, may provide this protection. The reaction of methionine and related thioether complexes with $Rh_2(OAc)_4$ has been reported by Pneumatikakis et al. and others^{38, 42, 53}. This Chapter explores the reaction when glutathione is added after methionine is bound to the $Rh_2(OAc)_4$. Scheme 6-1 summarizes the series of possible reactions that were used to investigate the potential protection offered by methionine (Met) against competition by GSH. First, when Met is added to the dirhodium complex. Using absorption spectra and ESI-mass spectral data, the products formed can be determined: either a single Met binds (Scheme 6-1, Equation 1, also Figure 6-1J) or two Met bind (Scheme 6-1, Equation 2a, also Figure 6-1K). Next, GSH is added, and again, Scheme 6-1 shows the possible outcomes: either displacement of one Met bound (Scheme 6-1, Equation 2b, also Figure 6-1L), addition to the 2nd axial position (Scheme 6-1, Equation 3), or complete occupation of both axial positions (Scheme 6-1, Equation 4). The question then is, does Met offer any protection against axial ligation and therefore deactivation by strongly nucleophilic biological thiols, such as GSH and metallothionein, before the drug can reach its eventual target?



Scheme 6-1 Reaction equations depicting possible outcomes of glutathione added to methionine-bound $Rh_2(OAc)_4$.

The structures of each species described here in Scheme 6-1 Reaction equations depicting possible outcomes of glutathione added to methionine-bound $Rh_2(OAc)_4$ are shown in Figure 6-1. The reactions all depict axial ligation of the dirhodium core. The GSH coordinated cores will be monoanions or dianions in solution but following the ionisation process the mass spectral data show only monocations and monoanions

representing the redox nature of the ionisation process. Reproduced from reference¹⁸ with permission from the Royal Society of Chemistry.

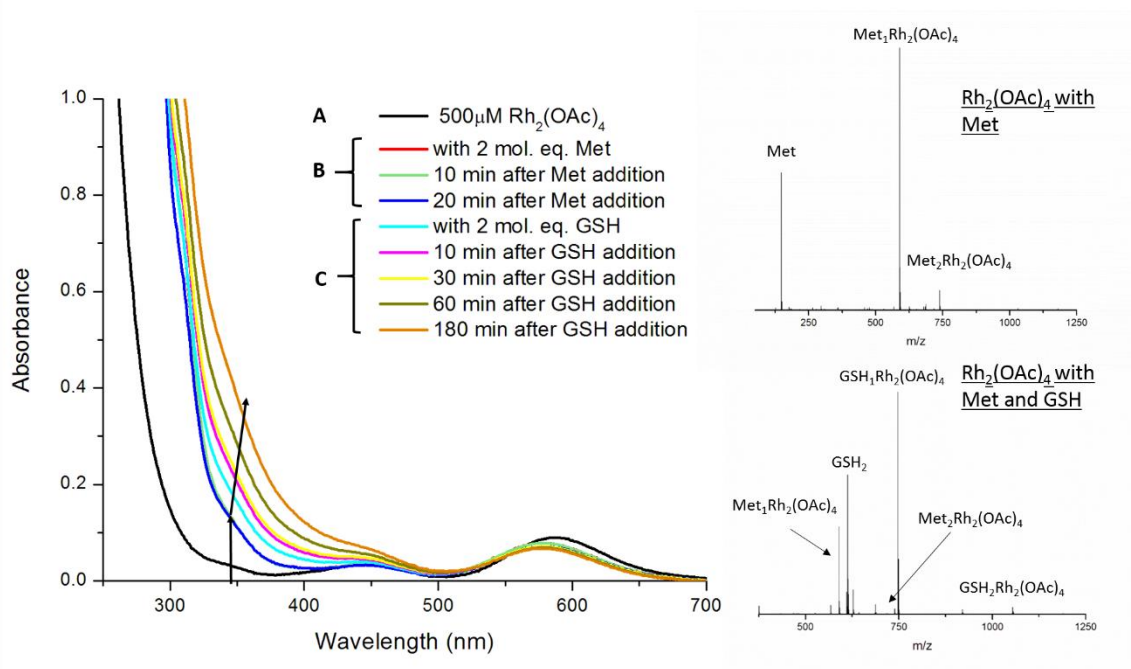


Figure 6-6 UV-visible absorption spectral changes following the reaction of an aqueous solution of 500 μM Rh₂(OAc)₄ with 2 mol. eq. of methionine (Met) following 20 minutes of mixing. 2 mol. eq. of glutathione was then added and the spectrum monitored. The absorption spectra (left) can be separated into three sections: A) black line, the initial blue solution; B) with 2 mol. eq. Met followed for 20 minutes, red, green, and blue lines; the red and green lines are obscured by the 20 minute blue line as the reaction was fast. C) after addition of 2 mol. eq. GSH, followed for 180 min, cyan, pink, yellow, green, brown lines. ESI-mass spectra of the initial methionine bound solution (right, top) and following glutathione addition (right, bottom) were recorded at 20 minutes and 60 minutes after mixing, respectively, in negative ion mode. Notable peaks: Met₁(Rh₂(OAc)₄) 589.9 m/z; (Met)₂(Rh₂(OAc)₄) 738.9 m/z; (GS)(Rh₂(OAc)₄) 747.8 m/z; (GS)₂(Rh₂(OAc)₄) 1054.9 m/z. There was no evidence for (Met)(GSH)Rh₂(OAc)₄ in the expected region of 890-895 m/z. Reproduced from D. L. Wong et al., reproduced with permission from the Royal Society of Chemistry.¹⁸

Figure 6-6 shows the absorption and ESI-mass spectra recorded for the reactions outlined in Scheme 6-1. The absorption spectrum follows the same trends as described above. The

starting spectrum of the $\text{Rh}_2(\text{OAc})_4$ in Figure 6-4(A) is the same as in Figure 6-1. The addition of 2 mol. eq. of Met results in a slight, but distinct blue-shift in the wavelength maximum of the $\text{Rh}_2(\pi^*) \rightarrow \text{Rh}_2(\sigma^*)$ metal-metal bond band from 589 to 570 nm, indicating as before, that while Met has bound to the complex, the Rh-Rh bond is still intact. The most significant change is the intensification of the band at 350 nm associated with the thioether coordination⁴⁰ (Figure 6-6B). The reaction is fast and there is no change after 20 minutes following mixing (B). Now the Met coordination is challenged by addition of 2 mol. eq. of GSH, which results in a slow change in the optical spectrum, with a significant increase in absorbance in the 353 nm region representing the competition of glutathione for the axial position occupied by the methionine (Figure 6-6C). There is a slight red shift in the 580 nm region that confirms the Rh-Rh bond is still present.

Negative ion mode ESI-mass spectra are very important in providing identification of the species present at each step (Figure 6-6, inset, top). Following the addition of the Met, the solution measured in the absorption as “B”, is primarily $(\text{Met})_1(\text{Rh}_2(\text{OAc})_4)$ at 589.9 m/z as shown in Scheme 6-1, equation 1, with a very small fraction of $(\text{Met})_2(\text{Rh}_2(\text{OAc})_4)$ at 738.9 m/z formed in equation 2a. Following GSH addition (lines “C” in the absorption spectra), the negative ion ESI-mass spectrum (Figure 6-6, inset, bottom) shows the presence of $[(\text{GS})_1(\text{Rh}_2(\text{OAc})_4)]$ at 747.8 m/z formed in Scheme 6-1, equation 2b, and also $[(\text{GS})_2(\text{Rh}_2(\text{OAc})_4)]$ at 1054.9 m/z formed in Scheme 6-1, equation 4. The reactions with GSH were slow, as indicated in the absorption spectra measured over 3 hours, and still possibly not at completion when the mass spectra were measured.

These results conclude that indeed Met does offer some protection because the displacement reaction is slow, and the binding by the strongly nucleophilic GS^- is impeded. However, from a pharmacokinetic point-of-view, the exact rates *in vivo* would need to be determined.

6.3.4 DFT Calculations Provide Insight into the Stability of the GSH Complexes

An accurate X-ray structure of the $\text{Rh}_2(\text{OAc})_4(\text{H}_2\text{O})_2$ was reported by Cotton et al. in 1971, showing specifically, for this paper, the location of the two water molecules on the z-axis defined by the Rh-Rh bond.⁵⁴ The Rh-Rh bond length calculated here for $\text{Rh}_2(\text{OAc})_4(\text{H}_2\text{O})_2$ is 2.390 Å, which compares well with the reported value of 2.386 Å.⁵⁴ For the results described above, we wanted to examine the electronic structure of the complex in solution and when axially coordinated by GSH. There were three specific questions: (i) how extensive is the stabilizing role of the acetate linkers (ii) what is the extent of the disturbance to the Rh-Rh 4d-based MO structure of the core caused by coordination of the glutathione thiolate ligand, and (iii) can the dramatic colour change from blue to yellow immediately after addition of the thiolates be explained from the calculated absorption spectrum using time dependent-DFT (TD-DFT) methods? A charge of -1 and -2 was entered in the Gaussian input file for $[\text{Rh}(\text{OAc})_4(\text{GS})(\text{H}_2\text{O})]^-$ and $[\text{Rh}(\text{OAc})_4(\text{GS})_2]^{2-}$, respectively, because the GS thiolate brings in a negative charge when it coordinates to the neutral dirhodium core.

i) **The electronic structure of $\text{Rh}_2(\text{OAc})_4$ and $\text{Rh}_2(\text{OAc})_4(\text{H}_2\text{O})_2$ to determine the effect of axial coordination by the water solvent**

Axial coordination of the Rh_2 core has been the subject of much study^{38, 40, 42, 44, 45, 48, 53, 55-58} since the electronic structure for the metal-metal bonded species suggested a single bond, that would leave $5p_z$ or the $4d_z^2$ as available, empty orbitals. The electronic structure leading to the Rh-Rh bond and its bond order, are reflected in the absorption spectrum. Polarized crystal spectra of Martin et al.⁵⁹ (1979, revised slightly by Miskowski et al. in 1984)⁶⁰ provided key information in the assignment; first of the lowest energy, visible region band to the π^* to σ^* transition, followed at higher energies to mixtures of Rh-based MOs to the σ^* orbital and also ligand to Rh-Rh core transitions. A more recent report by Futera et al. in 2011,⁶¹ reported the electron occupancies based on DFT calculations. For completeness in our discussion of the GSH to the axial Rh(II) bond formation, we have included DFT results for the axial ligand-free core Figure 6-7, and the H_2O ligated core in Figure 6-8.

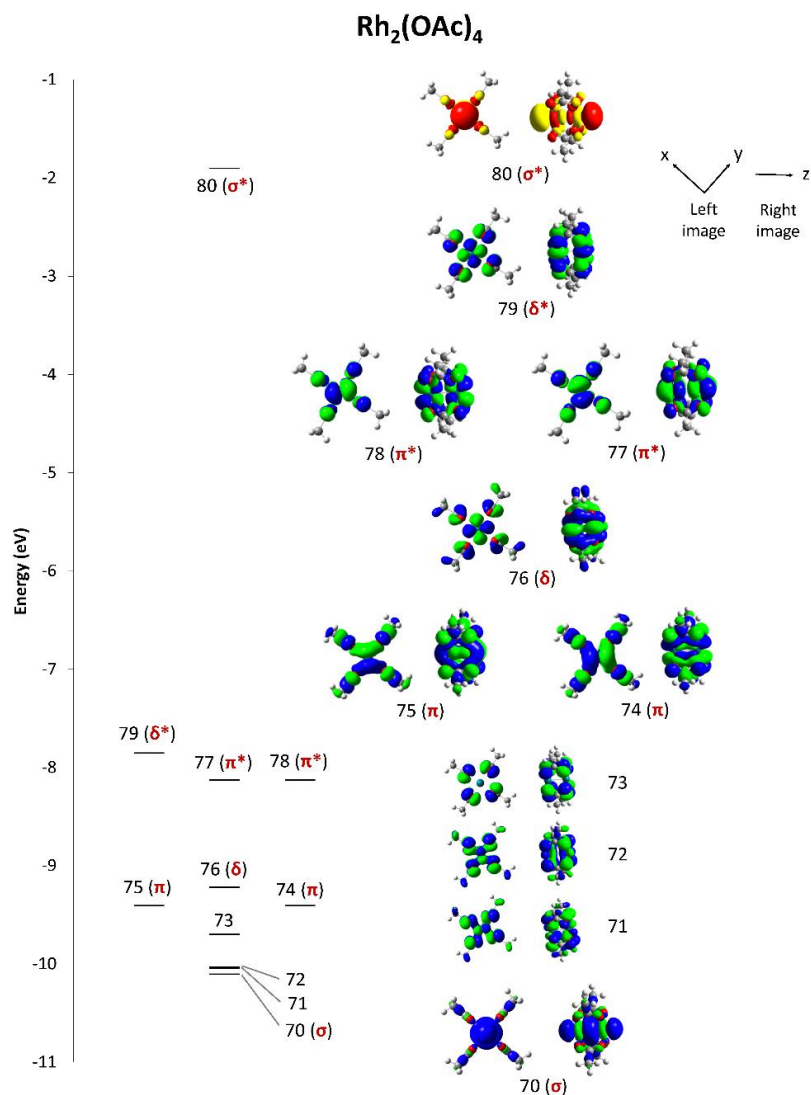


Figure 6-7 MO energies and isoelectric density surfaces for the MOs that contribute to the visible-near UV absorption spectra for $[\text{Rh}_2(\text{OAc})_4]$, from DFT geometry optimization calculations.

Yellow and red surfaces represent unoccupied MOs, blue and green surfaces represent occupied MOs. The Rh-Rh core MOs are identified where clear. The isoelectric surfaces are displayed in two orientations: (left) looking down the Rh-Rh bond so exposing the x/y plane and (right) looking down the x/y plane at the horizontally aligned Rh-Rh bond.

Both orientations are easiest to see starting with the σ^ orbital at the top of the stack of orbitals. An expanded version is available in Appendix D. Calculations and image from A. Zhang in D. L. Wong et al., reproduced with permission from the Royal Society of Chemistry.¹⁸*

Figure 6-7 shows the DFT results for the dirhodium core with just the acetate linkages. The MO order follows the expected sequence with the exception of the increased energy of the δ^* MO (79). The gas phase calculation shows that δ^* lies just above the π^* MOs (77 and 78). We have labelled the well-known MOs with 4d origin (the occupied: σ (70), π (74, 75), δ (76), π^* (77, 78), and δ^* (79) and the lowest unoccupied MO, σ^* (80)). The isoelectric surface images provide the spatial distribution of these orbitals, showing two orientations. On the left, the view is looking down the Rh-Rh bond, so this is the x/y direction. On the right, the viewing direction is perpendicular to the Rh-Rh bond, which is aligned horizontally to show the axial ligands and acetate linker MOs. Expanded views of all the MO surfaces are presented in Appendix D.

In aqueous solution the axial positions are coordinated by water (as in the X-ray structures of Cotton et al. (1971)⁵⁴) and this represents the species expected for optical and ESI-MS measurements. The MO energies and surfaces are shown in Figure 6-8. The coordination of the two water molecules increases the electron density of the two rhodium atoms, raising the energy of all the MOs in this region. Particularly, the σ MO (86) now lies above the δ (85) and π (83 & 84). In addition, the energy of the σ^* MO (90) is raised roughly 1 eV with respect to that orbital without the ligands (Figure 6-7, MO 80). As seen below (Figure 6-12), the lowest energy absorption band is blue-shifted from the 800 nm of the anhydrous $\text{Rh}_2(\text{OAc})_4$ to 600 nm for the dihydrate, because the π^* to σ^* energy gap increases. Except for the rise in σ (86), the ordering does not change, with the occupied δ (85) and δ^* (89) being located above the respective π and π^* MOs (83, 84, and 87, 88). The surfaces again provide interesting contrasts in the electron distribution for the linking acetates, the two waters, and the two Rh atoms. Symmetry rules mean that the water MOs are only involved in significant overlap with the z-axis σ and σ^* MOs (86 & 90).

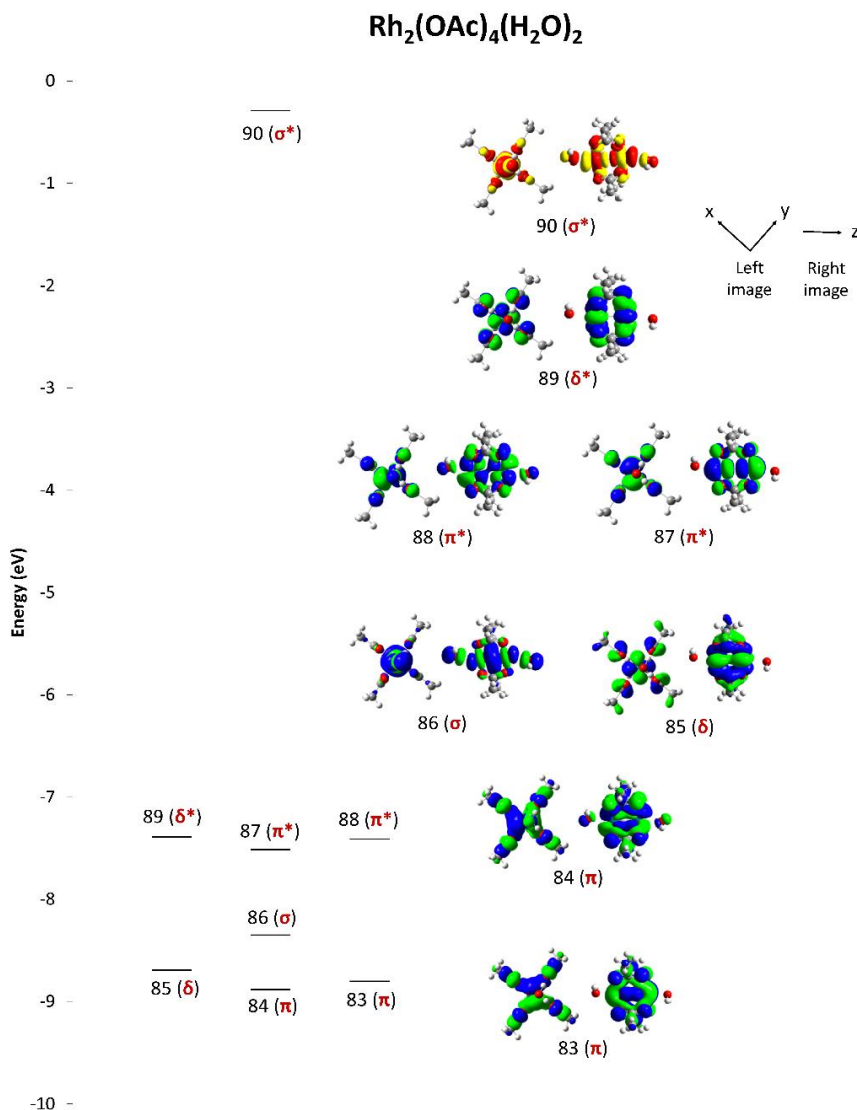


Figure 6-8 MO energies and isoelectric density surfaces for the MOs that contribute to the visible-near UV absorption spectra for $[\text{Rh}_2(\text{OAc})_4(\text{H}_2\text{O})_2]$ from DFT geometry optimization calculations.

Yellow and red surfaces represent unoccupied MOs, blue and green surfaces represent occupied MOs. The Rh-Rh core MOs are identified where clear. The isoelectric surfaces are displayed in two orientations: (left) looking down the Rh-Rh bond so exposing the x/y plane and (right) looking down the x/y plane at the horizontally aligned Rh-Rh bond. Both orientations are easiest to see starting with the σ^ orbital at the top of the stack of orbitals. An expanded version is available in Appendix D. Calculations and image from A. Zhang in D. L. Wong et al., reproduced with permission from the Royal Society of Chemistry.¹⁸*

ii) The electronic structure when thiol is coordinated: $[\text{Rh}_2(\text{OAc})_4(\text{GS})(\text{H}_2\text{O})]^-$ and $[\text{Rh}_2(\text{OAc})_4(\text{GS})_2]^{2-}$

The ESI-MS data in Figure 6-5 show the presence of both the mono- and di- GS^{2-} complexes, although the di- GS^{2-} product is in extremely low abundance. Figure 6-9 and Figure 6-10 show the interaction between the GS^- MOs and the dirhodium MOs. Figure 6-11 shows the expanded view of the σ^* , σ , and π^* MOs for $[\text{Rh}_2(\text{OAc})_4(\text{GS})(\text{H}_2\text{O})]^-$ and $[\text{Rh}_2(\text{OAc})_4(\text{GS})_2]^{2-}$. The MO structure for the mono-adduct (Figure 6-9) shows a significant rise in the energy of all the MOs compared to the bisacuated structure (Figure 6-10). This is due to the increased density on the Rh atoms from the axial coordination of the thiolate ligand. This time, because of the lack of axial symmetry, the σ (164) and one of the π^* (165) MOs rise in energy, now above the π^* (163) and δ^* (162). The surfaces show that the three residues of the tripeptide, GS^- , interact strongly with many of the Rh-Rh MOs, and not with the tetraacetate MOs. For example, of the highest lying occupied MOs, only π^* (163), δ^* (162), and δ (155) do not have significant contribution from the GS^- MOs. MOs 159, 160, and 156 are located mainly on the GS^- . The extensive overlap of the GS^- density with the Rh-Rh core MOs (Figure 6-11) accounts for the retention of the GS^- coordination of the $\text{Rh}_2(\text{OAc})_4$ complex in the ESI-mass spectrometer under the dehydrating conditions of the MS vacuum (Figure 6-5). Figure 6-10 shows the results of the calculations for $[\text{Rh}_2(\text{OAc})_4(\text{GS})_2]^{2-}$. The large donation of density from the two anionic glutathiones in $[\text{Rh}_2(\text{OAc})_4(\text{GS})_2]^{2-}$ raises the energy of the Rh-Rh σ MO (241) above π (240). With two GS^- there is significant overlap of the MOs of the tripeptide with all the Rh-Rh core MOs (Figure 6-11), shuffling the energy stack considerably. MOs 242-232 are located on the two GS^- ligands. Despite searching down to MO 220, an MO with symmetry characteristics of the δ (like MO 155 in Figure 6-10) were not found. The surfaces provide much more detail concerning the overlap of electron density than text can do justice to, so we direct the reader to Appendix D. The H_2O in $[\text{Rh}_2(\text{OAc})_4(\text{GS})(\text{H}_2\text{O})]^-$ does not coordinate to the dirhodium, instead it hydrogen bonds to the acetate linkers, seen in Figure 6-9.

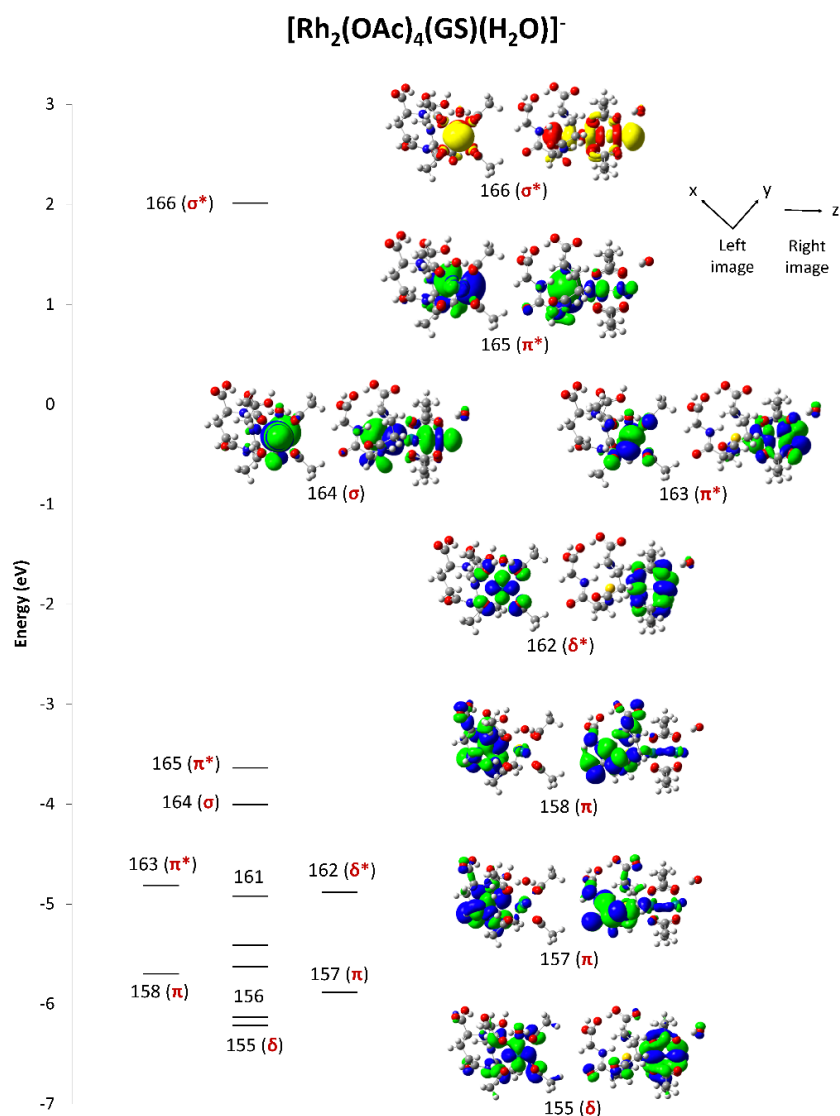


Figure 6-9 MO energies and isoelectric density surfaces for the MOs that contribute to the visible-near UV absorption spectra for [Rh₂(OAc)₄(GS)(H₂O)]⁻ from DFT geometry optimization calculations.

Yellow and red surfaces represent unoccupied MOs, blue and green surfaces represent occupied MOs. The Rh-Rh core MOs are identified where clear. The isoelectric surfaces are displayed in two orientations: (left) looking down the Rh-Rh bond so exposing the x/y plane and (right) looking down the x/y plane at the horizontally aligned Rh-Rh bond.

Both orientations are easiest to see starting with the σ^ orbital at the top of the stack of orbitals. An expanded version is available in Appendix D. Calculations and image from A. Zhang in D. L. Wong et al., reproduced with permission from the Royal Society of Chemistry.¹⁸*

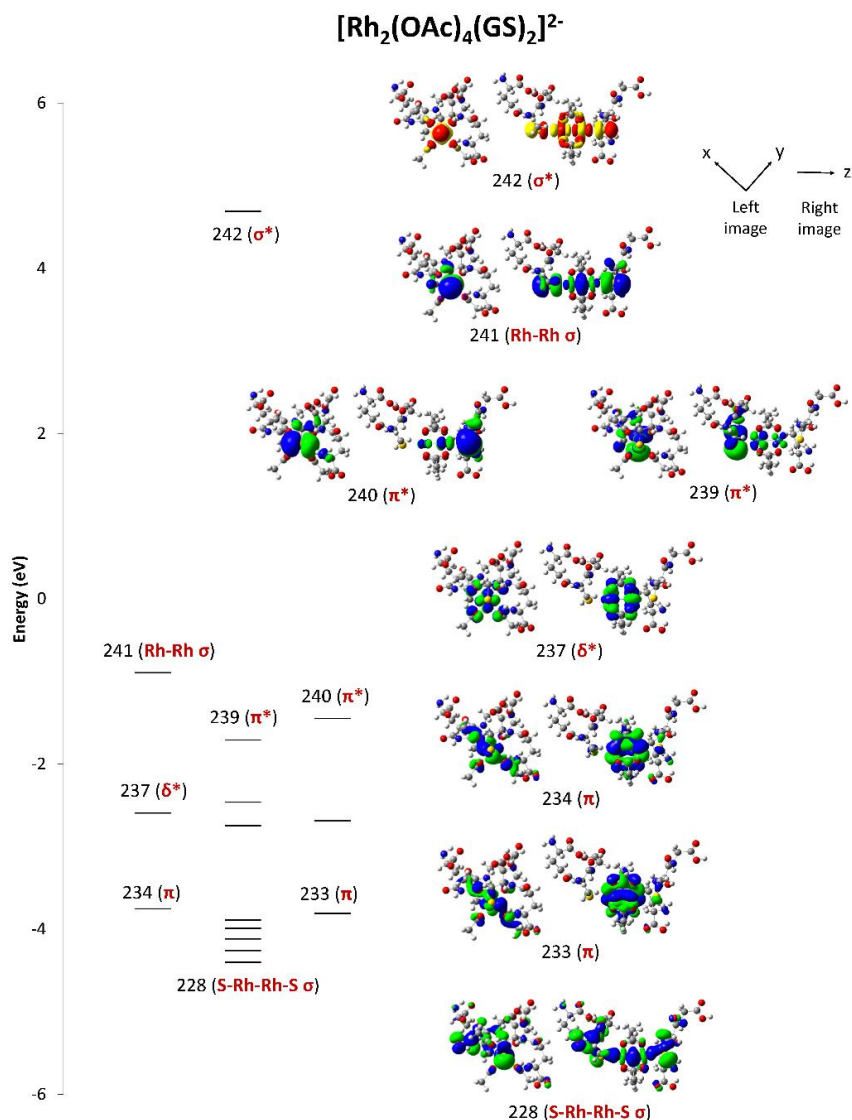


Figure 6-10 MO energies and isoelectric density surfaces for the MOs that contribute to the visible-near UV absorption spectra for $[\text{Rh}_2(\text{OAc})_4(\text{GS})_2]^{2-}$ from DFT geometry optimization calculations.

Yellow and red surfaces represent unoccupied MOs, blue and green surfaces represent occupied MOs. The Rh-Rh core MOs are identified where clear. The isoelectric surfaces are displayed in two orientations: (left) looking down the Rh-Rh bond so exposing the x/y plane and (right) looking down the x/y plane at the horizontally aligned Rh-Rh bond. Both orientations are easiest to see starting with the σ^ orbital at the top of the stack of orbitals. An expanded version is available in Appendix D Calculations and image from A. Zhang in D. L. Wong et al., reproduced with permission from the Royal Society of Chemistry.¹⁸*

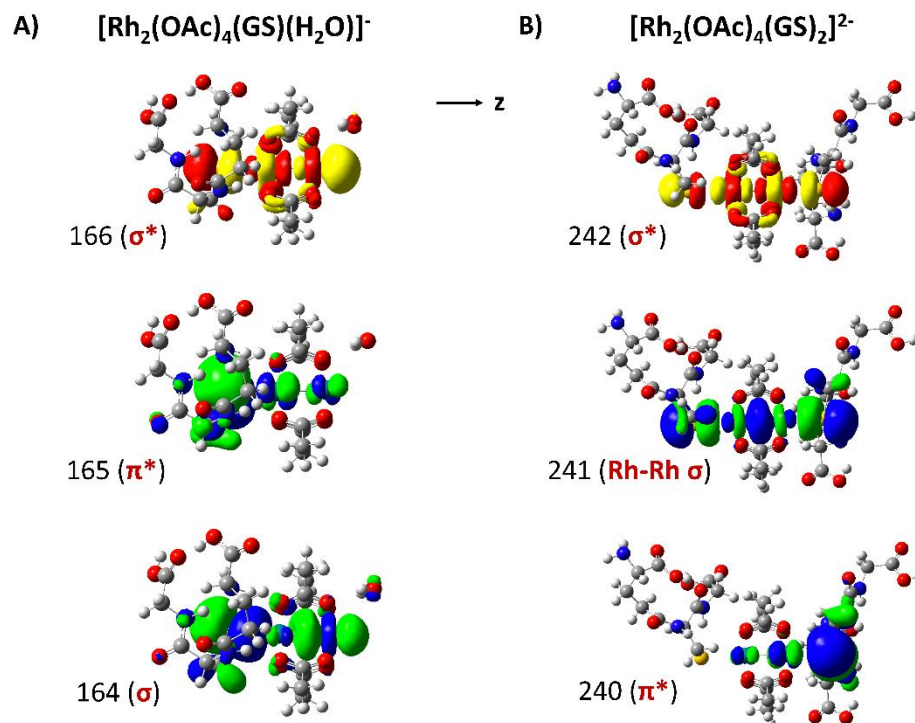


Figure 6-11 Electron density surface representation of the highest occupied and lowest unoccupied orbitals for $[\text{Rh}_2(\text{OAc})_4(\text{GS})(\text{H}_2\text{O})]^-$ and $[\text{Rh}_2(\text{OAc})_4(\text{GS})_2]^{2-}$.

These surfaces show the extensive overlap of the axially coordinated GS^- with the σ and π MOs of the Rh-Rh bond. An expanded version is available in Appendix D. Calculations and image from A. Zhang in D. L. Wong et al., reproduced with permission from the Royal Society of Chemistry.¹⁸

iii) Calculated absorption spectra for $[\text{Rh}_2(\text{OAc})_4]$, $[\text{Rh}_2(\text{OAc})_4(\text{H}_2\text{O})_2]$, $[\text{Rh}_2(\text{OAc})_4(\text{GS})(\text{H}_2\text{O})]^-$, and $[\text{Rh}_2(\text{OAc})_4(\text{GS})_2]^{2-}$

Figure 6-12A shows the calculated absorption spectra, labelled with the Excited States (ES) that show significant oscillator strength (a list of the excited states are available in Appendix D). Figure 6-12B shows the molecular orbital contributions to each excited state for $[\text{Rh}_2(\text{OAc})_4(\text{H}_2\text{O})_2]$, $[\text{Rh}_2(\text{OAc})_4(\text{GS})(\text{H}_2\text{O})]^-$.

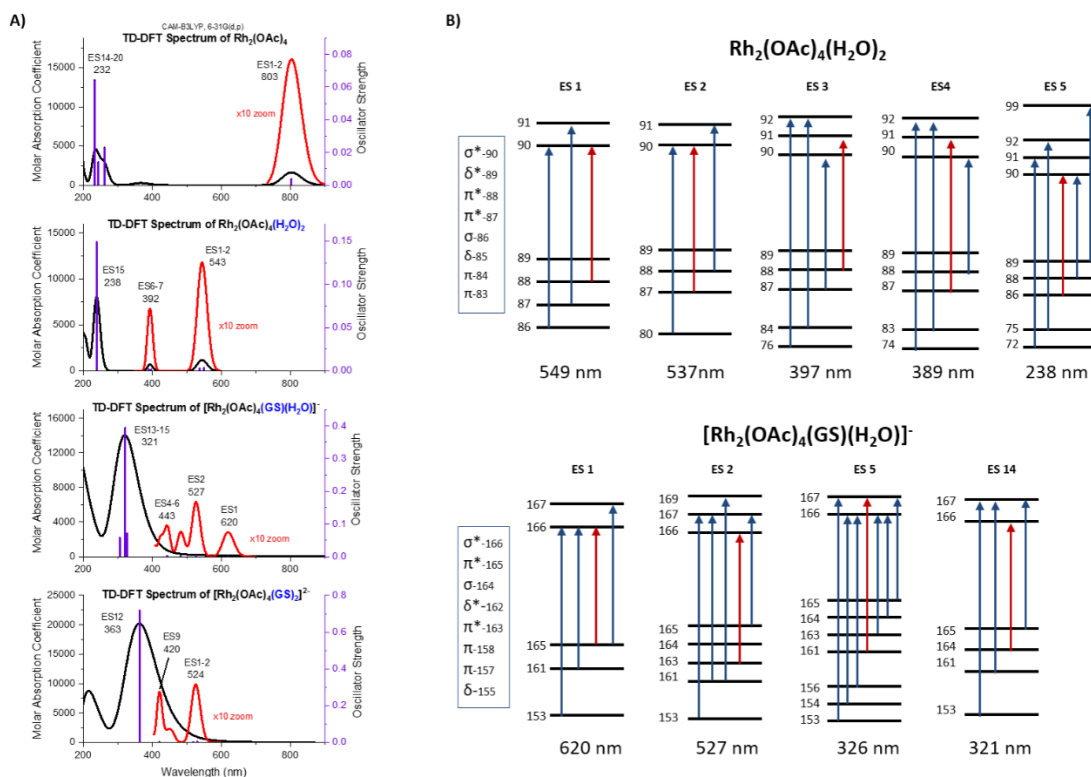


Figure 6-12 Calculated absorption and orbital contributions to the excited states from TD-DFT calculations for $\text{Rh}_2(\text{OAc})_4$ and the complex coordinated by water and GS^{1-} . A) Calculated absorption spectra for $[\text{Rh}_2(\text{OAc})_4]$, $[\text{Rh}_2(\text{OAc})_4(\text{H}_2\text{O})_2]$, $[\text{Rh}_2(\text{OAc})_4(\text{H}_2\text{O})(\text{GS})]^-$, and $[\text{Rh}_2(\text{OAc})_4(\text{GS})_2]^{2-}$. The labels “ES1,” etc. identify the Excited States for which the oscillator strength for the transition from ES_0 is greater than 0.001. The excited states calculated from TD-DFT are tabulated in Appendix D. (B) Orbital participation in the excited states above 230nm with oscillator strengths >0.001 for $[\text{Rh}_2(\text{OAc})_4(\text{H}_2\text{O})_2]$ and $[\text{Rh}_2(\text{OAc})_4(\text{H}_2\text{O})(\text{GS})]^-$. The red arrow represents the transition with the highest contribution. The detailed contributions are shown in Table S1 in Appendix D. The MOs of the Rh_2 core are shown in the two boxes. Calculations and image from A. Zhang in D. L. Wong et al., reproduced with permission from the Royal Society of Chemistry.¹⁸

TD-DFT calculations were carried out for the four complexes described above, however, as the only two that are described in the experimental optical data for are the bis-aquated and the mono-added GS-, only those results are described here. The full results for the calculations between 900 and 200 nm are shown in Appendix D, with the resulting

spectral data shown in Figure 6-12. The data in Figure 6-2 identify two visible region bands for the bisaquated complex, at 589 and 448 nm before intense absorbance below 300 nm giving these solutions a sky blue colour. The calculations for the bisaquated predict bands at 549 and 537 nm, and 397 and 389 nm, with a much more energetic and intense band at 238 nm. The relative intensities and band energies are reproduced very closely by the calculations. The calculation for the bisaquated complex (Figure 6-8) shows that the visible region bands arise from pairs of transitions that add contributions from each of the Rh 4d orbital set. Symmetry labels are added to allow the mixing to be seen clearly. The δ^* MO does not contribute significantly to any absorption. The predicted absorption is essentially purely the Rh core offset by the electron density from the two waters.

6.3.5 Origins of the Electronic Absorption Spectrum

[Rh₂(OAc)₄(H₂O)₂]

The bisaquated dirhodium tetraacetate is a sky blue colour in solution with the lowest energy band at 589 nm, Figure 6-2. The TD-DFT results (Figure 6-12) assign this band to a mixture of transitions from the π^* and σ (86, 87, & 88) to the σ^* (90) and MO 91, but not from the δ^* (89) because of application of selection rules. However, the major contribution to the oscillator strength is from π^* (88) to σ^* (90). The theoretical absorption spectrum (Figure 6-12A) shows the presence of three distinct absorption bands (labelled ES1/2, ES3/4, ES5) that arise from pairs of transitions involving all the dirhodium MOs as shown in Figure 6-12B. The predominant transition remain π^* to σ^* for the visible region bands. The lack of strong absorption between 500 and 300 nm accounts for the blue colour. The ES3/4 can be seen in the absorption spectrum at 448 nm (Figure 6-2). These four transitions all involve a significant contribution from the acetate-Rh MOs. However, ES5 is strongly connected with a σ (86) to σ^* (90) transition, which involves the two coordinated waters and not the acetates.

[Rh₂(OAc)₄(GS⁻)(H₂O)]⁻

Addition of thiols results in a yellow colouration (Figure 6-2) arising from the increase in absorption at 353 nm. The calculated results for the mono-thiolate (Figure 6-12A and B)

show the presence of new transitions in the visible and near-UV regions. The calculations again place the lowest energy transition near 600 nm, as seen in the experimental spectrum, but now introduce a series of bands, mostly very weak, but with the most intense new band being at 326 nm (ES5). These bands result from charge transfer from GS⁻-dominated MOs to the σ^* (166) Rh₂ core MO. By plotting the theoretical spectrum with realistic band widths, the origins of the shoulder in Figure 6-2 as the GSH is added are seen. The CD spectrum Figure 6-3, indicates the asymmetry introduced by the chiral GS⁻ binding to the Rh₂ core between 250 and 370 nm, a region associated in the calculations with bands at 321 and 326 nm.

The theoretical electronic absorption spectrum of [Rh₂(OAc)₄(GS)₂]²⁻

The calculation for the di-GS⁻ shows an increase in the charge-transfer transition below 400 nm (Figure 6-12, ES3-8) and the blue-shift of the lowest energy transition near 530 nm (ES1) is associated with stronger contributions from both coordinated glutathiones.

Table 6-1 summarizes the computational results for the Rh-Rh bond length, the energies of the σ , σ^* , and π^* MOs for the four complexes. As more electron donating groups are added, these MOs increase in energy, and the Rh-Rh bond length increases. With the increase of electron density on the rhodium, the Rh-Rh single bond is weakened. In addition, the data show that as a result of the interaction between the axial ligands and the Rh-Rh MOs, the axial ligands become more involved in the structure of the complex.

Table 6-1 Computational parameters derived from TD-DFT calculations. *Calculations from A. Zhang in D. L. Wong et al., reproduced with permission from the Royal Society of Chemistry.*¹⁸

Complex	Rh-Rh bond length /Å	E(σ) /eV	E(σ^*) /eV	E(π^*) /eV
Rh ₂ (OAc) ₄	2.370	-10.104	-1.902	-8.126
[Rh ₂ (OAc) ₄ (H ₂ O) ₂]	2.390	-8.349	-0.291	-7.411
[Rh ₂ (OAc) ₄ (GS)(H ₂ O)] ⁻	2.464	-4.006	2.013	-3.637
[Rh ₂ (OAc) ₄ (GS) ₂] ²⁻	2.471	-0.895	4.691	-1.447

6.4 Conclusions

Glutathione is well known as a strongly coordinating thiol that exists in high cellular concentration. It is upregulated in homeostatic response to soft and potentially toxic metals. In the results described above, glutathione binds to $\text{Rh}_2(\text{OAc})_4$, forming primarily the mono-adduct with retention of the single Rh-Rh bond. This means that glutathione binds axially and does not disrupt the intended, therapeutically-important, structure, but does block one of the axial sites. In the cellular milieu, this may mean that dirhodium carboxylates can survive and retain their anti-cancer activity. The computational results provide insight into the extensive overlap of the glutathione molecular orbitals with the $\text{Rh}_2(\text{OAc})_4$ core orbitals, leading to interpretation of the strength of the glutathione cysteine thiolate-rhodium bond. The calculations also allow an understanding of the optical spectral properties, showing how the introduction of axial ligands introduce new, strong absorption in the 300-400 nm region, and blue-shifting the lowest energy band at 500-600 nm. The presence of the axial ligand results in significant charge transfer in each of the optical transitions. The calculated MO energies for the four species studied show that the presence of the axial ligand is to destabilize all orbitals as a result of the introduction of electron density onto the rhodium core. Significantly, the relative energy of the Rh σ is raised with respect to δ and π . Despite the extensive overlap of the glutathione orbitals with the Rh MO, the acetate linker MOs remain largely unaffected, which accounts for the observation that the acetates are retained following axial coordination with GSH.

The results from the previous Chapters show that the cysteine-rich metallothionein protein not only binds $\text{Rh}_2(\text{OAc})_4$, but sequentially deconstructs the complex by replacing the four carboxylate ligands with the metallothionein cysteine thiolates.⁴⁹ In this case, the $\text{Rh}_2(\text{OAc})_4$ would be deactivated. Metallothionein has long been associated with a detoxification role, and this reaction with $\text{Rh}_2(\text{OAc})_4$ is just one example of this property. However, glutathione is present in at least 100 times greater concentration in the cytoplasm than metallothionein. This suggests, based on the results presented here, that a major feature in the design for these therapeutic rhodium carboxylates should be the incorporation of weakly coordinated sulfur at the axial position of the dirhodium core. If

such groups were included in the overall design, the results presented above suggest that the complex could remain intact longer in the cell and be somewhat protected against rapid metabolic deconstruction.

Metallo drugs offer a future of tunable therapeutic complexes that will be applicable to a large number of diseased states; well-known examples include Platinol (Pt), Ridaura (Au), and Trisenox (As).⁶² For the drug to be effective, the delivered form of the metal complex must be as designed. Pro-drugs are designed to change, following metabolism, into the active therapeutic agent, in which case the metabolic pathways must be well known. In other cases, it is assumed that the metal complex will be unchanged following passage into the cell. The plasma and cellular cytoplasm contain coordinating biomolecules that will bind tightly to these xenobiotic metals that form the therapeutic complex, changing the complex's properties. If this change significantly alters their therapeutic activity, then this drug has no value, and may result in higher toxicity. Understanding the potential coordination chemistry that can take place in either the plasma or the cytoplasm is important in the design and subsequent application of these drugs. The data confirm the view that the dirhodium(II) tetraacetate could easily be targeted by the intracellular thiols like glutathione, but could be protected by weak axial ligands commonly present in the cellular milieu, and still be able to bind to their intended biological targets.

6.5 References

1. P. Nicotera and S. Orrenius, in *Biological Reactive Intermediates III*, Springer, 1986, pp. 41-51.
2. A. Meister and M. E. Anderson, Glutathione, *Annual review of biochemistry*, 1983, **52**, 711-760.
3. B. A. Arrick and C. F. Nathan, Glutathione metabolism as a determinant of therapeutic efficacy: a review, *Cancer Res.*, 1984, **44**, 4224-4232.
4. F. Zunino, G. Pratesi, A. Micheloni, E. Cavalletti, F. Sala and O. Tofanetti, Protective effect of reduced glutathione against cisplatin-induced renal and systemic toxicity and its influence on the therapeutic activity of the antitumor drug, *Chem.-Biol. Interact.*, 1989, **70**, 89-101.

5. N. Traverso, R. Ricciarelli, M. Nitti, B. Marengo, A. L. Furfaro, M. A. Pronzato, U. M. Marinari and C. Domenicotti, Role of glutathione in cancer progression and chemoresistance, *Oxid. Med. Cell. Longev.*, 2013, **2013**.
6. H. J. Forman, H. Zhang and A. Rinna, Glutathione: overview of its protective roles, measurement, and biosynthesis, *Molecular aspects of medicine*, 2009, **30**, 1-12.
7. G. K. Balendiran, R. Dabur and D. Fraser, The role of glutathione in cancer, *Cell Biochemistry and Function: Cellular biochemistry and its modulation by active agents or disease*, 2004, **22**, 343-352.
8. D. M. Townsend, K. D. Tew and H. Tapiero, The importance of glutathione in human disease, *Biomed. Pharmacother.*, 2003, **57**, 145-155.
9. D. M. Townsend and K. D. Tew, The role of glutathione-S-transferase in anti-cancer drug resistance, *Oncogene*, 2003, **22**, 7369.
10. S. Goto, T. Iida, S. Cho, M. Oka, S. Kohno and T. Kondo, Overexpression of glutathione S-transferase π enhances the adduct formation of cisplatin with glutathione in human cancer cells, *Free Radic. Res.*, 1999, **31**, 549-558.
11. K. D. Tew, Glutathione-associated enzymes in anticancer drug resistance, *Cancer Res.*, 1994, **54**, 4313-4320.
12. A. Albert, C. Brauckmann, F. Blaske, M. Sperling, C. Engelhard and U. Karst, Speciation analysis of the antirheumatic agent Auranofin and its thiol adducts by LC/ESI-MS and LC/ICP-MS, *J. Anal. At. Spectrom.*, 2012, **27**, 975-981.
13. A. Meister, Glutathione-ascorbic acid antioxidant system in animals, *J. Biol. Chem.*, 1994, **269**, 9397-9400.
14. M. E. Anderson, A. Naganuma and A. Meister, Protection against cisplatin toxicity by administration of glutathione ester, *FASEB J.*, 1990, **4**, 3251-3255.
15. G. Noctor and C. H. Foyer, Ascorbate and glutathione: keeping active oxygen under control, *Annu. Rev. Plant Biol.*, 1998, **49**, 249-279.
16. J. K. C. Lau and D. V. Deubel, Loss of ammine from platinum (II) complexes: implications for cisplatin inactivation, storage, and resistance, *Chem. Eur. J.*, 2005, **11**, 2849-2855.
17. A. Casini, A. Karotki, C. Gabbiani, F. Rugi, M. Vašák, L. Messori and P. J. Dyson, Reactivity of an antimetastatic organometallic ruthenium compound with metallothionein-2: relevance to the mechanism of action, *Metallomics*, 2009, **1**, 434-441.

18. D. L. Wong, A. Zhang, A. S. Faponle, S. P. de Visser and M. J. Stillman, Glutathione binding to dirhodium tetraacetate: a spectroscopic, mass spectral and computational study of an anti-tumour compound, *Metallomics*, 2017, **9**, 501-516.
19. V. Mah and F. Jalilehvand, Mercury (II) complex formation with glutathione in alkaline aqueous solution, *J. Biol. Inorg. Chem.*, 2008, **13**, 541-553.
20. V. Mah and F. Jalilehvand, Cadmium (II) complex formation with glutathione, *J. Biol. Inorg. Chem.*, 2010, **15**, 441-458.
21. V. Mah and F. Jalilehvand, Glutathione complex formation with mercury (II) in aqueous solution at physiological pH, *Chem. Res. Toxicol.*, 2010, **23**, 1815-1823.
22. V. Mah and F. Jalilehvand, Lead (II) complex formation with glutathione, *Inorg. Chem.*, 2012, **51**, 6285-6298.
23. N. Scott, K. M. Hatlelid, N. E. MacKenzie and D. E. Carter, Reactions of arsenic (III) and arsenic (V) species with glutathione, *Chem. Res. Toxicol.*, 1993, **6**, 102-106.
24. B. O. Leung, F. Jalilehvand, V. Mah, M. Parvez and Q. Wu, Silver (I) complex formation with cysteine, penicillamine, and glutathione, *Inorg. Chem.*, 2013, **52**, 4593-4602.
25. E. Volckova, L. P. Dudones and R. N. Bose, HPLC determination of binding of cisplatin to DNA in the presence of biological thiols: implications of dominant platinum-thiol binding to its anticancer action, *Pharm. Res.*, 2002, **19**, 124-131.
26. S. Goto, K. Yoshida, T. Morikawa, Y. Urata, K. Suzuki and T. Kondo, Augmentation of transport for cisplatin-glutathione adduct in cisplatin-resistant cancer cells, *Cancer Res.*, 1995, **55**, 4297-4301.
27. N. Burford, M. D. Eelman, D. E. Mahony and M. Morash, Definitive identification of cysteine and glutathione complexes of bismuth by mass spectrometry: assessing the biochemical fate of bismuth pharmaceutical agents, *Chem. Commun.*, 2003, 146-147.
28. A. K. Godwin, A. Meister, P. J. O'Dwyer, C. S. Huang, T. C. Hamilton and M. E. Anderson, High resistance to cisplatin in human ovarian cancer cell lines is associated with marked increase of glutathione synthesis, *Proc. Natl. Acad. Sci. U.S.A.*, 1992, **89**, 3070-3074.
29. S.-I. Hamada, M. Kamada, H. Furumoto, T. Hirao and T. Aono, Expression of glutathione S-transferase- π in human ovarian cancer as an indicator of resistance to chemotherapy, *Gynecol. Oncol.*, 1994, **52**, 313-319.

30. R. A. Hromas, P. A. Andrews, M. P. Murphy and C. P. Burns, Glutathione depletion reverses cisplatin resistance in murine L1210 leukemia cells, *Cancer letters*, 1987, **34**, 9-13.
31. P. A. Andrews, M. A. Schiefer, M. P. Murphy and S. B. Howell, Enhanced potentiation of cisplatin cytotoxicity in human ovarian carcinoma cells by prolonged glutathione depletion, *Chem.-Biol. Interact.*, 1988, **65**, 51-58.
32. C. M. Rudin, Z. Yang, L. M. Schumaker, D. J. VanderWeele, K. Newkirk, M. J. Egorin, E. G. Zuhowski and K. J. Cullen, Inhibition of glutathione synthesis reverses Bcl-2-mediated cisplatin resistance, *Cancer Res.*, 2003, **63**, 312-318.
33. A. Erck, E. Sherwood, J. Bear and A. Kimball, The metabolism of rhodium (II) acetate in tumor-bearing mice, *Cancer Res.*, 1976, **36**, 2204-2209.
34. R. Howard, T. Spring and J. Bear, The interaction of rhodium (II) carboxylates with enzymes, *Cancer Res.*, 1976, **36**, 4402-4405.
35. K. Sorasaene, P. K.-L. Fu, A. M. Angeles-Boza, K. R. Dunbar and C. Turro, Inhibition of transcription in vitro by anticancer active dirhodium (II) complexes, *Inorg. Chem.*, 2003, **42**, 1267-1271.
36. A. M. Angeles-Boza, H. T. Chifotides, J. D. Aguirre, A. Chouai, P. K.-L. Fu, K. R. Dunbar and C. Turro, Dirhodium (II, II) complexes: molecular characteristics that affect in vitro activity, *J. Med. Chem.*, 2006, **49**, 6841-6847.
37. A. Dorcier, W. H. Ang, S. Bolano, L. Gonsalvi, L. Juillerat-Jeannerat, G. Laurency, M. Peruzzini, A. D. Phillips, F. Zanobini and P. J. Dyson, In vitro evaluation of rhodium and osmium RAPTA analogues: the case for organometallic anticancer drugs not based on ruthenium, *Organometallics*, 2006, **25**, 4090-4096.
38. F. P. Pruchnik, R. Starosta, Z. Ciunik, A. Opolski, J. Wietrzyk, E. Wojdat and D. Dus, Tetraacetatodirhodium (II) complexes with tris (methoxyphenyl) phosphines, their reactivity, structure, and antitumor activity, *Can. J. Chem.*, 2001, **79**, 868-877.
39. F. Pruchnik and D. Dus, Properties of rhodium (II) complexes having cytostatic activity, *J. Inorg. Biochem.*, 1996, **61**, 55-61.
40. R. Głaszczka, J. Jaźwiński, B. Kamiński and M. Kamińska, Adducts of rhodium (II) tetraacylates with methionine and its derivatives: ¹H and ¹³C nuclear magnetic resonance spectroscopy and chiral recognition, *Tetrahedron Asymmetry*, 2010, **21**, 2346-2355.
41. N. Katsaros and A. Anagnostopoulou, Rhodium and its compounds as potential agents in cancer treatment, *Crit. Rev. Oncol. Hematol.*, 2002, **42**, 297-308.

42. R. Głaszczka and J. Jaźwiński, In situ complexation of rhodium (II) tetracarboxylates with some derivatives of cysteine and related ligands studied by ^1H and ^{13}C nuclear magnetic resonance spectroscopy, *J. Coord. Chem.*, 2016, **69**, 3703-3714.
43. G. Gasser, I. Ott and N. Metzler-Nolte, Organometallic anticancer compounds, *J. Med. Chem.*, 2010, **54**, 3-25.
44. E. B. Boyar and S. D. Robinson, Rhodium (II) carboxylates, *Coord. Chem. Rev.*, 1983, **50**, 109-208.
45. L. Trynda and F. Pruchnik, Interaction of tetra- μ -acetatodirrhodium (II) with human serum albumin, *J. Inorg. Biochem.*, 1995, **58**, 69-77.
46. B. Desoize, Metals and metal compounds in cancer treatment, *Anticancer Res.*, 2004, **24**, 1529-1544.
47. H. T. Chifotides and K. R. Dunbar, Interactions of metal–metal-bonded antitumor active complexes with DNA fragments and DNA, *Accounts Chem. Res.*, 2005, **38**, 146-156.
48. P. Jakimowicz, L. Ostropolska and F. P. Pruchnik, Interaction of $[\text{Rh}_2(\text{O}_2\text{CCH}_3)_4(\text{H}_2\text{O})_2]$ and $[\text{Rh}_2(\text{O}_2\text{CCH}(\text{OH})\text{Ph})_2(\text{phen})_2(\text{H}_2\text{O})_2](\text{O}_2\text{C}-\text{CH}(\text{OH})\text{Ph})_2$ With Sulfhydryl Compounds and Ceruloplasmin, *Metal-based drugs*, 2000, **7**, 201-209.
49. D. L. Wong and M. J. Stillman, Destructive interactions of dirrhodium (II) tetraacetate with β metallothionein rh1a, *Chem. Commun.*, 2016, **52**, 5698-5701.
50. FQS Poland, Scigress Molecular Modeling Software, 6.0.0, 2016. Retrieved from http://www.fqs.pl/chemistry_materials_life_science/products/scigress.
51. Gaussian, Inc., Gaussian 09, Revision D.01, 2016.
52. A. Presta and M. J. Stillman, Chiral copper (I)—Thiolate clusters in metallothionein and glutathione, *Chirality*, 1994, **6**, 521-530.
53. G. Pneumatikakis and P. Psaroulis, Interactions of tetra- μ -acetato dirrhodium (II) with sulfur-containing aminoacids, *Inorganica Chim. Acta*, 1980, **46**, 97-100.
54. F. Cotton, B. DeBoer, M. LaPrade, J. Pipal and D. Ucko, The crystal and molecular structures of dichromium tetraacetate dihydrate and dirrhodium tetraacetate dihydrate, *Acta Crystallographica Section B: Structural Crystallography and Crystal Chemistry*, 1971, **27**, 1664-1671.
55. F. P. Pruchnik, Structure and reactivity of rhodium (II) complexes, *Pure Appl. Chem.*, 1989, **61**, 795-804.

56. J. G. Norman Jr and H. J. Kolari, Strength and trans influence of the rhodium-rhodium bond in rhodium (II) carboxylate dimers, *J. Am. Chem. Soc.*, 1978, **100**, 791-799.
57. G. Christoph and Y. Koh, Metal-metal bonding in dirhodium tetracarboxylates. Trans influence and dependence of the rhodium-rhodium bond distance upon the nature of the axial ligands, *J. Am. Chem. Soc.*, 1979, **101**, 1422-1434.
58. T. Kawamura, H. Katayama, H. Nishikawa and T. Yamabe, Ligand dependence of the electronic configuration of the rhodium-rhodium bond in Rh²⁵⁺ complexes as studied by electron spin resonance and electrochemistry, *J. Am. Chem. Soc.*, 1989, **111**, 8156-8160.
59. D. S. Martin Jr, T. R. Webb, G. A. Robbins and P. E. Fanwick, Polarized electronic absorption spectra for dirhodium (II) tetraacetate dihydrate, *Inorg. Chem.*, 1979, **18**, 475-478.
60. V. M. Miskowski, W. P. Schaefer, B. S. Sadeghi, B. D. Santarsiero and H. B. Gray, Polarized electronic spectra of dirhodium (II) tetraacetate, *Inorg. Chem.*, 1984, **23**, 1154-1162.
61. Z. Futera, T. s. Koval, J. Leszczynski, J. Gu, M. Mitoraj, M. Srebro and J. V. Burda, Exploring a reaction mechanism for acetato ligand replacement in paddlewheel tetrakisacetatodirhodium (II, II) complex by ammonia: computational density functional theory study, *J. Phys. Chem. A*, 2011, **115**, 784-794.
62. I. Romero-Canelón and P. J. Sadler, Systems approach to metal-based pharmacology, *Proc. Natl. Acad. Sci. U.S.A.*, 2015, **112**, 4187-4188.

Chapter 7

7 Conclusions: Xenobiotic Metals in Therapeutic Agents as Models for Toxicity*

As a result of the Internet and the technological age, decades worth of electronic metal waste have been produced at a rate higher than can be sustainably dealt with. From this waste, xenobiotic metals are being introduced into the ecosystem. Already, metallic particulates of Pt, Pd, Os, Rh, and Ir are evident in the environment from their use in catalytic converters in the automotive industry.¹⁻⁴ With the new age of smart devices, a host of exotic xenobiotic consumer waste will become a global concern.

Metallotherapeutics leverage the properties of xenobiotic metals in the treatment of cancers and tumors, and, in addition, anti-inflammatory, or anti-microbial agents in other medical treatments. However, metallotherapeutics directly expose humans to these xenobiotic metals, and this risk must be considered when determining the pharmacokinetics of these drugs. Often these treatments are intravenously administered, and this means that the metallo-drug will encounter a host of adduct-forming proteins in the blood plasma (e.g. albumin).

With its 20 cysteine thiols, metallothionein (MT) is a small protein with a powerful Lewis basicity that makes it highly reactive towards metal ions. Additionally, isoforms with single amino acid mutations may assist in the binding of metals using modes other than homoleptic cysteine coordination. This type of flexible bonding could also be considered as an example of non-traditional binding when discussing the metallation of MTs.

In the research described in this Thesis, I have postulated that these potentially toxic metal complexes could be intercepted by MT. Because of its flexible structure, it is well known that MT does not have specific, well-defined metal binding sites, unlike typical metalloproteins. Thus, MT is able to accommodate the specific coordination demands of many different metals, but the protein itself is not innocent in its coordination when these metals bind as complexes. This is because the thiolate ligands are such strong sigma donors, that they displace the original metal-bound ligands. In this way, one might say

**A version of this chapter is in preparation for publication
D. L. Wong and M. J. Stillman (2019)*

that MT “digests” the complex. The experimental data reported in this Thesis provide a number of major novel findings. Clearly, the first is that metallocomplexes are not immune to coordination by this ubiquitous protein, and their bound form may be subsequently modified. Secondly, MT does not (as noted above) exert its coordination through the traditional binding site model of metalloproteins, rather the structures formed depend entirely on the conformation of the 20 cysteines and the incoming complex. Thirdly, the apoprotein is a folded structure that is highly fluxional and dependent on the surrounding solution environment. The flexibility of the backbone allows MT to effectively ensnare incoming metal complexes, encapsulating them within the protein core.

7.1 Exotic Metals as Medicines

This Thesis has introduced the reader to the double-edged sword that xenobiotic metals represent to humans. Some of this class of metals can be used therapeutically and, in that sense, they are beneficial. On the other hand, exposure from metal waste pollution is toxic, and, therefore, detrimental. However, if metallothionein becomes involved in the pharmacokinetic pathways of any of these routes of exposure, new metabolic pathways may result that may be more or less beneficial or detrimental. This mechanistic dilemma leaves many unanswered questions concerning the relative value of the beneficial use of xenobiotic metals in consumer goods, which must be reflected in the challenge of safe and sustainable heavy metal recovery. Before revisiting the conclusions drawn from the specific experiments reported in this Thesis, I will first introduce brief examples of d-block metals currently in therapeutic and diagnostic use, to put into context the specific studies I have reported on cisplatin and dirhodium(II) tetraacetate. The examples of the exotic metals described below are: Technetium, Rhenium, Platinum, Ruthenium, Rhodium, and Gold.

Technetium

^{99m}Tc , with its emission of 140.5 keV γ -rays and biological half-life of 6 hours,⁵ makes this synthetic metal a versatile imaging agent.⁶ The groundbreaking research by Morelock and Tolman on utilizing MT as a radiolabel drug delivery mechanism showed that the

stable decay product, $^{99}\text{TcO}^{3+}$ bound readily to MT. Significantly, coordination determined using extended X-ray absorption fine structure (EXAFS) showed the Tc was bound to both N/O ligand donors as well as the cysteine thiols.⁷ $^{99\text{m}}\text{Tc}$ has been used to effectively image many organs, the first being the liver.⁸ These types of diagnostic agents used in medicine are likely encapsulated by MT for up take in all tissues.

Rhenium

With similar properties to ^{99}Tc , ^{186}Re and ^{188}Re have also been utilized for the radiopharmaceutical imaging of cancerous liver tissue.⁹

The binding reaction of Re to MT has been investigated by Palacios et al. in the form of $[\text{facRe}(\text{CO})_3]$ and these Re moiety-containing complexes were observed to bind significantly slower compared to the analogous reaction with $[\text{facTc}(\text{CO})_3]$.¹⁰ The same study showed that of the four human isoforms of MT, the most Cu-philic, MT3, reacted most readily with the Re complex. This was likely due to the presence of a histidine residue in MT3, that is not present in the other isoforms.

Platinum

Platinum and its anti-cancerous effects introduced the world to metal based cancer therapeutics. Its original anticancer activity was discovered by Rosenberg et al.,¹¹ and it is now a flourishing billion dollar industry with a variety of analogs of refined activity, examples are shown in Figure 7-1.¹² Since its discovery and subsequent use, it has been found that many cancer types have developed resistance following prolonged treatment.¹³
¹⁴ A number of these platinum resistant cancer types display an increased expression in nuclear MT, correlated to platinum treatment.¹⁵⁻¹⁷

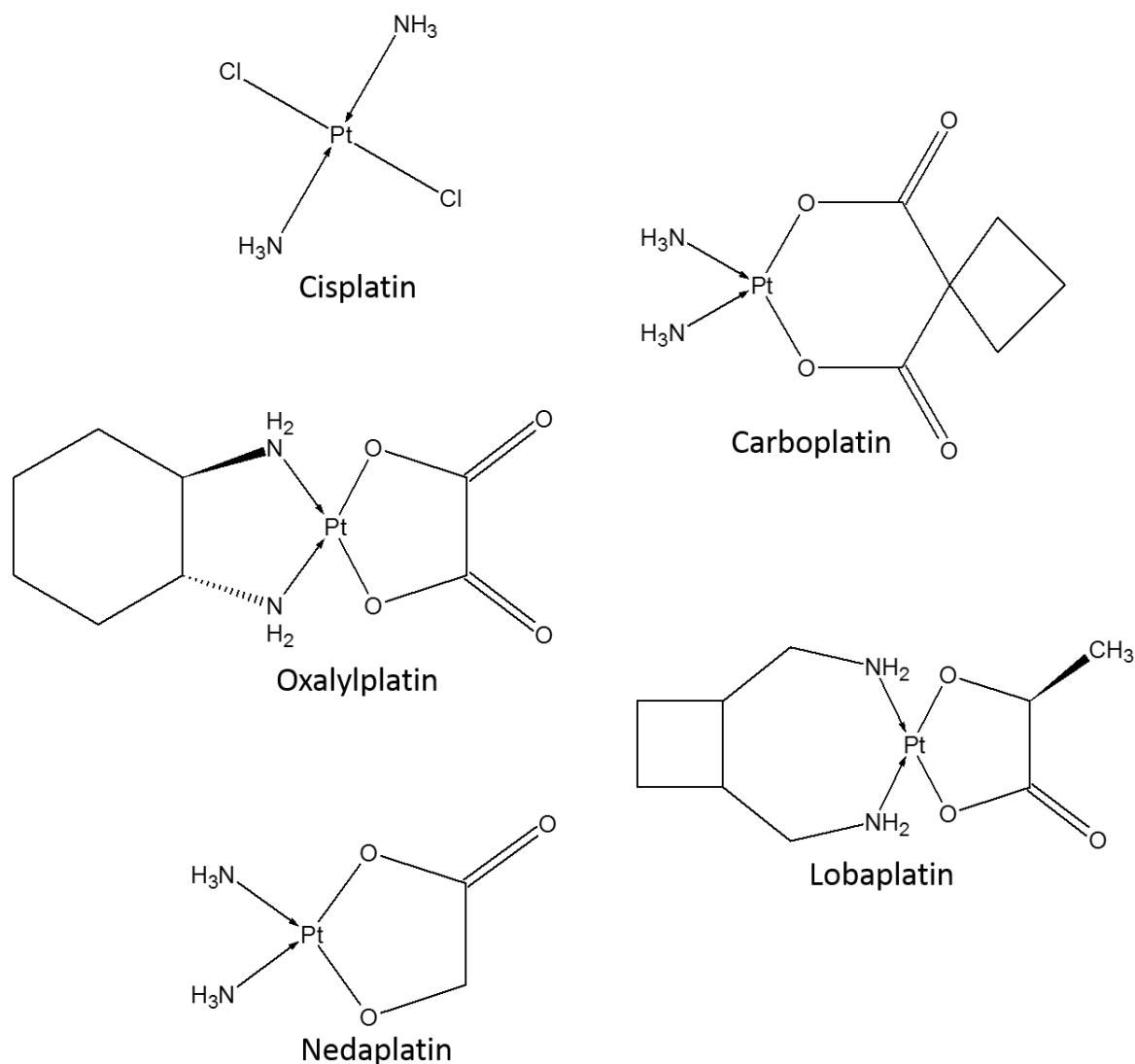


Figure 7-1 Cisplatin and its subsequently developed analogs.

MT reacts readily with cisplatin,¹⁸⁻²⁰ more so than its transplatin analog.²¹ With cisplatin, the ammine ligands are removed by the cysteine thiolates of MT,²² but transplatin retains its ammines.²¹ There are a variety of newly developed analogs of cisplatin designed to increase selectivity by adopting ligand structures that are more stable at biological levels. These are currently in use as effective treatments of a variety of cancer types.¹² An example of a novel therapeutic, is platinum(II) 9-aminoacridine, a structure resistant to MT1a reactivity.²³ The downside of these platinum based anti-cancer treatments are their side effects (nephrotoxicity, neurotoxicity, nausea) and their limited selectivity. As a

result, researchers are currently surveying non-platinum metal complexes for similar anticancer therapeutic activity.

Ruthenium

Ruthenium complexes are studied for their low toxicity and antimetastatic behavior, with many displaying strong anti-tumor activity. The most promising examples of these Ru complexes are shown in Figure 7-2. Imidazolium *trans*-imidazolidimethylsulfoxidetetrachloro-ruthenate (NAMI-A) is a stable Ru(III) prodrug that is converted to its active Ru(II) state upon entering the reducing environment of the cancerous cell. *Trans*-tetrachlorobis(indazole)ruthenate(III) (KP1019) imparts its activity by binding with the iron transport protein transferrin,²⁴ interfering with iron uptake of the nutritionally-starved cancer cells. RAPTA agents are Ru(II) arene piano stool compounds that carry a 1,3,5-triaza-7-phosphaadamantane (PTA) ligand. They are a family of potent cytotoxics that significantly reduce metastatic activity.²⁵ The organometallic, arene structure proves to be a robust chemical architecture withstanding thiolate attack, and continues to show promise with Rh and Os analogs in selective anti-tumor activity.²⁶

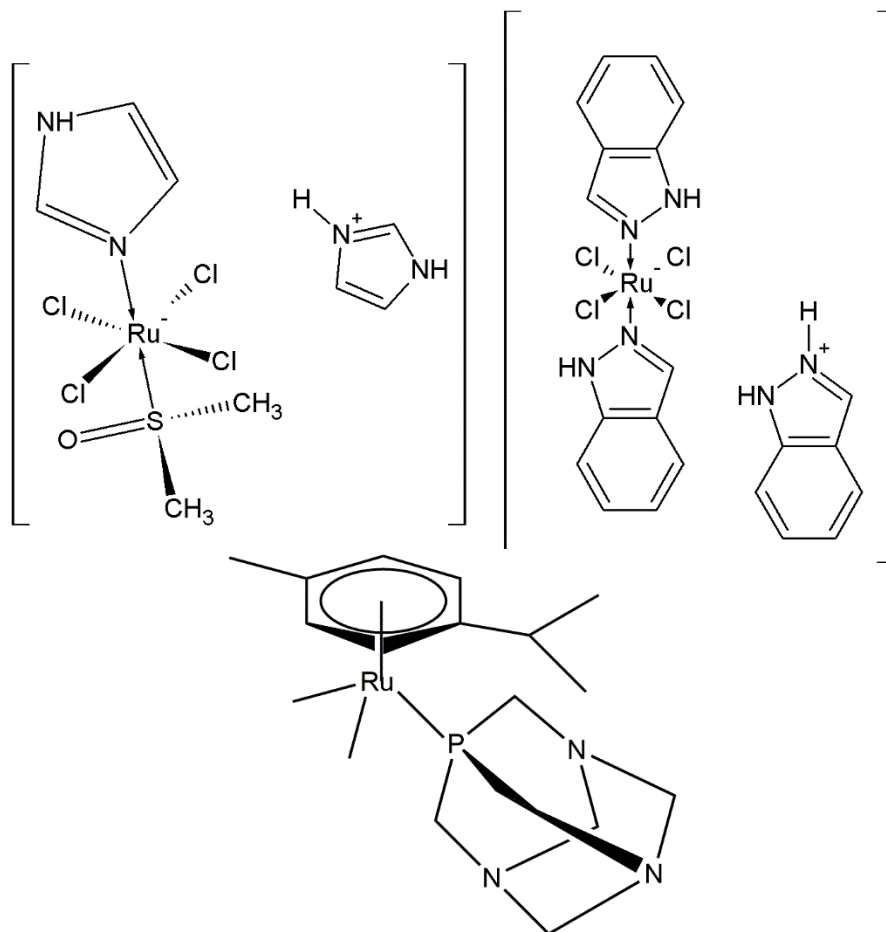


Figure 7-2 Structures of Ru(II) complexes NAMI-A (Left), KP1019 (Right), and RAPTA-C (bottom).

Rhodium

Rhodium was considered as an alternative to Ruthenium because it is more inert biologically. It is also promising as a radiosensitizer, for direct enzyme inhibition, and photodynamic therapy. Rh^{3+} complexes exhibit therapeutic effects by inhibiting beta amyloid aggregation, kinase inhibition, and DNA intercalation.²⁷

Dirhodium carboxylate anti-tumor activity has been known since the 1970's,²⁸⁻³¹ but due to the serious nephrotoxic side effects, they are not currently used. However, the construction of these bimetallics can be finely tuned with their ligand decoration, and these complexes has been the subject of much research.^{27, 32-40}

Gold

Au(I) salts have been used for decades to relieve the chronic side effects of rheumatoid arthritis, in a multi-action approach known as chrysotherapy.⁴¹ Chrysotherapeutic effects include anti-inflammatory and antimicrobial response, inhibition of T-cell proliferation and enzyme inhibition.⁴² The Au(I) complexes are known to interact with MTs, and are deactivated upon binding. This includes the well-known therapeutic agent, aurothiomalate.⁴³

Some Au(III) complexes show activity against cisplatin-resistant cells,⁴⁴ demonstrating promising alternatives for non-platinum therapeutics. These include the tetrapyrrole Au(III) porphyrin,⁴² Au(III) corrole complexes,⁴⁵ and multi-dentate N donor ligands,⁴⁶ and as such, these new structural designs are focused on improving their durability as cytotoxic agents.

7.2 MT Metabolism of Metal-based Drugs

After introducing examples of metal-based drugs above, and the known interactions of these metals with MT, I now return to the conclusions drawn from the experiments performed in this Thesis.

Chapter 3: Human MT Metallation with Cisplatin

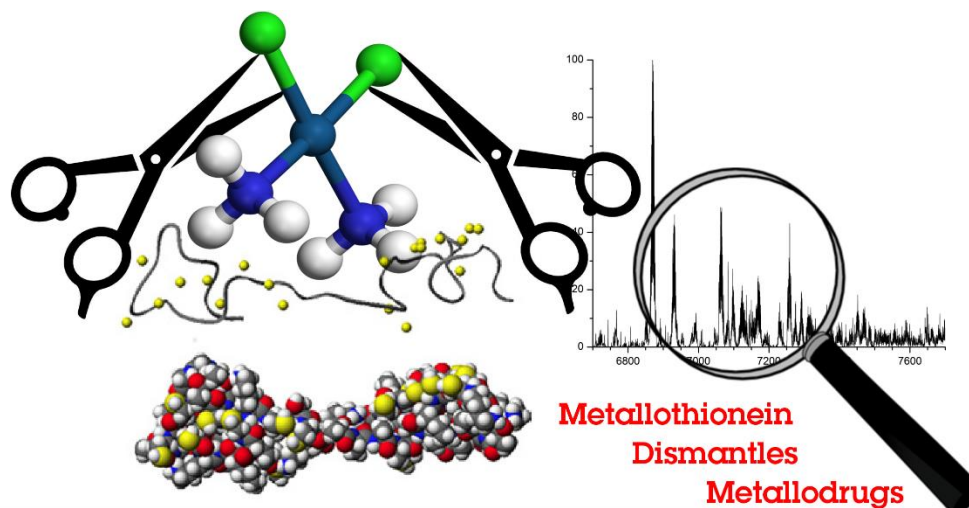


Figure 7-3 Graphical abstract for the breakdown of cisplatin by MT using ESI-MS.

*Reproduced from D. L. Wong and M. J. Stillman, with permission from the Royal Society of Chemistry.*²²

In vitro reactions involving cisplatin and transplatin binding to mammalian MTs were studied previously using HPLC and NMR spectroscopy. ESI-MS was used to provide quantitative detail of the effects of transmetallation of Zn-MT by Pt(II), but there were no details concerning the initial metal displacement reaction.^{21, 47} Chapter 3 describes the initial binding and dissection of cisplatin when bound to MT1A utilizing ESI-MS to quantify the mechanism for these primary ligand substitution reactions, Figure 7-3. Hagrman et al. showed that there were multiple phases to the cisplatin-MT reaction, but the first phase occurred far too rapidly to be observed using LC methods.⁴⁸ With the high resolution and time resolving power of the ESI TOF MS, it was possible to measure the rates of the first 4 metallation reactions, k_{1-4} , and to propose a detailed mechanism for the interaction between cisplatin and MT.²²

Chapters 4 and 5: Human MT Metallation with Dirhodium(II) Tetraacetate

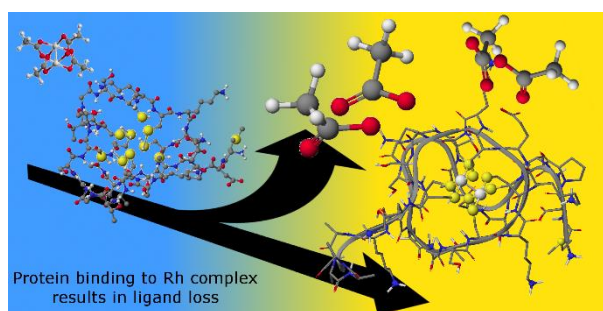


Figure 7-4 Graphical abstract depicting the encapsulation of a Rh-Rh core by the β -MT domain.

*Reproduced from D. L. Wong and M. J. Stillman, with permission from the Royal Society of Chemistry.*⁴⁹

The biological uptake of Rh and its related platinum group metals has gained interest with the reports of metal particles in soil and freshwater species near routes of heavy traffic.^{1, 50-52} This increase in the presence of such biologically exotic metals has been linked to the advent of platinum-based catalytic converters in automobiles to reduce noxious

emissions. However, these metal-based catalysts are not completely stable; thermal decomposition and mechanical sintering results in these metal particulates being released into the environment.

A way to study the possible physiological effects of toxic rhodium exposure from this pollution is to examine the use of rhodium-based platinum alternatives in chemotherapy.

The work described in Chapter 4, and 5 proves that MT can play an active role in the metabolic destruction of dirhodium metallocomplexes; a result that had not been reported in the literature previously.^{49, 53} The sequestration of a dirhodium(II) tetraacetate by MT results in the removal of the acetate ligands, leaving the Rh-Rh core intact. Chapter 4 described the reaction with the 9 cysteine, β -domain fragment, which easily accommodates one and only one Rh₂ core. In Chapter 5, the reaction with the full, 20 cysteine, two domain protein is more complex, with multiple metal binding conformations possible due to the elegant flexibility of MT. Rh uptake by MT is fixed at a Rh_n:MT ratio, where n = multiples of 2. MT-to-MT metal-transfer equilibration would result in odd-numbered stoichiometries, which were not observed. The resulting encapsulated Rh-Rh core was visualized as being embedded in the MT structure using molecular dynamics. Rh₂(OAc)₄ is easily taken up by MT and the resulting product *in vivo* may exhibit nephrotoxic effects similar to Cd-MT^{54, 55} due to its comparable size.

Chapter 6: Strength of the Cysteine Thiolate Metal Coordination- Studies with Glutathione

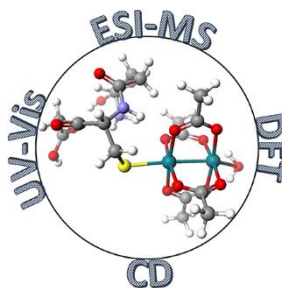


Figure 7-5 Graphical abstract emphasizing the harmony of the methods used to explain the properties of the metal-thiolate bond.

*Calculations and image from A. Zhang in Wong et al., reproduced with permission from the Royal Society of Chemistry.*⁵⁶

Reactions with glutathione provide a model system from which we can understand the reaction of the dirhodium complex with MT. Glutathione on its own does not dismantle the tetraacetate cage under our anaerobic conditions. However, the GSH clearly did bind to the dirhodium complex, based on the changes in the optical spectrum, and this prompted a computational investigation into the strength of the resulting metal-thiolate bond.

Strong electron donation from the thiolates of the cysteines raises the energy of the Rh-Rh bond MO, weakening the Rh-Rh single bond. This was observed from the increase in the calculated bond lengths with the coordination of the glutathione. The effect of acetate replacement with multiple glutathione molecules would be of interest in order to understand the hyperchelative effect of MT, and the change in energy that results from the stepwise replacement of the acetate ligands.

7.3 A New Biological Role for MT

Active Disassembly and Binding Metals of Complexes

In the work described in Chapters 3, 4, 5, and 6, I have introduced the dilemma of beneficial and detrimental pathways for which metallothionein may be implicated. In the six decades of research since its discovery, the reactions of metallothioneins with metal ions have been well documented and, in this Thesis, we have defined these as traditional reactions (for e.g. Zn(II) and Cd(II),⁵⁷ see Scheller et al. for a comprehensive list).⁵⁸ However, in the context of these xenobiotic metals, I have described the metallation as non-traditional. Reactions of coordination complexes with MT are far more complicated. Metallothionein is a multidentate hyperchelator, which in its action, envelopes and systematically exchanges its ligands in an irreversible fashion, deconstructing the incoming metal complexes using its 20 electrophilic cysteine thiolates.

Historically, MT was considered to bind Zn(II) and Cd(II) into well-defined clustered structures. The reactions reported at the time were analyzed based on the assumption that

metallation always involved complete cluster formation and metal saturation, even with mixed-metal products. However, Yang, Maret and Vallee, through the analysis of cellular content, identified and confirmed the *in vivo* presence of partially-metallated metallothionein (5 Zn(II) instead of 7) and postulated that there would be free thiols based on the assumption that incomplete clusters formed.⁵⁹ With recent data, particularly with the advent of ESI-MS studies, including those shown in this Thesis, it is now clear that the partially-metallated metallothioneins may not require cluster formation, instead the 5 Zn(II) referred to above have been shown to bind with terminal thiolates. We now understand the metallation mechanism and chelating behavior of MT and its isoforms better than before. This new recognition that partially metallated metallothioneins do not require cluster formation leads to the description of the non-traditional binding of xenobiotic metals that have been described here.

As we approach the future with computers and electronics becoming deeply integrated into daily life, the possibility of chronic exposure to xenobiotic metal waste increases. The issue is that the combined controlled and uncontrolled (legal and illegal) extraction, purification, recycling and reclamation results in the incorporation of these metals into the food chain. At this point, the studies described in this Thesis suggests that non-traditional binding to metallothionein will occur. Metallothioneins in all Life will be required to adapt as a result.

In cancer, the abhorrent growth and replication of diseased cells causes an overdrive in protein expression, of which cellular thiols like MT are heavily implicated. The studies described in this Thesis suggest that the exacerbation of this metal scavenging by the increased amount of cellular MT will greatly hinder the efficacy of metal-based anticancer drugs.

We have now completed the description of the aggressive attack of therapeutic metallocomplexes by this cellular metal gatekeeper, metallothionein (MT). The metallation of *de novo* MT would be the first response in the inherent cellular defense against xenobiotic metals. Therefore, in closing, and as a final comment on the chemistries described in this Thesis, I conclude that the epic method by which MT

eviscerates metal complexes uniquely allows MT to adopt novel, and unprecedented structural properties to defend the cell against these intruding xenobiotic complexes.

7.4 References

1. K. S. Egorova and V. P. Ananikov, Which metals are green for catalysis? Comparison of the toxicities of Ni, Cu, Fe, Pd, Pt, Rh, and Au salts, *Angew. Chem. Int. Edit.*, 2016, **55**, 12150-12162.
2. D. Cinti, M. Angelone, U. Masi and C. Cremisini, Platinum levels in natural and urban soils from Rome and Latium (Italy): significance for pollution by automobile catalytic converter, *Sci. Total Environ.*, 2002, **293**, 47-57.
3. M. Moldovan, M. Palacios, M. Gomez, G. Morrison, S. Rauch, C. McLeod, R. Ma, S. Caroli, A. Alimonti and F. Petrucci, Environmental risk of particulate and soluble platinum group elements released from gasoline and diesel engine catalytic converters, *Sci. Total Environ.*, 2002, **296**, 199-208.
4. I. Kalavrouziotis and P. Koukoulakis, The environmental impact of the platinum group elements (Pt, Pd, Rh) emitted by the automobile catalyst converters, *Water Air Soil Pollut.*, 2009, **196**, 393.
5. M. Morelock, T. Cormier and G. Tolman, Technetium metallothioneins, *Inorg. Chem.*, 1988, **27**, 3137-3140.
6. M. M. Morelock and G. Tolman, in *Metallothionein II*, Springer, 1987, pp. 247-253.
7. W. B. Jones, T. E. Elgren, M. M. Morelock, R. Elder and D. E. Wilcox, Technetium metallothionein: spectroscopic and EXAFS study of $^{99}\text{TcO}^{3+}$ binding to Zn_7 -metallothionein, *Inorg. Chem.*, 1994, **33**, 5571-5578.
8. L. B. Sorensen and M. Archambault, Visualization of the liver by scanning with Mo^{99} (molybdate) as tracer, *J. Lab. Clin. Med.*, 1963, **62**, 330-340.
9. J. Dilworth and S. Parrott, The biomedical chemistry of technetium and rhenium, *Chem. Soc. Rev.*, 1998, **27**, 43-55.
10. J. Lecina, Ò. Palacios, S. Atrian, M. Capdevila and J. Suades, Rhenium and technetium tricarbonyl, $\{\text{M}(\text{CO})_3\}^+$ (M= Tc, Re), binding to mammalian metallothioneins: new insights into chemical and radiopharmaceutical implications, *J. Biol. Inorg. Chem.*, 2015, **20**, 465-474.
11. B. Lippert, *Cisplatin: chemistry and biochemistry of a leading anticancer drug*, John Wiley & Sons, 1999.

12. T. C. Johnstone, K. Suntharalingam and S. J. Lippard, The next generation of platinum drugs: targeted Pt (II) agents, nanoparticle delivery, and Pt (IV) prodrugs, *Chem. Rev.*, 2016, **116**, 3436-3486.
13. P. A. Andrews, M. P. Murphy and S. B. Howell, Metallothionein-mediated cisplatin resistance in human ovarian carcinoma cells, *Cancer Chemother. Pharmacol.*, 1987, **19**, 149-154.
14. M. Kartalou and J. M. Essigmann, Mechanisms of resistance to cisplatin, *Mutat. Res.-Fund. Mol. Mech. Mut.*, 2001, **478**, 23-43.
15. E. S. Woo, A. Monks, S. C. Watkins, A. S. Wang and J. S. Lazo, Diversity of metallothionein content and subcellular localization in the National Cancer Institute tumor panel, *Cancer Chemother. Pharmacol.*, 1997, **41**, 61-68.
16. P. Surowiak, V. Materna, A. Maciejczyk, M. Pudełko, E. Markwitz, M. Spaczyński, M. Dietel, M. Zabel and H. Lage, Nuclear metallothionein expression correlates with cisplatin resistance of ovarian cancer cells and poor clinical outcome, *Virchows Arch.*, 2007, **450**, 279-285.
17. P. Surowiak, V. Materna, I. Kaplenko, M. Spaczyński, M. Dietel, H. Lage and M. Zabel, Augmented expression of metallothionein and glutathione S-transferase pi as unfavourable prognostic factors in cisplatin-treated ovarian cancer patients, *Virchows Arch.*, 2005, **447**, 626-633.
18. A. Pattanaik, G. Bachowski, J. Laib, D. Lemkuil, C. Shaw, D. Petering, A. Hitchcock and L. Saryan, Properties of the reaction of cis-dichlorodiammineplatinum (II) with metallothionein, *J. Biol. Chem.*, 1992, **267**, 16121-16128.
19. M. Knipp, Metallothioneins and platinum (II) anti-tumor compounds, *Curr. Med. Chem.*, 2009, **16**, 522-537.
20. A. J. Żelazowski, J. S. Garvey and J. D. Hoeschele, In vivo and in vitro binding of platinum to metallothionein, *Arch. Biochem. Biophys.*, 1984, **229**, 246-252.
21. A. V. Karotki and M. Vašák, Reaction of human metallothionein-3 with cisplatin and transplatin, *J. Biol. Inorg. Chem.*, 2009, **14**, 1129-1138.
22. D. L. Wong and M. J. Stillman, Capturing platinum in cisplatin: kinetic reactions with recombinant human apo-metallothionein 1a, *Metallomics*, 2018, **10**, 713-721.
23. K. G. Samper, C. Vicente, V. Rodríguez, S. Atrian, N. Cutillas, M. Capdevila, J. Ruiz and Ó. Palacios, Studying the interactions of a platinum (II) 9-aminoacridine complex with proteins and oligonucleotides by ESI-TOF MS, *Dalton Trans.*, 2012, **41**, 300-306.

24. C. G. Hartinger, S. Zorbas-Seifried, M. A. Jakupec, B. Kynast, H. Zorbas and B. K. Keppler, From bench to bedside—preclinical and early clinical development of the anticancer agent indazolium trans-[tetrachlorobis (1H-indazole) ruthenate (III)](KP1019 or FFC14A), *J. Inorg. Biochem.*, 2006, **100**, 891-904.
25. R. E. Morris, R. E. Aird, P. del Socorro Murdoch, H. Chen, J. Cummings, N. D. Hughes, S. Parsons, A. Parkin, G. Boyd and D. I. Jodrell, Inhibition of cancer cell growth by ruthenium (II) arene complexes, *J. Med. Chem.*, 2001, **44**, 3616-3621.
26. Z. Almodares, S. J. Lucas, B. D. Crossley, A. M. Basri, C. M. Pask, A. J. Hebden, R. M. Phillips and P. C. McGowan, Rhodium, iridium, and ruthenium half-sandwich picolinamide complexes as anticancer agents, *Inorg. Chem.*, 2014, **53**, 727-736.
27. D.-L. Ma, M. Wang, Z. Mao, C. Yang, C.-T. Ng and C.-H. Leung, Rhodium complexes as therapeutic agents, *Dalton Trans.*, 2016, **45**, 2762-2771.
28. A. Erck, L. Rainen, J. Whileyman, I. Chang, A. Kimball and J. Bear, Studies of rhodium (II) carboxylates as potential antitumor agents, *Proc. Soc. Exp. Biol. Med.*, 1974, **145**, 1278-1283.
29. A. Erck, E. Sherwood, J. Bear and A. Kimball, The metabolism of rhodium (II) acetate in tumor-bearing mice, *Cancer Res.*, 1976, **36**, 2204-2209.
30. J. Bear, J. H. Gray, L. Rainen, I. Chang, R. Howard, G. Serio and A. Kimball, Interaction of Rhodium (II) carboxylates with molecules of biologic importance, *Cancer Chemother. Rep.*, 1975, **59**, 611-620.
31. R. Howard, T. Spring and J. Bear, The interaction of rhodium (II) carboxylates with enzymes, *Cancer Res.*, 1976, **36**, 4402-4405.
32. G. Pneumatikakis and P. Psaroulis, Interactions of tetra- μ -acetato dirhodium (II) with sulfur-containing aminoacids, *Inorganica Chim. Acta*, 1980, **46**, 97-100.
33. E. B. Boyar and S. D. Robinson, Rhodium (II) carboxylates, *Coord. Chem. Rev.*, 1983, **50**, 109-208.
34. N. Katsaros and A. Anagnostopoulou, Rhodium and its compounds as potential agents in cancer treatment, *Crit. Rev. Oncol. Hematol.*, 2002, **42**, 297-308.
35. K. Sorasaene, P. K.-L. Fu, A. M. Angeles-Boza, K. R. Dunbar and C. Turro, Inhibition of transcription in vitro by anticancer active dirhodium (II) complexes, *Inorg. Chem.*, 2003, **42**, 1267-1271.
36. A. M. Angeles-Boza, P. M. Bradley, P. K.-L. Fu, S. E. Wicke, J. Bacsá, K. R. Dunbar and C. Turro, DNA binding and photocleavage in vitro by new dirhodium (II) dppz complexes: correlation to cytotoxicity and photocytotoxicity, *Inorg. Chem.*, 2004, **43**, 8510-8519.

37. A. M. Angeles-Boza, H. T. Chifotides, J. D. Aguirre, A. Chouai, P. K.-L. Fu, K. R. Dunbar and C. Turro, Dirhodium (II, II) complexes: molecular characteristics that affect in vitro activity, *J. Med. Chem.*, 2006, **49**, 6841-6847.
38. Z. Futera, T. s. Koval, J. Leszczynski, J. Gu, M. Mitoraj, M. Srebro and J. V. Burda, Exploring a reaction mechanism for acetato ligand replacement in paddlewheel tetrakisacetatodirhodium (II, II) complex by ammonia: computational density functional theory study, *J. Phys. Chem. A*, 2011, **115**, 784-794.
39. F. Vohidov, S. E. Knudsen, P. G. Leonard, J. Ohata, M. J. Wheadon, B. V. Popp, J. E. Ladbury and Z. T. Ball, Potent and selective inhibition of SH3 domains with dirhodium metalloinhibitors, *Chem. Sci.*, 2015, **6**, 4778-4783.
40. A. E. Garcia and F. Jalilehvand, Aerobic reactions of antitumor active dirhodium (II) tetraacetate $\text{Rh}_2(\text{CH}_3\text{COO})_4$ with glutathione, *J. Biol. Inorg. Chem.*, 2018, **23**, 231-239.
41. T. Zou, C. T. Lum, C.-N. Lok, J.-J. Zhang and C.-M. Che, Chemical biology of anticancer gold (III) and gold (I) complexes, *Chem. Soc. Rev.*, 2015, **44**, 8786-8801.
42. C. F. Shaw, Gold-based therapeutic agents, *Chem. Rev.*, 1999, **99**, 2589-2600.
43. G. Schmitz, D. Minkel, D. Gingrich and C. Shaw III, The binding of gold (I) to metallothionein, *J. Inorg. Biochem.*, 1980, **12**, 293-306.
44. C. T. Lum, R. W.-Y. Sun, T. Zou and C.-M. Che, Gold (III) complexes inhibit growth of cisplatin-resistant ovarian cancer in association with upregulation of proapoptotic PMS2 gene, *Chem. Sci.*, 2014, **5**, 1579-1584.
45. R. D. Teo, H. B. Gray, P. Lim, J. Termini, E. Domeshek and Z. Gross, A cytotoxic and cytostatic gold (III) corrole, *Chem. Commun.*, 2014, **50**, 13789-13792.
46. L. Messori, F. Abbate, G. Marcon, P. Orioli, M. Fontani, E. Mini, T. Mazzei, S. Carotti, T. O'Connell and P. Zanello, Gold (III) complexes as potential antitumor agents: solution chemistry and cytotoxic properties of some selected gold (III) compounds, *J. Med. Chem.*, 2000, **43**, 3541-3548.
47. M. Knipp, A. V. Karotki, S. Chesnov, G. Natile, P. J. Sadler, V. Brabec and M. Vařák, Reaction of Zn_7 Metallothionein with cis- and trans- $[\text{Pt}(\text{N-donor})_2\text{Cl}_2]$ anticancer complexes: trans-PtII complexes retain their N-donor ligands, *J. Med. Chem.*, 2007, **50**, 4075-4086.
48. D. Hagrman, J. Goodisman, J. C. Dabrowiak and A.-K. Souid, Kinetic study on the reaction of cisplatin with metallothionein, *Drug Metab. Dispos.*, 2003, **31**, 916-923.

49. D. L. Wong and M. J. Stillman, Destructive interactions of dirhodium (II) tetraacetate with β metallothionein rh1a, *Chem. Commun.*, 2016, **52**, 5698-5701.
50. G. Rentschler, I. Rodushkin, M. Cerna, C. Chen, F. Harari, R. Harari, M. Horvat, F. Hrubá, L. Kasparová and K. Koppová, Platinum, palladium, rhodium, molybdenum and strontium in blood of urban women in nine countries, *Int. J. Hyg. Environ. Health*, 2018, **221**, 223-230.
51. M. Mauro, M. Crosera, C. Bianco, G. Adami, T. Montini, P. Fornasiero, M. Jaganjac, M. Bovenzi and F. L. Filon, Permeation of platinum and rhodium nanoparticles through intact and damaged human skin, *J. Nanoparticle Res.*, 2015, **17**, 253.
52. S. Zimmermann and B. Sures, Lessons learned from studies with the freshwater mussel *Dreissena polymorpha* exposed to platinum, palladium and rhodium, *Sci. Total Environ.*, 2018, **615**, 1396-1405.
53. D. L. Wong and M. J. Stillman, Metallothionein: An Aggressive Scavenger—The Metabolism of Rhodium (II) Tetraacetate ($\text{Rh}_2(\text{CH}_3\text{CO}_2)_4$), *ACS Omega*, 2018, **3**, 16314-16327.
54. Z. A. Shaikh and C. Tohyama, Urinary metallothionein as an indicator of cadmium body burden and of cadmium-induced nephrotoxicity, *Environ. Health Perspect.*, 1984, **54**, 171.
55. C. Tohyama, Z. A. Shaikh, K. Nogawa, E. Kobayashi and R. Honda, Urinary metallothionein as a new index of renal dysfunction in “Itai-Itai” disease patients and other Japanese women environmentally exposed to cadmium, *Arch. Toxicol.*, 1982, **50**, 159-166.
56. D. L. Wong, A. Zhang, A. S. Faponle, S. P. de Visser and M. J. Stillman, Glutathione binding to dirhodium tetraacetate: a spectroscopic, mass spectral and computational study of an anti-tumour compound, *Metallomics*, 2017, **9**, 501-516.
57. M. J. Stillman, C. F. Shaw and K. T. Suzuki, *Metallothionein: Synthesis, structure, and properties of metallothioneins, phytochelatins, and metal-thiolate complexes*, Wiley-VCH, 1992.
58. J. S. Scheller, G. W. Irvine and M. J. Stillman, Unravelling the mechanistic details of metal binding to mammalian metallothioneins from stoichiometric, kinetic, and binding affinity data, *Dalton Trans.*, 2018, **47**, 3613-3637.
59. Y. Yang, W. Maret and B. L. Vallee, Differential fluorescence labeling of cysteinyl clusters uncovers high tissue levels of thionein, *Proc. Natl. Acad. Sci. U.S.A.*, 2001, **98**, 5556-5559.

Appendix A: Observed Rate Constants for Experiments Performed in Chapter 2

Figure	Constant Conditions	Variable Conditions	K_{obs} (10^6s^{-1})	Standard Deviation
pH Titration	4 M GdmCl 2.5 eq. Cd (II) 10 °C	pH 5	215.48	3.127 (1.45%)
		pH 6	317.95	2.842 (0.89%)
		pH 7	422.40	5.084 (1.20%)
		pH 7.5	918.93	8.412 (0.92%)
		pH 8	2150.00	41.75 (1.94%)
Cd Titration	pH 5 0 M GdmCl 10 °C	1 eq	830.89	21.57 (2.60%)
		2.5 eq	353.97	3.797 (1.07%)
		5 eq	182.60	1.252 (0.69%)
	pH 5 4 M GdmCl 10 °C	1 eq	404.28	7.262 (1.80%)
		2.5 eq	215.48	3.127 (1.45%)
		5 eq	147.17	1.313 (0.89%)
	pH 8 0 M GdmCl 10 °C	1 eq	7198.20	265.4 (3.69%)
		2 eq	4690.10	72.29 (1.54%)
		2.5 eq	3633.30	78.59 (2.16%)
		3 eq	1953.90	19.02 (0.97%)
		4 eq	1459.70	10.27 (0.70%)
		5 eq	2318.80	11.29 (0.49%)
	pH 8 4 M GdmCl	1 eq	1238.10	9.705 (0.78%)
		2.5 eq	2150.00	41.75 (1.94%)

	10 °C	5 eq	878.86	14.15 (1.61%)
GdmCl Titration	pH 5 2.5 eq. Cd (II) 10 °C	0 M	353.97	3.797 (1.07%)
		1 M	265.67	1.827 (0.69%)
		2 M	252.91	1.58 (0.62%)
		4 M	215.48	3.127 (1.45%)
Temperature Dependence	pH 5 0 M GdmCl 2.5 eq. Cd (II)	10.1 °C	353.97	3.797 (1.07%)
		15.3 °C	407.14	4.142 (1.02%)
		18.1 °C	468.10	7.597 (1.62%)

Appendix B: Known Kinetic and Equilibrium Binding Constants for MTs

Table 2. Reports of kinetic data for the metallation of individual metallothioneins							
Metal	Organism **	Isoform	Fragment/ Protein	Stoichiometry	Technique	Rate constants k [$M^{-1} s^{-1}$]	Reference
As	human ²⁰	MT1a	α	As ₃ MT	ESI-MS	k_1 5.5 k_2 6.3 k_3 3.9	¹
	human ²⁰	MT1a	β	As ₃ MT	ESI-MS	k_1 3.6 k_2 2.0 k_3 0.6	¹
	human ²⁰	MT1a	$\beta\alpha$	As ₆ MT	ESI-MS	k_1 25 k_2 24 k_3 19 k_4 14 k_5 8.7 k_6 3.7	²
Bi	rabbit	MT2	$\beta\alpha$	Bi ₇ MT	UV-visible absorption, ¹ H NMR	k_1 5.8×10^{-3} (Cd displacement) k_2 1.0×10^{-4} (Cd displacement) k_1 7.2×10^{-3} (Zn displacement) k_2 5.9×10^{-5} (Zn displacement)	³
Cd	human ²⁰	MT1a	α	Cd ₄ MT	Stopped flow spectrophotometry	k_{1-4} 60.4 (native) k_{1-4} 3.32 (denatured)	⁴
	horse kidney ²⁰	MT	$\beta\alpha$	Cd ₇ MT	Absorption spectroscopy	2.7×10^{-6} (Demetallatio n by EDTA)	⁵
	rabbit ²⁰	MT2	$\beta\alpha$	Cd ₇ MT	Stopped flow spectrophotometry	pH 4.1 60±10 pH 4.6 140±30 pH 5.1 280±50 pH 5.4 350±100	⁶
	rabbit ²⁰	MT2	α	Cd ₄ MT	Stopped flow spectrophotometry	pH 4.6 170±60 pH 5.1 350±100 pH 5.4 460±200	⁶
Zn	rabbit ²⁰	MT2	$\beta\alpha$	Zn ₇ MT	Stopped flow spectrophotometry	pH 4.6 10±1 pH 5.2 15±1	⁶

						pH 5.8 28±2 pH 6.3 43±7 pH 6.6 100±15 pH 7.2 300±100	
	rabbit ²⁰	MT2	α	Zn ₄ MT	Stopped flow spectrophotometry	pH 6.6 90±10 pH 7.2 230±100 pH 7.5 690±300	⁶
Pt	rabbit ²⁰	MT	βα	Pt ₇ MT	Atomic absorption spectroscopy, UV absorption, HPLC	0.14 (to apo- MT) 0.75 to Cd/Zn-MT 0.53 to Cd ₇ MT 0.65 to Zn ₇ MT	⁷
Zn	horse kidney ²⁰	MT	βα	Zn ₇ MT	Absorption	Demetallation by EDTA <i>k</i> ₁ fast <i>k</i> ₂ 14.2x10 ⁻⁴ <i>k</i> ₃ 2.0x10 ⁻⁴	⁵

** superscript shows the number of cysteines in the peptide

Metal	Isoform	Fragment/P rotein	Stoichiometry	Technique***	Binding constant value (logK)	Reference
Cu	MT2	$\beta\alpha$	Cu ₁₀ MT	ESI-MS, pH 7.5	<i>K</i> 14.6	⁸
	MT1a	$\beta\alpha$	Cu ₂₀ MT	ESI-MS ¹ pH 7.4	<i>K</i> ₁ 15.5 <i>K</i> ₂ 15.0 <i>K</i> ₃ 14.6 <i>K</i> ₄ 19.3 <i>K</i> ₅ 14.6 <i>K</i> ₆ 18.9 <i>K</i> ₇ 12.9 <i>K</i> ₈ 13.1 <i>K</i> ₉ 13.7 <i>K</i> ₁₀ 15.5 <i>K</i> ₁₁ 10.7 <i>K</i> ₁₂ 11.2 <i>K</i> ₁₃ 12.9 <i>K</i> ₁₄ 9.5 <i>K</i> ₁₅ 9.5 <i>K</i> ₁₆ 8.6 <i>K</i> ₁₇ 8.1 <i>K</i> ₁₈ 7.0 <i>K</i> ₁₉ 6.1 <i>K</i> ₂₀ 5.0	⁹
Pb	MT3	$\beta\alpha$	Pb ₇ MT	ITC, pH 6.0	<i>K</i> ₁₋₂ 11.7 <i>K</i> ₃₋₄ 10.2 <i>K</i> ₄₋₇ 8.7	¹⁰
Zn	MT2	$\beta\alpha$	Zn ₇ MT	Fluorescence spectroscopy ² pH 7.4	<i>K</i> ₁₋₄ 11.8 <i>K</i> ₅ 10.45 <i>K</i> ₆ 9.95 <i>K</i> ₇ 7.7	¹¹
	MT3	$\beta\alpha$	Zn ₇ MT	ITC, pH 6.0	<i>K</i> ₁₋₄ 10.8 <i>K</i> ₅ 10.5 <i>K</i> ₆ 9.9 <i>K</i> ₇ 7.7	¹⁰
	MT1a	$\beta\alpha$	Zn ₇ MT	ESI-MS ³	<i>K</i> ₁ 12.35 <i>K</i> ₂ 12.47 <i>K</i> ₃ 12.52 <i>K</i> ₄ 12.37 <i>K</i> ₅ 12.21 <i>K</i> ₆ 12.05 <i>K</i> ₇ 11.80	¹²

**superscript shows the number of cysteines in the peptide

***Explanations:

¹ determined by analysis of the pH dependent titration data

² binding strength was determined using competitors and fluorogenic dye

³ binding constant values were determined through competition of zinc binding to carbonic anhydrase

1. T. T. Ngu and M. J. Stillman, Arsenic binding to human metallothionein, *J. Am. Chem. Soc.*, 2006, **128**, 12473-12483.
2. T. T. Ngu, A. Easton and M. J. Stillman, Kinetic analysis of arsenic– metalation of human metallothionein: significance of the two-domain structure, *J. Am. Chem. Soc.*, 2008, **130**, 17016-17028.

3. H. Sun, H. Li, I. Harvey and P. J. Sadler, Interactions of bismuth complexes with metallothionein (II), *J. Biol. Chem.*, 1999, **274**, 29094-29101.
4. G. W. Irvine, K. E. Duncan, M. Gullons and M. J. Stillman, Metalation kinetics of the human α -metallothionein 1a fragment is dependent on the fluxional structure of the apo-protein, *Chem. Eur. J.*, 2015, **21**, 1269-1279.
5. T.-Y. Li, A. J. Kraker, C. F. Shaw and D. H. Petering, Ligand substitution reactions of metallothioneins with EDTA and apo-carbonic anhydrase, *Proc. Natl. Acad. Sci. U.S.A.*, 1980, **77**, 6334-6338.
6. J. Ejnik, J. Robinson, J. Zhu, H. Försterling, C. F. Shaw III and D. H. Petering, Folding pathway of apo-metallothionein induced by Zn^{2+} , Cd^{2+} and Co^{2+} , *J. Inorg. Biochem.*, 2002, **88**, 144-152.
7. D. Hagrman, J. Goodisman, J. C. Dabrowiak and A.-K. Souid, Kinetic study on the reaction of cisplatin with metallothionein, *Drug Metab. Dispos.*, 2003, **31**, 916-923.
8. L. Banci, I. Bertini, S. Ciofi-Baffoni, T. Kozyreva, K. Zovo and P. Palumaa, Affinity gradients drive copper to cellular destinations, *Nature*, 2010, **465**, 645.
9. J. S. Scheller, G. W. Irvine, D. L. Wong, A. Hartwig and M. J. Stillman, Stepwise copper (I) binding to metallothionein: a mixed cooperative and non-cooperative mechanism for all 20 copper ions, *Metallomics*, 2017, **9**, 447-462.
10. M. Carpenter, A. S. Shah, S. DeSilva, A. Gleaton, A. Su, B. Goundie, M. Croteau, M. Stevenson, D. Wilcox and R. Austin, Thermodynamics of Pb (II) and Zn (II) binding to MT-3, a neurologically important metallothionein, *Metallomics*, 2016, **8**, 605-617.
11. A. Krężel and W. Maret, Dual nanomolar and picomolar Zn (II) binding properties of metallothionein, *J. Am. Chem. Soc.*, 2007, **129**, 10911-10921.
12. T. B. Pinter and M. J. Stillman, The zinc balance: Competitive zinc metalation of carbonic anhydrase and metallothionein 1A, *Biochemistry*, 2014, **53**, 6276-6285.

Appendix C: Supplementary Structures and Energies for Rh₂ bound MT

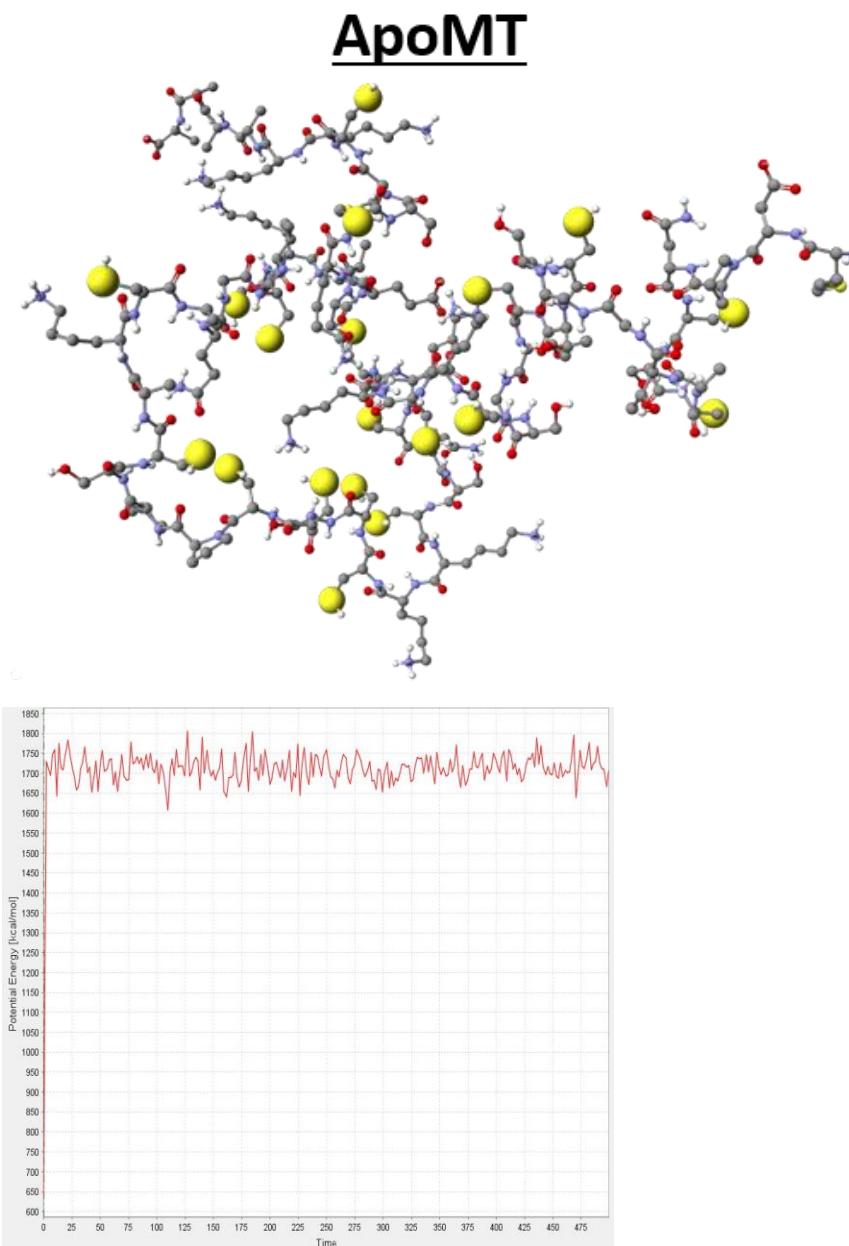


Fig S. 4. Top: Apo-MT MD result. Cysteine S shown in yellow. Bottom: Potential Energy trajectory over time. Reproduced from reference.¹ Copyright 2018 American Chemical Society.

ApoMT

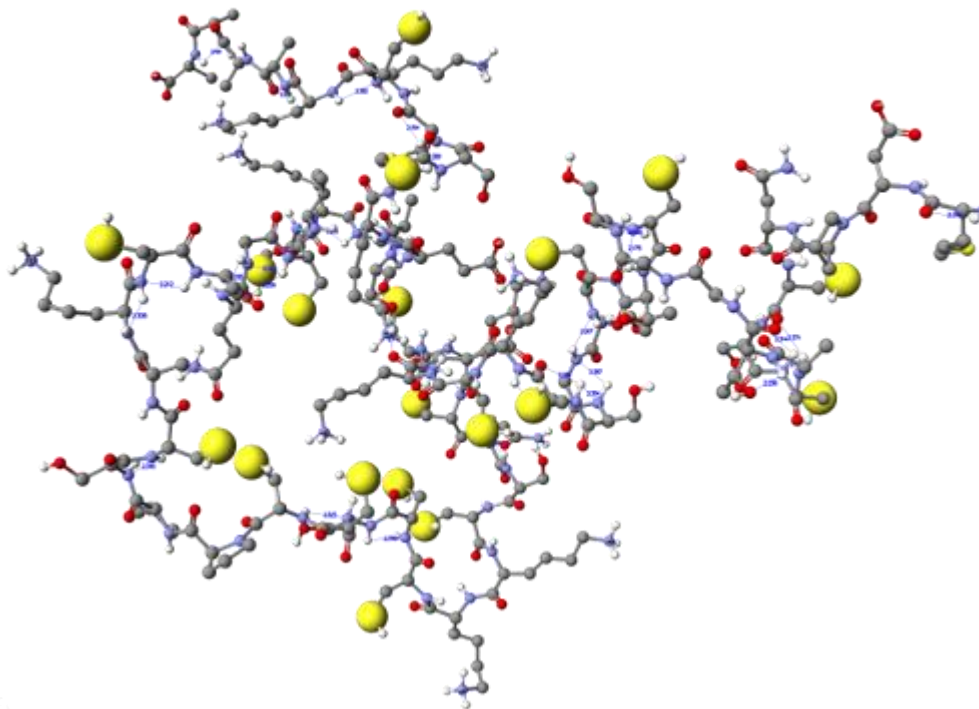


Fig S. 5. Apo-MT MD result. Cysteine S shown in yellow. H bond interactions are indicated in blue. Reproduced from reference.¹ Copyright 2018 American Chemical Society.

Rh₂MT

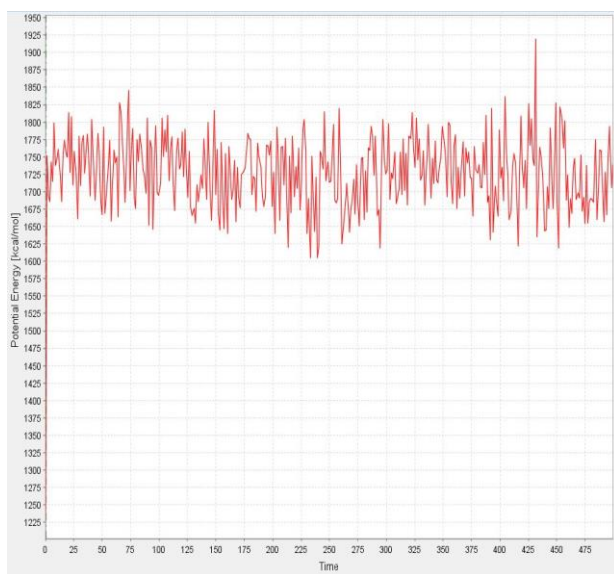
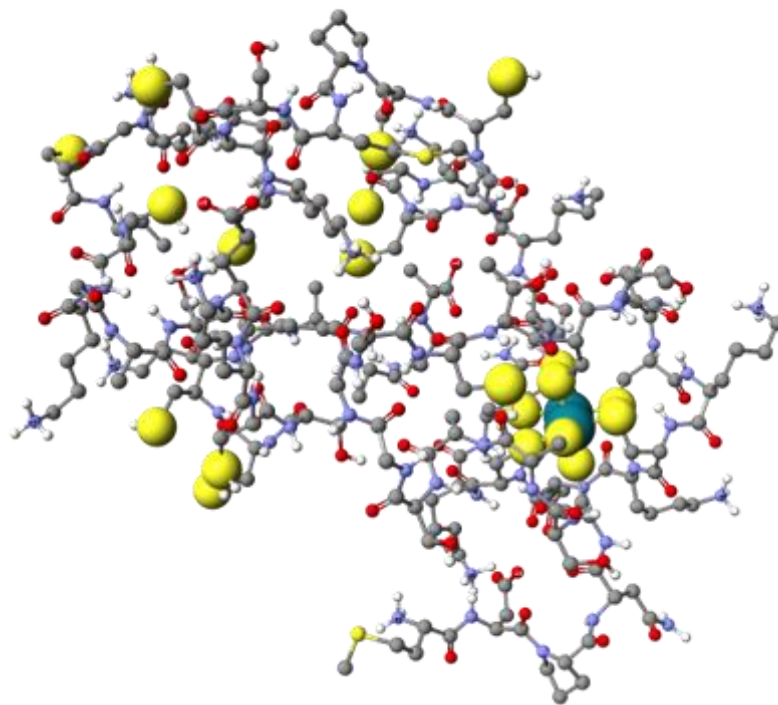


Fig S. 6. Top: Rh₂MT MD result. Cysteine S shown in yellow. Rh shown in teal. Bottom: Potential Energy trajectory over time Reproduced from reference.¹ Copyright 2018 American Chemical Society.

Rh₂βMT

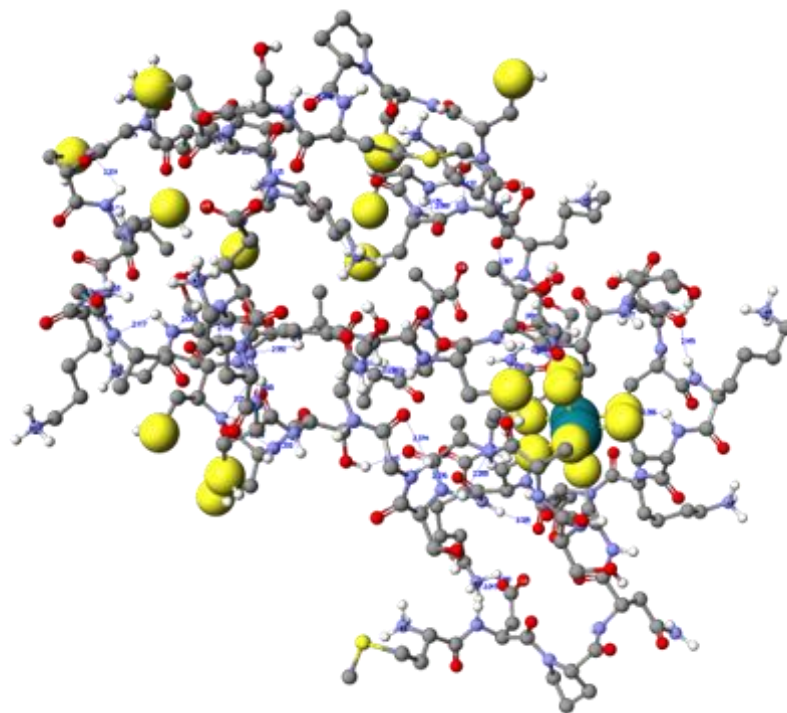


Fig S. 7. Rh₂MT MD result with Rh₂ in the β-domain. Cysteine S shown in yellow. Rh shown in teal. H bond interactions are indicated in blue. Reproduced from reference.¹
Copyright 2018 American Chemical Society.

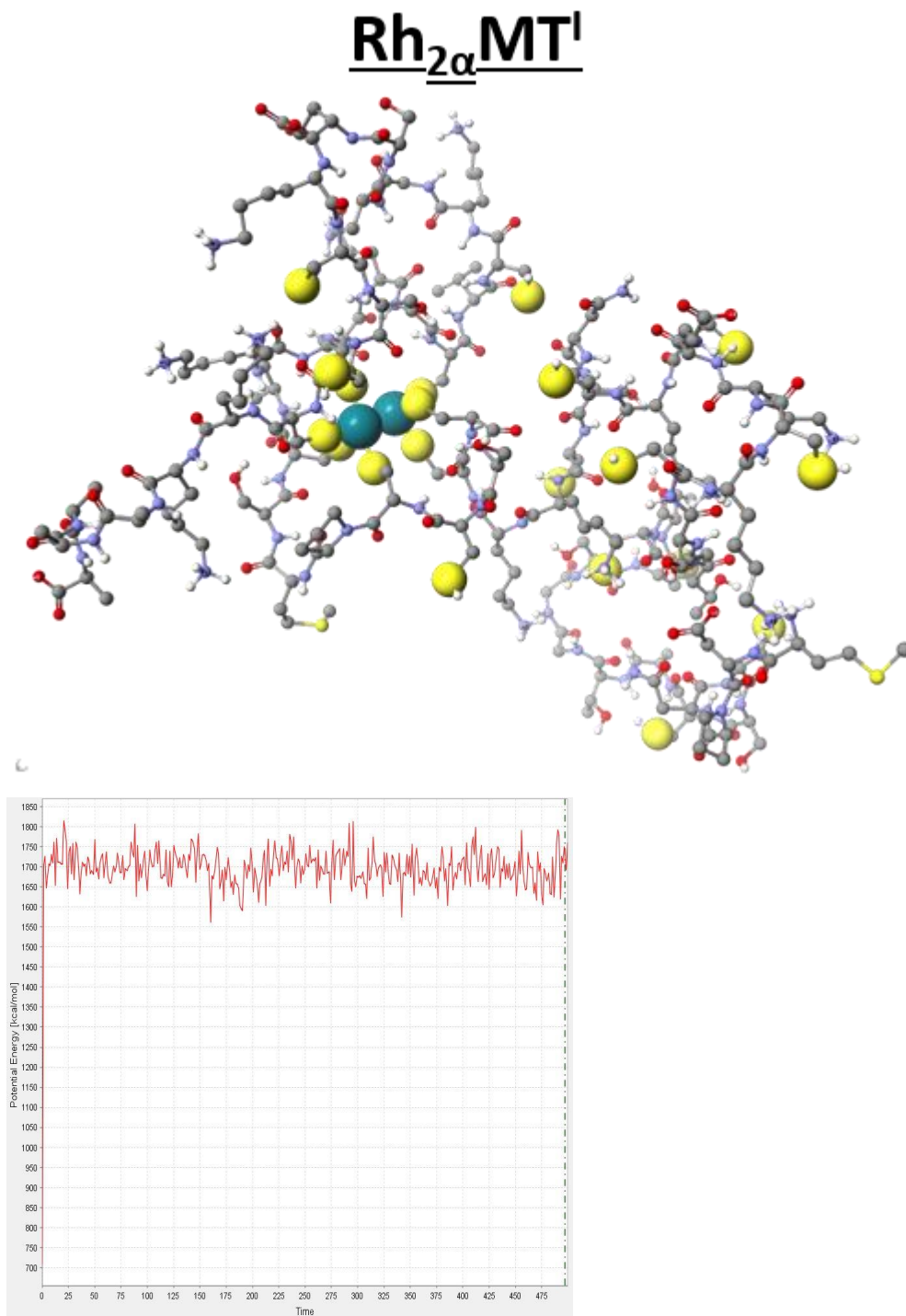


Fig S. 8. Top: Rh₂MT MD result with Rh₂ in a conformation in the α-domain. Cysteine S shown in yellow. Rh shown in teal. Reproduced from reference.¹ Copyright 2018 American Chemical Society.

Rh₂MT^I

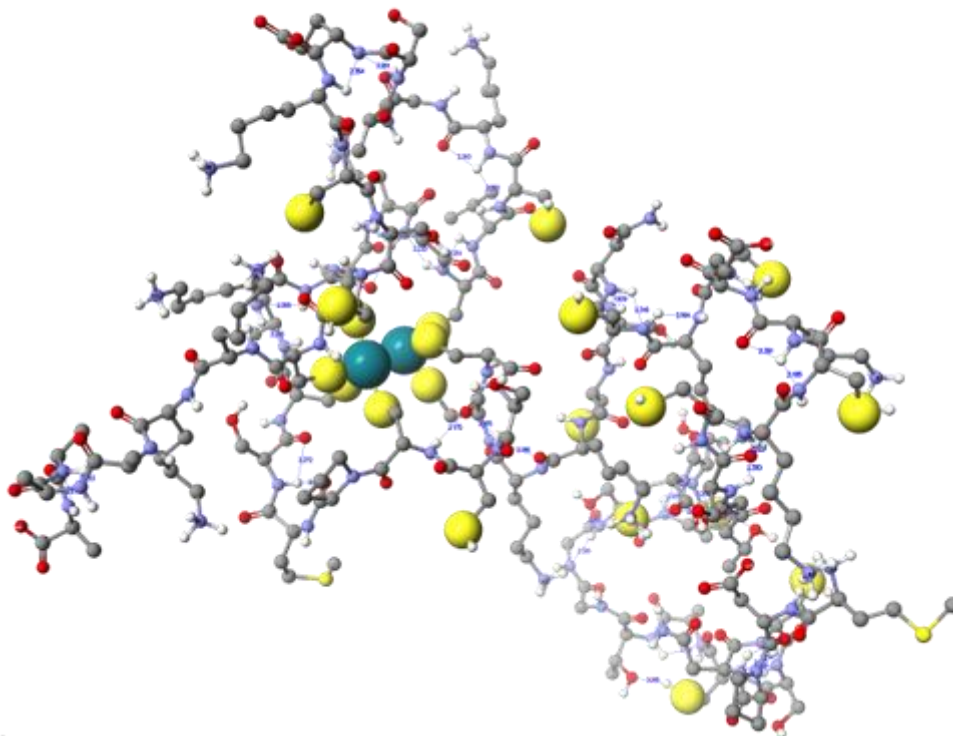


Fig S. 9. Rh₂MT MD result with Rh₂ in a conformation in the α -domain Cysteine S shown in yellow. Rh shown in teal. H bond interactions are indicated in blue. Reproduced from reference.¹ Copyright 2018 American Chemical Society.

Rh₂MT^{II}

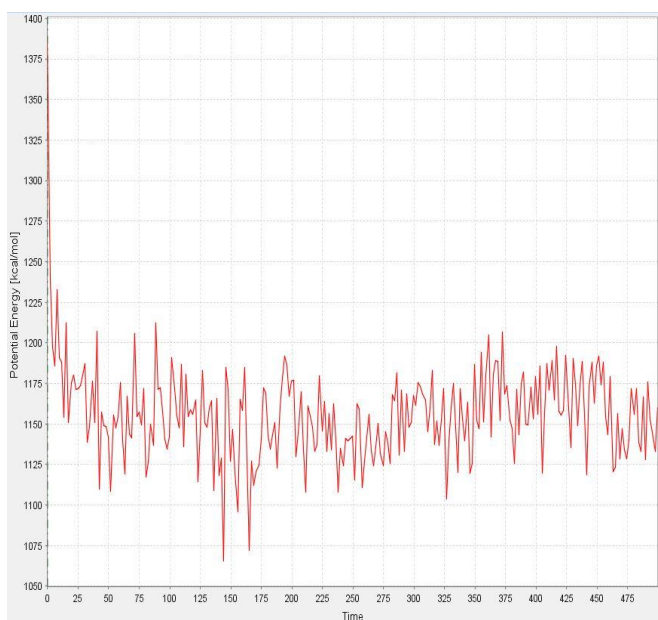
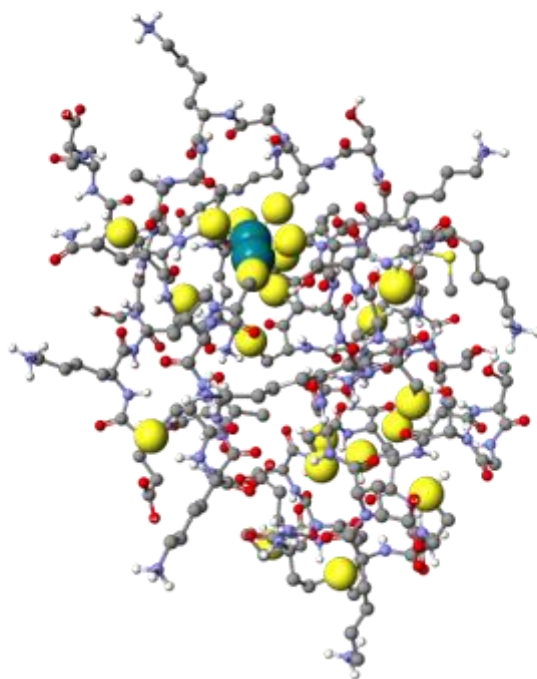


Fig S. 10. Top: Rh₂MT MD result with Rh₂ in an alternate conformation in the α -domain. Cysteine S shown in yellow. Rh shown in teal. Bottom: Potential Energy trajectory over time. Reproduced from reference.¹ Copyright 2018 American Chemical Society.

Rh₂MT^{II}

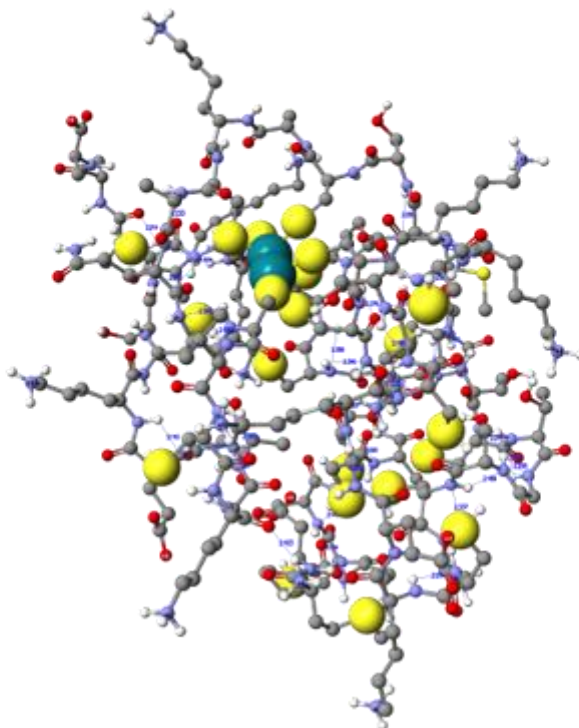


Fig S. 11. Rh₂MT MD result with Rh₂ in an alternate conformation in the α -domain. Cysteine S shown in yellow. Rh shown in teal. H bond interactions are indicated in blue. Reproduced from reference.¹ Copyright 2018 American Chemical Society.

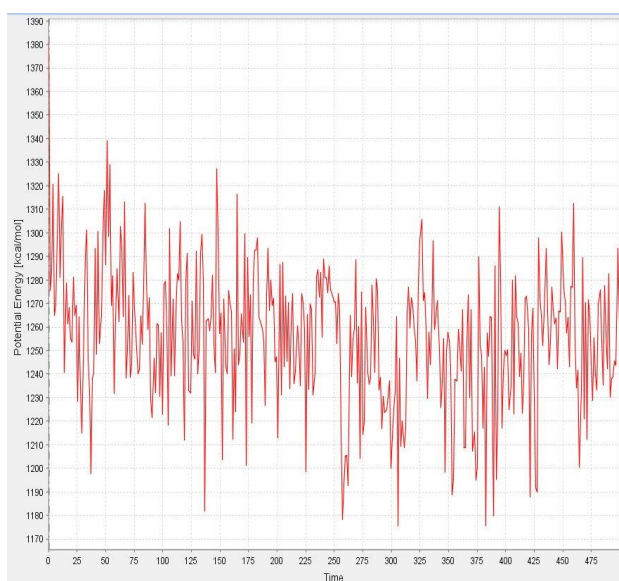
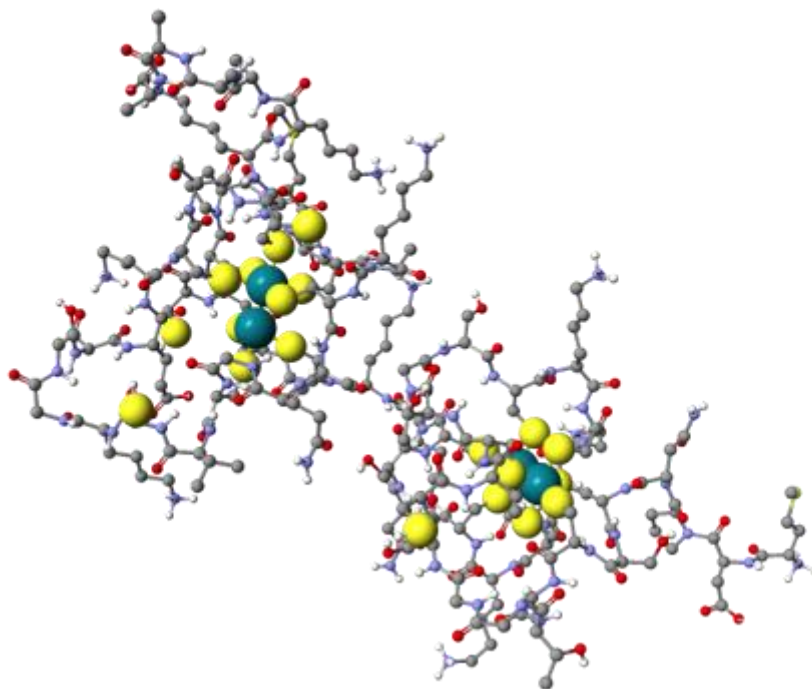
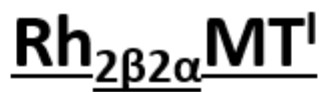


Fig S. 12. Top: Rh₄MT MD result with Rh₂ in the β -domain and Rh₂ in a conformation in the α -domain. Cysteine S shown in yellow. Rh shown in teal. Bottom: Potential Energy trajectory over time. Reproduced from reference.¹ Copyright 2018 American Chemical Society.

Rh₂β₂αMT^I

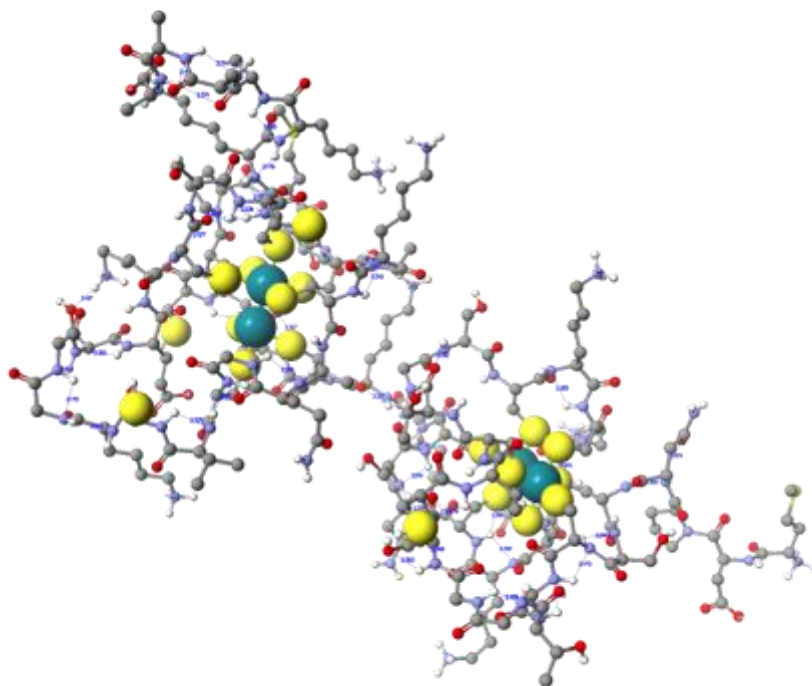


Fig S. 13. Rh₄MT MD result with Rh₂ in the β-domain and Rh₂ in a conformation in the α-domain. Cysteine S shown in yellow. Rh shown in teal. H bond interactions are indicated in blue. Reproduced from reference.¹ Copyright 2018 American Chemical Society.

Rh₂β₂αMT^{II}

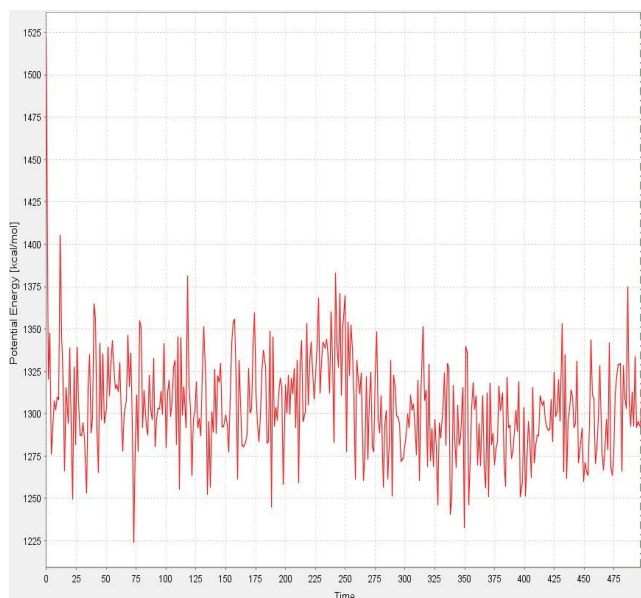
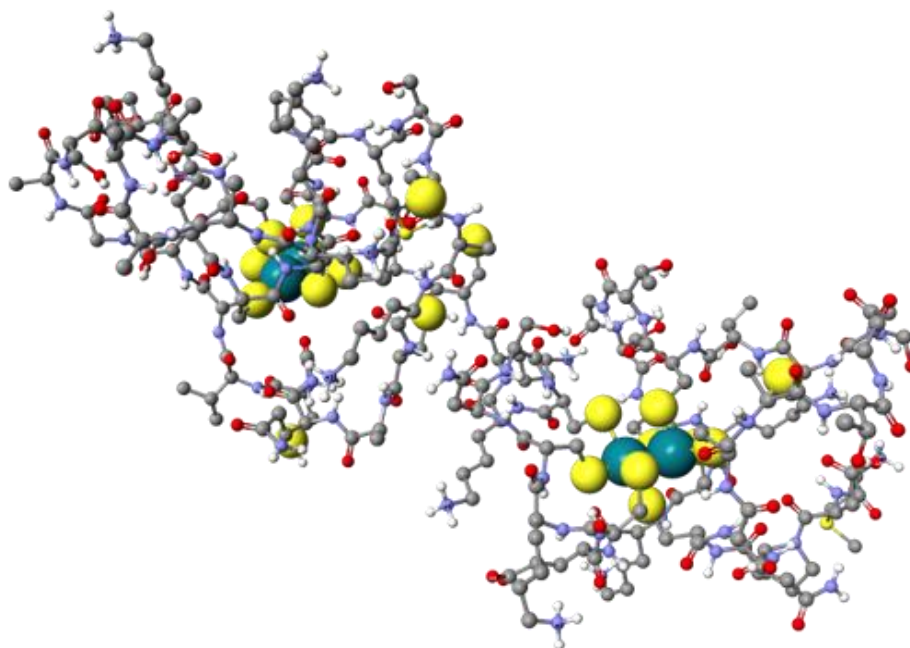


Fig S. 14. Top: Rh₄MT MD result with Rh₂ in the β-domain and Rh₂ in an alternate conformation in the α-domain. Cysteine S shown in yellow. Rh shown in teal. Bottom: Potential Energy trajectory over time. Reproduced from reference.¹ Copyright 2018 American Chemical Society.

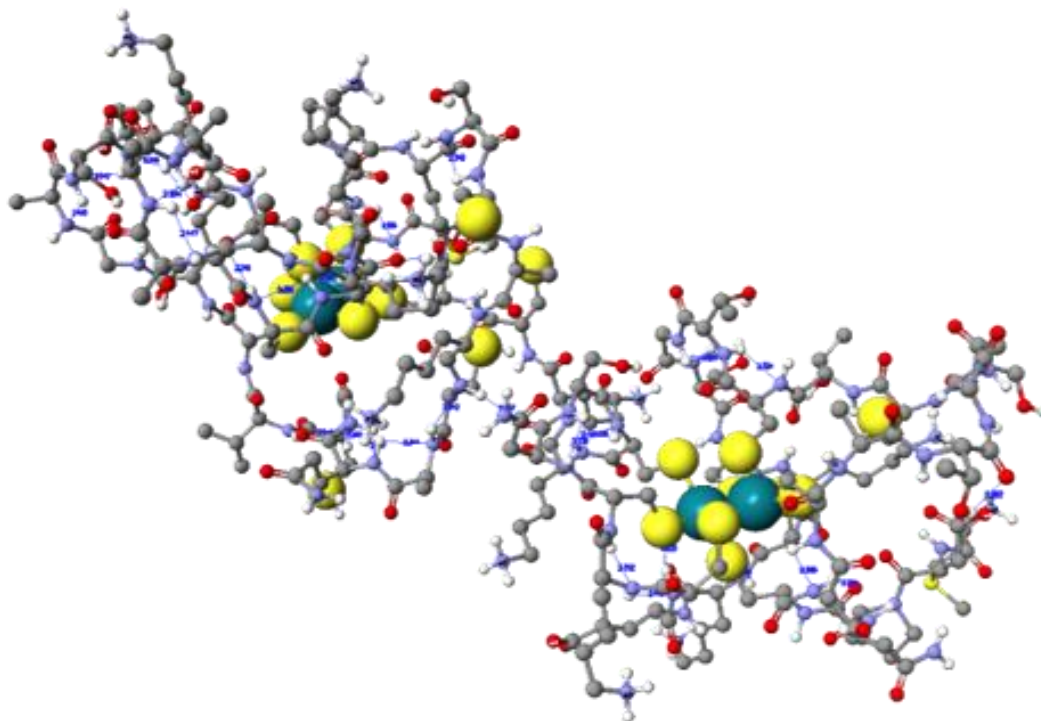
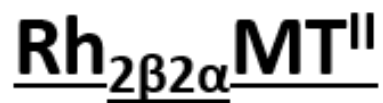


Fig S. 15. Rh₄MT MD result with Rh₂ in the β -domain and Rh₂ in an alternate conformation in the α -domain. Cysteine S shown in yellow. Rh shown in teal. H bond interactions are indicated in blue. Reproduced from reference.¹ Copyright 2018 American Chemical Society.

Rh₄MT

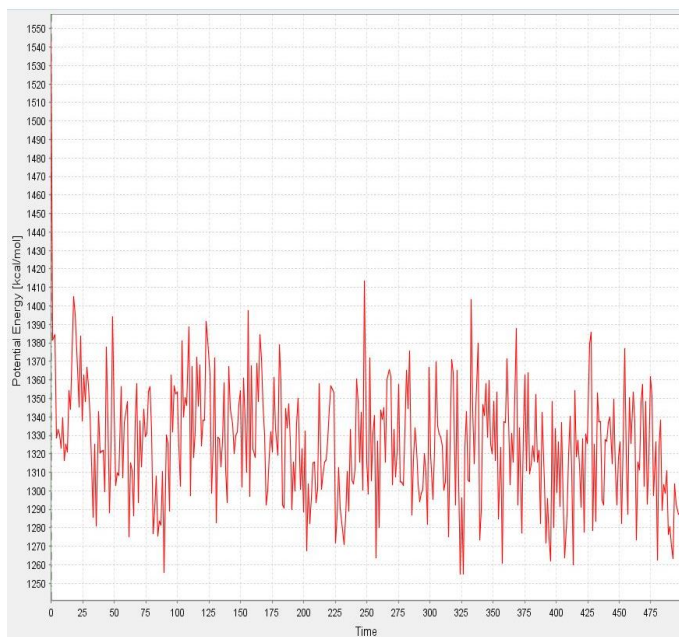
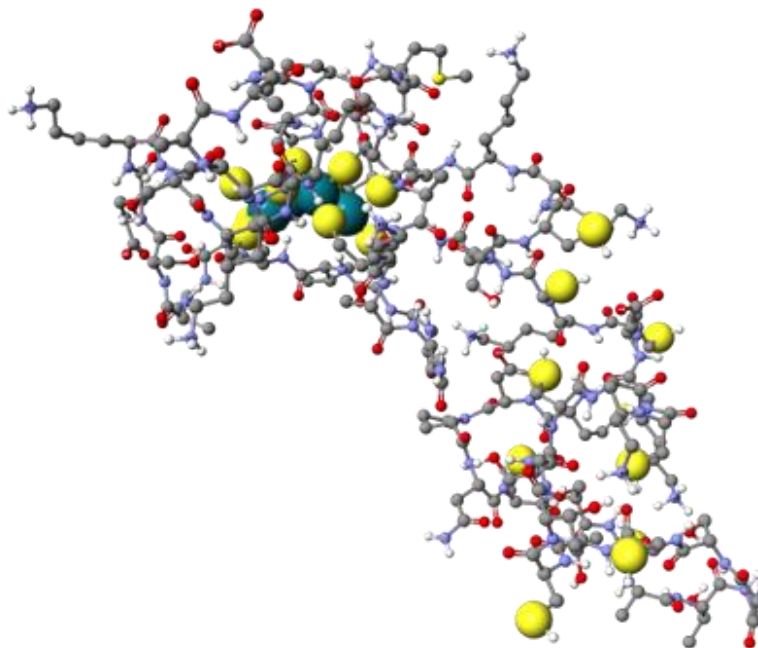


Fig S. 16. Top: Rh₄MT MD result with Rh₄ in the α -domain. Cysteine S shown in yellow. Rh shown in teal. Bottom: Potential Energy trajectory over time. Reproduced from reference.¹ Copyright 2018 American Chemical Society.

Rh₄MT

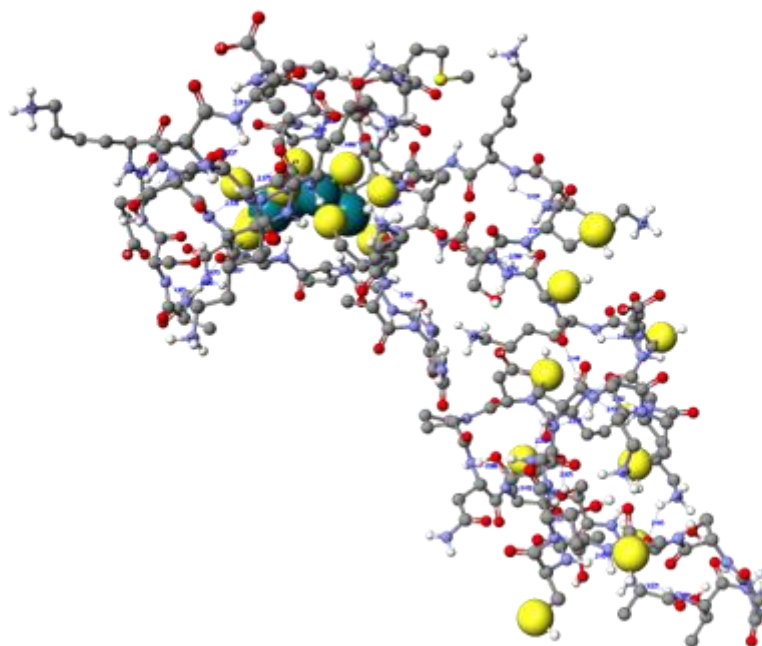


Fig S. 17. Rh₄MT MD result with Rh₄ in the α -domain. Cysteine S shown in yellow. Rh shown in teal. H bond interactions are indicated in blue. Reproduced from reference.¹
Copyright 2018 American Chemical Society.

Rh₂β4αMT

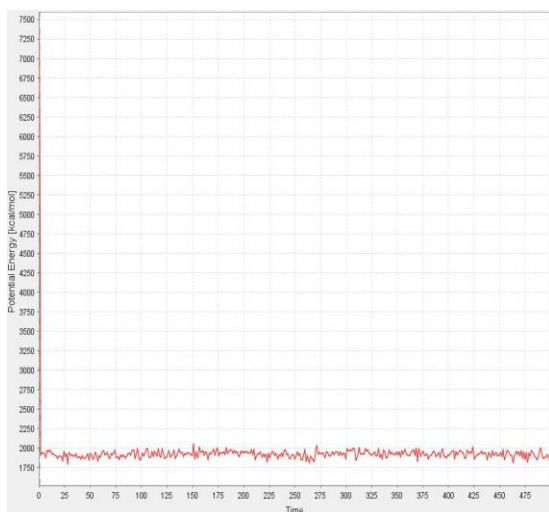
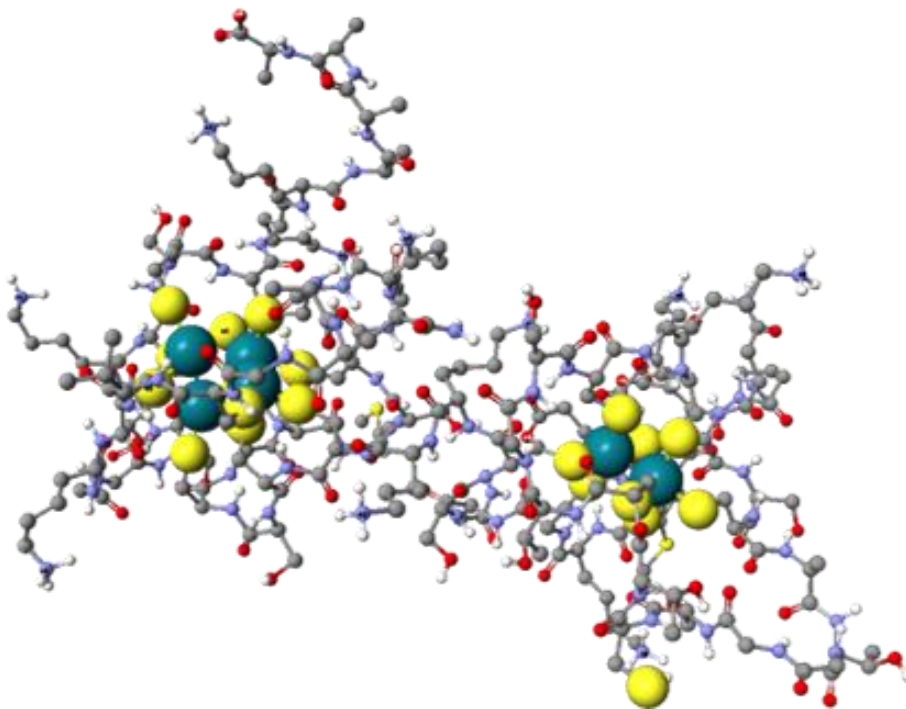


Fig S. 18. Top: Rh₆MT MD result with Rh₂ in the β-domain and Rh₄ in the α-domain. Cysteine S shown in yellow. Rh shown in teal. Bottom: Potential Energy trajectory over time. Reproduced from reference.¹ Copyright 2018 American Chemical Society.

Rh₂β₄αMT

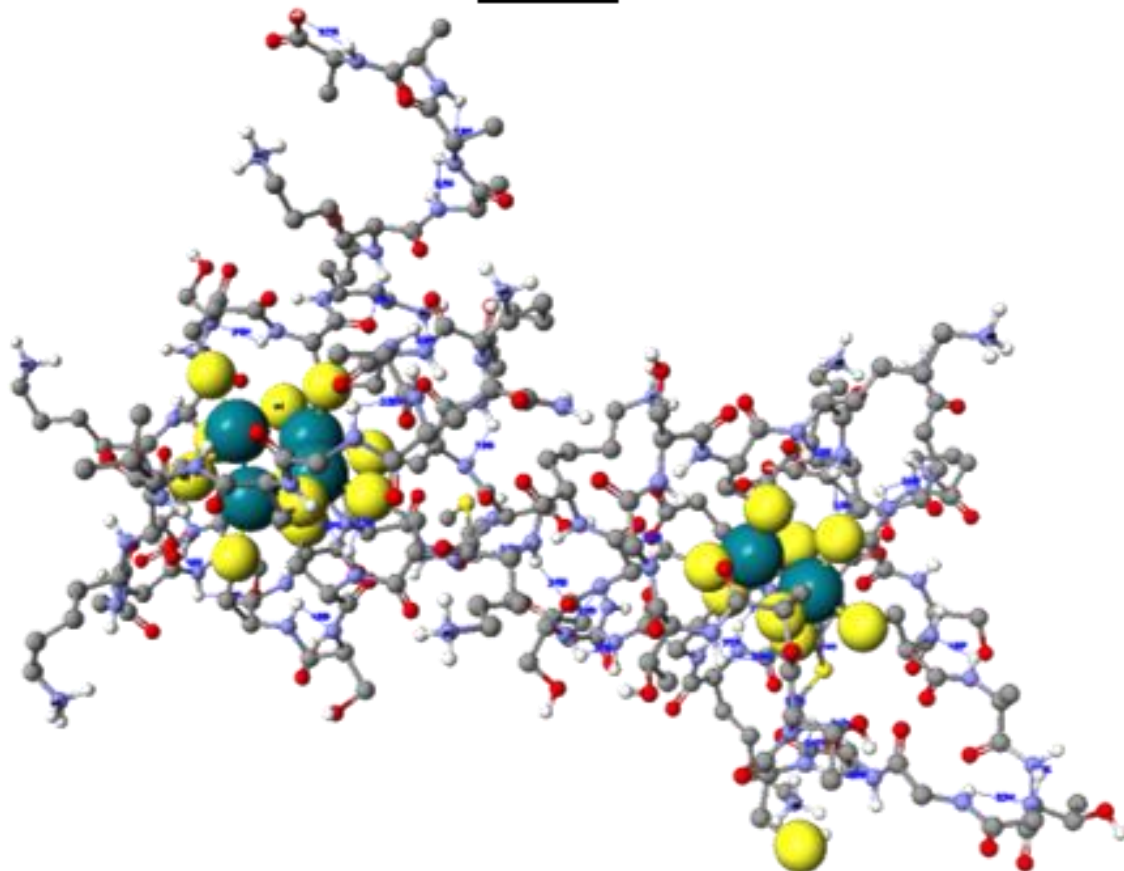


Fig S. 19. Rh₆MT MD result with Rh₂ in the β-domain and Rh₄ in the α-domain. Cysteine S shown in yellow. Rh shown in teal. H bond interactions are indicated in blue.

Reproduced from reference.¹ Copyright 2018 American Chemical Society.

1. D. L. Wong and M. J. Stillman, Metallothionein: An Aggressive Scavenger—The Metabolism of Rhodium (II) Tetraacetate (Rh₂ (CH₃CO₂)₄), *ACS Omega*, 2018, **3**, 16314-16327.

Appendix D: Surfaces and Orbital Energies for GSH bound to $\text{Rh}_2(\text{OAc})_4$

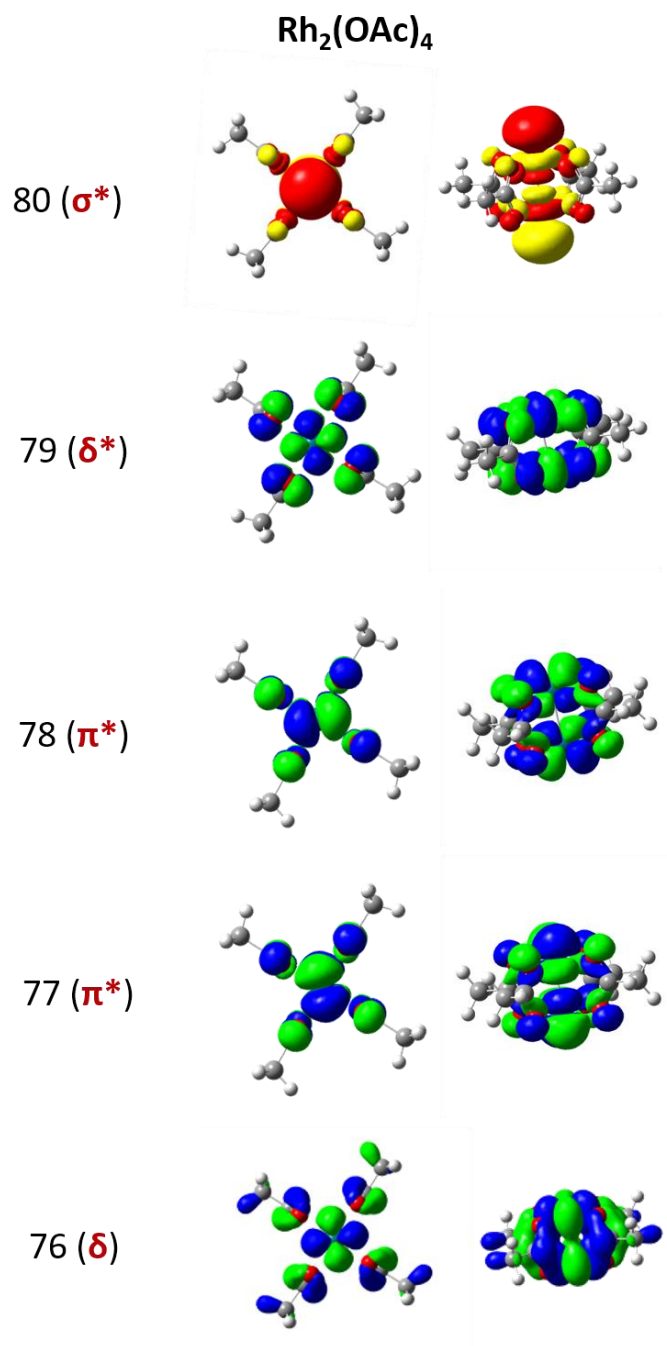


Fig S1. Expanded views of $\text{Rh}_2(\text{OAc})_4$ molecular orbital surfaces, part 1/2. Calculations and image from A. Zhang in reference, ¹ reproduced with permission from the Royal Society of Chemistry.

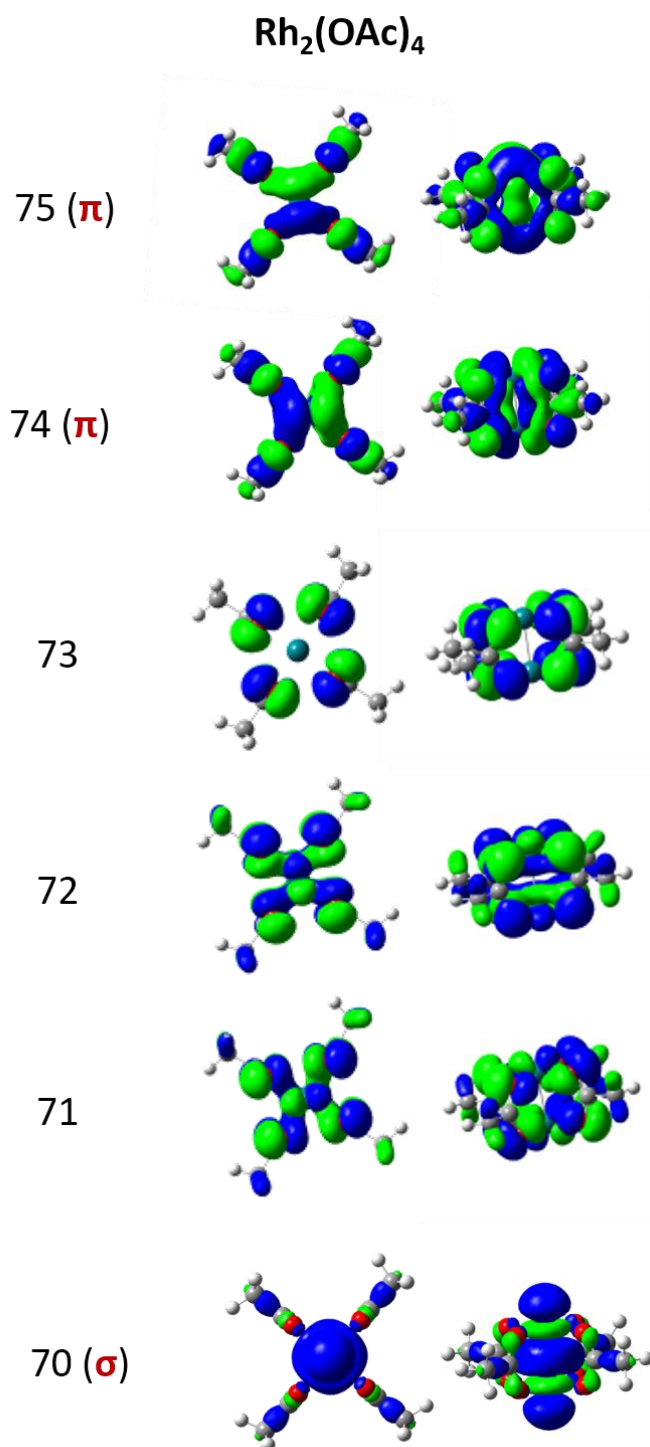


Fig S2. Expanded views of $\text{Rh}_2(\text{OAc})_4$ molecular orbital surfaces, part 2/2. Calculations and image from A. Zhang in reference,¹ reproduced with permission from the Royal Society of Chemistry.

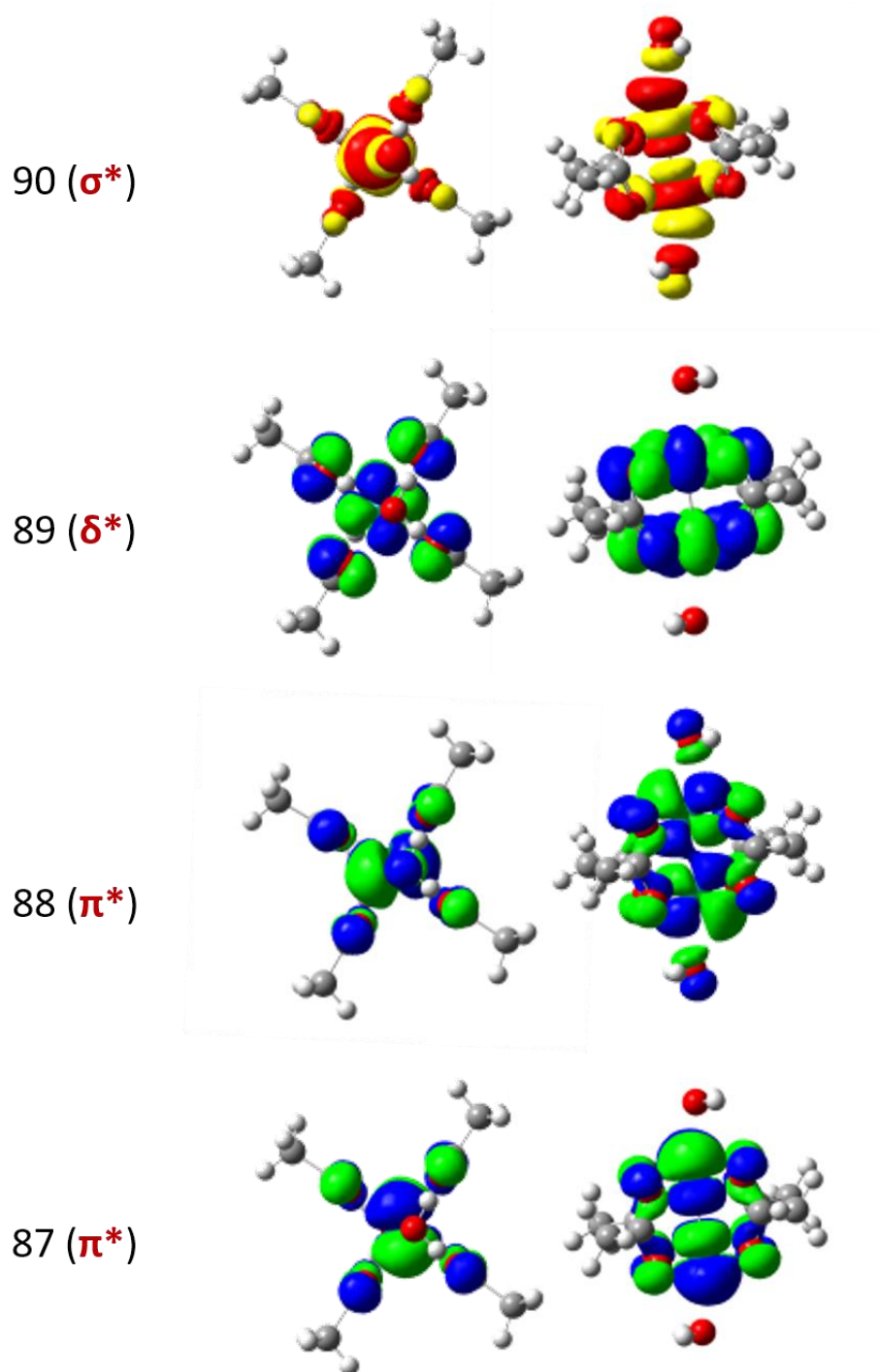
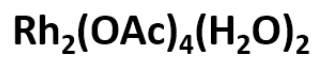


Fig S3. Expanded views of $\text{Rh}_2(\text{OAc})_4(\text{H}_2\text{O})_2$ molecular orbital surfaces, part 1/2. Calculations and image from A. Zhang in reference,¹ reproduced with permission from the Royal Society of Chemistry.

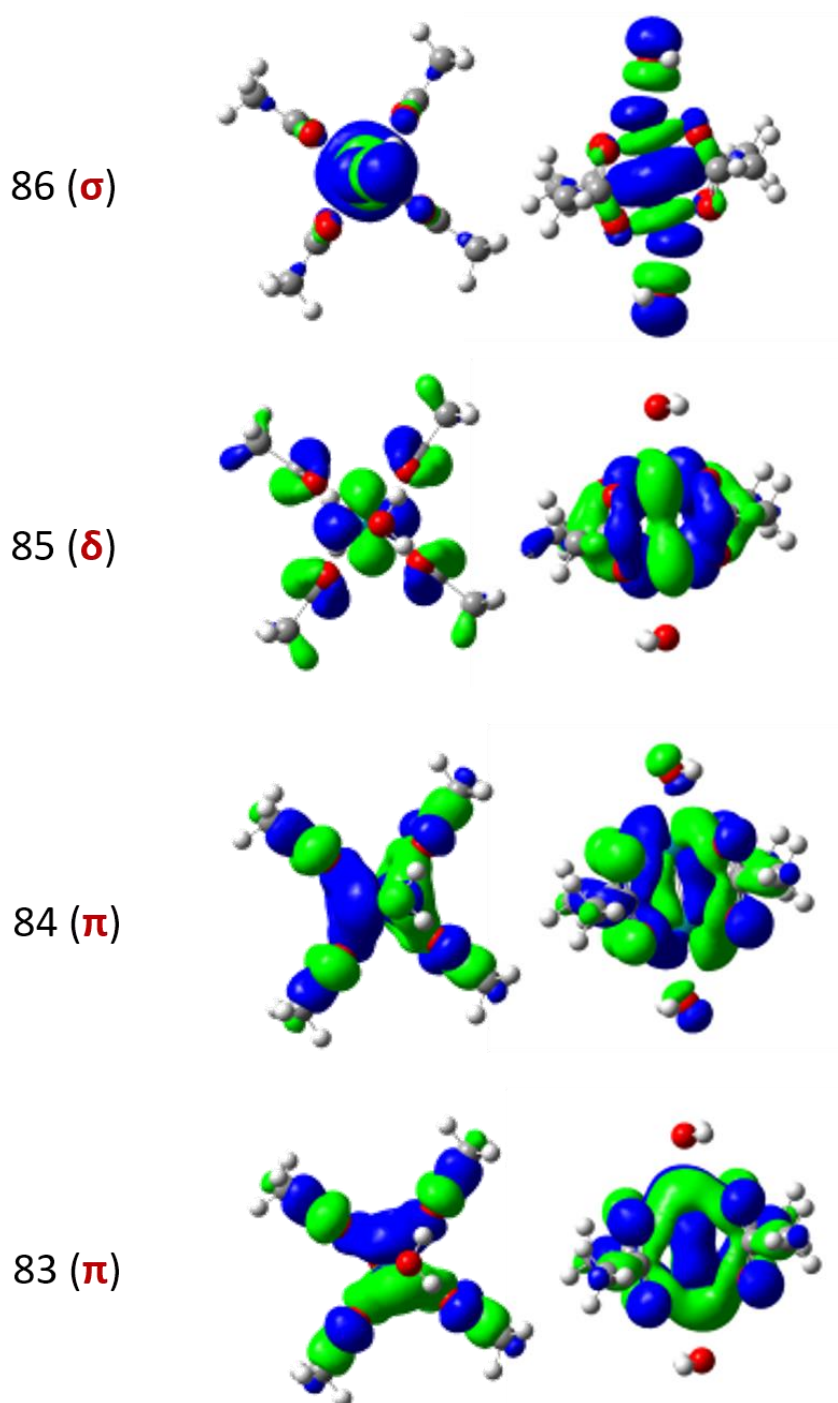
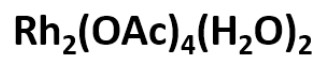


Fig S4. Expanded views of $\text{Rh}_2(\text{OAc})_4(\text{H}_2\text{O})_2$ molecular orbital surfaces, part 2/2. Calculations and image from A. Zhang in reference,¹ reproduced with permission from the Royal Society of Chemistry.

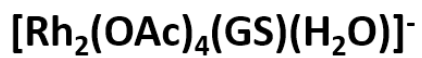
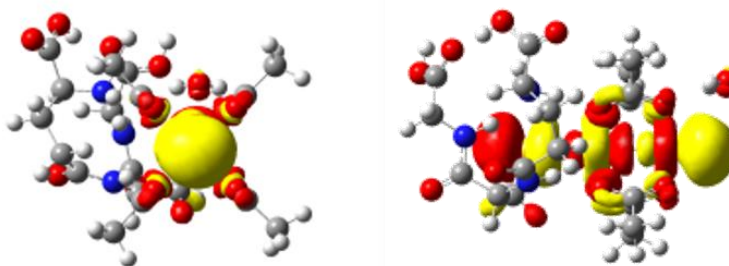
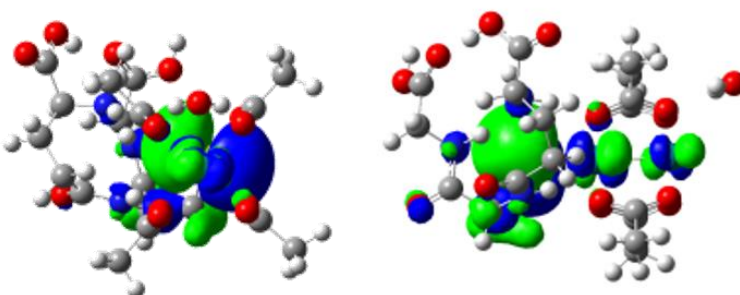
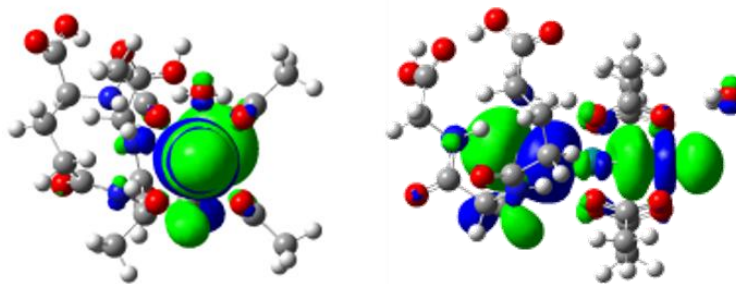
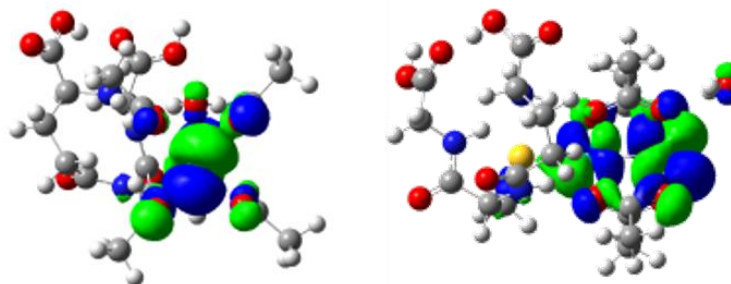
166 (σ^*)165 (π^*)164 (σ)163 (π^*)

Fig S5. Expanded views of $[\text{Rh}_2(\text{OAc})_4(\text{GS})(\text{H}_2\text{O})]^-$ molecular orbital surfaces, part 1/2. Calculations and image from A. Zhang in reference, ¹ reproduced with permission from the Royal Society of Chemistry.

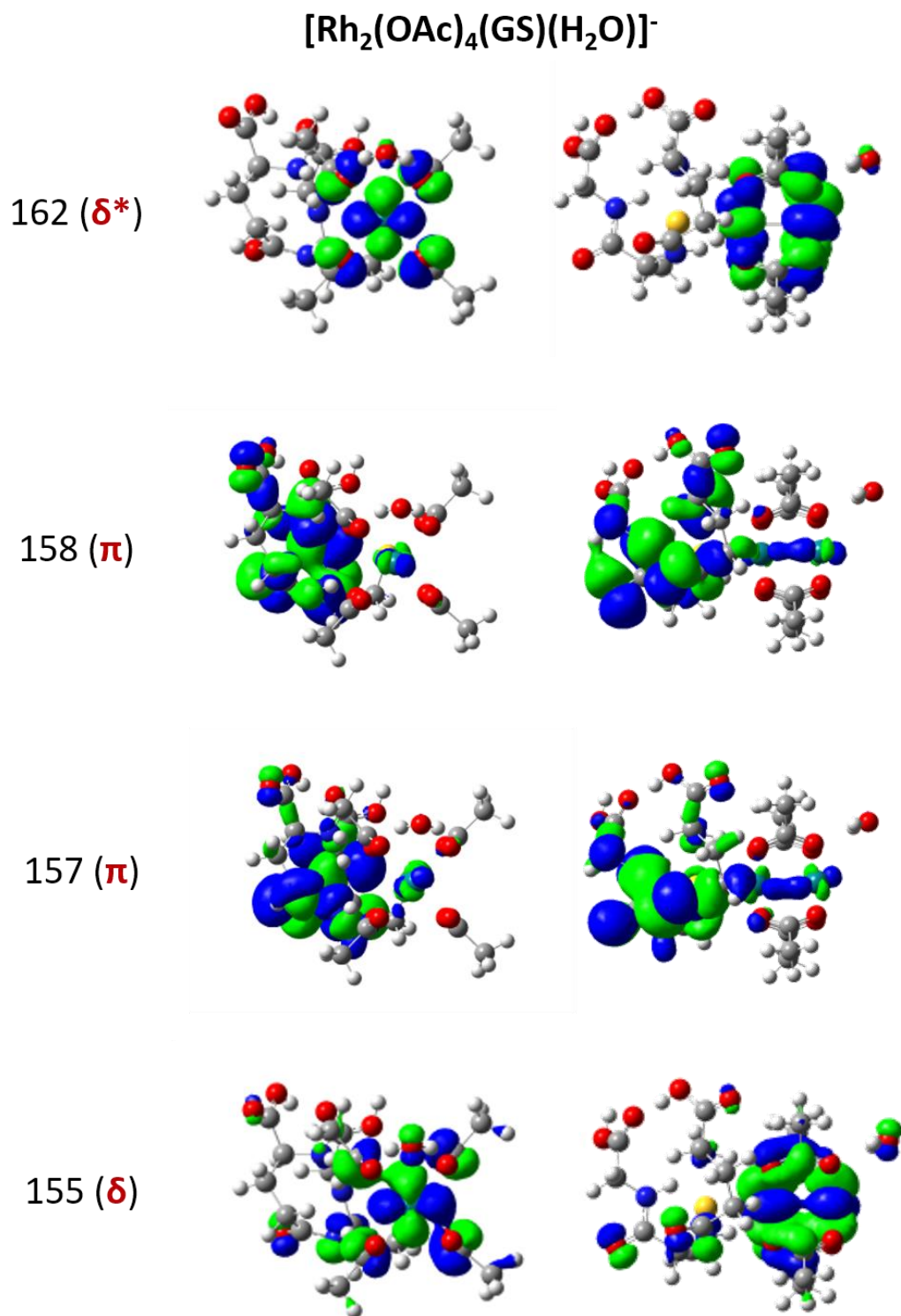


Fig S6. Expanded views of $[\text{Rh}_2(\text{OAc})_4(\text{GS})(\text{H}_2\text{O})]^-$ molecular orbital surfaces, part 2/2. Calculations and image from A. Zhang in reference,¹ reproduced with permission from the Royal Society of Chemistry.

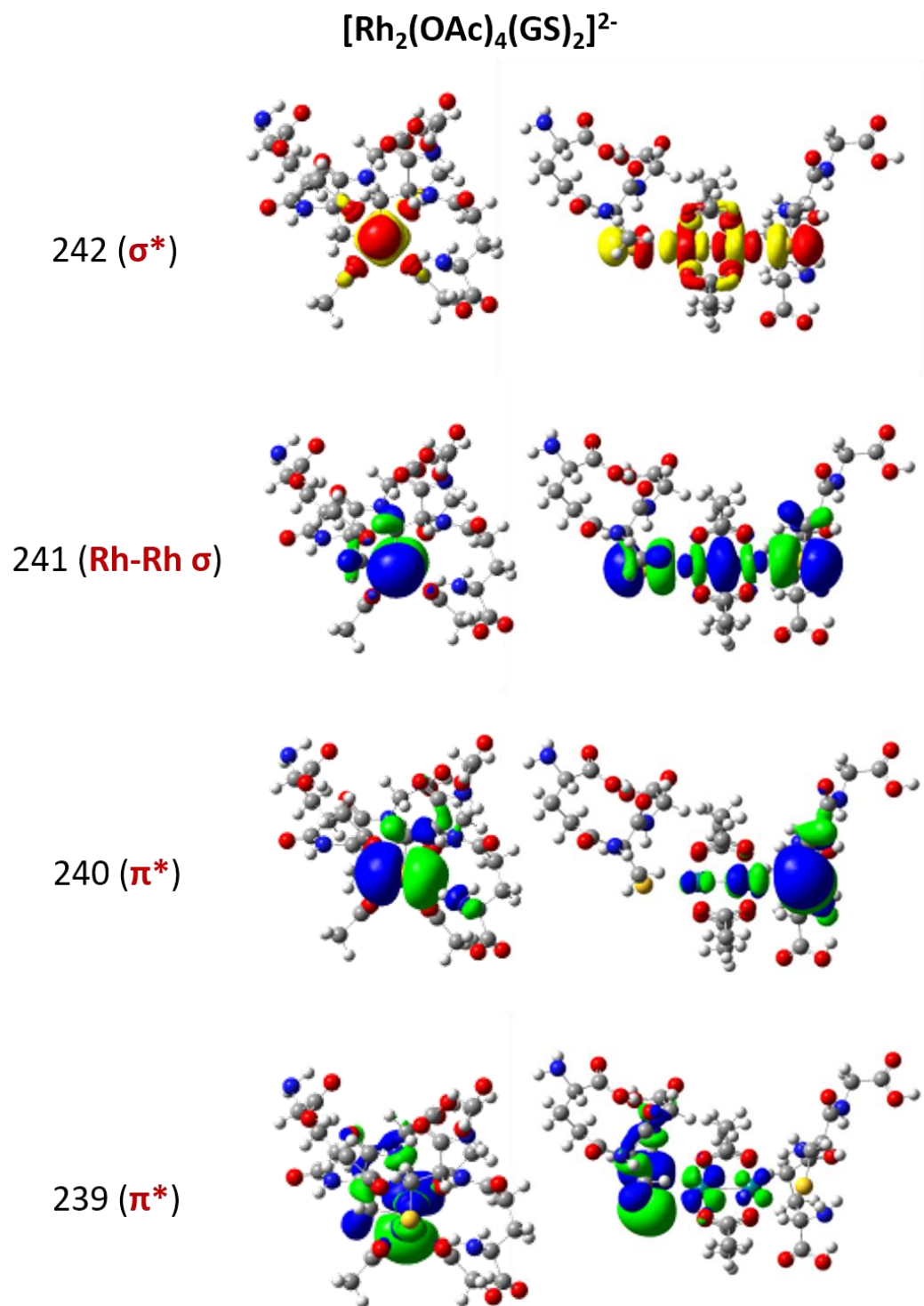


Fig S7. Expanded views of $[\text{Rh}_2(\text{OAc})_4(\text{GS})_2]^{2-}$ molecular orbital surfaces, part 1/2. Calculations and image from A. Zhang in reference,¹ reproduced with permission from the Royal Society of Chemistry.

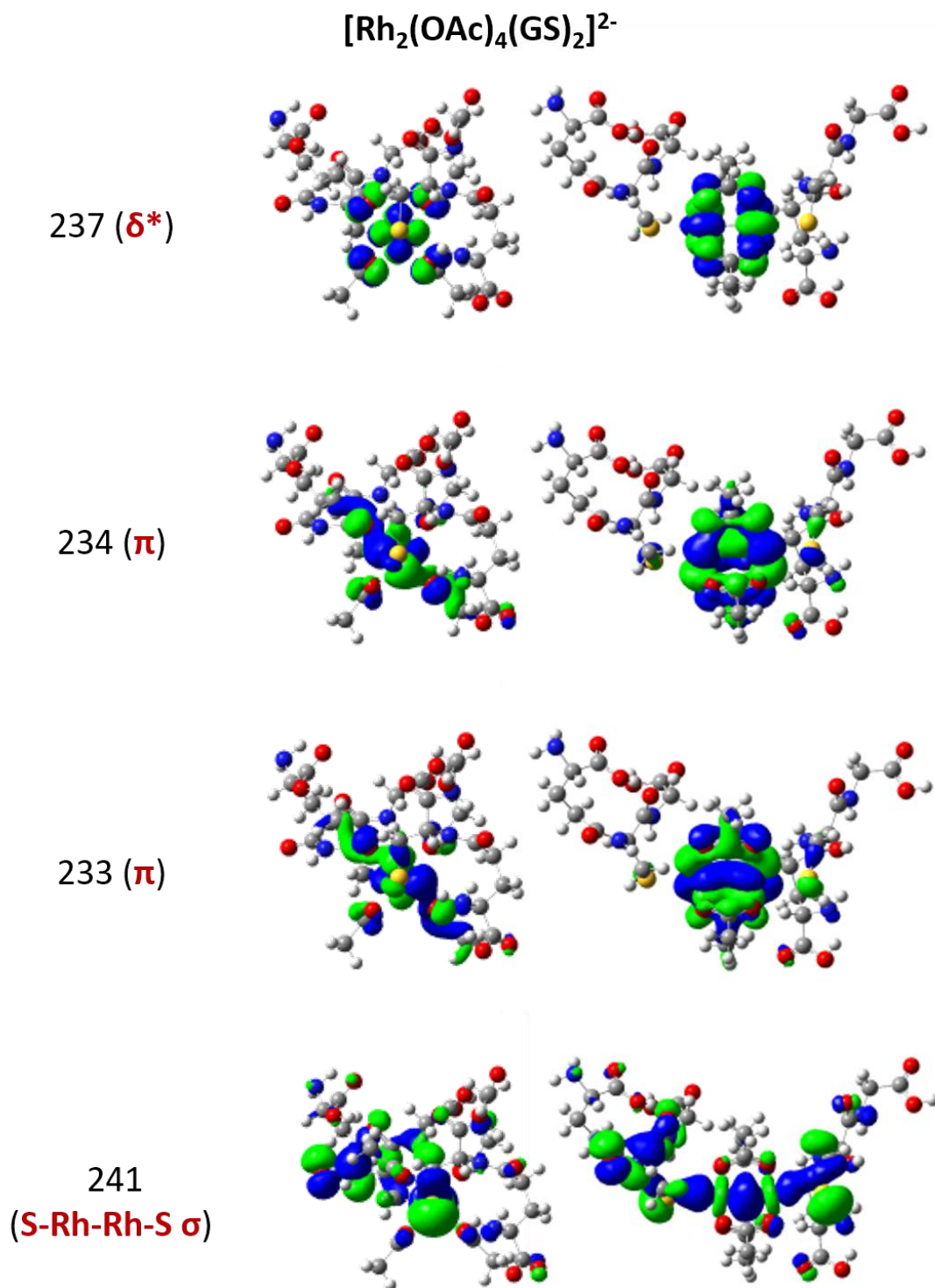


Fig S8. Expanded views of $[\text{Rh}_2(\text{OAc})_4(\text{GS})_2]^{2-}$ molecular orbital surfaces, part 2/2. Calculations and image from A. Zhang in reference, ¹ reproduced with permission from the Royal Society of Chemistry.

Table S1. Transition contributions for excited states (ES) with oscillator strength (f) greater than 0.001. Calculations from A. Zhang in reference, ¹ reproduced with permission from the Royal Society of Chemistry

Rh₂(OAc)₄				
ES	Transition	Contribution	Energy [eV (nm)]	f
1	72 → 80	0.12995	1.5418 (804.16)	0.0037
	78 → 80	0.67953		
2	71 → 80	0.13086	1.5426 (803.75)	0.0037
	77 → 80	0.67956		
14	72 → 80	0.68665	4.7555 (260.72)	0.0229
	78 → 80	-0.12489		
15	71 → 80	0.68635	4.7676 (260.06)	0.232
	77 → 80	-0.12557		
16	69 → 80	0.69654	5.1009 (243.06)	0.0140
17	68 → 80	0.69633	5.1094 (242.66)	0.0142
20	62 → 81	0.14182	5.3426 (232.07)	0.0643
	63 → 80	-0.14773		
	66 → 82	-0.12428		
	70 → 80	0.61243		
	79 → 87	-0.11805		
	79 → 88	0.14491		

Rh₂(OAc)₄2H₂O				
ES	Transition	Contribution	Energy [eV (nm)]	f
1	86 → 90	0.10876	2.2561 (549.55)	0.0034
	87 → 91	0.17148		
	88 → 90	0.65326		
2	80 → 90	0.10439	2.3078 (537.23)	0.0027
	87 → 90	0.65256		

	88 → 91	0.19584		
6	76 → 92	-0.11427	3.1246 (396.80)	0.0018
	84 → 92	-0.20679		
	87 → 90	-0.22219		
	88 → 91	0.61712		
7	74 → 92	-0.12927	3.1860 (389.15)	0.0019
	83 → 92	0.20788		
	87 → 91	0.62609		
	88 → 90	-0.19353		
15	72 → 91	0.13910	5.2099 (237.98)	0.1489
	75 → 92	-0.11732		
	86 → 90	0.61760		
	88 → 90	-0.10257		
	89 → 99	0.20974		

[Rh₂(OAc)₄1GS]⁻

ES	Transition	Contribution	Energy [eV (nm)]	f
1	153 → 166	-0.12239	2.0002 (619.85)	0.0013
	161 → 166	-0.30150		
	165 → 166	0.57168		
	165 → 167	-0.11791		
2	153 → 167	-0.12419	2.3540 (526.69)	0.0029
	161 → 167	-0.20202		
	161 → 169	0.10319		
	163 → 166	0.44851		
	163 → 167	0.12743		
	165 → 167	0.35148		
4	153 → 167	-0.13409	2.5712 (482.20)	0.0013
	161 → 167	-0.15160		
	162 → 169	0.14879		

	163 →166	-0.37276		
	163 →167	-0.12279		
	163 →169	0.14540		
	165 →166	0.13916		
	165 →167	0.43725		
6	161 →166	0.23994	2.7976 (443.18)	0.0016
	161 →169	0.32872		
	162 →169	-0.10429		
	163 →166	0.10738		
	163 →167	-0.24660		
	163 →169	0.34638		
	165 →166	0.20374		
	165 →169	-0.13194		
13	153 →167	0.19539	3.8002 (326.26)	0.0704
	154 →166	-0.10185		
	156 →166	-0.16372		
	161 →167	0.42275		
	163 →166	0.12060		
	164 →166	0.26718		
	165 →167	0.31264		
14	153 →167	-0.10584	3.8639 (320.88)	0.3938
	161 →167	-0.24010		
	164 →166	0.58547		
	165 →167	-0.15724		
15	138 →166	0.13137	4.0651 (305.00)	0.0569
	152 →166	0.22820		
	154 →166	0.23745		
	156 →166	0.46218		
	157 →166	0.12203		
	160 →166	-0.10821		
	161 →167	0.15066		

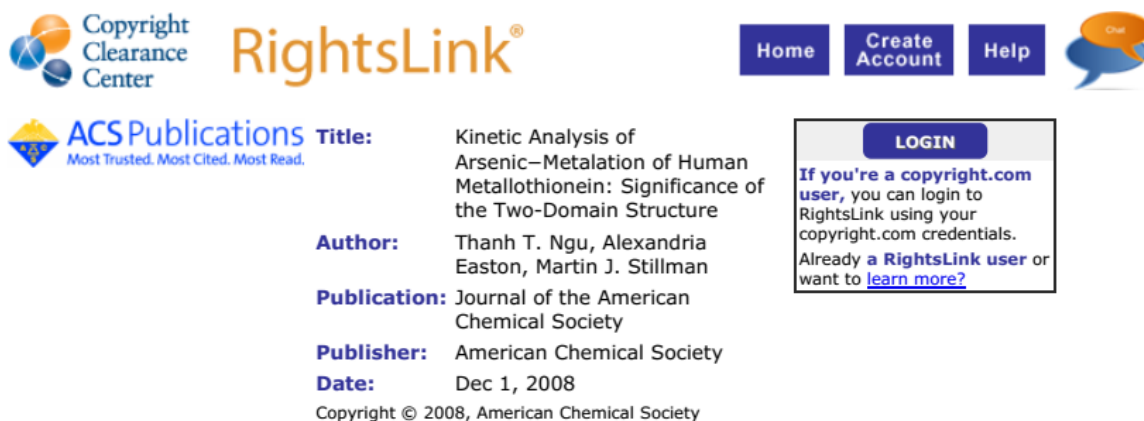
	163 → 166	-0.10670		
	164 → 166	0.19565		
[Rh₂(OAc)₄2GS]²⁻				
ES	Transition	Contribution	Energy [eV (nm)]	f
1	232 → 245	-0.12926	2.3396 (529.93)	0.0029
	235 → 242	0.13289		
	235 → 244	-0.14224		
	236 → 242	0.42475		
	236 → 244	-0.21641		
	239 → 242	-0.21184		
	239 → 244	0.15268		
	240 → 242	0.29186		
	240 → 244	-0.11257		
2	234 → 245	-0.12280	2.3866 (519.50)	0.0021
	235 → 242	0.31121		
	235 → 244	0.16534		
	236 → 244	-0.17550		
	238 → 242	0.28945		
	238 → 244	0.22085		
	239 → 242	-0.23043		
	240 → 242	-0.19450		
	240 → 244	-0.20986		
9	232 → 245	0.12454	2.9522 (419.98)	0.0035
	233 → 244	0.14644		
	234 → 244	-0.14958		
	235 → 244	0.17043		
	235 → 245	0.22699		
	236 → 242	0.15648		
	236 → 244	0.33913		

	236 → 245	-0.15082		
	238 → 245	0.25701		
	239 → 242	-0.11774		
	239 → 244	-0.13665		
	240 → 245	-0.10547		
	241 → 244	-0.11128		
12	241 → 242	0.67072	3.4198 (362.55)	0.7178

1. D. L. Wong, A. Zhang, A. S. Faponle, S. P. de Visser and M. J. Stillman, Glutathione binding to dirhodium tetraacetate: a spectroscopic, mass spectral and computational study of an anti-tumour compound, *Metallomics*, 2017, **9**, 501-516.

Appendix E: Copyright Permissions

In Chapter 1 and 7, all figures were made by Ms. Daisy Wong and are unpublished elsewhere, except for Figure 1-10 which was used with permission from the American Chemical Society from the article “Kinetic Analysis of Arsenic-Metalation of Human Metallothionein: Significance of the Two-Domain Structure” by Ngu et al. and their permission requirements have been followed as described below.



Copyright Clearance Center **RightsLink®** Home Create Account Help Chat

ACS Publications Most Trusted. Most Cited. Most Read.

Title: Kinetic Analysis of Arsenic–Metalation of Human Metallothionein: Significance of the Two-Domain Structure

Author: Thanh T. Ngu, Alexandria Easton, Martin J. Stillman

Publication: Journal of the American Chemical Society

Publisher: American Chemical Society

Date: Dec 1, 2008

Copyright © 2008, American Chemical Society

LOGIN

If you're a **copyright.com** user, you can login to RightsLink using your copyright.com credentials. Already a **RightsLink** user or want to [learn more?](#)

PERMISSION/LICENSE IS GRANTED FOR YOUR ORDER AT NO CHARGE

This type of permission/license, instead of the standard Terms & Conditions, is sent to you because no fee is being charged for your order. Please note the following:

- Permission is granted for your request in both print and electronic formats, and translations.
- If figures and/or tables were requested, they may be adapted or used in part.
- Please print this page for your records and send a copy of it to your publisher/graduate school.
- Appropriate credit for the requested material should be given as follows: "Reprinted (adapted) with permission from (COMPLETE REFERENCE CITATION). Copyright (YEAR) American Chemical Society." Insert appropriate information in place of the capitalized words.
- One-time permission is granted only for the use specified in your request. No additional uses are granted (such as derivative works or other editions). For any other uses, please submit a new request.

The figures used in Chapters 2, 3, 4, and 6 were created by Ms. Daisy Wong and published in Royal Society Journals, and their permission requirements have been followed as described below.

Author reusing their own work published by the Royal Society of Chemistry

You do not need to request permission to reuse your own figures, diagrams, etc, that were originally published in a Royal Society of Chemistry publication. However, permission should be requested for use of the whole article or chapter except if reusing it in a thesis. If you are including an article or book chapter published by us in your thesis please ensure that your co-authors are aware of this.

Reuse of material that was published originally by the Royal Society of Chemistry must be accompanied by the appropriate acknowledgement of the publication. The form of the acknowledgement is dependent on the journal in which it was published originally, as detailed in 'Acknowledgements'.

The images used in Chapter 6 are open for public use under the American Chemical Society AuthorChoice License:

Metallothionein: An Aggressive Scavenger—The Metabolism of Rhodium(II) Tetraacetate ($\text{Rh}_2(\text{CH}_3\text{CO}_2)_4$)

Daisy L. Wong  and Martin J. Stillman* 

Department of Chemistry, The University of Western Ontario, 1151 Richmond Street, N6A 5B7 London, Ontario, Canada

ACS Omega, 2018, 3 (11), pp 16314–16327

DOI: 10.1021/acsomega.8b02161

Publication Date (Web): November 30, 2018

Copyright © 2018 American Chemical Society

*E-mail: stillman@uwo.ca.

ACS AuthorChoice - This is an open access article published under an ACS AuthorChoice License, which permits copying and redistribution of the article or any adaptations for non-commercial purposes.

 Cite this: ACS Omega 2018, 3, 11, 16314-16327

 RIS Citation 

Curriculum Vitae

Name: Daisy Wong

Post-secondary Education and Degrees: The University of Western Ontario
London, Ontario, Canada
2009-2014 B.Sc. 2014-2019 Ph.D.

Honours and Awards: Ontario Graduate Scholarship
2014-2015, 2017-2018, 2018-2019

Related Work Experience

Teaching Assistant
The University of Western Ontario
2014-2018

Substitute Lecturer
The University of Western Ontario
2014-2018

CanBIC Local Organizing Committee
Georgian Bay Conference on Bioinorganic Chemistry
2011, 2015, 2017, 2019

Publications:

1. "Kinetics of competitive Cd²⁺ binding pathways: the realistic structure of intrinsically disordered, partially metallated metallothioneins" D. L. Wong, N. C. Korkola, M. J. Stillman. (2019) *Metallomics* DOI: 10.1039/C8MT00347E
2. "Metallothionein: An Aggressive Scavenger—The Metabolism of Rhodium(II) Tetraacetate (Rh₂(CH₃CO₂)₄)" D. L. Wong & M. J. Stillman, (2018) *ACS Omega*, 3(11), 16314-16327.
3. "Capturing Platinum in Cisplatin: Kinetic Reactions with Recombinant Human apo-Metallothionein 1a" D. L. Wong & M. J. Stillman, (2018) *Metallomics*, 10(5), 713-721.
4. "Glutathione binding to dirhodium tetraacetate: a spectroscopic, mass spectral and computational study of possible deactivation processes of an anti-tumour compound", Wong, D. L., Zhang, A., Faponle, A. S., de Visser, S. P., & Stillman, M. J. (2017). *Metallomics*, 9(5), 501-516. DOI: 10.1039/C7MT00040E
5. "Stepwise copper(I) binding to metallothionein: a mixed cooperative and non-cooperative mechanism for all 20 copper ions," Scheller, J. S., Irvine, G. W., Wong, D. L., Hartwig, A., & Stillman, M. J. (2017). *Metallomics*, 9(5), 447-462. DOI: 10.1039/C7MT00041C
6. "Lead(II) Binding in Metallothioneins" in *Lead: Its Effects on Environment and Health*, Volume 17 of *Metals Ions in Life Sciences*, Wong, D. L., Merrifield-MacRae,

M. E., & Stillman, M. J. (2017). Edited by Sigel, Astrid / Sigel, Helmut / Sigel, Roland K.O., ISSN 1559-0836, Berlin, Boston: De Gruyter.

7. "Destructive interactions of dirhodium(II) tetraacetate with β -metallothionein rh1a" Wong & M. J. Stillman, 52, (2016). *Chemical Communications*, D. L.: 5698-5701. DOI: 10.1039/C5CC10319C.

Publications in Progress

1. "Spectroscopic and molecular orbital study of bulky fluorinated Zinc phthalocyanines: extreme electron-withdrawing groups and their effect on tetrapyrrole electronic structures, aggregation and reactivity." D. L. Wong, D. Chan, A. Zhang, H. H. Patel, C. Colomier, R. D. Cohen, A. P. J. Brunskil, A. Loas, S. M. Gorun, and M. J. Stillman. Manuscript completed.
2. "Metallothioneins." D. L. Wong and M. J. Stillman in *Comprehensive Coordination Chemistry III, Volume 8: Bio-Coordination Chemistry*, Eds. Y. Lu and L. Que, Jr., Elsevier. Manuscript completed.

Selected International Presentations

Oral Presentations

1. 2017-08-16 – "Anti-Tumour Complex $\text{Rh}_2(\text{OAc})_4$ and its Interactions with Glutathione and Human Metallothionein;" 6th International Symposium on Metallomics, Vienna, Austria
2. 2017-05-25 – "Anti-Tumour Complex $\text{Rh}_2(\text{OAc})_4$ and its Interactions with Glutathione and Human Metallothionein;" 6th Georgian Bay Conference on Bioinorganic Chemistry (CANBIC), Parry Sound, Canada
3. 2017-01-27 - "Mass Spectrometric Studies of Human Metallothionein and Glutathione Binding to the Anti-tumour Complex, Dirhodium Tetraacetate"; Gordon Research Seminar: Bioinorganic Chemistry, Ventura, CA, USA, Jan 26-29, 2017.
4. 2015-07-24 – "Studies of Dirhodium(II) Tetraacetate with Human Metallothionein", Poster Slam Oral Presentation, 17th International Conference on Biological Inorganic Chemistry, China National Convention Centre, Beijing, China

Poster Presentations

1. 2018-07-5 - "Farming Photons: Fluorinated Zn-Phthalocyanine Photosensitizers in Dye Sensitized Solar Cells" 10th International Conference on Porphyrins and Phthalocyanines: Munich, Germany, July 1-6, 2018
2. 2017-01-24 - "Mass Spectrometric Studies of Human Metallothionein and Glutathione Binding to the Anti-tumour Complex, Dirhodium Tetraacetate"; Gordon Research Conference: Metals in Biology, Ventura, CA, USA, Jan 22-27, 2017
3. 2015-07-21 – "Studies of Dirhodium(II) Tetraacetate with Human Metallothionein", 17th International Conference on Biological Inorganic Chemistry, China National Convention Centre, Beijing, China
4. 2015-07-14 – "Studies of Dirhodium(II) Tetraacetate with Human Metallothionein", 5th Asian Coordination Chemistry Conference, University of Hong Kong, Hong Kong (SAR), China